DEUTSCHES ELEKTRONEN-SYNCHROTRON

DESY-THESIS-2002-002
January 2002

Measurement of Diffractive Heavy Vector Meson Photoproduction at HERA with the ZEUS Detector

by

B. Mellado

ISSN 1435-8085

NOTKESTRASSE 85 - 22607 HAMBURG

To be sure that your reports and preprints are promptly included in the HEP literature database
send them to (if possible by air mail):

DESY Zentralbibliothek Notkestraße 85 22603 Hamburg Germany	DESY Bibliothek Platanenallee 6 15738 Zeuthen Germany

Measurement of Diffractive Heavy Vector Meson Photoproduction at HERA with the ZEUS Detector

Bruce Mellado

Submitted in partial fulfillment of the
requirements for the degree
of Doctor of Philosophy
in the Graduate School of Arts and Sciences
COLUMBIA UNIVERSITY

2001

Abstract

Measurement of Diffractive Heavy Vector Meson Photoproduction at HERA with the ZEUS Detector

Bruce Mellado

The central aim of this thesis has been the measurement of the elastic process $ep \to eJ/\psi p$, studied through the electronic decay in the photoproduction regime over a larger energy range than attained in previous measurements. This has been achieved by the development of a new trigger algorithm, the calibration of the ZEUS calorimeter in a dynamic range unexplored before, and extensive detector and background studies. Results have been obtained with data collected during the 1999 and 2000 running periods. The accuracy of these results largely overshoots that of previous measurements and allow us to draw two main conclusions: data are consistent with no saturation; the photoproduction of J/ψ is driven by a mixture of "hard" and "soft" physics. The cross-section ratio, $\sigma(\psi(2S))/\sigma(J/\psi)$, has been calculated using the electron decay channel and is consistent with the suppression of the production of $\psi(2S)$ with respect to that of the J/ψ, as expected by the quark parton model. Results of the search for Υ resonances using the electron decay channel with data taken during the 1996-2000 running periods have been reported. No clear evidence of Υ resonances has been found. An overview of VM production at HERA has shown that $Q^2 + M_V^2$ is a good choice of the scale of the interaction. Data indicate that the dynamics that drive the increase with energy of the total DIS and VM cross-sections are similar.

Contents

List of Figures

List of Tables

Acknowledgments

Graduate school has been an extraordinarily challenging and intense experience that has changed me as a person. It is a chapter in my life I will never be able to forget and which I will always relate to in the future. The knowledge and experience acquired during these years has changed forever my way of thinking and approaching problems in science and my interaction with people.

At the center of this experience stand two outstanding physicists, Allen and Frank. Their leadership and guidance have been crucial during these years of work within the Columbia group. Their competence as scientists and leaders is stunning. It is not only their competence in particular questions of the physics and experimental techniques developed in ZEUS the only valuable thing that they were able to teach me. It is their way of approaching and solving problems, their ability to establish the right balance between theory and experiment, physics analysis and hardware, and to define the strategic guidelines for the accomplishment of scientific goals that I came to appreciate most. Without a clear scientific method it is almost impossible to achieve a goal in science as the path to it is never straightforward. I can only be thankful for everything that I have managed to learn from these great teachers.

I do not want to downplay the tremendous significance of my interaction with the other physicists of the ZEUS Collaboration. ZEUS has been an extraordinary school of physics. I would like to thank all the physicists of the ZEUS Collaboration for the invaluable experience obtained during these years of interaction. I would specially like to thank an outstanding physicist, Erich, whose ability to discern between the relevant and the secondary issues in the solution of physics problems and to focus on the essence

of the physics analysis has impressed me greatly. Equally impressive is his extensive scientific knowledge. Now I regret not having had the chance to learn more from him.

I would like to give special thanks to Sasha, Laura, Tetsuo and the coordinators of the diffractive group, Michele, Peppe, Pat and Yuji. Their help and competence have been central throughout the course of the work on the physics analyses. I also wish to give thanks for their help to Robert, Alessia, Alessandro, Leszek, Florian, Mario and Marc. I am indebted to Halina and Aharon for most valuable discussions on vector meson production at HERA.

I would like to thank the managements of the ZEUS Collaboration and DESY for encouraging scientific research, crucial for acquiring hardware and analysis experience and bringing to completion this thesis work.

Many thanks to all the members of the thesis committee for taking the time to go through the thesis, specially to Al Mueller for his guidance in the latest stage of the thesis writing.

On a personal note I would love to thank Raphe, Tulika, Xiang, Sampa and John for their warmth and comprehension. They have filled with joy what is supposed to be the hardest stage of thesis writing.

I am immensely indebted to Mara, my parents, Rafael and Maribel, my sister, Elena, and my brother, Pablo, for their love and comprehension in this difficult stage of my life. To them I dedicate this work.

Preface

HERA is an accelerator complex that collides electrons, e (or the anti-matter equivalent with positive charge, positrons, e^+) with protons, p, at very high energies. The electrons are particles without internal structure. The protons, on the contrary, are known to have constituents: quarks and gluons (or generically, partons). From ep collisions, physicists want to learn how quarks and gluons interact with each other. This is a fundamental question of modern particle physics, that will also shed light on one of the existing puzzles: why have "bare" quarks and gluons never been observed in nature but appear to be confined in larger particles like the proton?

In ep collisions the electron interacts with the constituents of the proton via the emission of a photon. This photon carries a significant fraction of the energy of the incoming electron and has a certain wavelength. Depending on the wavelength of the photon two qualitatively different types of interactions are identified: short distance or "hard" interactions and long distance or "soft" interactions.

The theoretical framework that describes the dynamics of the interactions between quarks and gluons is Quantum Chromodynamics (QCD). HERA is an ideal scenario to test and refine QCD, particularly in a kinematic region where theoretical predictions are difficult or impossible. QCD is well able to describe with high accuracy the dynamics of "hard" interactions. Quarks and gluons couple to each other with a coupling strength, α_s, which depends on how "hard" the interaction is. The "harder" the interaction, the smaller α_s is. While calculations are reliable for $\alpha_s \ll 1$, in the regime of "soft" interactions or large α_s ($\alpha_s \approx 1$), such calculations are unreliable. The dynamics of these "soft" interactions are related closely to the dynamics of confinement.

In collisions, quarks and gluons are likely to radiate other quarks and gluons so that a high density of partons will exist. The more energy transmitted in the collision, the more QCD radiation is expected. The density of partons cannot increase indefinitely, it should saturate at some point. The identification and understanding of high density QCD (saturation) is a challenge both theoretically and experimentally.

At HERA, electrons and protons are collided at energies much larger than the binding energy of the constituents of the proton. One can think of an ep collision at HERA as a solid object violently hitting a fragile bag containing quarks and gluons loosely bound to each other. One might expect this compound object to radiate a huge number of partons in such a collision. However, HERA surprised the physics community with the observation that in a significant fraction of ep collisions the proton does not even break up. This phenomenon, observed earlier in hadron-hadron collisions, is called diffraction. The high rate of diffractive reactions at HERA must be a reflection of the dynamics of confinement.

Diffractive processes at HERA have become an attractive laboratory in which to attack the challenges mentioned above. In this work, the diffractive production of J/ψ mesons in the reaction $ep \to eJ/\psi p$ is reported. The optical theorem predicts that the energy dependence of the rate of the production of J/ψ is steep. This enhances the sensitivity of the reaction $ep \to eJ/\psi p$ to possible saturation effects. Additionally, the kinematics of the production of J/ψ requires that the radiated photon have a wavelength between the "hard" and "soft" regimes. In conclusion, the reaction $ep \to eJ/\psi p$ opens a window of opportunity to search for saturation effects and study the interplay between "hard" and "soft" QCD interactions.

In order to maximally exploit the reaction $ep \to eJ/\psi p$ to study these effects, it was necessary to extend the energy range of the measurement. This represented an experimental challenge. An experimental technique was developed to meet this challenge and results of the rate of the production of J/ψ at HERA are reported.

Chapter 1

Introduction

1.1 The Standard Model

The present level of knowledge about the structure of nature is embodied by the Standard Model (SM). The HERA [1] accelerator at DESY [2] and its experiments are primarily meant to scrutinize the consistency of the Standard Model via the exploration of the structure of the proton. During its ten years of operation HERA has made an incalculable contribution to the present knowledge of the dynamics of the micro-world. In particular, HERA has driven one part of the Standard Model, QCD, to a higher level of development. The knowledge of the structure of the proton acquired at HERA is crucial for the planning and interpreting of future searches for the Higgs boson, one of the cornerstones of the SM.

1.1.1 Fundamental Particles

The SM provides a classification, Table 1.1, of the fundamental particles known today. There are six leptons classified according to their electromagnetic charge, Q_{em}, electron number, muon number and tau number. They fall into three families or generations.

[1] Hadron-Elektron-Ring-Anlage.

[2] Deutsches Elektronen-Synchrotron.

There are also six antileptons with all electromagnetic charge signs reversed. The positron, for instance, carries charge of +1 and electron number -1, etc... Quarks, as

	Leptons		Quarks	
	l	Q_{em}	q	Q_{em}
First Generation	e	-1	d	$-\frac{1}{3}$
	ν_e	0	u	$\frac{2}{3}$
Second Generation	μ	-1	s	$-\frac{1}{3}$
	ν_μ	0	c	$\frac{2}{3}$
Third Generation	τ	-1	b	$-\frac{1}{3}$
	ν_τ	0	t	$\frac{2}{3}$

Table 1.1: Leptons and quarks in the Standard Model are classified in three generations.

leptons, are fermions, particles with spin $\frac{1}{2}$ and share the similarity that they become heavier as one goes from the first generation to the third generation. There are six "flavors" of quarks. Again, all signs would be reversed in the table of antiquarks. Each quark and antiquark comes in three colors.

1.1.2 Fundamental Forces and Interactions

There are four kinds of fundamental forces known in nature: gravitational, weak, electromagnetic and strong. Each of these forces is mediated by the exchange of gauge bosons. The electromagnetic charge and the mass of the gauge bosons are given in Table 1.2. The electromagnetic and weak forces are unified in the Standard Model. The fields associated with these forces, as well as the fields associated with the strong force, are spin-1 fields, describing the photon γ, the electroweak gauge bosons $W^{\pm}$ and Z, and the gluons g. The interactions of the force fields with the fermionic constituents of matter as well as their self-interactions are described by Abelian and non-Abelian $SU(3) \times SU(2) \times U(1)$ gauge theories.

Gauge Bosons		
B	Q_{em}	M (GeV/c^2)
γ	0	0
$W^{\pm}$	± 1	80.42
Z^0	0	91.19
gluon	0	0

Table 1.2: Gauge Bosons in the Standard Model.

1.1.3 Strong Interaction and QCD

The theory of strong interactions, Quantum Chromodynamics (QCD), relies on the idea of quarks and the color degree of freedom.

The theory of strong interactions needed to accommodate the fact that quarks behave as free particles in collisions, referred to as asymptotic freedom. The solution of the problem came with the renormalibility of non-Abelian gauge theories. The coupling of QCD can be expressed in leading order as:

$$\alpha_s(Q^2) = \frac{1}{-\beta_0/(4\pi)\log(Q^2/\Lambda^2_{QCD})} \tag{1.1}$$

where Q^2 sets the scale of the interaction (see Section 1.2.1) and β_0 is a parameter. The coupling $\alpha_s(Q^2)$ decreases with Q^2 and approaches zero in the limit of a very large energy (or momentum transfer):

$$\alpha_s(Q^2) \to 0 \qquad \text{for} \qquad Q^2 \to \infty \tag{1.2}$$

For Q^2 much larger than Λ^2_{QCD}, the value of the coupling constant, α_s, is small and a perturbation description is valid for the strong interactions. Such calculations break down for $Q^2 \lesssim \Lambda^2_{QCD}$ as the value of α_s grows large. The value of Λ^2_{QCD} marks the boundary between a world of quasi-free quarks and gluons and a world of hadrons. This scale has to be determined experimentally and turns out to be ≈ 300 MeV^2.

Interactions at a scale much larger than Λ^2_{QCD} are called "hard" interactions. Interactions which are at a scale comparable to or smaller than Λ^2_{QCD} are considered

"soft" and are generally not calculable with perturbative QCD. The problem of non-perturbative QCD is closely related to the question of confinement [3]. The study of the intermediate region between these two kinds of processes, the transition region, is a major motivation behind this work.

1.2 Deep Inelastic Scattering (DIS)

With the construction of the linear accelerator at SLAC [4], experiments on ep deep inelastic scattering (DIS) gave direct evidence that protons have internal structure [1]. The deep inelastic structure functions were found to be independent of the momentum transfer between the incoming electron and the target proton and only depend on the Bjorken scaling variable x [2] (Scaling).

Feynman introduced the parton model, a picture to understand the data at SLAC [3]. The model assumes the proton to consist of point-like constituents, or partons. It was suggested [4] that the partons in nucleons were quarks. This is commonly known as the Quark Parton Model (QPM).

A number of fixed target experiments to study DIS were performed after the observation of scaling. These experiments collided leptons with hadron targets. HERA allows the extension by two orders of magnitude the kinematic coverage toward very large values in the momentum transfer and toward very low values in x.

1.2.1 Kinematics of DIS

The scattering of unpolarized electrons (positrons) on unpolarized protons, as found from leading order in perturbation theory is shown in Figure 1.1 and is described through the exchange of an electroweak gauge boson. The electron (positron) and

[3] Confinement is an expression of the fact that "bare" quarks or gluons have never been observed experimentally.

[4] Stanford Linear Accelerator Center.

proton in the initial state are denoted by the four vectors e and p, respectively. The final state consists of the scattered lepton and the hadronic final state system with four vectors e' and p', respectively. Depending on the type of the exchanged electroweak gauge boson, one distinguishes two classes of events: Neutral Current (NC) (electroweak gauge boson: virtual photon γ^* or Z^0 boson) and Charged Current (CC) (electroweak gauge boson: $W^\pm$ boson) events.

The following variables provide a relativistically-invariant formulation of the unpolarized inelastic ep event kinematics [5]:

$$s = (e+p)^2 \simeq 4E_eE_P \tag{1.3}$$

$$Q^2 = -(e-e')^2 = -(p-p')^2 = -q^2 \tag{1.4}$$

$$x = \frac{Q^2}{2(p\cdot q)} \quad 0 \le x \le 1 \tag{1.5}$$

$$y = \frac{p\cdot q}{p\cdot e} \quad 0 \le y \le 1 \tag{1.6}$$

$$W^2 = (p+q)^2 = (p')^2 = m_p^2 + \frac{Q^2}{x}(1-x) \approx y\,s \tag{1.7}$$

s is the square of the center-of-mass energy of the electron-proton system. With $E_e = 27.5\,\text{GeV}$ and $E_P = 820,920\,\text{GeV}$, the center-of-mass energy at HERA is $300,320\,\text{GeV}$. W is the center-of-mass energy of the gauge boson proton system. The kinematically accessible region is $W < \sqrt{s}$. The Bjorken scaling variable, x, is interpreted in the QPM as the fraction of the proton momentum carried by the struck parton. The fraction of the incoming electron energy carried by the exchanged gauge boson, y, in the rest frame of the proton, is also known as inelasticity. The momentum transfer squared, Q^2, is related to x and y in DIS by $Q^2 \simeq s\,x\,y$.

[5] In this work, the natural system of units is used, i.e. $\hbar = 1$ and $c = 1$.

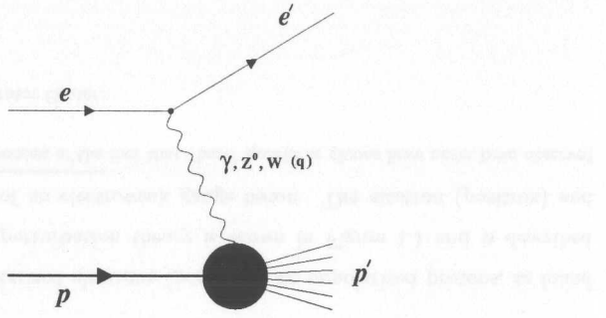

Figure 1.1: Feynman diagram describing unpolarized ep scattering to lowest order perturbation theory.

1.2.2 Structure Functions and Parton Densities

NC scattering is considered first. The cross-section, σ, in terms of y and Q^2 is related to the proton structure function, F_2 [5]:

$$\left(\frac{d^2\sigma}{dydQ^2}\right) = \frac{2\pi\alpha_{em}^2 Y_+}{yQ^4}\left(F_2 - \frac{y^2}{Y_+}F_L\right) \tag{1.8}$$

where α_{em} is the electromagnetic coupling, $Y_+ = 1 + (1-y)^2$ and $F_L = F_2 - 2xF_1$ is known as the longitudinal structure function.

Additionally, one can interpret the ep cross-section as the product of a flux of virtual photons and the total cross-section $\sigma_{tot}^{\gamma^* p}$ for the scattering of virtual photons on protons [5]. At small enough Q^2 the following relation holds:

$$\sigma_{tot}^{\gamma^* p} \approx \frac{4\pi^2\alpha_{em}}{Q^2}F_2(x,Q^2) \tag{1.9}$$

At fixed Q^2, $\sigma_{tot}^{\gamma^* p} \propto W^\lambda$, where λ is a parameter extracted from data. From Equation (1.9) it follows:

$$F_2 \propto x^{-\lambda} \tag{1.10}$$

The kinematic plane available in x and Q^2 of the proton structure function for various fixed target experiments and HERA collider experiments, H1 and ZEUS, is shown

in Figure 1.2. The fixed target experiments contributing to this plot are NMC [6], BCDMS [7], E665 [8], SLAC, CCFR [9].

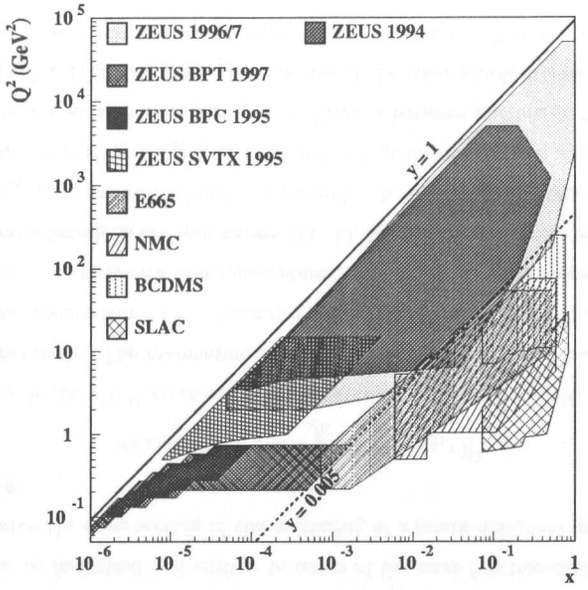

Figure 1.2: Kinematic plane in the $Q^2 - x$ of the measurement of the structure function of the proton for various fixed target experiments and HERA collider experiments, H1 and ZEUS.

DIS may be viewed within the framework of the QPM where the proton consists of point-like constituents that move freely inside it. If one views ep scattering as incoherent electromagnetic scattering of electron-partons, then

$$F_2(x) = x \sum_i e_i^2 f_i(x) \tag{1.11}$$

[6]New Muon Collaboration, experiment at CERN.
[7]Bologna, CERN, Dubna, Munich, Saclay.
[8]Collaboration at FNAL.
[9]Columbia, Chicago, FNAL, Rochester.

where e_i is the charge of parton i in units of the proton charge, and f_i is the distribution of probability density [10] of finding a parton i with a fractional momentum x.

The parton densities in the hadron cannot be calculated from QCD with the tools available today. However, based on the factorization theorem [6], QCD can tell us how the parton distributions evolve with Q^2. The Dokshitzer-Gribov-Lipatov-Altarelli-Parisi (DGLAP) evolution equations [7] describe the evolution of quark q and gluon g probability density distributions:

$$\frac{\partial}{\partial \ln Q^2}\begin{pmatrix} q \\ g \end{pmatrix} = \frac{\alpha_s(Q^2)}{2\pi}\begin{bmatrix} P_{qq} & P_{qg} \\ P_{gq} & P_{gg} \end{bmatrix} \otimes \begin{pmatrix} q \\ g \end{pmatrix} \tag{1.12}$$

where the splitting functions, P_{ij}, provide the probability of finding parton i in parton j with a given fraction of parton j momentum. These functions are calculable in QCD.

In leading order of perturbation QCD, it can be shown that at small x [8]:

$$\frac{\partial F_2(x,Q^2)}{\partial \ln Q^2} \propto \alpha_s(Q^2) x g(x,Q^2) \tag{1.13}$$

The strong increase of F_2 as $x \to 0$ (see Expression (1.10)) observed at HERA may be interpreted as the growth of the gluon density in the proton in the low x regime.

1.2.3 The Dipole Model

Some properties of the high density parton cloud are clearer in the frame where the proton is at rest. In this frame, the virtual photon fluctuates into a quark-antiquark pair, $q\bar{q}$, upstream of the proton target, and this pair then interacts with the proton. In this frame, the fluctuation is long-lived, with $\tau \approx 1/(m_{q\bar{q}}x)$, where $m_{q\bar{q}}$ is the mass of the quark-antiquark system.

As shown in Figure 1.3 the problem of the interaction is reduced to the scattering of a dipole (the quark-antiquark pair acts as a QCD color dipole) from the intact proton. The size of the color dipole, or the transverse distance, r, of the quark-

[10]Probability density distributions are usually referred to as parton densities.

antiquark pair is a convenient degree of freedom from the point of view of the QCD interaction [9, 10, 11, 12, 13]. The average r, $\langle r \rangle$, is related to Q^2 as $\langle r \rangle \propto 1/Q^2$.

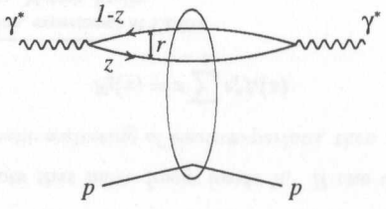

Figure 1.3: Diagrammatical representation of the basic process underlying γp scattering in the rest frame of the proton. The photon fluctuates into a quark-antiquark pair long upstream of the proton, a color dipole that subsequently scatters on the proton.

Central is the ansatz that the dissociation of the photon and the subsequent scattering can be factorized and written in terms of the wave function of the photon convoluted with the cross-section of the scattering of a quark-antiquark system from the proton [14]:

$$\sigma_{T,L}(x,Q^2) = \int d^2r \int_0^1 dz \; |\Phi_{T,L}(z,r)|^2 \sigma_{q\bar{q}-p} \tag{1.14}$$

where $\sigma_{T,L}$ is the $\gamma^* p$ [11] cross-section for transverse and longitudinally polarized photons, respectively. The momentum fraction of the quark-antiquark pair with respect to the four-momentum of the incoming photon are z and $1-z$. $\Phi_{T,L}$ is the wave function of the transverse and longitudinally polarized photons, respectively. These photon wave functions are well known [11, 13, 15]. The color dipole scattering cross-section, $\sigma_{q\bar{q}-p}$, in general, a function of x and r, is the underlying quantity of interest to us. The properties of $\sigma_{q\bar{q}-p}$ may be outlined qualitatively from simple arguments. For values of r smaller than the typical distance between partons in the proton, R_0, $\sigma_{q\bar{q}-p} \propto \langle r \rangle^2 \propto 1/Q^2$. As the transverse size of the color dipole becomes greater than R_0, the cross-section should saturate and reach a plateau [12]. This qualitative behavior

[11] Photon with non-zero virtuality, Q^2, is also referred to as γ^*.

[12] This type of saturation follows from the fact that the total photoproduction cross-section is finite.

is depicted in Figure 1.4. The effects of saturation will be felt for values of $r \gtrsim R_0$. If the value of R_0 is large the effects of saturation will be felt at relatively large values of r or small virtualities, Q^2, as depicted in Figure 1.4 (a). If the value of R_0 is small the effects of saturation will be felt at relatively small values of r or relatively large virtualities, Q^2, as depicted in Figure 1.4 (b).

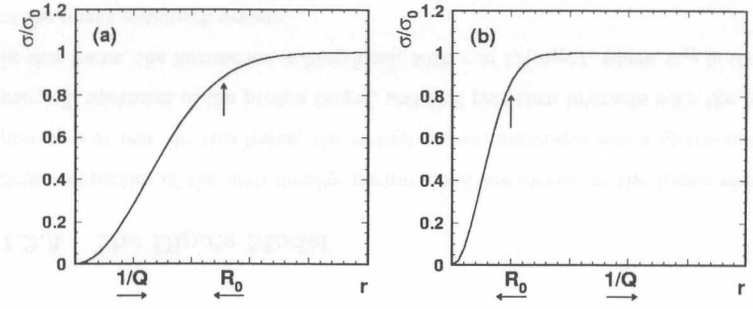

Figure 1.4: Qualitative behavior of the color dipole cross-section, $\sigma_{q\bar{q}-p}$, as a function of the transverse distance between quarks. Plot (a) and (b) correspond the ratio of $\sigma_{q\bar{q}-p}$ to the asymptotic σ_0 for two different values of the average distance between partons in the proton, R_0.

A. H. Mueller was the first to suggest [11] that the dipole cross-section is sensitive to the gluon density distribution in the proton. The scattering of the color dipole from the proton may occur through the exchange of two gluons connecting each quark in the dipole with the proton target.

1.2.4 Saturation of Parton Densities

The x and Q^2 behaviors of the parton density distributions in the proton at very small values of x is one of the most challenging and appealing problems of QCD. The issue of possible sensitivity of HERA data to saturation of the energy dependence of the cross-sections at high energy has become a central one. Saturation of the energy dependence

of cross-section may be viewed due to the saturation of parton densities in the proton at low x: if the density of partons in the proton stops growing as $x \to 0$, the cross-section will stop growing with energy (see Expression (1.10)).

About twenty years ago it was suggested that the parton distributions might cease to grow at small values of x and fixed Q^2 [16]. QCD calculations show that the density of gluon fields grows rapidly with $\ln(x)$ at fixed Q^2. It is expected that the gluon fields begin to overlap. If one moves to even lower values of x one may expect annihilation or recombination of gluons. The same considerations apply to the quark fields.

One can introduce a gluon density damping factor, or screening correction to QCD inspired parameterizations of the corresponding parton density distributions [17] (for a review of this approach see [18]).

Saturation of parton densities may also be expressed in terms of unitarity constraints on the growth of the cross-section, as embodied by the Froissart bound [19]:

$$\sigma_{tot}^{\gamma^* p} \leq \frac{\pi}{m_\pi^2} \left(\ln \frac{s}{s_0} \right)^2 \tag{1.15}$$

where m_π is the mass of the pion and s_0 is an unknown scale factor. The cross-section of proton-proton scattering keeps growing up to the highest energies provided by the Tevatron, suggesting that saturation effects are not visible at that energy. However, data taken by the ISR [20] was reviewed and interpreted in terms of the impact parameter of proton-proton scattering showing evidence of saturation of the growth of the cross-sections with energy [21].

Unitarity effects leading to saturation of parton densities have been also studied within the framework of the dipole model by separating the small size and large size components of the transverse distance between the quark and antiquark [22].

Golec-Biernat and Wüsthoff [23] proposed a simple ansatz for the dipole cross-section incorporating saturation behavior at large distances, r:

$$\sigma_{q\bar{q}-p}(x, r) = \sigma_0 (1 - e^{-r'^2}) \tag{1.16}$$

where $r' = \frac{r}{2R_0(x)}$, $R_0 \propto x^\lambda$ and λ is a parameter. The x dependence of the characteristic

parameter, R_0, is an additional ingredient introduced by the model.

1.3 Structure of the Thesis

After ten years of operation, HERA has elevated to a new level of development our knowledge of QCD, the theory of strong interactions. At the same time, HERA physics has highlighted two challenging topics closely related to the dynamics of strong interactions:

1. Perturbative QCD has been tested with great success at HERA. What about the transition from perturbative to non-perturbative QCD?

2. HERA discovered the increase of the parton densities in the proton as $x \to 0$. If the density of partons in the proton stops growing with $1/x$, the cross-section will stop growing with energy (saturation). Has HERA reached a new regime of high density QCD?

The first look at the scaling violations [24] (see Figure 1.5) suggested a different behavior of the scaling violation of the proton structure function (see Expression (1.13)) at low x and low Q^2 at HERA from that observed at higher x with data taken by fixed target experiments. QCD fits [13] are able to accommodate the scaling violation reaching a "plateau" at moderate Q^2, $1 \lesssim Q^2 \lesssim 10\,\text{GeV}^2$ at the expense of the coexistence of "valence-like" gluon density and singular behavior of the quark densities [25, 26], as illustrated in Figure 1.6 [25].

In Figure 1.5, x and Q^2 are correlated. It is necessary to separate x and Q^2 in order to disentangle topics 1 and 2. One needs to find a reaction that is able to probe the gluon density at different values of x at a fixed scale, μ^2, comparable to the values of Q^2 in the region of the "plateau". The reaction $ep \to eJ/\psi p$ meets this requirement by probing the gluon density at a scale $\mu^2 = \xi M_{J/\psi}^2$, where ξ is a parameter such that $\xi < 1$ and $x = (M_{J/\psi}^2 + Q^2)/W^2$ (see Section 2.6.2).

[13] QCD fits are based on the next-to-leading order (NLO) DGLAP formalism (see Section 1.2.2).

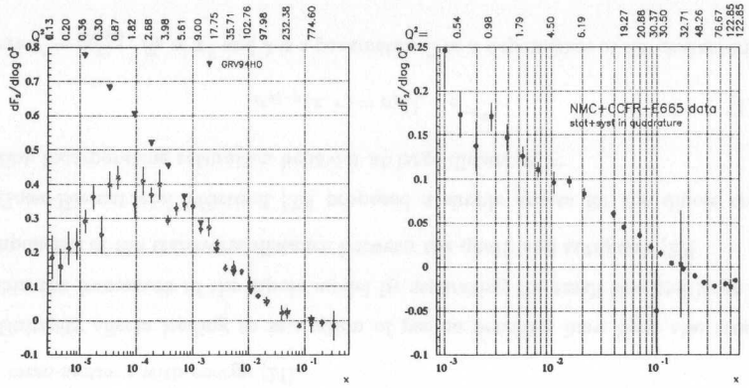

Figure 1.5: The "Caldwell Plots" illustrate the different behavior of the scaling violation of the proton structure function in two regimes. The left Plot corresponds to HERA data and the right Plot to data from fixed target experiments. The average values of Q^2 for the extraction of each value of $\frac{dF_2}{d\ln Q^2}$ are given on top.

The reaction $(ep \to eJ/\psi p)$ also offers the chance to study certain aspects of the interface between perturbative and non-perturbative QCD. In particular, it is relevant to express the results obtained in terms of the parameters of the Pomeron trajectory (see Chapter 2).

The ZEUS Collaboration measured $\sigma(ep \to eJ/\psi p)$ in the photoproduction regime ($Q^2 \approx 0$) in the range $40 < W < 140\,\text{GeV}$ [27]. It is the main focus of this work to provide a more precise measurement of $\sigma(ep \to eJ/\psi)$ in the photoproduction regime in an extended W range. This can be achieved by studying the production of J/ψ through $J/\psi \to e^+e^-$. This implies detecting electromagnetic clusters in a regime of energies, E, ($E < 10\,\text{GeV}$) unexplored before in the ZEUS detector. Several things need to be accomplished in order to meet this challenge:

- The development of a trigger selection algorithm highly efficient in the entire W range. Trigger efficiencies need to be known with relatively high precision. This is presented in Chapter 5.

- The error on the contamination from the diffractive process $(ep \to eJ/\psi N)$ needs to be understood to a better precision. This is accomplished with the use of the FPC (see Chapter 8).

- It is necessary that the MC describes well the final state in the entire W range of the measurement. For this purpose, it is necessary to study the energy scale and resolution of the UCAL at low energies (see Appendix A), the CTD momentum scale and resolution (see Appendix B), the alignment of the UCAL and SRTD (see Appendix C) and the calibration of the energy response of the SRTD (see Appendix D).

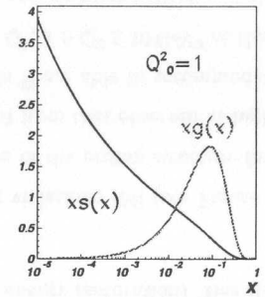

Figure 1.6: Quark and gluon densities at $Q^2 = 1\ \text{GeV}^2$.

Results of $\sigma(ep \to eVp)$ with $V = J/\psi, \psi(2S), \Upsilon$ are reported in Chapters 9, 10 and 11, respectively. The relevance of these results is discussed in Chapter 12.

The reaction $(ep \to eVp)$ is a diffractive process. The diffractive production of vector mesons (VM, V) is viewed in close interconnection with the NC DIS (see Chapters 1 and 2). The dipole approach establishes the interconnection between different reactions in ep collisions in a straightforward way. The elastic VM production is viewed as a whole in Chapter 12. It is illustrated that $Q^2 + M_V^2$ is a good choice of the scale of the interaction in elastic VM production. This is a necessary step to illustrate the complementarity of elastic VM production to DIS.

Chapter 2

Diffractive Vector Meson Production at HERA

Before tackling the issue of the significance of diffractive VM production at HERA, it is appropriate to touch upon diffractive processes in general. Diffractive processes represent a fraction of the total cross-section in collisions at high energy and are related to it. The study of diffractive processes represents an alternative approach to the problem of the interface of hard to soft physics and the saturation of parton densities in the proton. These are central aspects of the significance of HERA physics. Diffractive processes display a number of basic properties which differentiate them from other processes in high energy collisions. It is useful to briefly review two pre-QCD phenomenological frameworks, Regge phenomenology and vector dominance model. These two frameworks are useful tools to study the basic properties of diffractive processes in particular, and collisions at high energy, in general.

2.1 Diffraction

It has been observed in hadron-hadron scattering that a significant fraction of interactions are elastic [1] and quasi-elastic [2]. The process underlying diffractive quasi-elastic scattering is usually referred to as diffractive dissociation. The diffractive scattering of two particles A and B are either of the type $A + B \to A + N$ (single diffraction), or $A + B \to N + Y$ (double diffraction). The quantum numbers of the particles N and Y are strongly correlated with the corresponding quantum numbers of the incoming particles. It was also observed that the basic features of these processes seem to be independent of the type of the incoming hadrons, i.e. seem to be universal. The basic features of these interactions may be summarized as follows:

- The differential cross-section, $\frac{d\sigma}{dt}$, displays a sharp exponential fall, $\frac{d\sigma}{dt} \propto e^{bt}$. This is illustrated in Figure 2.1 [3]. As the energy increases, the forward elastic peak becomes exponential and a second diffractive maximum appears. This behavior is similar to that observed in optical diffraction. Using this approach, the slope parameter, b, $b = R^2/4$, where R is the transverse radius of the interaction.

- Large masses of the dissociated system, M_N, are highly suppressed in single diffraction. The differential cross-section for $M_N^2 \gtrsim 4\,\mathrm{GeV}^2$, is found to behave like

$$\frac{d\sigma}{M_N^2} \propto 1/M_N^2 \tag{2.1}$$

  Diffractive dissociation may be pictured as quasi-elastic scattering between two hadrons where one of them is excited into higher mass state [30]. The excitation of one of the colliding hadrons occurs coherently [28]. The condition for coherence requires the longitudinal momentum transfer to be smaller than the inverse of

[1] The term elastic is used when incoming hadrons remain "intact" in the interaction.

[2] The term quasi-elastic is used when at least one of the scattered hadrons gets excited into a state of higher mass, yet the mass of this state is similar to the mass of the incoming hadron.

[3] This Plot is taken from [28, 29].

the longitudinal size of the proton. This condition translates into

$$\frac{M_N^2}{s} < \frac{m_\pi}{m_p} \approx 0.15 \tag{2.2}$$

where m_π and m_p are the mass of the pion and the proton, respectively [4].

- Rapidity [5] "gaps" occur between the final states in diffractive scattering. The lack of QCD radiation between the final state leads to the conclusion that diffraction is mediated by a color singlet state commonly called Pomeron, a hypothetical particle that shares the quantum numbers of the vacuum. The absence of radiation in these rapidity gaps leads to Equation (2.1) [30]. Because of the absence of radiation the cross-section should be independent of the pseudorapidity [6], η, and $\eta \propto -lnM_N^2$.

The optical theorem relates the total cross-section to the imaginary part of the forward elastic amplitude:

$$\sigma_{tot}(s) = \frac{1}{s}\, Im\, T_{el}(s,t)|_{t=0} \tag{2.3}$$

and

$$\left.\frac{d\sigma_{el}}{dt}\right|_{t=0} = \frac{1}{16\pi s^2}\,|T_{el}(s,0)|^2 \tag{2.4}$$

The optical theorem is represented schematically in Figure 2.2. Dispersion relations establish the connection between the real and imaginary parts of the forward amplitude. At high energies, the elastic amplitude is mainly imaginary [7]. Therefore, from

[4] The transverse size of the proton is assumed to be $\approx 1/m_\pi$. This assumption is consistent with the size of the t-slope observed experimentally in elastic pp scattering.

[5] In the center of mass system rapidity is defined as $y = \frac{1}{2} ln \frac{E+P_z}{E-P_z}$ where E and P_z are the energy and longitudinal momentum of the particle in that system.

[6] Pseudorapidity is usually used in place of rapidity and is defined as $\eta = ln\frac{2p_L}{p_T}$ where p_L and p_T are the longitudinal and transverse components of the particle with respect to the direction of the beam.

[7] This argument is used here for qualitatively discussions only. The real part of the amplitude is proportional to the energy derivative of the amplitude. The stronger the energy dependence is the larger will be the real part of the amplitude. This effect is not negligible in ep collisions where cross-section are known to increase relatively steeply.

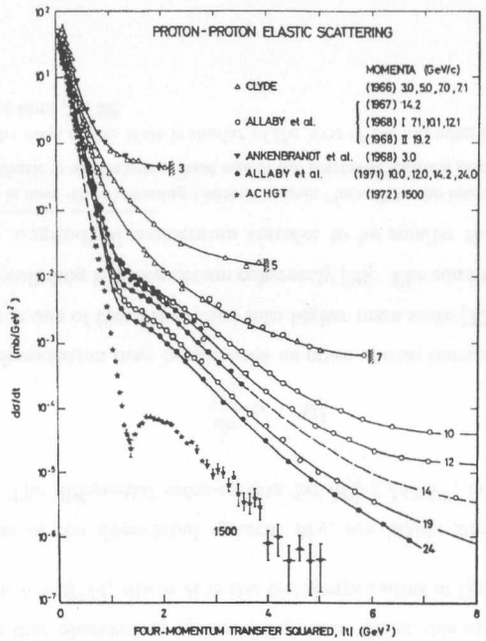

Figure 2.1: Differential cross-section, $\frac{d\sigma}{dt}$, for pp elastic scattering for different values of the center of mass energy of the colliding particles, s. As energy increases a classical diffraction pattern appears.

Equations (2.3) and (2.4) it follows:

$$\sigma_{el}(s) \propto \sigma_{tot}^2(s) \tag{2.5}$$

The diffractive elastic cross-section should grow as the square of the total cross-section. This is a central observation regarding the relevance of the study of the diffractive elastic processes.

Comprehensive reviews of the physics of diffraction may be found in [28, 31].

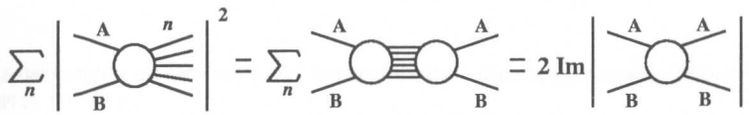

Figure 2.2: Schematic representation of the optical theorem.

2.2 Regge Phenomenology

Before the invention of QCD, the dynamics of hadron interactions were sometimes viewed as due to exchange of mesons, particularly pions (One Pion Exchange or OPE). This approach was successful in describing some basic properties of hadron-hadron collisions, but soon it was realized that this picture was far too simplistic. Additionally, the exchange of resonances with spin J leads to scattering amplitudes proportional to s^J. For high spins, this behavior flagrantly violates the Froissart bound (see Equation (1.15)).

Regge theory resolved such problems in this approach to hadron-hadron interactions. Regge theory is based on the analytical continuation of the scattering amplitude into the complex angular momentum plane. Crucial for the development of this theory was the use of complex angular momenta by Regge [32]. One views the exchange of all resonances as an exchange of a new object: the Regge trajectory.

For the reaction $A + B \rightarrow C + D$ with $t < 0$ and $s \gg -t$ the amplitude of the scattering should behave like [33]:

$$T(s,t) \approx F(t) \left(\frac{s}{s_0}\right)^{\alpha(t)} \tag{2.6}$$

where $\alpha(t)$ is the Regge trajectory. The Regge trajectory is assumed to be linear with t, $\alpha(t) = \alpha(0) + \alpha' t$ [33]. $F(t)$ is an unknown function that describes the t dependence of the scattering amplitude. The function $F(t)$ accommodates the exponential form of the elastic differential cross-section observed experimentally at low $|t|$. Assuming a single exponential form of the t dependence of the elastic differential cross-section and

the linear form of the Regge trajectory, from Equation (2.4) it follows:

$$\left.\frac{d\sigma_{el}}{dt}\right|_{t=0} \propto e^{b_0 t} \left(\frac{s}{s_0}\right)^{2(\alpha(t)-1)} = e^{b(s)t} \left(\frac{s}{s_0}\right)^{2(\alpha(0)-1)} \tag{2.7}$$

where

$$b(s) = b_0 + 2\alpha' ln\left(\frac{s}{s_0}\right) \tag{2.8}$$

Expression (2.8) predicts the s dependence of the t-slope. This involves the "shrinkage" of the forward peak. This leads to an effective power of the s dependence of the cross-section, $\sigma \propto s^\delta$ with

$$\delta \approx 4\left(\alpha(0) - \frac{\alpha'}{b} - 1\right) \tag{2.9}$$

Through the optical theorem Regge theory gives a prediction of the behavior of the total hadron-hadron cross-sections with energy. From Equation (2.3) it follows:

$$\sigma_{tot}(s) \propto s^{\alpha(0)-1} \tag{2.10}$$

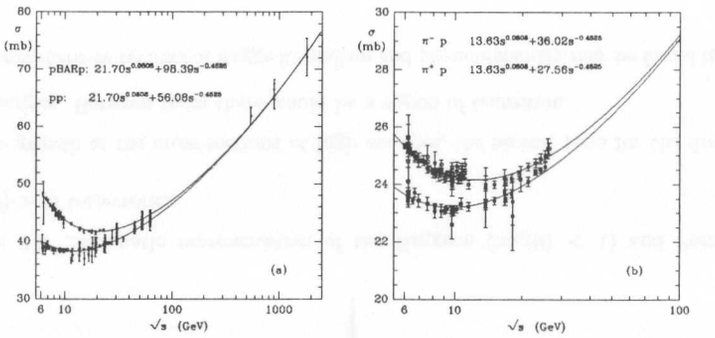

Figure 2.3: The total cross-section as a function of the center-of-mass energy for pp, $p\bar{p}$, $\pi^{\pm}p$ scattering. Cross-sections drop with energy at moderately low energies, $s < 10$ GeV^2. However, the cross-sections show an universal rise at high energies of the form of $\sigma \propto s^{0.08}$.

This remarkable prediction was successful in describing the behavior of the hadron-hadron cross-sections when this formalism was invented. Figure 2.3 shows that at

moderately low energies, $s < 10\ \mathrm{GeV}^2$, hadron-hadron cross-sections drop with energy. This can be explained by the exchange of a Regge trajectory with $\alpha(0) < 1$, the Reggeon trajectory, $I\!R$. Already at that time the drop in the hadron-hadron cross-sections was seen to flatten out indicating a change in the behavior that had initially motivated the Regge formalism. As proved by Pomeranchuk [34], cross-sections approach a constant value as the energy of the collision approaches infinity [8]. From the point of view of Regge formalism, this behavior of the hadron-hadron cross-sections would be consistent with a trajectory with $\alpha(0) \approx 1$. This type of trajectory was called the Pomeron [9] trajectory, $I\!P$.

The appearance of the Pomeron changed as experiments showed that the hadron-hadron cross-sections increas with energy at $s \gtrsim 10\,\mathrm{GeV}^2$ (see Figure 2.3). In terms of the Regge formalism, this translates into $\alpha_{I\!P}(0) > 1$. This is illustrated in Figure 2.4. Regge trajectories are based on real particles. However, no real particle existed neither back then nor today that may fit into a trajectory with $\alpha(0) > 1$. Nowadays, the term Pomeron is used generically as a hypothetical Regge trajectory with an intercept greater than unity to accommodate the increase of cross-sections with energy at high energy.

A global fit of available data on hadron-hadron collisions was performed by Donnachie and Landshoff (DL) [35]:

$$\sigma_{tot} = X s^{\epsilon} + Y s^{-\eta} \tag{2.11}$$

where X, ϵ, Y and η are free parameters [10]. Parameters ϵ and η are related to the Pomeron and Reggeon trajectories, respectively: $\alpha_{I\!P}(0) = 1 + \epsilon$ and $\alpha_{I\!R}(0) = 1 - \eta$. The fit yields $\epsilon = 0.0808$ and $\eta = 0.4524$. The first term in Equation (2.11) is responsible

[8] Pomeranchuk argued that the strength of strong interactions approaches zero exponentially for large values of the impact parameter of the colliding particles.

[9] Pomeranchuk proved that the cross-sections $\sigma(AB) = \sigma(\overline{A}B)$ in the high energy limit. This hypothetical particle would share the quantum numbers of the vacuum and its couplings to A and $\overline{A}$ would be the same.

[10] Parameter X is the same for particles and antiparticles in virtue of Pomeranchuk's theorem.

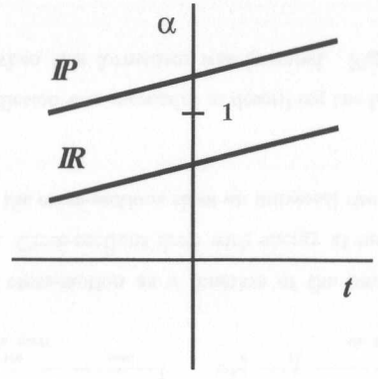

Figure 2.4: Schematic representation of the Reggeon ($\alpha_{I\!R}(0) < 1$) and Pomeron ($\alpha_{I\!P}(0) > 1$) trajectories.

for the growth of the cross-sections at high energies, the second term for the drop at low energies. Between them there would be a region of transition.

Comprehensive reviews of Regge formalism and phenomenology may be found in [33, 36, 37].

2.3 Vector Dominance Model (VDM)

Basic features of the hadron-hadron interactions are shared by photon-hadron interactions starting at energies of the order of $\sim 1\,\mathrm{GeV}$. The energy dependence is very similar, as illustrated in Figure 2.5. This Figure shows the total $\gamma^* p$ cross-section, $\sigma_{tot}^{\gamma^* p}$, as a function of W^2 at different Q^2. Starting from the photoproduction cross-section it is clearly seen that γp behaves the same way as pp scattering (see Figure 2.3). The similarity is not only qualitative. The energy dependence of the γp cross-section is described by Equation (2.11) up to a normalization factor proportional to $\alpha_{em} = 1/137$. The measurement of the amplitude of the Compton scattering in $\gamma\gamma$ collisions shows that the latter is purely imaginary as in the case of hadron-hadron collisions. Another

striking similarity is the resonant structure of the cross-section of $\gamma-$hadron collisions.

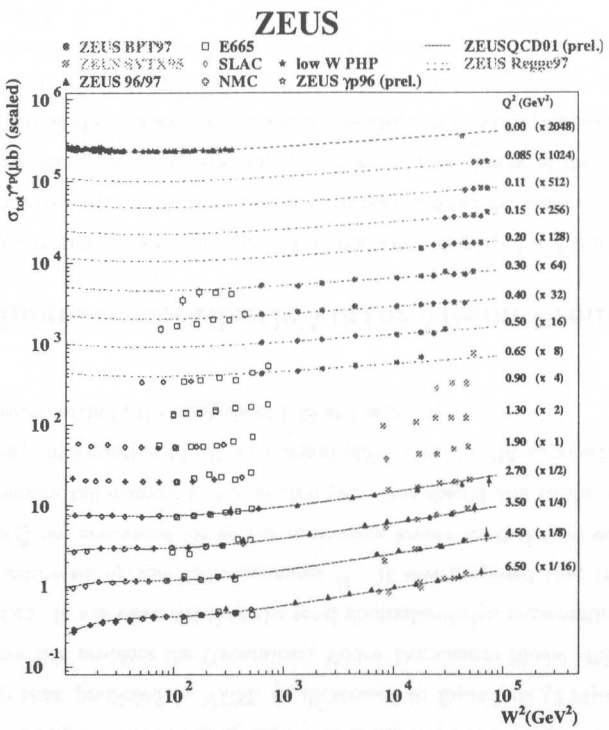

Figure 2.5: The total γ^*p cross-section, $\sigma_{tot}^{\gamma^*p}$, as a function of W^2 at different Q^2. Various data sets measured with the ZEUS detector are shown along with data from fixed target experiments. Also, the photoproduction cross-section from ZEUS is compared with data from fixed target experiments. The solid line corresponds to a QCD fit and the dashed line to Regge inspired fit to ZEUS and fixed target data.

The Vector Dominance Model (VDM) [38] embodies a number of ideas that evolved together with experimental results. Bearing in mind the striking similarities between the photon-hadron interactions and purely hadronic interactions, the physical photon

may be viewed as a superposition of two states:

$$|\gamma\rangle = A|\gamma_B\rangle + \sqrt{\alpha_{em}}|h\rangle \tag{2.12}$$

were $|\gamma_B\rangle$ stands for a "bare" photon that does not interact hadronicaly, and $|h\rangle$ stands for the "hadronic component" of the photon. The factor A is introduced to secure the proper normalization of the photon wave function. The contribution of the interaction of the "bare" photon is small at high energies. The hadronic part of the photon undergoes hadronic interactions. VDM postulates a specific structure of $|h\rangle$. The photon couples to a VM field with a strength, $(e_{em}\, M_V^2/f_V)$, where e_{em} is the electromagnetic charge, M_V is the mass of the VM and f_V is a constant specific to each type of VM. This coupling was initially proposed for real photons. In the general case of photons of a given virtuality, Q^2, the "hadronic" wave function may be written as:

$$\sqrt{\alpha_{em}}\,|h\rangle = \sum_V \frac{e_{em}M_V^2}{f_V}\frac{1}{M_V^2+Q^2}|V\rangle \tag{2.13}$$

where $|V\rangle$ [11] stands for the wave function of the VM. The γh interaction is translated into the sum of Vh interactions. The cross-section of the interaction γh for transverse and longitudinally polarized γ is expressed in terms of the cross-section of the Vh scattering. If one assumes that the VM conserves the helicity of the photon one can write [41]:

$$\sigma_T^{\gamma h} = \sum_V \left(\frac{e_{em}M_V^2}{f_V}\right)^2 \left(\frac{1}{M_V^2+Q^2}\right)^2 \sigma_T^{Vh} \tag{2.14}$$

and

$$\sigma_L^{\gamma h} = \sum_V \left(\frac{e_{em}M_V^2}{f_V}\right)^2 \left(\frac{1}{M_V^2+Q^2}\right)^2 \eta \left(\frac{Q^2}{M_V^2}\right)^2 \sigma_L^{Vh} \tag{2.15}$$

where $\sigma_T^{\gamma h}$ and $\sigma_L^{\gamma h}$ are the total γh cross-sections for transverse and longitudinally polarized photons with virtuality Q^2, respectively. σ_T^{Vh} and σ_L^{Vh} are the total Vh photoabsorbtion ($Q^2 = 0$) cross-sections for longitudinal and transverse polarized VM's, respectively and $\eta = \sigma_L^{Vh}/\sigma_T^{Vh}$ is determined experimentally [12].

[11] The sum runs over all existing VM. The dominant contribution comes from light VM's (ρ^0, ω, ϕ) discovered in early 60's. Heavier VM's ($J/\psi, \Upsilon$) were found some ten years later [39, 40].

[12] In principle, η is a function of the center of mass energy of the interaction. It has been observed from elastic ρ^0 production at HERA that at high energies η is constant with energy [42]

VDM has a strong predictive power of the γh cross-section. Formulae (2.14)-(2.15) relate the cross-section of γh scattering at any photon virtuality to the total photoabsorbtion VM cross-sections. Using the optical theorem one can relate the total photoabsorbtion cross-section of Vh scattering to the diffractive production of VM's [43]:

$$\sigma_{tot}^{\gamma h} = \sum_V \sqrt{16\pi \left(\frac{e_{em}}{f_V}\right)^2 \frac{d\sigma}{dt}(\gamma h \to Vh)\Big|_{t=0}} \tag{2.16}$$

where $\frac{d\sigma}{dt}(\gamma h \to Vh)\big|_{t=0}$ refers to the diffractive $\gamma h \to Vh$ cross-section extrapolated to $t = 0$.

The VDM approach proved successful in describing photoproduction and even low Q^2 electroproduction, but failed to describe the Q^2 dependence of the cross-section in DIS [44]. Also, the ratio of longitudinal to transverse cross-sections in DIS grew much slower than predicted in VDM, as illustrated in Equations (2.14)-(2.15). In order to solve this problem the Generalized Vector Dominance Model [45] (GVDM) was formulated. It was observed that the total photoabsorbtion cross-section was not completely saturated by the VM resonances [13]. It was proposed that the missing fraction of $\sigma_{tot}^{\gamma h}$ not accounted for by the resonances known at that time would come from a continuum tail coupled to the photon [46]. One should add to the sum in the right hand side of Equation (2.15) an integral [45]. The GVDM approach has been revived in recent years in the analysis of DIS at low x [47].

2.4 Kinematics of Elastic Vector Meson Production

The schematic representation of elastic VM production is displayed in Figure 2.6. The kinematic variables relevant to the reaction have been defined in Section 1.2.1: s, the center of mass energy of the ep system; W, center of mass energy of the γp system; $-Q^2$, the square of the momentum transfer at the electron vertex; t, the square of the

[13] Careful analysis of experimental data showed that the first three terms in the sum in Equation (2.16) account for 78% of $\sigma_{tot}^{\gamma h}$. Some 22% was missing. The contribution from J/ψ would account for no more than 3%.

momentum transfer at the proton vertex. At low Q^2, electrons interact with the proton via the radiation of a photon. The reaction may be treated effectively as $\gamma p \to Vp$. The four vector of the exchanged photon is determined by the four vectors of the incoming (e) and scattered (e') electron [14]. A fraction of the energy of the incoming electron is transferred to the radiated photon. Relevant to the $\gamma p \to Vp$ reaction is W.

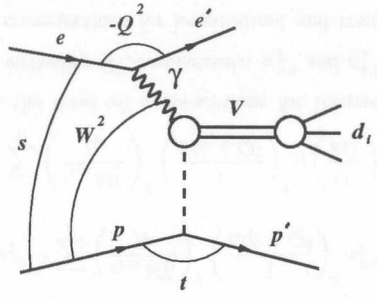

Figure 2.6: Representation of diffractive vector meson production at HERA.

The measurement of VM's at HERA is done exclusively. Events with a certain topology that correspond to the decay of VM's are chosen. Light VM's are searched in events where a specific final state is observed: ρ^0 in $\pi^+\pi^-$, ω in $\pi^+\pi^-\pi^0$ and ϕ in K^+K^-. Heavy VM's ($J/\psi, \psi(2S)$ and Υ) are usually searched for through their leptonic decays ($\mu^+\mu^-$ and e^+e^-) [15]. The four vector of the VM observed in the final state is equal to the sum of the four vectors of the decaying particles:

$$V = \sum_i d_i \tag{2.17}$$

where the sum runs over all the decay products of the VM, d_i are the four vector of the decay products of the VM, V is the four vector of the VM. The reconstruction of the

[14] HERA collides e^-p and e^+p. In the regime of photoproduction, or $Q^2 \ll M_{Z^0}^2$, the sign of the incoming lepton is irrelevant.

[15] The mass of the J/ψ and $\psi(2S)$ are below the threshold of the creation of τ. Υ is heavy enough. However, τ decays before reaching the tracking system, therefore, this decay is not useful for the search of Υ resonances.

kinematics of the event relies on the reconstruction of the four-vector of the decaying particles. The reconstruction of the kinematics in the production of heavy VM's in the regime of photoproduction ($Q^2 \approx 0$) will be covered in detail in Section 7.3.1.

2.5 Decay Angular Distributions

The decay angular distributions of the VM are of great relevance to this analysis. It is necessary to establish experimentally that the VM conserves the helicity of the photon. Formula (2.24) assumes that the VM retains the helicity of the photon (see Section 2.6.2). The calculation of the VM production ratio would be more complicated otherwise and it would require the knowledge of the probability with which the VM changes helicity with respect to the helicity of the incoming photon. Non-zero probabilities of helicity flip would lead to mixing of the transverse and longitudinal amplitudes.

For the purpose of studying the helicity of the final state and the mixing probability a formalism was developed [48] within the formalism of sequential multi-body decay. This formalism is built in the so called helicity s-channel. When the decay angles are viewed in this frame and the helicity of the VM conserves the helicity of the photon it is said that the s-channel helicity conservation (SCHC) holds.

The VM is boosted to the rest frame of the γp center of mass system. The quantization axis is defined in that rest frame along the direction of flight of the VM. This is illustrated in Figure 2.7. Three planes are defined in the γp center of mass system, the scattering plane, or the plane formed by the incoming and outgoing electrons, the production plane, or the plane formed by the outgoing VM and proton, and the decay plane made by the products of the decay of the VM. Three relevant angles are defined. The angle θ_h, is the angle between one of the decaying particles [16] and the quantization axis in the VM rest frame, ϕ_h is the angle between the decay plane and the production

[16] Usually the positron in $V \to e^+e^-$ is used to define θ_h.

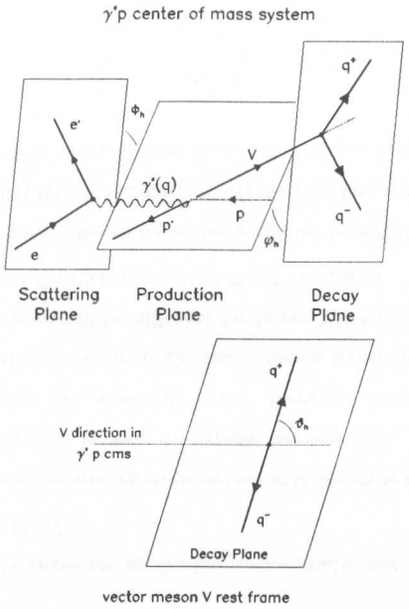

Figure 2.7: The definition of decay angles in the helicity system. The VM is boosted to the rest frame of the γp system. The quantization axis is defined in that frame along the direction of flight of the VM.

plane and Φ_h is the angle between the production plane and the scattering plane.

In the case of the decay of the VM into two spin-$\frac{1}{2}$ particles, the probability distribution of decay angles in the rest frame of the VM may be expressed in terms of the elements of the VM spin matrix:

$$W(\theta_h, \psi_h) = \frac{3}{4\pi}\left[\frac{1}{2}(1 - r^{04}_{00}) + \frac{1}{2}(3r^{04}_{00} - 1)\cos^2\theta_h \right. \\ \left. + r^{04}_{1-1}\sin^2\theta_h \cos 2\psi_h + \sqrt{2}\mathcal{R}\{r^{04}_{10}\}\sin 2\theta_h \cos\psi_h\right] \tag{2.18}$$

where $\psi_h = \phi_h - \Phi$, r^{04}_{00}. r^{04}_{10} and r^{04}_{1-1} are spin matrix elements. r^{04}_{00} is related to the probability of the VM to be produced in helicity zero state, r^{04}_{10} to the interference

between helicity non-flip and single flip amplitudes and r_{10}^{04} to the interference if the helicity non-flip and double flip amplitudes.

Taking the one dimensional projections in $\cos\theta_h$ and ϕ_h (fixing one and integrating over the other) one obtains the following Expressions for the differential distributions [49]:

$$\frac{1}{N}\frac{dN}{d\cos\theta_h} = \frac{3}{8}\left[1 + r_{00}^{04} + \left(1 - 3r_{00}^{04}\right)\cos^2\theta_h\right] \tag{2.19}$$

and

$$\frac{1}{N}\frac{dN}{d\phi_h} = \frac{1}{2\pi}\left[1 + r_{1-1}^{04}\cos 2\phi_h\right] \tag{2.20}$$

If s-channel helicity is conserved (SCHC) then the spin density matrix parameters r_{00}^{04} and r_{1-1}^{04} should be zero. Assuming SCHC, r_{00}^{04} can be related to the ratio of the cross-sections for longitudinal and transverse photons, R:

$$R = \frac{1}{\epsilon}\frac{r_{00}^{04}}{1 - r_{00}^{04}} \tag{2.21}$$

where ϵ is the virtual photon polarization, i.e. the ratio of the flux of longitudinally polarized photons to the flux of transversely polarized photons. The mean value of ϵ over the kinematic range sampled by the ZEUS experiment is $\epsilon = 1.043$.

2.6 Theoretical Models

2.6.1 Models Based on VDM and Regge Theory

Figure 2.8 shows the schematic representation of elastic VM production at HERA from the point of view of a combination of VDM and Regge formalisms. The photon fluctuates into a VM which scatters on the proton via the exchange of the Pomeron.

The parameters of the Pomeron trajectory were determined by DL from a global fit to photoproduction data (see Expression (2.11)), yielding $\alpha(t) = 1.08 + 0.25t$ [35]. This trajectory is referred to as "soft" Pomeron because it reproduces the behavior of the cross-sections at small values of Q^2, a regime governed by soft physics.

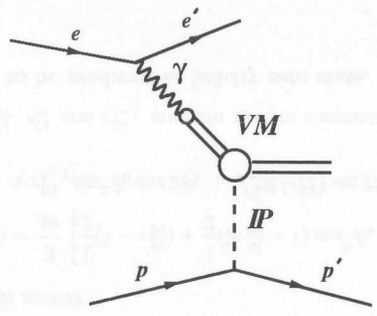

Figure 2.8: Elastic VM production at HERA in the combined VDM and Regge approach. The photon fluctuates into a VM which scatters on the proton via the exchange of a Pomeron.

The production of VM's via the exchange of the "soft" Pomeron predicts a weak W dependence of the cross-section ($\sigma \propto W^{\delta}$) with $\delta \approx 0.22$ (see Expression (2.9)). It also predicts a strong dependence of the t-slope with W (shrinkage) according to Expression (2.8).

The predictions made above are applicable to the production of light VM's (ρ^0, ω and ϕ) for which $M_V^2 \lesssim 1\,\mathrm{GeV}^2$.

As Q^2 grows, the rise of the total ep cross-section with energy is no longer compatible with the "soft" Pomeron [26]. In order to explain the new data, DL proposed the so called two-Pomeron model [50], a second, "hard" Pomeron, would arise with $\alpha(t) = 1.4{+}0.1t$. The cross-section is the sum of the two Pomeron terms plus their interference. The predictions made above will be different for heavy VM's (J/ψ and Υ) for which $M_V^2 \gg 1\,\mathrm{GeV}^2$, because of the inclusion of the "hard" Pomeron.

The intercept of the "hard" Pomeron may be calculated in pQCD within the Balitski-Fadin-Kuraev-Lipatov (BFKL) formalism [51]. Next-to-leading order calculations yield $\alpha_{BFKL}(0) \approx 1.165$ [52]. It is assumed that the value of $\alpha'_{BFKL} = 0$.

2.6.2 Models Based on the Dipole Approach

As pointed out in Section 1.2.3, the dipole approach is a handy framework for the study the dynamics of the $q\bar{q} - p$ scattering. Within the QPM a VM is considered to be a bound state of a $q\bar{q}$. The photon and the $q\bar{q}$ couple electromagnetically. Once the quark structure of the VM is established, one can easily figure out what is the production rate of a given VM with respect to others:

$$|V\rangle \propto |q\bar{q}\rangle \tag{2.22}$$

The production rate of a given VM is related to the square of the charges of the $q\bar{q}$. These relative rates, commonly called SU(5) [17] ratios, are shown in Table 2.1. The QPM was able to explain the suppression of the photoproduction rate of the ϕ and ω with respect to the ρ^0 [53].

	$\|V\rangle$	$e_V^2 \equiv e_{q\bar{q}}^2$	$\frac{e_{\rho^0}^2}{e_V^2}$
ρ^0	$1/\sqrt{2}(\|u\bar{u}\rangle - \|d\bar{d}\rangle)$	1/2	1
ω	$1/\sqrt{2}(\|u\bar{u}\rangle + \|d\bar{d}\rangle)$	1/18	9
ϕ	$\|s\bar{s}\rangle$	1/9	9/2
J/ψ	$\|c\bar{c}\rangle$	4/9	9/8
Υ	$\|b\bar{b}\rangle$	1/9	9/2

Table 2.1: The wave function of the elastic VM is expressed as a linear combination of $q\bar{q}$ wave functions. The square of the charges of the $q\bar{q}$ make up the so called SU(5) ratios. The last column correspond to the expected rate of the production of VM's with respect to the ρ^0.

The basics of the process from the point of view of the dipole approach is illustrated in Figure 2.9. The photon fluctuates into a $q\bar{q}$ pair long upstream of the proton, forming a color dipole that subsequently scatters on the proton. The $q\bar{q}$ pair forms a bound

[17] SU(n) symmetry, where n is the number of flavors. The number of known flavors is 6, however, the bound state of the heaviest t quark has not been found yet.

state, the VM, after scattering on the proton. In other words, the process is factorized. The amplitude of the process may be written as a convolution of three components [54]:

$$A_{T,L} = \int d^2\mathbf{r} \int_0^1 dz\ \Phi_V^{\star,T,L}(z,\mathbf{r})\sigma_{q\bar{q}-p}\Phi_\gamma^{T,L}(z,\mathbf{r}) \tag{2.23}$$

In analogy to Equation (1.14), the indexes T, L correspond to transverse and longitudinally polarized γ and VM, Φ_V is the wave function of the VM. Equation (2.23) leads to the following Expression for the cross-section of the VM production:

$$\sigma_{T,L}(\gamma p \to Vp) \propto \left| \int d^2\mathbf{r} \int_0^1 dz\ \Phi_V^{\star,T,L}(z,\mathbf{r})\sigma_{q\bar{q}-p}\Phi_\gamma^{T,L}(z,\mathbf{r}) \right|^2 \tag{2.24}$$

The total γp and diffractive $\gamma p \to Vp$ cross-section, expressed in the dipole approach, Equations (2.24)-(1.14), are closely interrelated through the dynamics that dwell within $\sigma_{q\bar{q}-p}$ [18]. The complementarity of elastic VM production to the total cross-sections measured in DIS comes out explicitly in these Expressions. The energy behavior of both cross-sections depends little on the details of the photon and VM wave functions. This crucial aspect of the analysis will be covered in Section 12.4.

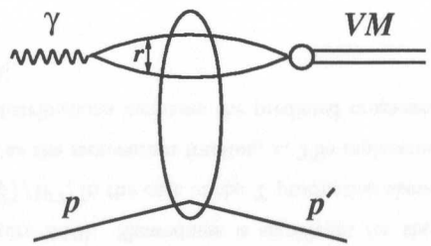

Figure 2.9: Diagrammatical representation of the basic process of $\gamma p \to Vp$ in the rest frame of the proton. The photon fluctuates into a $q\bar{q}$ pair long upstream of the proton, forming a color dipole that subsequently scatters on the proton. The $q\bar{q}$ pair forms a bound state, the VM, after scattering on the proton.

Within pQCD the $q\bar{q} - p$ scattering is understood through colorless exchange of gluons. This is depicted in Figure 2.10 in which the $q\bar{q}$ exchanges two gluons with the

[18] Formula (2.23) assumes that the VM carries the helicity of the photon. More on this in Sections 2.5 and 9.6.

proton. Hence, in the elastic production the gluon density in the proton is "probed" at a scale, μ, where $\mu^2 = \xi(Q^2 + M_V^2)$ such that perturbative calculations may be performed [19]. ξ is a numerical factor. It has been shown [55]:

$$\sigma_{tot}^{\gamma p \to Vp} \propto \left[xg(x,\mu^2)\right]^2 \tag{2.25}$$

where x is the average momentum fraction of the two gluons, such that $x = (Q^2 + M_V^2)/W^2$ and $\xi = 1/4$. From Expression (2.25) a value of δ ($\sigma \propto W^\delta$) follows $\delta \approx 0.8$, which is significantly larger than the one obtained with the exchange of a "soft" Pomeron (see Section 2.6.1).

It is claimed that only the cross-section for longitudinally polarized (for non-zero Q^2) VM may be derived with rigor in pQCD. In the leading $\alpha_s \ln \frac{Q^2}{\Lambda_{QCD}} \ln \frac{1}{x}$ approximation calculations lead to [56]:

$$\left.\frac{d\sigma_L^{\gamma^* p \to Vp}}{dt}\right|_{t=0} \propto \alpha_s^2 \left|(1+i\beta)xg(x,\mu^2)\right|^2 \tag{2.26}$$

where β is the ratio of the real to the imaginary part of the scattering amplitude.

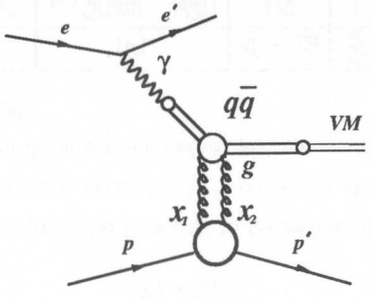

Figure 2.10: Elastic VM production at HERA in the perturbative QCD approach. The photon fluctuates into a $q\bar{q}$ pair. These couple to the proton via exchange of two gluons. The VM is created after the interaction.

[19] In general, μ is a function of t too, however, in the elastic production of heavy VM's $|t| \ll M_V^2$. The t dependence of μ may be neglected in this case.

Two sets of theoretical calculations are compared to data (see Section 12.1.2): Martin-Ryskin-Teubner (MRT) [57] and Frankfurt-Koepf-Strikman (FKS) [20] [59]. The main differences lie in the way both groups deal with higher order QCD corrections and the VM final state.

The uncertainty of the theoretical calculations affects mainly the absolute normalization of the predictions. This is due to the choice of the value of the mass of the quarks, the parameter ξ and the lack of full NLO corrections.

Two corrections are relevant in the production of Υ: the contribution from skewed parton distributions and off-diagonal matrix elements, and β. Skewedness is defined as the difference in momentum fractions between the outgoing (x_1) and returning (x_2) gluon (see Figure 2.10). Skewedness is significant for the production of Υ as $x_1 - x_2 = (Q^2 + M_V^2)/W^2$. In the case of the Υ production skewedness is of the same order of magnitude as the momentum fraction, x. The replacement of gluon densities by skewed parton distributions increases the predicted cross-section by more than a factor of two [60, 61].

[20] The last update to FKS calculations has been performed by Frankfurt-McDermott-Strikman (FMS) [58].

Chapter 3

HERA

3.1 The Electron-Proton Collider HERA

HERA, the Hadron Elektron Ring Anlage [62], is the world's first lepton proton collider, located at the DESY laboratory in Hamburg, Germany. Construction began in 1984. It was commissioned in 1991 and data taking started in spring 1992.

In the two collider experiments, H1 and ZEUS, the beams are brought to collision at zero crossing angle. Two fixed-target experiments, HERMES and HERA-B, make use of the electron and proton beams, respectively. HERMES studies the spin structure of the nucleon by scattering longitudinally polarized electrons off polarized gas jet targets such as hydrogen, deuterium or ^{3}He. Transversely polarized electrons are turned into longitudinally polarized electrons using spin rotators. The HERA-B experiment is designed to measure $\mathcal{CP}$-violation in the $B^0\overline{B^0}$-system. It uses collisions of the proton beam halo with a wire target for the production of B-mesons.

Figure 3.1 shows a schematic layout of the HERA accelerator complex. Two separate rings for electrons and protons, located in a 6.3 km long tunnel 15-30 m underground, use conventional and superconducting magnets respectively.

The proton accelerator chain starts with a 50 MeV H^- linear accelerator. Before injection into the DESY III synchrotron ring, the electrons are stripped off the H^-

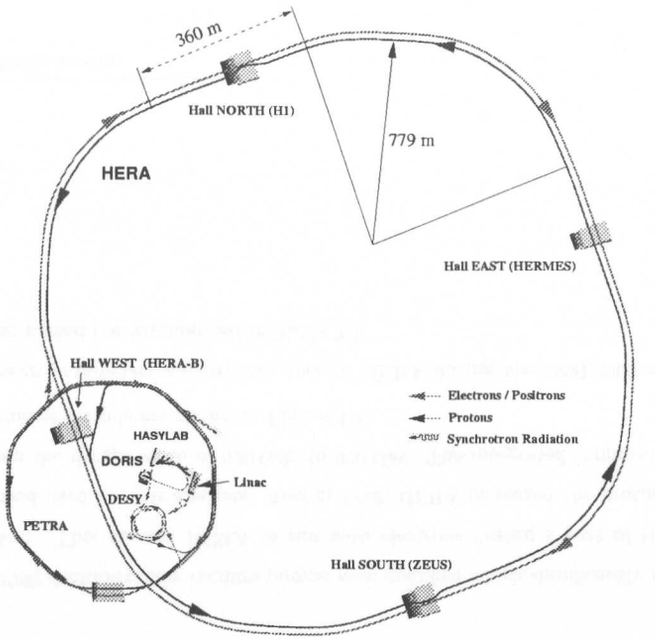

Figure 3.1: The HERA accelerator complex. Four experiments are located in the experimental halls South (ZEUS), West (HERA-B), North (H1), and East (HERMES).

ions. After subsequent acceleration to 7.5 GeV and 40 GeV in DESY III and PETRA II, respectively, the protons are injected into the HERA storage ring where they are accelerated to their final energies.

The electron injection starts with a 500 MeV linear accelerator filling the positron injection accumulator (PIA). In DESY II and PETRA II the electrons are accelerated to 7.5 GeV and 12 GeV, respectively, and then transferred to HERA where they are accelerated to 27.5 GeV.

HERA can be filled with up to 210 electron and 210 proton bunches with 96 ns

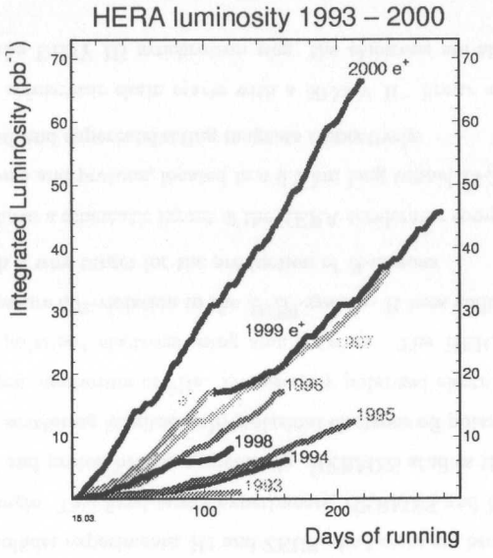

Figure 3.2: Integrated luminosity delivered by HERA during data taking periods 1993 - 2000 (until September 2000). From 1994 to 1997 protons were accelerated to 820 GeV. During the period 1998-2000 920 GeV protons were used.

spacing. In practice not all bunches are filled [1]. Noncolliding (unpaired) bunches allow to estimate the beam related background and empty bunches can be used to measure cosmic ray background rates and for other purposes. For instance events taken by the experiments in coincidence with empty bunches, i.e. events in which no activity from *ep* collisions is expected in the detectors, are used to study their response due to noise activity.

From mid 1994 to 1997 HERA accelerated positrons instead of electrons due to lifetime problems which were attributed to capturing of positively charged dust. During

[1] In 1999-2000 HERA was operated with typically 174 colliding bunches.

HERA parameters	Design Values		Values of 1999-2000	
	$e^{\pm}$	p	$e^{\pm}$	p
Circumference (m)	6336			
Energy (GeV)	30	820	27.6	920
Center-of-mass energy (GeV)	314		318	
Injection energy (GeV)	14	40	12	40
Maximum current (mA)	58	160	37	99
Number of bunches	210	210	174+15[1]	174+6[1]
Time between bunch crossings (ns)	96			
Horizontal beam size (mm)	0.301	0.276	0.200	0.200
Vertical beam size (mm)	0.067	0.087	0.054	0.054
Longitudinal beam size (mm)	8	110	8	170
Max. specific luminosity ($cm^{-2}s^{-1}mA^{-2}$)	$3.6 \cdot 10^{29}$		$9.9 \cdot 10^{29}$	
Max. inst. luminosity ($cm^{-2}s^{-1}$)	$1.5 \cdot 10^{31}$		$2 \cdot 10^{31}$	
Integrated luminosity per year (pb^{-1})	35		56	

Table 3.1: HERA design parameters and performance during 1999-2000 running.

the 1997-1998 shutdown new vacuum pumps were installed which significantly reduced this problem. This allowed HERA to run with electrons during a part of the data taking period used for this analysis. Also in 1998, HERA increased the proton beam energy from the design value of 820 GeV to 920 GeV. The integrated luminosities for these 3 running periods are shown in Figure 3.2.

The design parameters and performance of HERA during the 1999-2000 electron data taking period are summarized in Table 3.1.

[1] Non-colliding bunches.

Chapter 4

ZEUS a Detector at HERA

The ZEUS detector at HERA is a general purpose magnetic detector which has been in operation since 1992 [63]. It has been designed to study various aspects of electron-proton scattering. The design incorporates the large forward-backward asymmetry of the *ep* final state system due to the significant difference in the energy of the electron and proton beams which results in a center-of-mass system which is moving in the direction of the proton beam relative to the lab frame system. The ZEUS detector consists of various subcomponents to characterize the *ep* final state in terms of energy, direction and type of the produced final state particles, i.e. hadrons and leptons.

The coordinate system of the ZEUS detector is a right handed coordinate system with the origin ($X = Y = Z = 0$) at the nominal interaction point, the Z axis pointing in the proton beam direction, the Y axis pointing upwards and the X axis pointing horizontally towards the center of HERA. The polar angle θ is measured with respect to the positive Z axis and the azimuthal angle ϕ relative to the positive X axis. Thus, the polar angle of the proton and electron beam is equal to 0° and 180°, respectively.

Figures 4.1 and 4.2 show a cross-section of the ZEUS detector along and perpendicular to the beam direction, respectively.

In the center of ZEUS, the central tracking detector (CTD) [64] surrounds the interaction point. In the forward and rear directions additional tracking information is

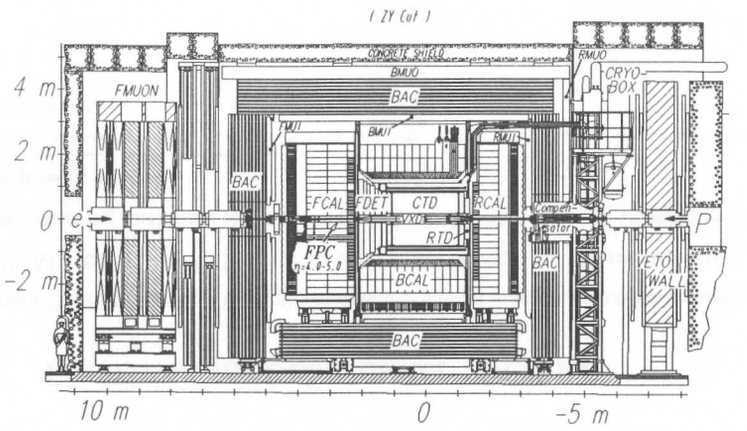

Figure 4.1: Cross-section of the ZEUS detector along the beam direction.

provided by the FTD/TRD and RTD chambers. The FTD consists of three sets of planar drift chambers with transition radiation detectors (TRD). The RTD is made of one planar drift chamber with three layers. Until 1995 a vertex detector (VXD) was installed around the beam pipe. In the 2000/2001 shutdown it was replaced by a silicon micro vertex detector (MVD) [65]. The whole tracking system is surrounded by a superconducting magnet providing a 1.43 T magnetic field.

A high resolution uranium calorimeter (UCAL) [66, 67, 68] is the prime device for the energy measurement of electrons and hadrons. It is subdivided into three parts: the forward calorimeter (FCAL), the barrel calorimeter (BCAL) and the rear calorimeter (RCAL). In order to detect electrons at very low scattering angles, a beam pipe calorimeter (BPC) [69, 70] has been installed on two sides of the beam pipe in the rear direction. In 1998 in the forward direction a Forward Plug Calorimeter (FPC) [71, 72, 73] has been installed in the beam pipe hole of the FCAL, extending the calorimetric coverage by one unit in pseudorapidity.

A small angle rear tracking detector (SRTD) in mounted in front of the RCAL and covers an area of $68 \times 68\,\mathrm{cm}^2$. Presampler detectors, RPRES and FPRES, which consist

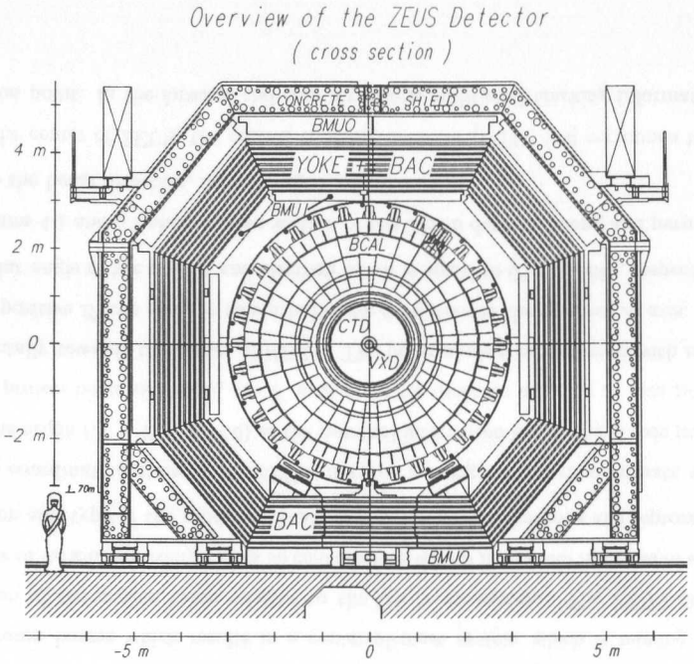

Figure 4.2: Cross-section of the ZEUS detector perpendicular to the beam direction.

of single layers of scintillator [74] plates, are installed in front of the RCAL and FCAL modules. In RCAL and FCAL a hadron-electron separator (HES) [75] consisting of a plane of 3×3 cm^2 silicon diodes is installed after 3 radiation lengths.

An iron yoke made of 7.3 cm thick iron plates surrounds the main calorimeter (UCAL) which provides a return path for the solenoid magnetic field flux. It is instrumented with proportional chambers to provide a measurement of energy leakage from the main calorimeter and serves, therefore, as a backing calorimeter (BAC). The iron yoke itself is magnetized to 1.6 T by copper coils to deflect muons. Limited streamer tubes are mounted inside and outside of the barrel (BMUI, BMUO) and the rear (RMUI, RMUO) iron yoke and are used for the muon momentum measurement. In the forward direction, limited streamer tubes which are mounted on the inside of the iron

yoke (FMUI) as well as drift chambers and limited streamer tubes (FMUO) mounted outside the iron yoke are used for the forward muon momentum measurement within a toroidal magnetic field of 1.7 T which is produced by two iron toroids.

An iron/scintillator veto wall at $Z = -7.3$ m is used to reject beam related background. Two lead/scintillator electromagnetic calorimeters in the electron beam direction at $Z = -34$ m and $Z = -107$ m are used to measure electrons from bremsstrahlung and photoproduction events and photons from bremsstrahlung events, used for the luminosity determination at ZEUS, and radiative events, respectively.

In the forward direction, a lead/scintillator counter at $Z = 5.1$ m, the proton remnant tagger (PRT), allows to obtain information about the hadronic final state in the forward direction for a range in pseudorapidity of $4.3 < \eta < 5.8$. A leading proton spectrometer (LPS) [76] at $Z = 26 - 96$ m is used to measure very forward scattered protons (transverse momentum < 1 GeV) using six stations of silicon strip detectors which are mounted very close to the beam. A forward neutron calorimeter (FNC) [77] of a lead/scintillator sandwich type is installed at $Z = 105.6$ m to detect very forward produced neutrons.

The most significant parameters of the ZEUS detector are summarized in Table 4.1. The following sections provide a brief description of those detector components which are relevant to the physics analysis presented in this thesis.

4.1 The Uranium Calorimeter (UCAL)

The main ZEUS calorimeter is a high resolution sampling uranium/scintillator calorimeter (UCAL) [66, 67, 68] [1]. It is the most essential detector for the reconstruction of the *ep* scattering final state and plays a crucial role together with the tracking system in the present analysis.

[1] Extensive literature about the development and optimization of the UCAL, history of test and calorimeters performance may be found in [80] and references therein.

Table 4.1: The principal ZEUS central detector parameters (1999-2000 status).

Component	Parameter	Value	Comment
Calorimeter	Angular coverage	$2.6 < \theta < 176.2°$	Extended to 178.4° in 1995
	σ/E(EM showers)	$0.18/\sqrt{E(\mathrm{GeV})} \oplus 0.02$	test beam [78]
			[68]
	EM E scale uncertainty	$1-3\,\%$	[78]
	σ/E(Hadronic showers)	$0.35/\sqrt{E(\mathrm{GeV})} \oplus 0.03$	test beam [66]
			[68]
	had E scale uncertainty	$3\,\%$	[78]
	position resolution	$\sim 1\,\mathrm{cm}$	EM showers, [79]
	time resolution	$< 1\,\mathrm{ns}$	for $E > 4.5\,\mathrm{GeV}$
Central	B-field (Tesla)	1.43	
Tracking	angular coverage	$11° < \theta < 168°$	
	σ/p_T	$0.005 \cdot p_T(\mathrm{GeV}) \oplus 0.016$	Full length tracks [78]
	z vertex resolution	$0.4\,\mathrm{cm}$	Full length tracks, $p_T > 5$ GeV
	$R-\phi$ vertex resolution	$0.1\,\mathrm{cm}$	Full length tracks, $p_T > 5$ GeV
Luminosity	normalization uncertainty	$1.8-2.25\,\%$	

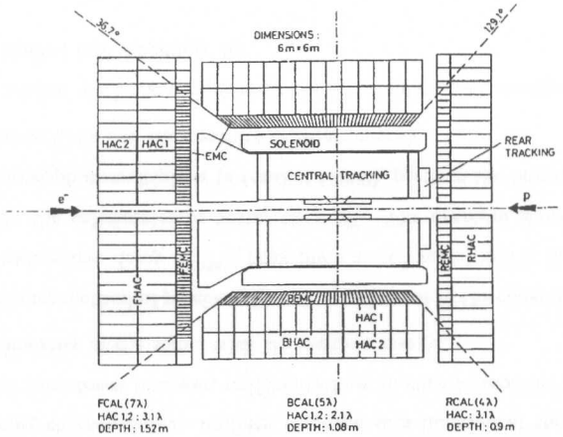

Figure 4.3: Schematic layout of the ZEUS UCAL. The UCAL surrounds the solenoid of the Central Tracking System (see Section 4.2) and it is subdivided in three sections, a forward (FCAL), a barrel (BCAL) and a rear (RCAL). The angular coverage, the depth in m and in interaction lengths, λ, are given for the three sections of the UCAL.

Figure 4.3 displays an schematic representation of the layout of the ZEUS Uranium Calorimeter. Taking into account the 20×20 cm^2 hole for the HERA beam pipe in the FCAL and the 8×20 cm^2 beam hole in the RCAL, the calorimetric coverage is $>$ 99.8% of 4π sr.

The calorimeter is vertically (FCAL and RCAL) and radially (BCAL) subdivided

	FCAL	BCAL	RCAL
η-range	3.8 - 1.0	1.1 - (-0.74)	(-0.72) - (-4.2)
θ-range	2.5° - 39.9°	36.7° - 129.1°	128.1° - 178.4°
EMC rad. length X_0	25.9	22.7	25.9
total abs. length λ	7.14	4.92	3.99

Table 4.2: Angular acceptance and longitudinal depth of the UCAL.

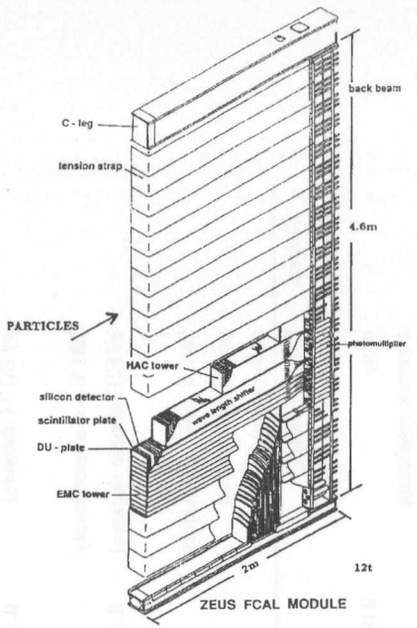

Figure 4.4: Layout of a FCAL module. It is longitudinally subdivided into one EMC and two HAC sections, which in turn are divided into cells. Each cell is read out by two wavelength shifter bars on opposite sides.

into modules (Figure 4.4), which themselves are subdivided into towers. Longitudinally, the towers are segmented into an electromagnetic (EMC) and two (RCAL only one) hadronic sections. The cells placed around the beam pipe conform are referred to as inner ring.

The thickness of the uranium and scintillator plates of the UCAL has been optimized to give equal signals for electrons and hadrons of equal energy ($e/h = 1$). Such a calorimeter is called compensating calorimeter. It has the advantage that for all jets of the same energy (ignoring muons and neutrinos in the jet) it produces the same signal size irrespective of their electromagnetic (electrons, photons) and hadronic (pions,

protons, etc) composition.

In order to achieve the desired characteristics of the final ZEUS calorimeter, in particular the excellent energy resolution for hadrons and particle jets, extreme care has been taken in the design and fabrication of all individual components: the optical readout comprising of scintillator plates, wave length shifters (WLS), light guides, photomultiplier tubes (PMT), PMT shielding against magnetic field and also the calorimeter electronics, depleted uranium plates, etc... As a result, the UCAL energy resolution measured under test beam conditions achieved for electrons is:

$$\frac{\sigma_E}{E} = \frac{18\%}{\sqrt{E/\mathrm{GeV}}} \oplus 2\% \tag{4.1}$$

and for hadrons

$$\frac{\sigma_E}{E} = \frac{35\%}{\sqrt{E/\mathrm{GeV}}} \oplus 1\% \tag{4.2}$$

The scintillator light is collected from the two opposite sides of the cells is transported to two PMT's via separate WLS plates. This experimental technique was developed first in [81] and further applied in the conditions of the ZEUS calorimeter [82].

A precise calibration of the UCAL is as important as an excellent energy resolution for hadrons and jets. The design and production of the calorimeter were aimed at ensuring that the ratio of measured signal to deposited particle energy be independent of position and time at the level of 1%. To achieve this aim the calorimeter has to fulfill the following characteristics: uniform response as a function of the position in each calorimeter from tower to tower, uniformity from module to module, signal stability in time and linearity of the signal with the particle energy.

The primary method of precise calibration makes use of the constant signal resulting from the radioactive decay of ^{238}U (half life $4.5 \cdot 10^9$ years) and is used as a reference to calibrate the calorimeter to better than 1%. The uranium signal (UNO) is used for monitoring photomultipliers (a total of 12000), perform the inter-calibration of the calorimeter sections and the absolute calibration scale.

In the present work the energy response and resolution at energies, E, $E \lesssim 10\,\mathrm{GeV}$ has been studied (see Appendix A).

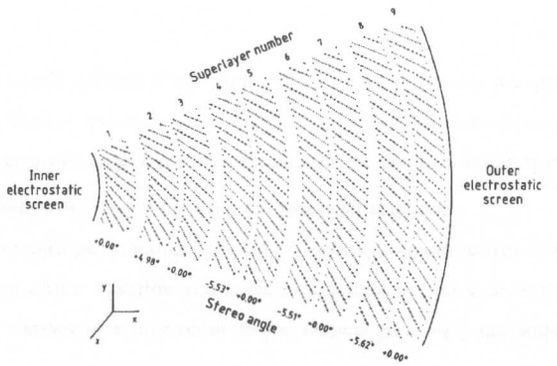

Figure 4.5: Layout of a CTD octant.

4.2 The Central Tracking Detector (CTD)

The central tracking detector (CTD) [64] provides a measurement of the direction and momentum of charged particles with high precision. A measurement of the mean energy loss dE/dx of charged particles within the gas chamber volume of the CTD provides in addition a means of particle identification.

The CTD is a cylindrical drift chamber. Its active volume has a length of 205 cm, an inner radius of 18.2 cm and an outer radius of 79.4 cm. It has a polar angle coverage of $15° < \theta < 164°$ and a full coverage of the azimuthal angle ϕ. The chamber is filled with a mixture of argon, CO_2 and ethane. Figure 4.5 shows the cross-section of an octant of the CTD. The CTD is designed as a multi-cell stereo superlayer chamber (SL). It consists of nine superlayers which are built out of single cells with eight sense wires each. The number of cells increases from the first superlayer having 32 cells to 96 cells for the last superlayer. The CTD in total consists of 576 cells with 4608 sense wires and 24192 field wires. Superlayers labelled with odd numbers as shown in Figure 4.5 have sense wires which run parallel to the beam axis whereas even labelled superlayers have sense wires which are declined by a certain angle with respect to the beam axis.

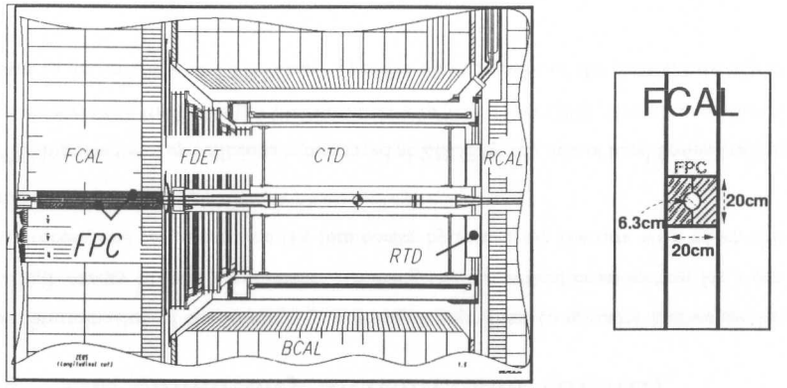

Figure 4.6: Longitudinal cut of the inner part of the ZEUS detector and front view of the forward calorimeter. The FPC is installed into the 20×20 cm^2 beam hole of the FCAL.

The angles of inclination are drawn on the bottom of each superlayer, as shown in Figure 4.5. The superlayers 1, 3 and 5 are instrumented with a z-by-timing system for trigger purposes ($\sigma_Z \simeq 4$ cm). The resolution of the CTD in $r - \phi$ is about 230 μm. The momentum resolution amounts to $\frac{\sigma(p)}{p} = 0.005 \cdot p \oplus 0.0016$ (p in GeV) for long tracks. The interaction vertex is measured on an event-by-event basis with a typical resolution along (transverse) to the beam direction of 0.4(0.1) cm.

In the present work the scale momentum reconstruction and resolution were determined independently from MC simulations (see Appendix B).

4.3 The Forward Plug Calorimeter (FPC)

The FPC, a sampling lead/scintillator calorimeters, was installed in 1998 into the forward beam hole of the UCAL. It extends the calorimetric coverage in pseudorapidity from $\eta \leq 4.0$ to $\eta \leq 5.0$. This is illustrated in Figure 4.6 The FPC was optimized to

detect particles of coming from the break up the proton in ep collisions.

Based on the results obtained with a lead/scintillator calorimeter of similar composition [83] the FPC is expected to be compensating ($e/h = 1$).

The energy resolution for electrons was found to be $\sigma_E/E = 34\%/\sqrt{E} \oplus 7\%$ and for pions the energy resolution of the combined signal from the FPC and the surrounding FCAL was determined to be $\sigma_E/E = 53\%/\sqrt{E} \oplus 11\% \oplus 3\% \ln(E)$ [73]. The last term in the expression of the energy resolution for hadrons of the FPC is due to longitudinal energy leakage.

The FPC plays a central role in the analysis of the major source of systematic error in the present work, the contamination from production of vector mesons via the dissociation of the proton. (see Section 8.1.1). The inclusion in the analysis of the FPC is one of the highlights of the contribution of the present work to the production of vector mesons at HERA.

4.4 The Small Angle Tracking Detector (SRTD)

In order to improve the measurement of the energy and angle of the scattered electromagnetic showers in the rear region of the ZEUS detector, a Small Angle Tracking Detector (SRTD) has been installed in 1994 [84]. It is attached to the front face of the RCAL and covers approximately an area of 34 cm radius around the beam pipe (Figure 4.7).

The SRTD consists of a horizontal and a vertical layer of 1 cm wide and 0.5 cm thick scintillator strips. Position and pulse height information is provided via optical fiber and photomultiplier readout. The SRTD is used to measure the electron impact position. A position resolution of ~ 0.3 cm has been achieved.

Electrons which lose energy through showers in the inactive material in front of the calorimeter, in general, deposit more energy in the SRTD than non-showering electrons. The measured energy deposit in the SRTD can be used to correct for this energy loss.

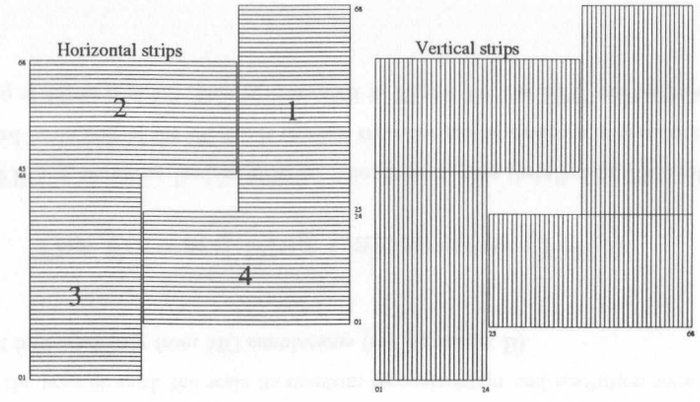

Figure 4.7: Orientation and numbering scheme of the strips of the two SRTD planes. The strip size is 0.98 cm × 24(44) cm. The asymmetric shape is due to the movement of the RCAL modules in 1995 in order to reduce the beam hole size.

The SRTD also provides a fast time measurement (resolution $\sim$ 2 ns), which is used to reject background events at the trigger level.

For details of the alignment and calibration of the SRTD in the conditions of the 1999 and 2000 running periods see Appendixes C and D.

4.5 The Luminosity Measurement (LUMI)

The determination of the luminosity is a major ingredient to measure a cross-section in a high energy physics experiment. Knowing the theoretical cross-section for a certain process, one can determine the luminosity by measuring the rate with which this particular process occurs.

The luminosity of ep collisions is measured at ZEUS by the rate of hard bremsstrahlung photons form the Bethe-Heitler process $ep \to e\gamma p$ [85]. From QED, this cross-section is known to an accuracy of 0.5%. Thus, a precise measurement of the photon rate allows

to precisely determine the *ep* luminosity at HERA.

Photons of the Bethe-Heitler process are detected at by a lead/scintillator calorimeter (LUMIG) [86, 87] (see Figure 4.8). The energy resolution amounts to $18\%/\sqrt{E}$ under test beam conditions. A carbon/lead filter which is installed in front of the LUMIG detector for shielding against synchrotron radiation reduces the achieved energy resolution under test beam conditions to $23\%/\sqrt{E}$. Two layers of orthogonal 1 cm wide scintillator strips are installed within the LUMIG provide a means of position reconstruction of the incoming photon. The position resolution has been determined to be 0.2 cm in X and Y.

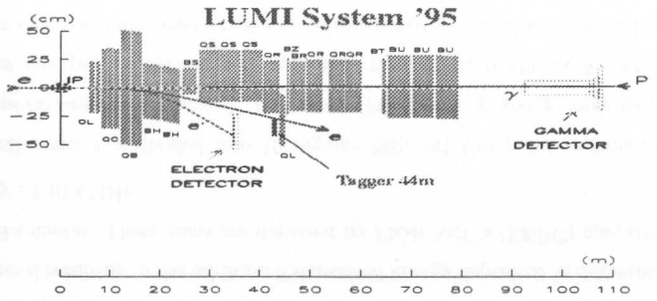

Figure 4.8: Layout of the luminosity monitor.

4.6 The ZEUS Data Acquisition System

The ZEUS data acquisition system (DAQ) takes care of reading out and processing the information from the complex ZEUS detector. The ZEUS detector with its subcomponents has a total of 250000 readout channels. The majority of events which leave a detectable signal in these subcomponents are not *ep* events. The total interaction rate is dominated by interactions of the proton beam with the residual gas in the beam pipe (beam gas interactions). This interaction yields activity in the ZEUS detector with a

rate on the order of $10 - 100$ kHz whereas the rate for *ep* physics events is only a few Hz.

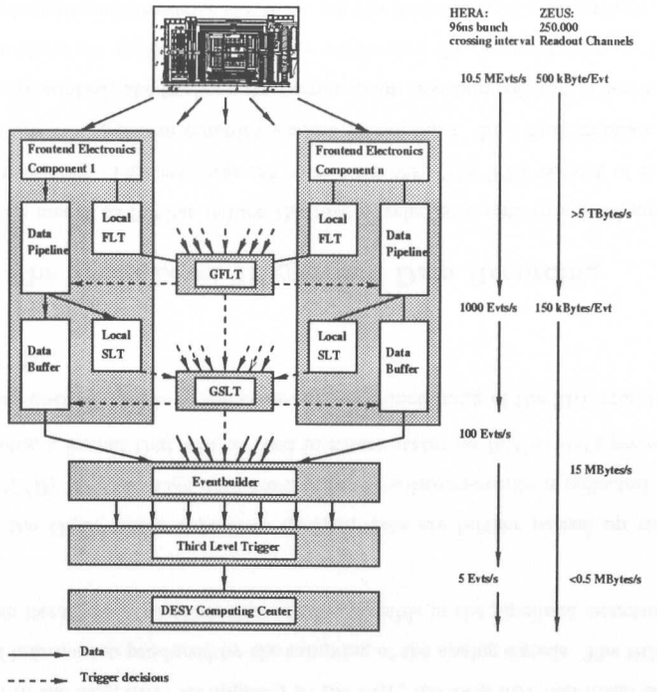

Figure 4.9: Schematic diagram of the ZEUS trigger and data acquisition system.

The ZEUS DAQ system consists of pipelined readout and a three level trigger structure [88, 89, 90]. The structure of the ZEUS DAQ is depicted in Figure 4.9.

4.6.1 Pipeline Readout System

Collisions at HERA happen every 96 ns. This is too fast so that any detector component may make the decision of taking or throwing out the event. Additionally, trigger decisions may be made on the basis of the combined information of various detectors.

The signal collection and transfer to the decision making system depends on the detector device. As a solution the data are kept in a pipeline and the decision of the FLT is adjourned by 4.4 μs after the collision [89].

Central for the ZEUS DAQ is the pipelining of the ZEUS Calorimeter. If the trigger decision is positive the data must be recovered from the pipeline. If negative the data will be overwritten as the pipeline is continuously recording data information.

A detailed description of the functioning and calibration of the front end electronics of the ZEUS calorimeter is available in [91].

4.6.2 First Level Trigger

In order to reach a decision, the trigger system receives part of the detected signal. In the case of the calorimeter trigger some 5% of the current produced by the PMT's is driven to the input of the trigger sum cards. In these devices the analog sum of currents is performed resulting in the addition if deposited energy deposited in different sections of the calorimeter. These sums are digitized by Flash ADC's (FADC) operating at the frequency of 10.4 MHz.

The calorimeter is divided into 16 regions [92]. At this point various hard wire digital operations are performed: quantities like energy, x and y component of the transverse energy of electromagnetic and hadronic sections of the UCAL, etc... These quantities calculates for various regions are transferred for global analysis and a regional comparison to a processing system which calculates and records some meaningful global information.

The description of the functioning of other ZEUS subcomponents FLT may be found in [93, 94, 63, 95].

The trigger information sent from the components of the ZEUS detector are sent to the GFLT. The component data include the regional information from the UCAL and tracking detectors. The data from the components are classified into 8 categories. Logical operations are generated from Yes/No bits to generate individual sub-triggers.

The final GFLT decision is issued from the logical OR of these sub-triggers. For each sub-trigger there is a pre-scaler to reduce the trigger rate or veto the sub-trigger when necessary.

4.6.3 Event Buffer and the Second Level Trigger

Triggered by the decision of the GFLT the main stream of analog signal coming from various subcomponents of the ZEUS detector is digitized. The results of the digitization are stored at the digitizer buffer and sent to the SLT. The SLT is subdivided in two sections, as a follow up of the structure of the FLT: the local SLT and the global SLT (GSLT). The digitized signals proceeding from the various ZEUS subcomponents are processed in the local SLT. As opposed to the FLT, the local SLT can make use of the full set of information produced by the sampling of the analog signals. The SLT is able to perform iterative calculations that are not possible in the pipelined structure of the FLT.

When the GSLT issues a positive decision data are further passed on the Event Builder (EVB). At this stage data from different subcomponents is collected and put into a tables, a format that will be used in future states for further data processing.

Detailed documentation of the structure and functioning of the SLT may be found in [96, 97, 98].

4.6.4 The Third Level Trigger and Data Recording

The TLT is meant to further reduce the rate of selected events to a level acceptable for data recording. This rate was set to ≈ 5 Hz [99]. The TLT consist of a farm of work stations that perform complex on-line calculations. In a first instance general veto cuts are applied, like timing cuts, cosmic muon rejection cuts etc. Then a number of physics filters are applied. This implies performing the reconstruction of the event and the calculation of kinematic variables. At this level the on-line algorithms are very

similar to those used off-line, with the difference that looser cuts on kinematic variables are applied.

The TLT performs the last decision in the chain of the ZEUS trigger system. An event that is accepted by the TLT is finally driven for recording to the DESY Computer Center, where data will be stored for further off-line analysis.

Chapter 5

Extension of Energy Range of the Measurement of the Production of Heavy VM's

A major motivation behind the present work is to extend the energy range of the measurement of the production of heavy VM's. So far, the products of the decay of vector mesons have been measured by the ZEUS Collaboration mainly with the CTD. Since the CTD has limited acceptance in the forward and backward regions, the W range accessible was restricted in the case of the J/ψ photoproduction to $40 < W < 140$ GeV [27]. The studies performed to develop a trigger that would provide high efficiency in an extended W range are presented in this Chapter. Considerations below have been derived for the case of the production of the J/ψ (see Chapter 9) , but they are applicable to the case of heavier VM's (see Chapters 10 and 11).

5.1 Kinematics of the Extension

The photoproduction regime is defined as the regime in which the angle of the scattered electron is too small to be seen in the RCAL. The minimum kinematically possible Q^2,

Q^2_{min}, is $Q^2_{min} = \frac{m_e^2 y^2}{(1-y)} \approx 10^{-10}\,\mathrm{GeV}^2$, the maximum allowed Q^2, Q^2_{max}, $Q^2_{max} \approx 1\,\mathrm{GeV}^2$, is determined by the geometry of the RCAL. The median Q^2, $\langle Q^2 \rangle \approx 5 \times 10^{-5}\,\mathrm{GeV}^2 \ll M_V^2$. Since $M_V^2 \gg Q^2_{max}$ the Q^2 dependence of the production cross-section has little impact and the median of the Q^2 determined mainly by the photon flux radiated by the incoming electron. Using the conservation of the energy in the reaction one may write down:

$$E_e + E_p = (1-x)E_p + E_{e'} + E_V \tag{5.1}$$

or

$$x = \frac{E_V - E_q}{E_p} \tag{5.2}$$

where x is the fraction of the energy of the incoming proton that participates in the creation of the VM and E_q is the energy carried by the photon. Since $E_p \gg E_V - E_q$, x$\ll$ 1. We may make use of another kinematic constraint, namely the fact that the final state has a known mass. For simplicity, we may consider the proton scattering with no transverse momentum ($t = 0$):

$$M_V^2 = (xp+q)^2 = x^2 m_p^2 + 2xp \cdot q + q^2 \approx 2xp \cdot q \approx xW^2 \tag{5.3}$$

or

$$x \approx \frac{M_V^2}{W^2} \tag{5.4}$$

From Equation (5.2) and (5.4) we get the W dependence of E_V:

$$E_V \approx E_q + \frac{E_p}{W^2} M_V^2 \approx \frac{E_e}{s} W^2 + \frac{E_p}{W^2} M_V^2 \tag{5.5}$$

In this simplification, the VM is produced with no transverse momentum with a longitudinal boost on either direction along the beam axis. The first term in Expression (5.5) is the energy transmitted by the incoming electron to the VM. This term grows with W. The second term corresponds to the energy transmitted by the proton and grows as W gets small. The W dependence of the energy of the produced VM is illustrated in Figure 5.1. If one derivates the Expression (5.5) with respect to W^2 in order to find the minimum one gets:

$$W_m^2 = \sqrt{\frac{sE_p M_V^2}{E_e}} \tag{5.6}$$

At $W < W_m$ the VM is boosted along the direction of the incoming proton, and at $W > W_m$ is boosted along the direction of the incoming electron.

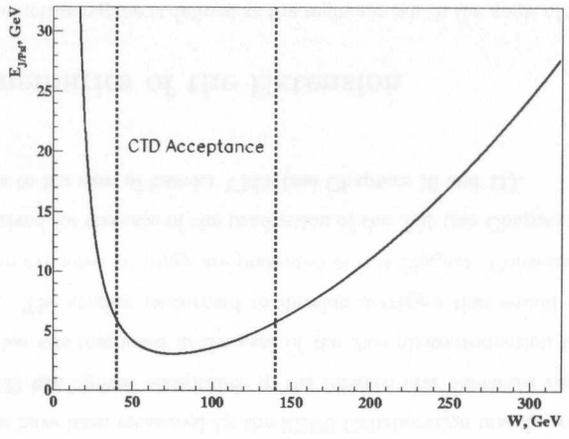

Figure 5.1: The energy of the VM in photoproduction may be approximated to the Expression (5.5). The J/ψ is produced in the region of the acceptance in W of the CTD almost at rest. Outside the acceptance of the CTD, as we go to low and high W the energy with which the J/ψ is produced grows. In this region the UCAL may be used to reconstruct the kinematics of the event.

In the case of the J/ψ, the value of $W_m \approx 75$ GeV, in the middle of the acceptance in W of the CTD. As the resolution of the tracking measurement degrades proportionally to the momentum, we can achieve the best resolution of the invariant mass of the decay particles when the J/ψ is produced with the least energy. This is achieved since the J/ψ is produced almost at rest at a value of W for which the acceptance of the CTD is maximum (see Figure 5.5). As the J/ψ is produced at a $W > W_m$ or $W < W_m$ its decay products start to miss the CTD, but can still be detected in the UCAL since the latter has a larger angular acceptance. In the case of the J/ψ decaying into e^+e^-, the energy of its decay products may be measured in the UCAL. Since the energy

resolution of clusters in the UCAL improves with energy, the kinematics of the events will be better reconstructed with the UCAL the further away W is from W_m.

5.2 Feasibility of the Extension

The energy of electromagnetic clusters may be reconstructed reliably by the UCAL starting from a minimum energy, E_{min}, above which the energy scale of the UCAL is stable and well known. The value of E_{min} has been determined to be around 3 GeV (see Appendix A). Also, electrons before reaching the UCAL have to cross a non-negligible amount of inactive material. The existence of inactive material degrades the energy resolution of such low energy clusters. The resolution of the di-e invariant mass, $M_{e^+e^-}$, reconstructed with UCAL clusters needs to be no worse than 500 MeV due to the minimum invariant mass requirement imposed at the trigger level, $M_{e^+e^-} > 1.5$ GeV (see Section 5.3). The relative error on the reconstructed $M_{e^+e^-}$ may be written as (neglecting the small impact of the uncertainty in the position reconstruction):

$$\frac{\delta M_{e^+e^-}}{M_{e^+e^-}} \approx \frac{1}{2}\left(\frac{\delta E_1}{E_1} \oplus \frac{\delta E_2}{E_2}\right) \tag{5.7}$$

where, δE_1 and δE_2 are the uncertainties in the determination of the energy of the first and second electron, respectively. The energy resolution of an electromagnetic cluster at low energy behaves as $\delta E \approx 0.27\sqrt{E}$ (see Appendix A). Therefore, we can easily calculate the upper bound for the resolution of $M_{e^+e^-}$ in the analysis; the resolution obtained by reconstructing an event with two clusters of minimum energy: $\delta M_{e^+e^-} < M_{J/\psi} 0.19/\sqrt{E_{min}} \simeq 300\,\text{MeV}$ [1].

In order to see the whether it is possible to implement successfully the UCAL information combined with the CTD we need to determine in what ranges of W the UCAL is necessary to reconstruct the kinematics of the event. It is convenient to divide the events according to the following topology:

[1]The resolution in $M_{e^+e^-}$ and other variables will be discussed in more detail in Chapter 7.

- Events with two CTD tracks [2].
- Events with one CTD track. The event is reconstructed together with the UCAL cluster created by the second electron.
- Events with no tracks. The event is fully reconstructed using two UCAL clusters.

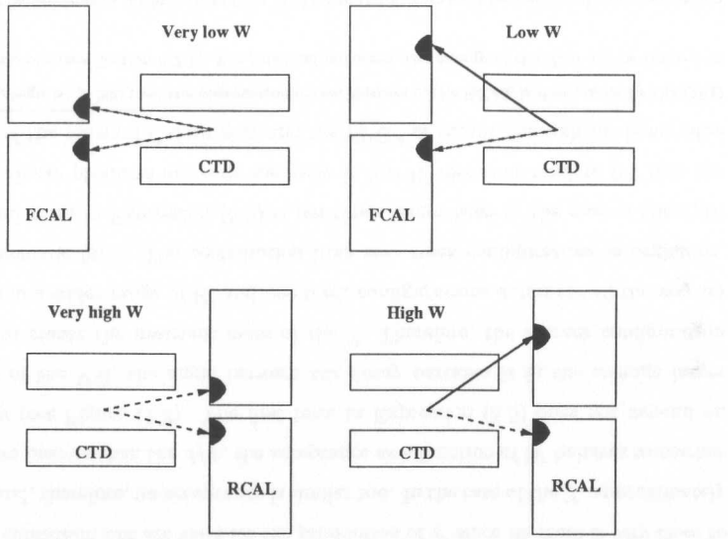

Figure 5.2: Schematic representation of the topology at very low W (upper left), low W (upper right), very high W (lower left) and high W (lower right).

The schematic representation of the new different topologies introduced for the extension of the W range of the measurement of heavy VM's is given in Figure 5.2. The relative fraction of these three different topologies change with W and depends mainly on the geometrical acceptance of the CTD and the mass of the VM. The relative

[2]Throughout the text the term track should me understood as quality track. The concept of quality track is defined differently at the trigger level (see Section 5.3) and at the off-line level (see Section 6.4).

fraction of these three different topologies is calculated with the help of MC and it is illustrated in the Figure 5.3 for the J/ψ.

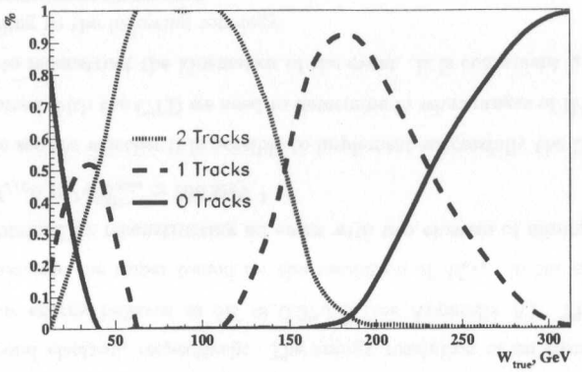

Figure 5.3: The relative fraction of 2 track, 1 track and 0 track topologies as a function of W for the production of J/ψ.

The decay particles are mainly balanced in transverse momentum, but their energy may be asymmetric. The restriction on the minimum energy of the cluster applies to the electron that misses the acceptance of the CTD. The electron that misses the acceptance of the CTD tends to have more energy than the first electron. In the case of the J/ψ, 1 track configurations are dominant in the range $150 < W < 230$ GeV. The energy of the J/ψ ranges between $6 < E_{J/\psi} < 15$ GeV. In this W range and in the worst scenario, the symmetric production of decay particles, the minimum energy of the electron that misses the acceptance of the CTD will be 3 GeV. The more asymmetric is the decay, the more energy will be transmitted to the electron that misses the acceptance of the CTD and the less we will be affected by the requirement on the minimum energy of the cluster (see Section 5.3.1). The loss of acceptance in the symmetric decays at $150 < W < 200$ GeV is well modelled by the MC. As will be discussed in Section 9.6, the parameters responsible for the angular distribution of the decaying particles are determined to a high degree of accuracy. The systematic error

due to this loss of acceptance is negligible (see Section 9.3). At W lower than 40 GeV, when the acceptance is already dominated by 1 track and zero track configurations the energy of the J/ψ grows rapidly and the events are basically unaffected by the requirement of the minimum energy of the cluster. Due to trigger considerations (see Section 5.3) zero track configurations were dropped at low W for the analysis.

Zero track configurations dominate in the range $230 < W < \sqrt{s}$ GeV. In this range, the average energy of the J/ψ ranges [3] $15 < E_{J/\psi} < E_e = 27.5$ GeV. In this case, both electrons miss the acceptance of the CTD and the energies of both clusters are affected by the minimum energy requirement. This time the most asymmetric configurations will be affected, the higher W the less one will be affected by this cut. Again, this effect is taken into account by the MC to a high degree of accuracy.

These considerations are valid for the production of ψ' since its mass is very close to the J/ψ and, therefore, its acceptance is similar too. In the case of the Υ, approximately three times heavier than the J/ψ, the acceptance as a function of W behaves somewhat differently (see Figure 11.3). The first term in Expression (5.5) does not depend on the mass of the VM, the angle between the decay particles is in the average larger in order to create the invariant mass of the Υ. Therefore, the 2 track configuration dominate in a wider range of W and one track configurations dominate all the way up to the kinematic limit. The contribution from zero track configurations is negligible. The second term in Expression (5.5) is ten times larger than in the case of the J/ψ. Since the decay products are very energetic at low W electrons tend to fall into the first ring of the Forward Calorimeter and the FPC [4] or escape through the beam pipe

[3] At very high $W > 290$ GeV the observation of two clusters in the RCAL is dominated by the QED Compton process (see Section 8.2.1). For practical purposes, the energy of the J/ψ will be limited to 21 GeV.

[4] Energy depositions in the first ring of the FCAL and the FPC cannot be used for the reconstruction of the kinematics of the event since this region of the Calorimeter displays too much activity. The cross-section of the process under study is much smaller than the total cross-section of inelastic ep collisions in which the proton breaks up and leaves energy depositions in the first ring of the FCAL and the FPC.

undetected. As a result, the acceptance of this process is negligible below $W < 30$ GeV. In this region the zero track configurations also give a negligible contribution. This analysis is restricted to the study of events with at least one track.

5.3 Trigger Selection Studies

The trigger configuration was tuned in the past to select events with two tracks in the CTD with a minimum $M_{e^+e^-}$. The implementation of 1 track and 0 track topologies required the introduction of changes at the three trigger levels. The new trigger logic had to accommodate not only new topologies of events but also a reduction of the trigger rate at the FLT (see Section 5.3.1). A central requirement to the trigger configuration was to secure running with no pre-scale. The uncertainty in the determination of the cross-section, $\sigma(\gamma p \rightarrow J/\psi p)$, in the central region is dominated by systematic errors. However, the statistical error in the extended range in W would give a significant contribution to the total error if the trigger selection were to be pre-scaled. The measurement of $\frac{d\sigma}{dt}(\gamma p \rightarrow J/\psi p)$ and the determination of the trajectory have important contributions from the statistical uncertainty.

Another additional requirement on the new trigger configuration was to accommodate the elastic electroproduction of heavy VM$\rightarrow e^+e^-$. These type of topologies have up to three electromagnetic clusters. This new trigger ensures the tagging of other topologies and, therefore, the extension of the W range of the measurement of the elastic electroproduction of heavy VM's [100].

The analysis was allocated a trigger selection with the name HFL06. This trigger selection slot makes use of slots at the FLT, SLT and TLT. The trigger selection was modified at the three trigger levels according to the requirements specified above. After a series of trigger rate tests, the new trigger configuration became operational on February 16th 1999. This trigger configuration suffered no changes till the end of data taking in September 2000 [5].

[5]With the exemption of the dedicated runs taken to study the proton dissociative background to the elastic process (see Section 8.1.1). These runs are not used for the analysis of the elastic process.

5.3.1 First Level Trigger

The old trigger configuration at the FLT relied fully on slot 58 [6]. The logic of this slot may be summarized as follows:

1. The global UCAL energy, CAL_E [7], $CAL_E > 2032$ MeV, OR the total energy in the FCAL outside the first ring, $FCAL_{E\ out\ bp\ stb}$, $FCAL_{E\ out\ bp\ stb} > 2500$ MeV. These cuts require some activity in the calorimeter coming from the decay products of the J/ψ. In the case of $J/\psi \rightarrow e^+e^-$, all the energy of the VM should be deposited in the UCAL.

2. The energy in the first ring of the FCAL,$FCAL_{Ebp}$, $FCAL_{Ebp} < 3750$ MeV. This is a standard trigger requirement for diffractive processes. It is meant to suppress events coming from the break up of the proton.

3. The number of quality tracks should be $1 \leq N_{qt} < 4$. This cut is meant to suppress high multiplicity events coming from the break up of the proton and reduces most of the solid angle space to a small number of isolated tracks. This and the previous requirement provide a rapidity gap between the products of the decay of the VM and the scattered proton, typical for diffractive events. Only a marginal fraction of events coming from non-diffractive processes will survive these cuts.

4. The Global electromagnetic energy, CAL_{EMC} [8], $CAL_{EMC} > 660$ MeV. This requirement suppresses events with low multiplicity with low energy charged pions coming from the break up of the proton.

[6]Each level trigger is subdivided in units, or slots. For instance FLT slot 58 will be referred to as FLT58.

[7]This quantity is defined as the sum of energy of all UCAL sections except for the cells close to the beam pipe hole in the RCAL and the FCAL.

[8]Cells close to the beam pipe hole in the RCAL and the FCAL.

The rate of the slot FLT58 needed to be reduced as HERA was steadily increasing the peak luminosity during the 1998 and the beginning of 1999 data taking. The typical rate of this slot at peak luminosity under the running conditions of the beginning of 1999 was approximately 10-12 Hz, a significant fraction of the total rate, ≈ 100 Hz. This rate needed to be reduced by at least 20%. It was decided to merge requirements 1 and 4 into one, by simply requiring a minimum amount of electromagnetic energy deposit outside the first rings of the FCAL and RCAL. The threshold would be set according to the trigger rate. This dependence was studied in a number of test runs. Initially, the threshold was set to 1052 MeV, yielding an unacceptable rate over 20Hz. In the second round of test runs the threshold was set to 1640 MeV giving a rate similar to the rate of the old configuration. As a result, the threshold had to be set to 1836 MeV [9]. The rate of slot FLT58 was lowered to 6-7 Hz. It was decided to leave requirement 2 unchanged.

To summarize, the new slot was set to:

1. The requirement $1 \leq N_{qt} < 4$ remains.
2. The threshold on the amount of electromagnetic energy is lowered $CAL_{EMC} > 1836$ MeV.
3. The elasticity requirement $FCAL_{Ebp} < 3750$ MeV.

The efficiency of the new definition of the slot FLT58 compared to that of the old one is given in Figure 5.4 a). At low W the new trigger configuration is less efficient [10]. This is due to the fact that the first three rings of the FCAL have been effectively "switched off" due to trigger rate considerations, affecting events in which one of the electrons falls into one of the first rings and the second is not energetic enough to pass the energy threshold. This effect is studied in Section 5.4. In the range $50 < W < 100$ GeV the new

[9] The significance of the effect of the threshold on the trigger efficiency will be studied in Section 5.4.

[10] Even though the new FLT trigger configuration is less efficient than the old one, thanks to the improvement of the trigger configuration at the SLT and TLT the overall efficiency of the new trigger configuration at low W is large than in the old one (see Figure 5.5).

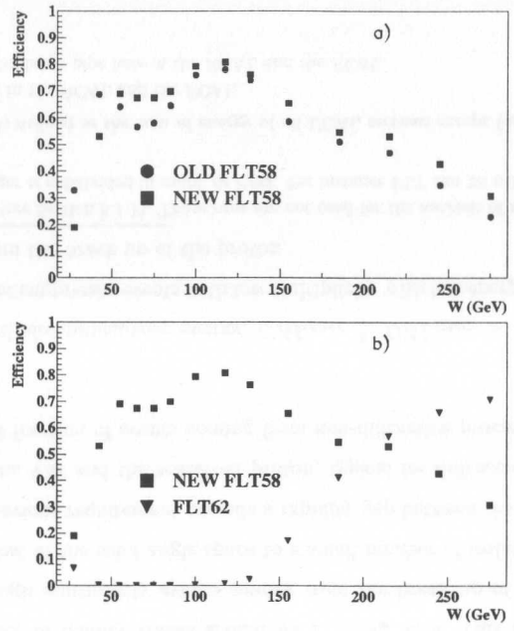

Figure 5.4: FLT trigger efficiencies as a function of W in MC. In Plot a) the efficiency of the new configuration is compared to that of the old. In Plot b) The efficiency of the new configuration of slot FLT58 is compared with the one of slot FLT62.

configuration is more efficient since the energy threshold set in the new configuration is lower than in the old one. This will result in the reduction of the systematic error due to uncertainties in the trigger efficiency determination (see Section 5.4). In the range $W > 100$ the overall the efficiency of the new configuration is somewhat greater than the old one.

In order to improve the acceptance for zero track configuration events, it was decided to make use of an existing trigger slot, FLT62. This slot triggers on two isolated electromagnetic clusters, ISOE. This slot yields a low rate and was not pre-scaled

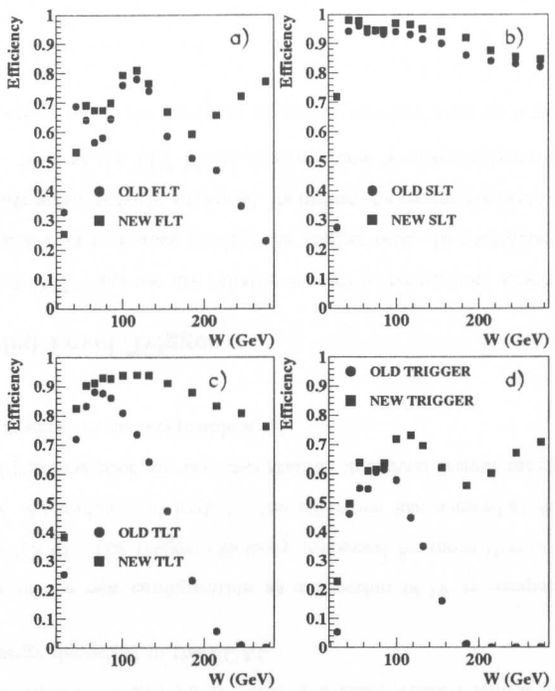

Figure 5.5: The trigger efficiencies of the new trigger selection compared to the old trigger selection calculated with MC of elastic photoproduction of J/ψ. Figure a) corresponds to the FLT, Figure b) to the SLT, Figure c) to the TLT and Figure d) to the combined efficiency of the three levels.

throughout the entire period of data taking. The minimum energy of the ISOE, E_{ISOE}, depends on the location of the electromagnetic cluster. If the electromagnetic cluster is located in the RCAL or in the BCAL, then $E_{ISOE} > 2000\,\text{MeV}$. If it is located in the FCAL, the energy threshold increases swiftly as cells come closer to the beam pipe hole. The efficiency of slot FLT62 as a function of the W calculated with MC is plotted in Figure 5.4 b). The efficiency of slot FLT62 grows as W increases since the decay electrons become more energetic.

The combined efficiency of the new configuration of slots FLT58 and FLT62 is shown is Figure 5.5 a) and is compared to the old configuration of slot FLT58. Thanks to the inclusion of slot FLT62 one observes a significant increase of the efficiency at high W.

5.3.2 Second Level Trigger

The trigger selection HFL06 makes use of the SLT slot SPP13. The old logic of this slot may be summarized as follows:

1. Trigger on slot FLT58.
2. The ratio P_z/E <0.96, where P_z and E are the third and fourth component of the four-vector of the depositions in the UCAL. This requirement is meant to further cut on beam-gas events. This cut also affects very low W events in which the decaying particles point to the forward region.
3. The total hadronic energy in the UCAL, $CCGetoth$, $CCGetoth < 1$ GeV. This requirement is meant to further cut on events coming from the break up of the proton.
4. The total energy in the UCAL, $CCGetote$, $CCGetote > 1.5$ GeV. This requirement is less strict than the energy threshold implemented at the FLT.
5. The transverse momentum, P_t, of all the tracks in the event $P_t > 0.45$ GeV. This requirement is means to further cut on low momentum pions in events with low multiplicity.

The efficiency of the old SLT (requirements 2-5, not including the requirement of a trigger at the FLT) as a function of W calculated with MC is displayed in Figure 5.5 b). Overall, the efficiency of this slot is very high, except for the range $W < 35$ GeV. This is due to the requirement 2. This requirement does not affect events with $W > 35$ GeV and, therefore, did not represent a problem for the old analysis. In order to improve the efficiency at low W, we needed to implement the necessary changes. Also, the

requirement 5 needed to be taken away. In one track and zero track topologies one of the decaying particles may leave a very short track, with some hits in the first Super layer of the CTD. The measurement of P_t is very unreliable for such kind of tracks. The resolution of the P_t of such tracks is not supposed to be described by MC, so the application of such a requirement would be dangerous for the analysis.

To summarize, the new slot was set to:

1. Trigger on slots FLT58 OR FLT62.
2. The OR of the following logic:

   - P_z/E <0.96 AND $CCGetoth$ < 1 GeV AND $CCGetote$ > 1.5 GeV (old logic).

   - P_z/E <0.96 AND $CCGetoth$ < 4 GeV AND $CCGetote$ > 6 GeV.

   - $CCGetoth$ < 1 GeV AND $Femc$ > 5 GeV, where $Femc$ is the electromagnetic energy deposited in the FCAL.

The efficiency of the new configuration as a function of W is compared to the old one in Figure 5.5 b). The trigger efficiency increased by more than a factor of 2 at W < 35 GeV. At middle and high W the efficiency has somewhat increased. The trigger rate of this new configuration was studied in special trigger rate test runs. The trigger rate increased to an acceptable level.

5.3.3 Third Level Trigger

The UCAL and CTD response are reliable enough to reconstruct kinematic variables and apply coarse cuts to reduce further the trigger rate. In particular, at this level tracking reconstruction is fairly advanced, including the reconstruction of vertexes (see Section 6.1.1). Also, at the TLT UCAL clusters have been reconstructed.

In the old configuration the invariant mass was reconstructed with two tracks. The

W of the event is calculated but no cut is applied on it. The logic of the old configuration may be summarized as follows:

1. Trigger on SLT slot SPP13.
2. The presence of a vertex.
3. The number of quality tracks, $N_{qt} \leq 4$.
4. At least one of the tracks should be matched [11] to an electromagnetic cluster [12].
5. The largest invariant mass of two tracks out of all possible combinations, $M^{max,t}_{e^+e^-}$, $M^{max,t}_{e^+e^-} > 1.5$ GeV.

In order to allow one track and zero tracks events we need to compute the invariant mass with the help of the additional information of UCAL clusters available at this level. To do this we need to implement a new algorithm that is able to combine the information of the CTD tracking and UCAL clusters. Prior to that it is necessary to define at the TLT the concept of quality track and ISOE:

- Quality track: A track that has left hits in at least first 2 superlayers of the CTD.

- ISOE: A cluster with $E > 1$ GeV and $E_{EMC}/E > 0.9$.

The resolution of a quality track is acceptable for the reconstruction of kinematic variables and it is well enough reproduced by MC. This definition of ISOE is motivated by the fact that the probability of having a pion fake an electromagnetic cluster is relatively small. On the other hand, the cross-section of the process under study is several orders of magnitude smaller than the total DIS cross-section and the presence of pionic background is sizeable. However, this definition of ISOE plus the requirement of a minimum invariant mass reduces the trigger rate to acceptable levels.

[11] The matching requirement is met when the distance between the location of the cluster and the intersection of the extrapolated track with the face of the UCAL is less than 30 cm.

[12] A cluster is considered electromagnetic if the ratio of the fraction of its energy deposited in the electromagnetic section of the UCAL, E_{EMC}, to the total energy is $E_{EMC}/E > 0.9$.

The new algorithm should be able to determine an electromagnetic object with the help of the combined information from the UCAL and the CTD. At this level an electromagnetic object is defined as:

- A track (no cluster matching required).

- An ISOE with no track matching to it.

In the central W range the energy of electrons decaying from the J/ψ is typically 1-2 GeV. Before the electron reaches the UCAL it needs to cross at least 1 X_0 of inactive material losing a significant fraction of its energy and creating a pre-shower. Clustering of energy depositions has been tested for energies $E > 10$ GeV, when the relative loss of energy due to the presence of inactive material and the effect of pre-showering is relatively small and the finding efficiency has been determined to be close to 100%. The cluster matching efficiency is not well known for energies $E < 10$ GeV. However, once an ISOE of whatever energy coming from the decay of the J/ψ is found in the angular acceptance of the CTD the probability of finding a track pointing to it is close to 100% and it is well modelled by the MC (see Section 5.4). In order to further reduce the trigger rate we may require that any electromagnetic cluster in the BCAL above a certain energy threshold [13] be matched to a track.

The algorithm determines a number electromagnetic objects, a minimum of two, and calculates the invariant mass of all possible combinations of pairs. In this scheme it is not necessary to require the presence of a vertex. However, the number of vertex tracks may be restricted.

The logic of the new configuration may be summarized as follows:

1. Trigger on SLT slot SPP13.

2. The number of quality tracks and ISOE's, N_{ISOE}, $N_{qt} + N_{ISOE} \geq 2$.

[13]The energy threshold may be determined by the minimum energy required for two clusters to yield an invariant mass of 1.5 GeV. This is approximately equal to 0.7 GeV.

3. The number of vertex tracks, N_{vt}, $N_{vt} \leq 2$.

4. $N_{ISOE} \leq 3$. This cut allows electroproduction events to be triggered.

5. The largest invariant mass of two electromagnetic objects out of all possible combinations, $M^{max}_{e^+e^-}$, $M^{max}_{e^+e^-} > 1.5$ GeV.

The efficiency of the new trigger configuration at the TLT compared to the old one is displayed in Figure 5.5 c). Overall, the new trigger configuration increases the efficiency, specially at very low and high W. The rapid loss of efficiency at low W is unavoidable due to the swift increase of the longitudinal boost of the VM in the direction of the proton. As a result, one of the electrons escapes through the beam pipe, preventing us from reconstructing the kinematics of the event. At high W the longitudinal boost is smaller and the loss of efficiency due to this effect is not so dramatic.

The combined efficiency of the trigger selection HFL06 (combined FLT, SLT and TLT efficiencies) is displayed in Figure 5.5 d). Significant is the efficiency gain at low W but especially at high W where the efficiency is relatively flat.

5.4 Trigger Efficiency Studies

The present Section is devoted to the measurement with data of the efficiency of the new trigger selection at the FLT. In Section 5.3.1 a new trigger configuration at the FLT is proposed, consisting of two slots: FLT58 and FLT62. It is necessary to study the dependence of the efficiency with the energy cuts applied in both slots. Also, we need to determine the tracking efficiency, in particular, for short tracks.

The present configuration at the FLT is advantageous for this study. The presence of two independent [14] trigger slots with certain overlap makes possible a cross check.

[14]These two slots are independent provided that the energy deposited in the UCAL outside the inner rings of the FCAL and RCAL is at least two times larger than the energy threshold set in slot FLT58.

5.4.1 Efficiency of slot FLT58

Events triggered by slot FLT62 are used to study the efficiency of slot FLT58. The schematic representation of the kind of topologies that are chosen to study the tracking efficiency is given in Figure 5.6. The left and right cartoons correspond to events with two ISOE's triggered by slot FLT62 with either one or two tracks in the CTD. The efficiency of finding one track and two tracks, $\epsilon^{1tr,2tr}$, of slot FLT58 is defined as:

$$\epsilon^{1tr,2tr} = \frac{N_A^{1tr,2tr}}{N_G^{1tr,2tr}} \tag{5.8}$$

where $N_G^{1tr,2tr}$ is the number of events with two ISOE's triggered by slot FLT62 with one track and two tracks, correspondingly and $N_A^{1tr,2tr}$ is the number of those events that have been triggered by slot FLT58.

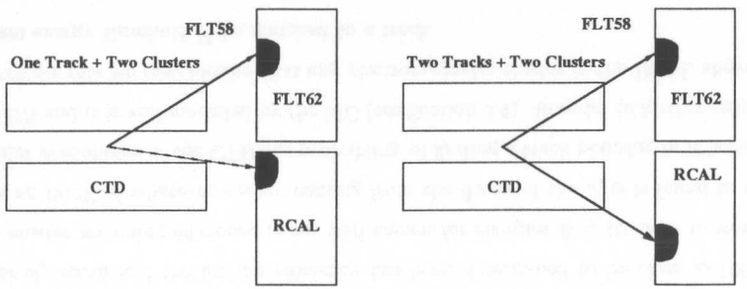

Figure 5.6: Schematic representation of the topologies chosen to study the tracking efficiency (FLT58) for short tracks. The left Plot corresponds to events with one quality track and two clusters triggered by slot FLT62. The right Plot corresponds to events with two tracks and two clusters triggered by slot FLT62 (see text).

The efficiency of the energy threshold at the FLT is almost 100% at energies that are roughly two times greater than the threshold (see below in this Section). This applies certain restrictions to the event selection if one track and two tracks configurations. Also, in order to reproduce the conditions of the final off-line analysis, for which the

acceptance is calculated it is convenient to restrict $M_{e^+e^-}$ of the two ISOE's. Common selection cuts may be summarized as follows:

- The Z component of the vertex, $|Z_{vertex}|$, $|Z_{vertex}| < 50$ cm.
- Require all tracks to originate from one vertex.
- $2.5 < M_{e^+e^-} < 3.7$ GeV.
- Trigger on slot FLT62.
- Elasticity requirement (see Section 6.4).

Additionally, one track configurations have to pass the following requirements

- Have hits at least in 3 superlayers [15].
- Distance of closest ISOE to the extrapolation of the track on the face of the UCAL, D, $D < 10$ cm.
- Energy of ISOE matched to track, E_{match}, $E_{match} > 4$ GeV.
- Energy of second ISOE, E_{match}, $E_{nomatch} > 3$ GeV.

Two track configurations have to pass the following cuts:

- At least one track with hits in 3 superlayers or more [16].
- Energy of two ISOE's $E > 3$ GeV.

Due to the restricted overlap between the two FLT slots, the distributions are dominated by tracks with hits in 3 superlayers.

[15] In the off-line selection a one track event is defined as an event with a quality track, i.e. a track with hits at least in three superlayers (see Section 6.4).

[16] In fact the existence of an additional shorter track in the event is not excluded. The efficiency for this configuration is different from the events with one quality track alone and, therefore, it is studied independently.

For the study of the tracking efficiency in MC, the ZEUSVM MC (see Section 7.2.1) is used. The topologies used in this analysis are mainly produced by QED non-resonant background (see Section 8.2.1). However, the calculation of the tracking efficiency is insensitive to the underlying process.

The number of events for each sample in data and MC and the corresponding efficiency are given in Table 5.1. The efficiency for one and two track events in data and MC agree within statistical errors.

	N_G^{1tr}	N_A^{1tr}	ϵ^{1tr}	N_G^{2tr}	N_A^{2tr}	ϵ^{2tr}
Data	409	367	0.897±0.014	550	540	0.982±0.006
MC	408	371	0.909±0.014	1835	1804	0.983±0.003

Table 5.1: Numbers for the tracking efficiency study with nominal set of cuts (see text).

In order to determine the systematic bias introduced by the energy cut $E_{match} > 4$ GeV applied in the selection of one track events this cut is changed. Table 5.2 shows the corresponding numbers after applying $E_{match} > 4$ GeV. The efficiency in data changes by some 0.7%.

	N_G^{1tr}	N_A^{1tr}	ϵ^{1tr}
Data	221	200	0.905±0.020
MC	170	154	0.906±0.023

Table 5.2: Numbers for the tracking efficiency of one track events with $E_{min} = 4.5$ GeV.

The same is done for tracks with hits in 3 superlayers only. Numbers are shown in Table 5.3. The change in the efficiency in both data and MC is insignificant.

Overall, the tracking efficiency at the FLT configurations of short tracks is well described by MC. The error associated to the determination of the tracking efficiency for single short tracks is 1.5%, which is dominated by limited statistics in data.

The slot FLT58 requires an energy deposition above a threshold. The efficiency of

	N_G^{1tr}	N_A^{1tr}	ϵ^{1tr}
Data	384	344	0.895±0.016
MC	398	362	0.91±0.015

Table 5.3: Numbers for the tracking efficiency of one track events with only for tracks with hits in 3 superlayers of the CTD.

this threshold needs to be studied, as well. The energy of the produced J/ψ comes mainly from the longitudinal boost, and this is dependent on W. In the middle W range the J/ψ is produced almost at rest, therefore, the threshold $CAL_{EMC} > 1836$ MeV may affect the efficiency of the selection significantly. As CAL_{EMC} does not include energy depositions in cells neighboring the beam hole of the RCAL and FCAL one track configurations in which one of the electrons falls in these regions are most affected.

The distribution of the sum of the momenta of the tracks in 2 track events, p, as a function of W is shown in Figure 5.7 a). The same distribution as a function of P_t^2 of the two tracks with $70 < W < 80$ GeV, for which the longitudinal boost is smallest is shown in Figure 5.7 b).

Due to both internal bremsstrahlung and bremsstrahlung radiation while crossing the beam pipe the average momentum measured in the CTD is systematically smaller than the energy deposited in the UCAL. In order to determine the efficiency curve in data and afterwards compare it to the one calculated by MC, it is necessary that the bremsstrahlung radiation be well simulated by MC. The adequacy of the simulation of the bremsstrahlung radiation by MC is tested with the help of the distribution of $M_{e^+e^-}$. The comparison of data and MC is satisfactory (see Section 9.1.1).

The following quantity is calculated in bins of the sum of the momenta of the tracks in the event:

$$\epsilon(p) = \frac{Number\ of\ events\ with\ CAL_{EMC} > 1836\ MeV}{Total\ Number\ of\ events} \tag{5.9}$$

Two different data sets were selected by independent triggers:

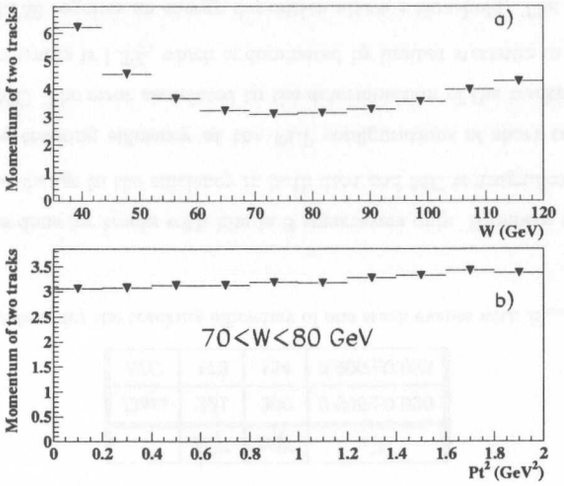

Figure 5.7: Plot a) is the distribution of the sum of the momenta of the tracks in 2 track events as a function of W. Plot b) shows the same distribution as a function of P_t^2 of the two tracks with $70 < W < 80$ GeV.

- Elastic QED Compton events with one track pointing to the BCAL and one isolated electromagnetic cluster in the RCAL. The topology of these events is reproduced schematically in Figure 5.8. These events are triggered by slot FLT30 [17]. In order to secure that this selection criterium be independent of slot FLT58, it is necessary to require a minimum deposition 3500 MeV at the FLT in the electromagnetic section of the RCAL excluding cells neighboring the beam pipe hole. The momentum distribution of the track is plotted in Figure 5.9 a). Interesting are tracks with momentum greater than 2 GeV.

[17]This trigger slot requires an electromagnetic cluster in the RCAL with a deposition of at least 3750 MeV. Typically, the energy of the photon in the RCAL is greater than 20 GeV. The invariant mass in these events passes the minimum threshold and make it through the TLT.

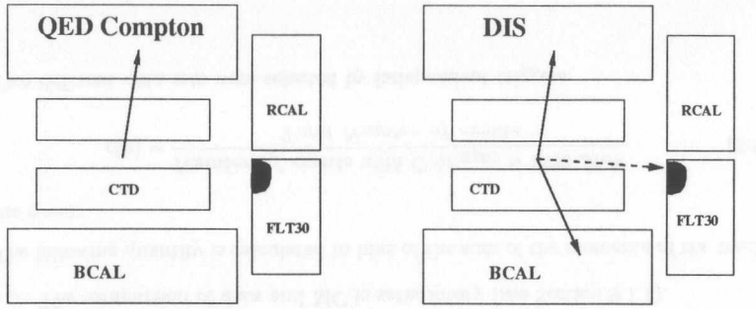

Figure 5.8: Schematic representation of the classes of events used to study the efficiency of the energy threshold required by slot FLT58. The upper Plot corresponds to elastic QED Compton events with the photon outside the first ring of the RCAL. The lower corresponds to J/ψ produced in electroproduction or DIS events.

- J/ψ produced in the electroproduction regime or DIS events. The topology of these events is reproduced schematically in Figure 5.8. There events are triggered by the trigger selection DIS05 [18]. The momentum distribution of tracks in these events is plotted in Figure 5.9 b).

Additionally, the following cuts are applied on both selections:

- The Z component of the vertex, $|Z_{vertex}|$, $|Z_{vertex}| < 50$ cm.
- Require all tracks originate from vertex.
- Elasticity requirement (see Section 6.4).

The efficiency $\epsilon(p)$ as calculated with the QED and DIS samples is shown in Figure 5.10. It should be noted that the DIS sample is dominated by two track events, where the QED sample is dominated by one track events. The efficiencies obtained

[18]The trigger selection requires an electromagnetic cluster of at least 7 GeV, $E - P_z > 30$ GeV and at least two tracks. These event are mostly triggered by FLT30.

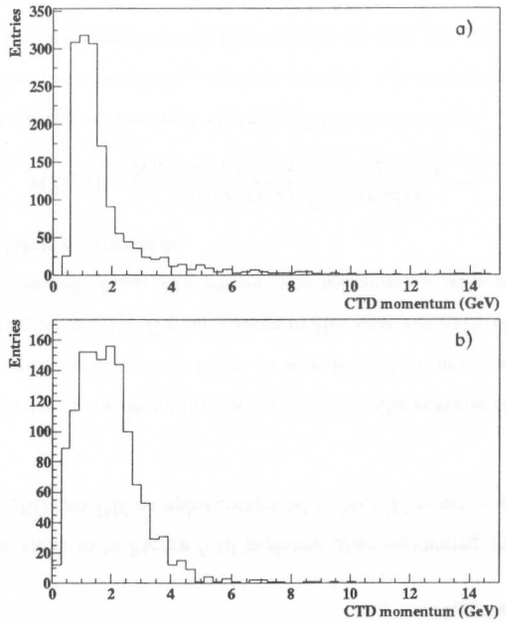

Figure 5.9: Plots a) and b) show the momentum distribution of CTD tracks in the QED sample and the J/ψ DIS sample, respectively.

with the two samples are consistent within statistical error. The combined efficiency calculated with both samples is shown and compared to the efficiency obtained with the ZEUSVM MC in Fig 5.11. The efficiency of slot FLT58 approaches 100% at high p. However, at lower p the MC is systematically more efficient that data. This effect needs to be corrected. The efficiency curves in data and MC are parameterized with the following functional form:

$$\epsilon(p) = 1 - e^{-a_1 p^{a_2}} \tag{5.10}$$

where a_1 and a_2 are free parameters. The size of the correction applied on MC as a

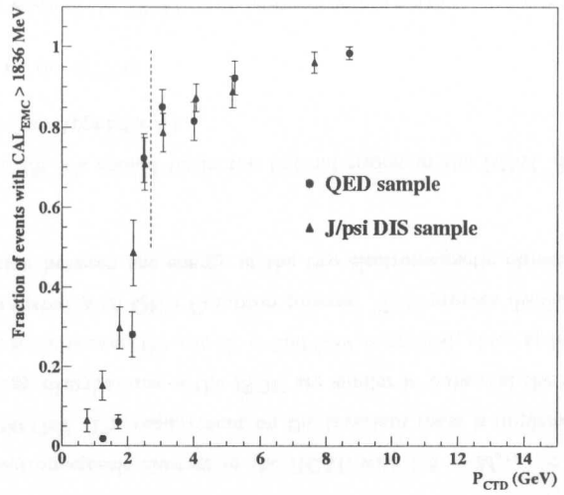

Figure 5.10: $\epsilon(p)$ (see text) calculated with the QED and DIS samples. The dashed line indicates minimum p for signal events.

function of p is shown in Figure 5.12. The size of the correction is less than 10% and affects a restricted class of events. The error associated to this correction is dominated by the propagation of the statistical error in the estimation of the efficiency in data due to limited statistics. The error band is illustrated in Figure 5.12 and is less than 5%.

5.4.2 Efficiency of slot FLT62

The efficiency of slot FLT62 is studied using events triggered by slot FLT58. The efficiency of slot FLT62 is the product of the efficiency of finding two ISOE's of an energy greater than a certain threshold. One could proceed to determine the efficiency of tagging on an ISOE and then calculate the efficiency of finding two ISOE's. However,

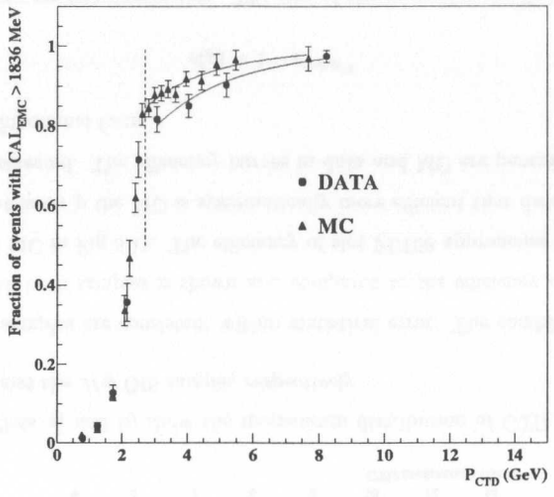

Figure 5.11: The same as in Figure 5.10 is shown after combining the efficiencies obtained with the QED and DIS samples compared to MC. The curves are parameterized (see text).

due to the kinematics of the decay products of the J/ψ the energies of the two ISOE's tend to be much different from each other. It was decided to measure the efficiency of slot FLT62 tagging on two ISOE's the energy of the least energetic of them is greater than a certain threshold, E_{min}. The efficiency is measured in data and calculated in MC using the following Expression:

$$\epsilon(E_{min}) = \frac{Number\ of\ FLT62\ tags}{Number\ of\ events\ with\ E_{<} > E_{min}} \tag{5.11}$$

where $E_{<}$ is the energy of the least energetic ISOE in the event. The efficiency is calculated for different values of E_{min} for data and MC independently. It is important that the energy distributions of the ISOE be similar in data and MC.

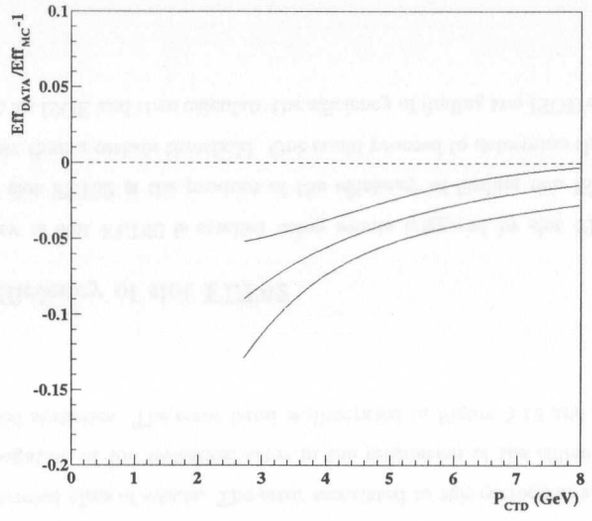

Figure 5.12: The correction applied on MC a function of p (see text). The band corresponds to the error associated to the correction.

The data sample used to calculate the efficiency passes the following off-line cuts:

- Two electromagnetic clusters in the RCAL with $2.5 < M_{e^+e^-} < 3.7$ GeV and $W < 290$ GeV. The requirement on the invariant mass is implemented so that the energy distributions of the ISOE are similar in data and the resonant MC. For the same reason, the cut $W < 290$ GeV is applied, since at higher W data are dominated with QED Compton process. This process displays a different correlation between the energy of the two electromagnetic objects in the final state.
- The two ISOE's should be in the fiducial region in the RCAL defined in the analysis (see Appendix A).
- Trigger on slot FLT58.

The energy scale of the UCAL is understood within small error down to energies of

3 GeV (see Appendix A). Interesting for the analysis are events in which $E_< > 3$ GeV. The data and MC sets are binned in $E_<$ for further analysis.

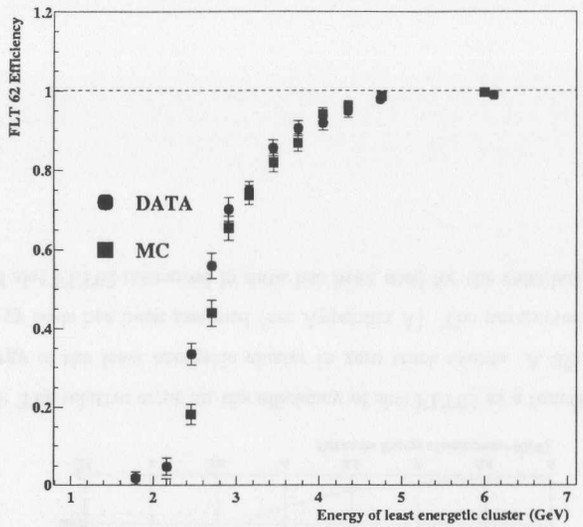

Figure 5.13: Efficiency of slot FLT62 as a function of the least energetic cluster in zero track events (see text). Solid circles corresponds to data and solid squares to MC.

The result of the calculation for data and MC according to Equation (5.11) is shown in Figure 5.13. The efficiency in data and MC are in good agreement for energies $E_< > 3$ GeV.

The efficiency curves in data and MC are parameterized to the functional form

$$\epsilon(E_<) = 1 - e^{-a_1 E_<^{a_2}} \tag{5.12}$$

where a_1 and a_2 are free parameters. The parameterizations of the efficiency in data and MC are within 1% at $E_< > 3$ GeV. The choice of the parameterization changes the result by less than 0.5%. However, the largest source of systematic error is not due to the different behavior of the efficiency curve in data and MC. It comes from the uncertainty of the determination of the energy scale of the UCAL at low energies.

The cut on $E_<$ imposed in the analysis off-line is systematically biased because of the uncertainty in the determination of the energy scale of the response of the UCAL. This uncertainty in the energy range of the analysis has been determined to be of the order of 3% (see Appendix A). If one propagates this uncertainty according to the parameterization of the efficiency of slot FLT62 an estimation of the systematic error on the cross-section may be determined. The relative error on the efficiency of slot FLT62 due to this systematic bias introduced is plotted as a function of E_{min} in Figure 5.14. The parameterization of the efficiency of slot FLT62 measured in data has been used for the calculation. The error on the efficiency of slot FLT62 grows rapidly as E_{min} decreases. The choice of E_{min} is made in order to reduce the total systematic error of the cross-section. Two competing effects contribute to the systematic error: the error on the efficiency of slot FLT62 and the error on the acceptance calculation. By cutting on $E_<$ one cuts on the most asymmetric configurations, in which the energy of the two electromagnetic objects differ most. The level of asymmetry of the events is correlated with the angular distribution of the decay products of the J/ψ. The systematic error due to this effect is larger the large E_{min}. As a result, an optimal value of E_{min} was determined to be $E_{min} = 3.5$ GeV. The error due to the uncertainty of the efficiency of slot FLT62 for $E_{min} = 3.5$ GeV is about 3%. This is reflected in the final systematic error of the cross-section (see Section 9.3).

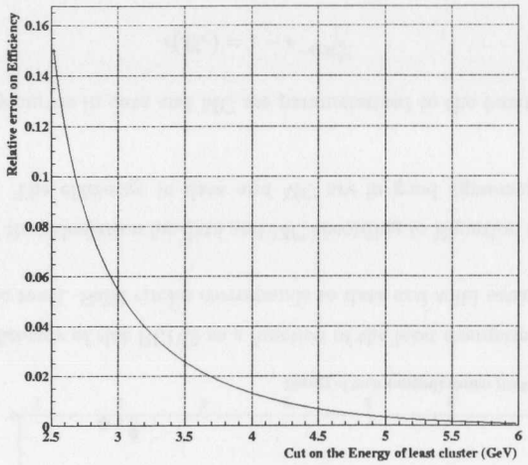

Figure 5.14: The relative error on the efficiency of slot FLT62 as a function of the cut on the energy of the least energetic cluster in zero track events. A 3% error on the UCAL energy scale has been assumed (see Appendix A). The parameterization of the efficiency of slot FLT62 measured in data has been used for the calculation.

Chapter 6

Data Selection

The data set used in this work was taken during the 1999 and 2000 running periods and corresponds to a luminosity of 55.34 pb^{-1}. The data selection is a multi-step process that may be divided into three groups. A schematic diagram of this process is given in Figure 6.1. Part of the process is performed on-line, or during data taking, and off-line, after data taking. The trigger step has been presented in Chapter 5. The second step is the event reconstruction, performed off-line. The most relevant elements of the event reconstruction are covered in Section 6.1. Various aspects of the event reconstruction are further corrected off-line (see Section 6.2). The event reconstruction opens the way to reconstructing the kinematic variables relevant to the physics analysis (see Section 6.3). The third step is called the off-line selection, which is specific to the type of physics analysis performed. The off-line event selection will be covered in Section 6.4.

An overview of the physics analysis environment of the ZEUS experiment can be found in [101].

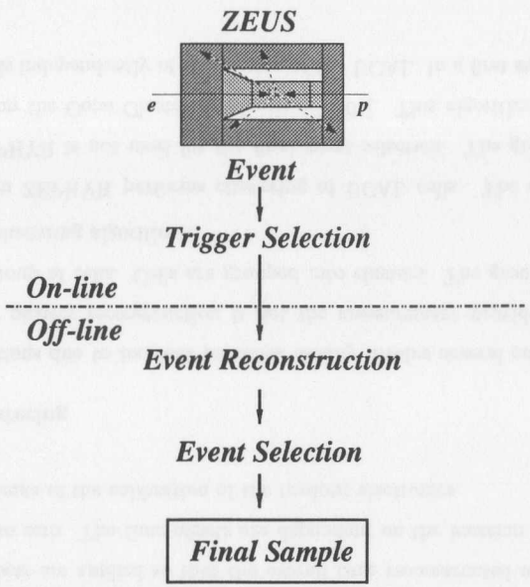

Figure 6.1: Schematic diagram of the steps involved in obtaining the final event sample in physics analysis.

6.1 Event Reconstruction

At this stage the data event has been selected by the trigger algorithm corresponding to the physics analysis. Events now are reconstructed by the ZEUS Physics Reconstruction program (ZEPHYR) [102]. The data passed from all the components of the ZEUS detector are reconstructed using calibration constants. Information from all components are put together by ZEPHYR to make up a reconstructed event. The most meaningful pieces of information for the reconstruction of the kinematics in the present analysis are the track and vertex reconstruction, the UCAL energy reconstruction and the reconstruction of the energy and position with the SRTD.

6.1.1 Track and Vertex Reconstruction

The track reconstruction is based on the package VCTRACK [103]. The tables created by this package contain the information about the momenta of the particles associated to every identified track in the event.

The track reconstruction uses hits in the CTD. Each track candidate begins with a track "seeds" in the outer superlayer of the CTD and then is extrapolated inward. An extended version of this package includes information from other tracking detectors such as RTD, FTD [1]. The initial identification of a track is based on a fit of all hits.

The determination of the vertex is crucial for the calculation of the kinematics of the event in the region $40 < W < 140$ GeV. The vertex sets the "origin" of the interaction and the angles of the particles in the events are calculated with respect to it. For the determination of the vertex of the events only tracks that cross the first superlayer of the CTD are considered. The fitted trajectories are extrapolated to the beam line. The extrapolations of all tracks in the event are averaged to obtain the primary vertex. A new fit is performed to determine the trajectories, now, with the constraint of being originated from the primary vertex. A χ^2 from the fit of each trajectory is calculated. Tracks with too large χ^2 are discarded. Tracks that originate from the main vertex are called vertex tracks.

6.1.2 UCAL Energy Reconstruction

6.1.2.1 Recalibration of the Energy and Time Measurement

The program ZEPHYR performs the recalibration of the energy and time measurements of each cell in the UCAL. The values of the energy and time measurements are written in the table called CALTRU. Various are the corrections applied:

- Bad channel suppression. The electronic readout and the response of each channel are calibrated and monitored on a daily basis. A list of channels which

[1] In this analysis the tracking reconstruction is based solely on the CTD.

readout does not pass certain performance standards are added into a bad channel list. The output of these channels is disregarded in the event reconstruction. ZEPHYR rejects fake energy depositions coming from "sparks". These "sparks" are identified when the output difference of the two channels that readout a cell is very large.

- The gain of the PMT of each channel changes with time. This effect is corrected by measuring the UNO current (see Section 4.1). The variation of the UNO current is monitored on a daily basis. The energy correction applied on the output of a channel is equal to the ratio of the nominal UNO current to the one measured.
- An energy deposition is recorded in the CALTRU table above a certain threshold. This energy threshold depends on the average level of UNO noise measured for each section of the UCAL. This threshold is set to 60 MeV for EMC cells, 100 MeV for HAC0 cells and 110 MeV for HAC1 and HAC2 cells.
- Time offsets are applied so that the overall time reconstructed with the UCAL is equal to zero. The time offsets are dependent on the location of the cell and the constants of the calibration of the readout electronics.

6.1.2.2 Clustering

Energy depositions due to incident particles usually involve several cells. Therefore, meaningful for physics reconstruction is not the measurement provided by a single cell but of a group of cells. Cells are grouped into clusters. The grouping of cells is performed by clustering algorithms.

The program ZEPHYR performs clustering of UCAL cells. The clustering performed by ZEPHYR is not used for the final event selection. The grouping of cells used is based on the Cone Clustering algorithm [104]. This algorithm performs the grouping of cells independently of the section of the UCAL. In a first stage, groupings

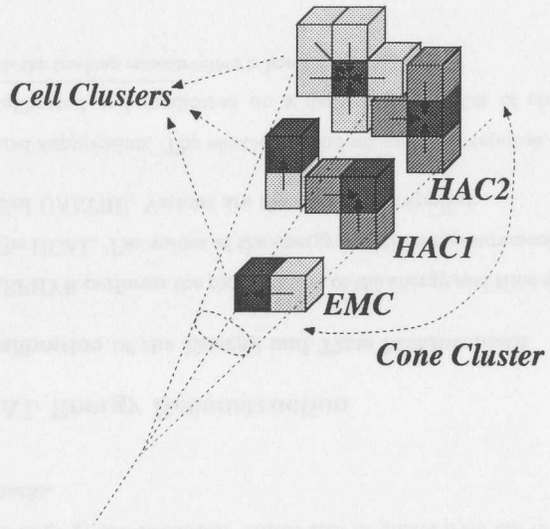

Figure 6.2: Schematic representation of the cone clustering algorithm.

of neighboring cells in each section of the UCAL (EMC, HAC1 or HAC2), or cell clusters, are identified. Then these cell clusters are grouped into cone clusters according to a probability function. This is illustrated in Figure 6.2. This probability function will depend on the angle of the cell cluster.

6.1.3 Reconstruction of Energy and Position with the SRTD

The measurement provided by the SRTD is used to improve the position and energy measurement of electromagnetic clusters in the RCAL. In the present analysis, the SRTD is used to reconstruct J/ψ candidates at high W where no tracking information is available. The position reconstruction is given by X and Y strips independently. Neighboring strips form clusters in the X and Y planes. Then clusters in the X and Y planes are paired to form hits [105]. SRTD clusters may be matched to UCAL clusters. The energy response of the SRTD is used to correct the energy of the UCAL cluster

matched to it according to the "presampler" principle. As the position reconstruction given by the SRTD is more accurate than that of the UCAL a hierarchy is established: to reconstruct the position of an electromagnetic cluster the information from the SRTD is used. If the latter is not available then the information from the RCAL is used.

6.2 Further Corrections

The following corrections are applied off-line on the energy response of the UCAL and the momentum reconstruction of the CTD in data and MC after a full event reconstruction has been performed.

6.2.1 CTD

The momentum and resolution was studied in data and MC independently using the resonant decay of the $J/\psi \to e^+e^-, \mu^+\mu^-$ (see Appendix B). The CTD momentum was scaled up in data by a factor 1.004 so that the reconstructed $M_{e^+e^-}$ peaks at $M_{J/\psi} = 3.097$ GeV. The error on the momentum scale is about 0.2%.

6.2.2 UCAL

Electromagnetic clusters are used for the reconstruction of the kinematics of the event in one track and zero track configurations. The BCAL is not used for the reconstruction of electromagnetic clusters.

A fiducial cut in the RCAL is applied, as illustrated in Figure A.1. Areas around the beam-pipe hole are taken out due to energy leakage and considerable inactive material. Also, electrons that fall within 1.5 cm of the interface between modules R11 and R12 and modules R12 and R13 are removed because of poor resolution.

The following corrections are applied on the energy and position electromagnetic

clusters:

- Inactive material correction is applied on both data and MC. The size of the correction is up to 10%. For those electromagnetic clusters that fall into the region of the SRTD the presampler correction given by this detector is used (see Appendix D). Additionally, the energy of electromagnetic clusters in the RCAL are corrected according to Expression (A.4).
- Correction on non-uniformities on electromagnetic clusters in the RCAL in both data and MC. The size of the correction is typically 1-3%.
- The position delivered by the SRTD is corrected. The relative shifts of the position reconstruction of the SRTD with respect to the ZEUS coordinates are shown in Section C.2.
- The energy of electromagnetic clusters in the FCAL is scaled up by 5% (see Section A.1.3).

6.3 Reconstruction of Kinematic Variables

As pointed out in Section 2.4 (see Equation (2.17)), the four vector of the VM is determined as the sum of the four vector of the decaying particles:

$$\vec{P}_V = \vec{P}_{e^+} + \vec{P}_{e^-} \tag{6.1}$$

$$E_V = E_{e^+} + E_{e^-} \tag{6.2}$$

$$M_V \approx \sqrt{2\left(E_{e^+}E_{e^-} - \vec{P}_{e^+}\vec{P}_{e^-}\right)} \tag{6.3}$$

where $\vec{P}_V, E_V, M_V$ are the momentum, energy and the mass of the VM candidate, respectively, and the subscripts e^+ and e^- correspond to the positron and electron of the decay of the VM respectively.

The invariant mass squared of the γp system is defined as (see Section 1.2.1):

$$W^2 = (p+q)^2 = m_p^2 - Q^2 + 2p\cdot q \approx 2E_p(E_\gamma - P_{\gamma z}) \tag{6.4}$$

where p, q are the four momenta of the incoming proton and photon, respectively, and $W^2 \gg m_p, Q^2$.

Further, it is necessary to make use of the conservation of the four momenta in the reaction. In the photoproduction regime $|P_{\gamma z}| \approx E_\gamma$ and $|P_{p'z}| \approx E_{p'}$. The latter is well substantiated, as the average transverse momentum of the out coming proton, P_{pt}^2, is much smaller than the square its energy:

$$P_{p'z} = \sqrt{1 - \frac{P_{p't}^2 + m_p^2}{E_{p'}^2}} \approx E_{p'} \left(1 - \frac{P_{p't}^2 + m_p^2}{2E_{p'}^2}\right) \approx E_{p'} \tag{6.5}$$

The same applies to the photon, $P_{\gamma z} \approx E_\gamma$, when the inequality $Q^2 \ll E_\gamma^2$ holds. Using the conservation of four momenta in the reaction it can be derived:

$$E_\gamma - P_{\gamma z} \approx E_V - P_{Vz} \tag{6.6}$$

If one plugs Equation (6.6) into Equation (6.4) one finally obtains:

$$W^2 \approx 2E_p (E_V - P_{Vz}) \tag{6.7}$$

The momentum transfer at the proton vertex, t, may be also derived in the case of photoproduction. As defined in Section 1.2.1, and using the conservation of the four momenta in the reaction:

$$t = (P_p - P_{p'})^2 = (P_V - q)^2 \approx M_V^2 - Q^2 - 2P_V \cdot q \tag{6.8}$$

The last term in Equation (6.8) may be re-written:

$$P_V \cdot q \approx E_\gamma (E_V + P_{Vz}) \approx \frac{1}{2}\left(E_V^2 - P_{Vz}^2\right) \tag{6.9}$$

From Equation (6.9) and (6.8) finally follows:

$$t \approx -P_{Vt}^2 \tag{6.10}$$

where P_{Vt}^2 is the square of the transverse momentum of the VM [2]. Q^2 has been neglected in Equation (6.8). In general, t will deviate from P_{Vt}^2 as Q^2 increases. This effect is taken into account by the MC simulation.

[2] P_{Vt}^2 is referred to further in the text as P_t^2.

VM production is usually viewed in terms of the energy of the center of mass of the colliding γp system. Alternatively, this process may be viewed in terms of the fraction of the proton momentum that participates in the creation of the VM:

$$M_V^2 = (xp + q)^2 \approx -Q^2 + 2xp \cdot q = -Q^2 + xW^2 \tag{6.11}$$

where x is the fraction of the momentum carried out from the proton in the reaction. From Equation (6.11) follows:

$$x \approx \frac{M_V^2 + Q^2}{W^2} \tag{6.12}$$

To conclude, the kinematics of the event coming from the reaction $\gamma p \rightarrow Vp$, to a good approximation, may be reconstructed with the help of the measured four-momenta of the decaying particles of the VM.

6.4 Off-line Selection

The following definitions are relevant at the off-line level:

- A **good track** is defined as a vertex track with hits in at least 3 superlayers of the CTD. Shorter tracks or non-vertex tracks are not considered.
- **Track-cluster matching** is defined when a cluster lies within 25 cm of the extrapolation of the track onto the face of the UCAL.
- A cluster is called **electromagnetic** if at least 90% of its total energy is concentrated in the EMC section of the UCAL and its energy is greater than 1 GeV.
- **Electromagnetic object** is defined as a good track (with or without an electromagnetic cluster matched to it. If a cluster is matched to the track it must be electromagnetic) or an electromagnetic cluster without a good track pointing to it (it may or may not be matched to a track that is not good) with at least 98% of its energy concentrated in the EMC section of the UCAL (unless the cluster

is within 1.5 cm of the interfaces of modules in which case the ratio should be at least 90%).

Off-line, the following requirements were imposed to select candidates for the reaction $ep \to eVp$:

- The event should be accepted by trigger selection slot HFL06 (see Section 5.3).
- Every single cluster in the UCAL with energy greater than 1 GeV should be electromagnetic.
- The event should have only two electromagnetic objects.
- The vertex is reconstructed in two and one track events. The Z component of the vertex is required to be $|Z_{vertex}| < 50\,\text{cm}$. No cut on the transverse distance of the vertex to the nominal interaction point was applied. In zero track events the vertex position is set to the nominal interaction point.
- In two track events tracks are required to be of opposite charge.
- In one track events the energy of the cluster not matched to the track should be $E_{nomatch} > 3$ GeV.
- In one track events the momentum of the good track should be greater than 2.8 GeV or the energy associated to the electromagnetic objects outside the first three things of the FCAL and the first ring of the RCAL should $E_{out} > 3$ GeV. This is motivated by the efficiency of slot FLT58 (see Section 5.4.1).
- In zero track events the energy of both clusters should be $E > 3.5$ GeV. This cut is motivated by the efficiency of slot FLT62 (see Section 5.4.2).
- The sum of the transverse momentum of the two electromagnetic objects should be $P_t^2 < 3\ \text{GeV}^2$.

- Disregard events with an electromagnetic object with energy greater than 20 GeV within a circumference of 20 cm around the beam pipe in the RCAL. This cut is mean to suppress DIS events with low multiplicity.
- Elasticity requirement:

  - FPC veto (see Section 8.1.1).

  - All clusters in the BCAL with energy greater than 0.7 GeV need to have a track matched to them.

  - Energy depositions in UCAL cells not associated [3] to the electromagnetic objects in the event have some maximum energy depending on its location: $E_{EMC} < 200\,\text{MeV}$, $E_{HAC0} < 250\,\text{MeV}$ and $E_{HAC1} < 300\,\text{MeV}$.
- $2 < M_{e^+e^-} < 20$ GeV and $20 < W < 290$ GeV.

A total of 37360 events pass the off-line selection cuts in the selected data sample. This sample is used for the study of the diffractive production of J/ψ (see Chapter 9), $\psi(2S)$ (see Chapter 10) and Υ (see Chapter 11).

[3] 25 cm away from the electromagnetic objects in the event.

Chapter 7

Monte Carlo Simulation and Acceptance Corrections

MC programs are used here primarily to calculate the geometrical acceptance of tagging the reaction $ep \to eVp$ under the conditions of the ZEUS detector (see Section 7.3.2). Each event generated contains a list of the kinematics particles participating in the reaction. The MC files generated by the corresponding MC generator are passed through a detailed simulation of the ZEUS detector based on the program GEANT [106]. Also relevant to analysis, is the implementation of MC generators that simulate the background processes to the physics under study. Each relevant background process has a dedicated MC generator.

7.1 Steps of Monte Carlo Simulation

The ZEUS Monte Carlo simulation consists of the next basic steps:

- Physics Generator. This is a program that generates events coming from the reaction $ep \to X$. Each event consists of a table of the four momenta of all the particles involved in the reaction: incoming, intermediate and final state.
- MOZART (Monte Carlo for ZEUS analysis, reconstruction and trigger) is a software that contains the full simulation of the ZEUS detector. The interaction of particles with the various components of the ZEUS detector is simulated by GEANT package [106]. The geometrical and material structure of components of the ZEUS detector as well as the mapping of the magnetic field in the volume of the CTD is known to MOZART. The program produces two types of tables, the table that contains the full information of all particles created in the event and tables that contain the output of various components of the ZEUS detector.
- ZGANA (ZG313 Analysis) [107]. This is a program that simulates the three-level trigger of the ZEUS detector. This program simulates the response of the various subcomponents of the ZEUS detector, as available at the various trigger levels.

Once the generated MC file has been processed through the steps enumerated it is ready to go through the event reconstruction by the program ZEPHYR [102]. After this the MC file undergoes the same off-line treatment as data.

7.2 Monte Carlo Generators

7.2.1 ZEUSVM

ZEUSVM [108] is the physics generator used to produce the basic process $ep \to eVp$ depicted in Figure 2.6. This program generates kinematic distributions according to basic phenomenological functional relations with a minimal number of free parameters. The basic steps involved in the generation are [100]:

- The four-vector of the scattered electron is generated. The Q^2 and y distributions of the scattered electron are generated according to the following parameterization of the total $\gamma p \to Vp$ cross-section, $\sigma_{tot}^{\gamma p \to Vp}$:

$$\sigma_{tot}^{\gamma p \to Vp}(Q^2, W) \propto \frac{W^{\delta}}{(M_V^2 + Q^2)^n} \tag{7.1}$$

where δ and n are parameters of the generation.

- The four momentum of the scattered proton, with a momentum transfer t, is generated according to a single exponential function:

$$\frac{d\sigma_{tot}^{\gamma p \to Vp}}{dt} \propto e^{bt} \tag{7.2}$$

  where b is a parameter of the generation.

- The distributions of the helicity angles are generated flat. In order to estimate the acceptance correction the helicity angle distributions are reweighted so as to preserve SCHC (see Section 2.5).

To summarize, the free parameters of the ZEUSVM generator are δ, n and b, which govern the W, Q^2 and t distributions, correspondingly. The acceptance correction calculation (see Expression (7.4)) is primarily sensitive to the choice of the parameters δ and b. The acceptance calculation in bins of W and t is also sensitive to the choice of n since it affects the way the observed P_t^2 and t are related to each other. The choice of the parameters is a result of an iterative procedure. The parameters δ and b are set so that they coincide with the corresponding parameters obtained from the fit of the resulting cross-section of the diffractive production of J/ψ (see Sections 9.4 and 9.5). This MC program was interfaced with packages to calculate QED radiative corrections [108, 100]. This aspect of the generation will be covered in Section 7.2.3.

From now on ZEUSVM will refer to the MC program interfaced with the packages of QED corrections, unless specified otherwise.

7.2.2 DIPSI

DIPSI Monte Carlo program [109] is based on the model of Ryskin [55]. The photon radiated by the incoming electron fluctuates into a $q\bar{q}$ pair, which then interacts with the proton via the exchange of gluon ladders. The parameters of the generator are the parameters of the physics model, the strong coupling constant, the two-gluon form factor and the gluon momentum density of the proton. Once the parameters of the model are fixed the Q^2, W and t generated distributions are calculated according to the formalism developed by Ryskin. The helicity angle distributions are generated according to SCHC.

DIPSI is not interfaced to the packages that calculated QED corrections to the reaction.

7.2.3 Higher Order QED Radiation

Two types of higher order QED radiation $ep \to eVp \to e(e^+e^-)p$ are applied: radiative corrections to the line of the scattered electron and final state radiation to the decaying electrons of the VM.

The first set of QED radiation is calculated with the package HERACLES [110]. HERACLES calculates QED corrections corresponding to the diagrams displayed in Figure 7.1: Initial state radiation, final state radiation, vertex correction and Vacuum polarization. The effect of higher QED radiation on the incoming electron line on the acceptance calculation is discussed in Section 7.3.4.

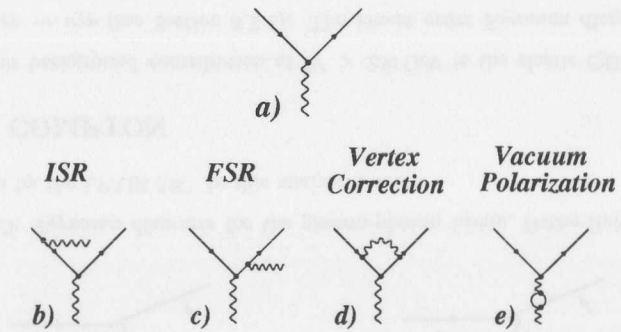

Figure 7.1: The leading term a) and higher order QED radiation. Corrections from diagrams b)-e) are calculated with HERACLES.

The second set of QED radiation corresponds to the final state radiation of leptons

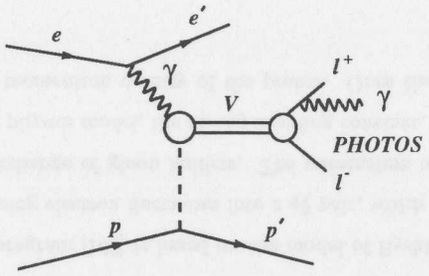

Figure 7.2: PHOTOS is interfaced to the ZEUSVM MC program. It calculates QED final state radiation corrections to the decay of $V \to l^+l^-$. In this analysis $l = e$.

of the decay of the VM. In the case of $l = e$, the probability of radiating a hard photon is not negligible (see Section 7.3.4). The radiation of a photon by a lepton from the decay of the VM is illustrated in 7.2. This process is also usually called internal bremsstrahlung. The program that takes care of the calculation of these corrections is PHOTOS [111].

The intrinsic radiative decay $V \to l^+l^-\gamma$ where γ does not come from internal QED bremsstrahlung is severely suppressed, as it violates C-parity of the VM and is not simulated by the physics generator. The effect of hard final state radiation of the electrons of the decay of the J/ψ is discussed in Section 7.3.4.

7.2.4 LPAIR

One of the major background contributions to the production of heavy VM's is the elastic QED lepton pair, $ep \to el^+l^-p$ (see Section 8.2.1). The Feynman diagram of this process corresponds to photon-photon fusion, Bethe-Heitler process (see Figure 7.3). This process cannot be distinguished from the resonant decay $V \to l^+l^-$. The contribution from this non-resonant process is subtracted statistically (see Section 8.2.1).

This process is generated by the MC program LPAIR [112], an adaptation to the ZEUS software environment of the original work [113].

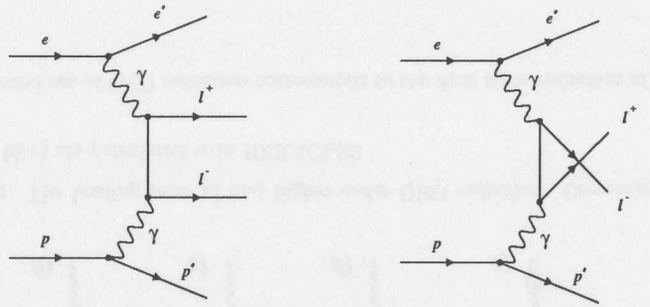

Figure 7.3: Feynman diagrams for the photon-photon fusion, Bethe-Heitler process, generated by the LPAIR MC. In this analysis $l = e$.

7.2.5 COMPTON

The major background contribution at $W > 230\,\text{GeV}$ is the elastic QED Compton process, $ep \to e\gamma p$ (see Section 8.2.1). The lowest order Feynman diagrams of the QED Compton process are shown in Figure 7.4. This process displays in the final state a photon and an electron that carry the energy of the incoming electron. Initial state radiation of the incoming electron will reduce the energy of the outgoing electron and γ. Therefore, the events in the detector will look like an event coming from the electronic decay of VM's at high W. Events of this topology will be boosted toward the very rear of the ZEUS detector where tracking information is not available, and as a result, it is not possible to determine the charge of the particles. The contribution from this non-resonant process is subtracted statistically (see Section 8.2.1).

The elastic QED Compton process is generated by the MC program COMPTON [114]. This program includes QED corrections of higher orders to the diagrams displayed in Figure 7.4.

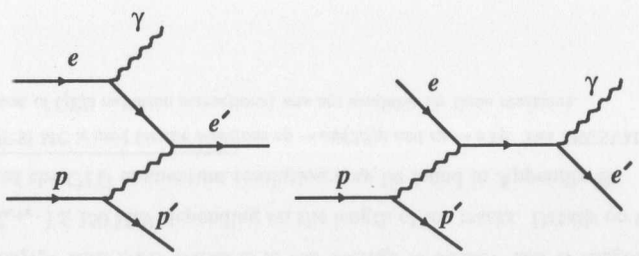

Figure 7.4: Lowest order Feynman diagrams of the QED Compton process. This process is generated by the COMPTON MC.

7.2.6 EPSOFT

This package is meant to generate events of the diffractive production of VM's with dissociation of the proton, $ep \to eVN$, as depicted in Figure 7.5. The production of VM's via the dissociation of the proton into resonant-like states is the largest source of resonant background in the analysis (see Section 8.1.1). EPSOFT [115] is a MC program that generates this type of reaction, in which $M_N > m_p + m_\pi$, where M_N is the mass of the dissociative system.

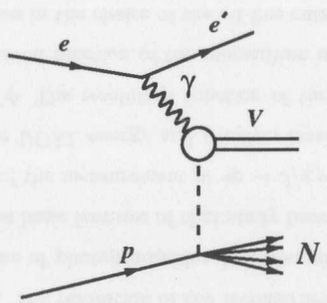

Figure 7.5: Diagrammatical representation of diffractive production of VM's at HERA with dissociation of the proton into an state N.

The version of the program used in this analysis is EPSOFT1.1 [116] [1]. This version contains a simulation of the particle multiplicity of the proton dissociative system with $M_N \gtrsim 2\,\text{GeV}$, tuned to reproduce events in hadron-hadron collisions. This simulation describes satisfactorily the hadronization of the dissociative final state as observed in the ZEUS detector.

The generation of M_N is done according to the following parameterization of the diffractive proton dissociative cross-section:

$$\frac{d\sigma}{dt dM_N^2} \propto \frac{e^{bt}}{M_N^\beta} \tag{7.3}$$

where b and β are parameters of the generator. These parameters are chosen so that the MC simulation describes properly the properties of the final state of the diffractive dissociative system in data. This parameterization of the diffractive proton dissociative cross-section is satisfactory for $M_N \gtrsim 3\,\text{GeV}$. This is not the case for lower masses. This will be discussed in Section 8.1.1.

Other MC generators of diffractive production of VM's via proton dissociation are used to estimate the model dependence in the studies performed on the contamination from proton dissociation. These MC generators model in different ways the hadronization of the dissociated proton. These are the EPSOFT MC version 2.0 (EPSOFT2.0) [117], and the DIFFVM MC [118]. Two versions of the DIFFVM MC are used that implement two different schemes of hadronization: the DIFFVM+JETSET and the DIFFVM+ISO MC. The JETSET package [119] splits the proton into a $q - qq$ system, the uncoupled q scatters by emitting a Pomeron. The DIFFVM+ISO MC corresponds to a generation of particles according to the isotropic phase space decay [120].

[1] From now on this version will be referred to as EPSOFT.

7.3 Monte Carlo Studies

7.3.1 Reconstruction of Kinematic Variables

The nominal MC program used in the analysis is the ZEUSVM MC in the reaction $ep \to eJ/\psi p$ [2]. The resolution of the reconstructed kinematic variables is studied with the help of this MC. The resolution of the reconstructed kinematic variables for $J/\psi \to e^+e^-$ in the regime of photoproduction has been studied in the past for two track topologies [121]. The basic features of that study have been reproduced here. In this work, the energy W of the measurement of $\gamma p \to J/\psi p$ is extended. This implies the implementation of the UCAL energy and position measurement of the electrons, decay products of the J/ψ. The resolution function of the UCAL response behaves differently than the resolution function of the momentum measurement by the CTD. This has direct implications in the choice of the off-line cuts.

The conclusions reached in this Section are applicable to the $\psi(2S)$ as its mass is very close to that of the J/ψ. Qualitatively, this discussion is applicable to the Υ production.

Electrons of the decay of VM's are likely to radiate. Two are the types of radiation simulated by the MC: internal bremsstrahlung (see Section 7.3.4) and the bremsstrahlung when traversing material before reaching the UCAL. The momentum of the electron measured in the CTD will undershoot the momentum of the electron in the moment of the decay. This will translate into the distortion of the invariant mass reconstructed in the event. This is evident in the long tail of $M_{e^+e^-}$ toward low values of $M_{e^+e^-}$ in Plot a) in Figure 7.6. The "intrinsic" resolution of the reconstructed $M_{e^+e^-}$ with CTD tracks is in the average $\approx 35\,\text{MeV}$ and it ranges between $20 \lesssim \Delta(M_{e^+e^-}) \lesssim 150\,\text{MeV}$ depending on the length of the tracks. Details on the determination of the CTD momentum resolution may be found in Appendix B.

[2] The DIPSI MC is used for the reactions $ep \to e\psi(2S)p$ and $ep \to e\Upsilon p$. The ZEUSVM MC (with full simulation of QED radiation corrections) was not available for these reactions.

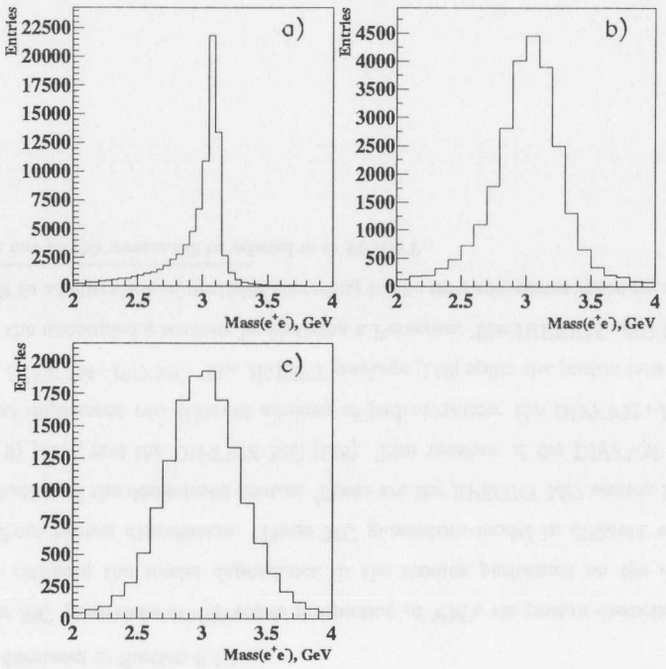

Figure 7.6: Distributions of reconstructed $M_{e^+e^-}$ with the ZEUSVM MC for J/ψ production. Plot a) corresponds to the reconstructed $M_{e^+e^-}$ with two track topologies. Plot b) and c) correspond to one track and zero track topologies, respectively.

Studies of the UCAL energy resolution in the regime $E_<10\,\text{GeV}$ are presented in Appendix A. The resolution of $M_{e^+e^-}$ is expected to degrade in one track and even more in zero track topologies. This is seen in Plots b) and c) of Figure 7.6. The resolution of the $M_{e^+e^-}$ reconstructed with one and zero track configurations ranges between $100 \lesssim \Delta(M_{e^+e^-}) \lesssim 300\,\text{MeV}$.

Plots a)-c) in Figure 7.7 show the difference between reconstructed W and generated W with two track, one track and zero track topologies, respectively. Plot d) in Figure 7.7 shows the difference between reconstructed W and generated W as a function

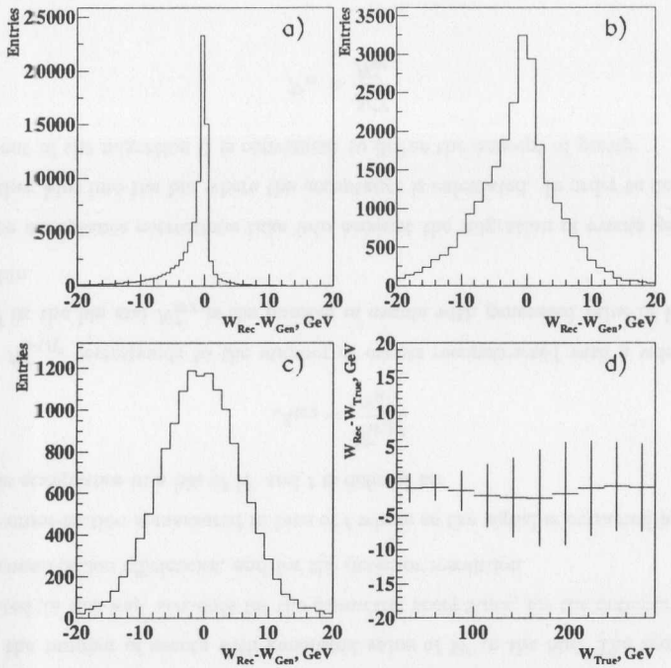

Figure 7.7: Distributions of reconstructed W compared with generated W with the ZEUSVM MC for J/ψ production. Plot a) corresponds to the comparison of reconstructed W with generated W with two track topologies. Plot b) and c) correspond to one track and zero track topologies, respectively. Plot d) shows the difference between reconstructed W and generated W as a function of W. The error bars correspond to the spread of the distributions.

of W. The error bars correspond to the spread of the distributions. The resolution of the reconstructed W varies between $2 \lesssim \Delta(W) \lesssim 10\,\mathrm{GeV}$.

Similarly, Figure 7.8 shows the distributions of reconstructed P_t^2 compared with generated P_t^2. Plot a) corresponds to two track topologies. Plot b) and c) correspond to one track and zero track topologies, respectively. Plot d) shows the difference between

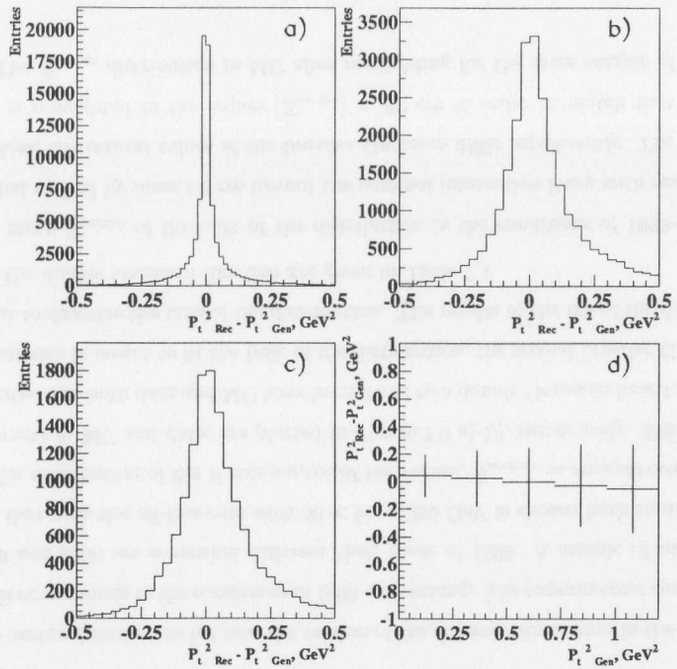

Figure 7.8: Distributions of reconstructed P_t^2 compared with generated P_t^2 with the ZEUSVM MC for J/ψ production. Plot a) corresponds to two track topologies. Plot b) and c) correspond to one track and zero track topologies, respectively. Plot d) shows the difference between reconstructed P_t^2 and generated P_t^2 as a function of P_t^2. Error bars correspond to the spread of the distributions.

reconstructed P_t^2 and generated P_t^2 as a function of P_t^2. The error bars correspond to the spread of the distributions. The resolution of the reconstructed P_t^2 varies between $0.1 \lesssim \Delta(P_t^2) \lesssim 0.35\,\mathrm{GeV}^2$ and it depends on P_t^2 and W.

7.3.2 Acceptance Correction

The events are generated with a cross-section proportional to W^{δ} and with an exponential t distribution proportional to $e^{(}bt)$ Good agreement between the generated and observed distributions is obtained for $\delta = 0.70$ and $b = 4.2\,\mathrm{GeV}^{-2}$. The Q^2 distribution are generated according to a parameterization of the cross-section $\sigma(\gamma^* p \rightarrow J/\psi p)$ given in Equation (7.1) with $n = 2.3$ [122]. Events were generated with $10 < W < 320\,\mathrm{GeV}$ and between Q^2_{min} and $Q^2 = 1\,\mathrm{GeV}^2$. The acceptance calculation is insensitive to the change of the parameter n. The helicity angle, θ_h was reweighted to $(1 + \cos^2\theta_h)$ distribution (see Section 2.5).

The acceptance correction in a bin of W, $\mathcal{A}_W$ is defined as:

$$\mathcal{A}_W = \frac{N^r_W}{N^g_W} \tag{7.4}$$

where, N^r_W corresponds to the number of events reconstructed with a value of W and N^g_W is the number of events with generated value of W in the bin. The acceptance, calculated in this way, accounts for the geometric acceptance, for the detector, trigger and reconstruction efficiencies, and for the detector resolution.

The cross-section is measured in bins of t where as the signal is extracted in bins of P^2_t. The acceptance in a bin of W and t is defined as:

$$\mathcal{A}_{W,t} = \frac{N^r_{W,P^2_t}}{N^g_{W,t}} \tag{7.5}$$

where, N^r_{W,P^2_t} corresponds to the number of events reconstructed with a value of W and P^2_t in the bin and $N^g_{W,t}$ is the number of events with generated value of W and t in the bin.

These acceptance corrections take into account the migration of events generated from other bins into the bin where the acceptance is calculated. In order to determine the extent of the migration it is convenient to define the concept of purity:

$$\mathcal{P}_W = \frac{N^{rg}_W}{N^r_W} \tag{7.6}$$

where N^{rg}_W is the number of events reconstructed and generated in the bin of W. Purity in a bin of W and t is defined as:

$$\mathcal{P}_{W,t} = \frac{N^{rg}_{W,P^2_t,t}}{N^r_{W,t}} \tag{7.7}$$

where $N^{rg}_{W,P^2_t,t}$ is the number of events reconstructed with the value of W and P^2_t in the bin and generated with W and t in the bin. The larger is the migration in a bin, the smaller will be its purity.

7.3.3 Vertex Distribution

The origin of the reaction, or the vertex, in real life is not exactly centered in the origin of the laboratory system. Since the acceptance calculation is sensitive to the location of the vertex, it is necessary to have the vertex distribution in MC look like that of data.

The vertex distribution fed into the version of the detector simulation in the present analysis corresponds to the conditions of 1998 data taking. The experimental conditions of 1999 and 2000 are somewhat different than those of 1998. A sample of two track events that pass the off-line cuts with $50 < W < 200$ GeV is chosen both in data and MC. The distribution of the Z component of the vertex, Z_{vertex}, as reconstructed with CTD tracks in MC and data, are plotted in Figure 7.9 a)-b), respectively. The Z_{vertex} distributions in both data and MC have been fitted to a double Gaussian function. The first Gaussian is meant to fit the bulk of the distribution, the second broader Gaussian is meant to describe the tails of the distribution. The results of the fits of the data and MC to the double Gaussian function are given in Table 7.1.

The mean Z_{vertex} of the bulk of the distribution in the conditions of 1999-2000 is somewhat shifted by some 1.6 cm toward the nominal Interaction Point with respect to 1998. Also, the central values of the broader Gaussian differ significantly. The Z_{vertex} in MC is reweighted in the region $|Z_{vertex}| < 50$ cm in order to match that of the data. The Z_{vertex} distribution in MC after reweighting for the same sample of events

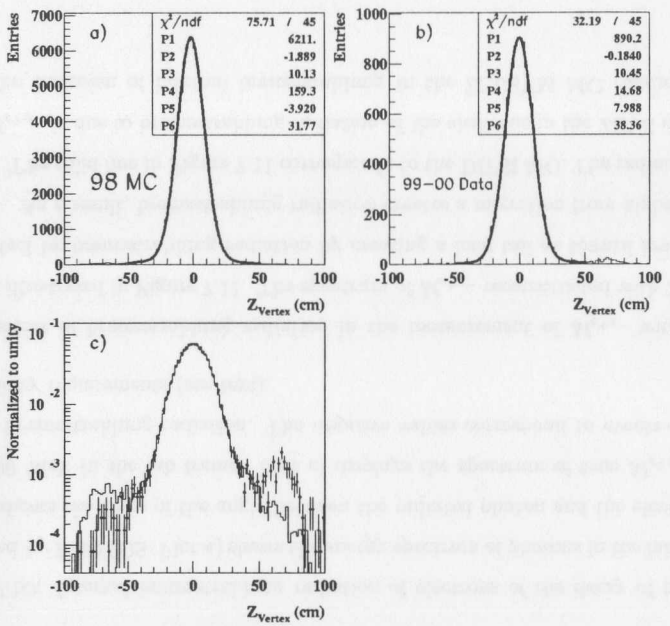

Figure 7.9: The Z coordinate of the vertex in data and MC. Plot a) corresponds to a fit to a double Gaussian of MC and b) of data. Plot c) shows comparison of Z_{vertex} between data and reweighted MC (see text).

compared with data is shown in Figure 7.9 c). The shape of the distributions in MC and data agree well in the region $|Z_{vertex}| < 50$ cm.

7.3.4 Effect of Radiation on Acceptance Corrections

Migration is partly due to bremsstrahlung radiation of hard photons by electrons of the decay of VM's. Internal bremsstrahlung radiation is modelled by the package PHOTOS and the bremsstrahlung radiation of electrons as they pass through the walls of the beam pipe and other components of ZEUS detector before they are detected in the UCAL is modelled by the ZEUS detector simulation.

	98 MC	99-00 data
A_2/A_1	0.02565	0.0165
Z_1 (cm)	-1.89	-0.18
σ_1 (cm)	10.13	10.45
Z_2 (cm)	-3.92	7.98
σ_2 (cm)	31.77	38.34

Table 7.1: Results of the fit of the Z_{vertex} distributions in data and in MC to a double Gaussian function. Parameters A_1, A_2 correspond to the normalization of the narrower and broader Gaussian functions, respectively. Parameters Z_1, Z_2 correspond to the means and σ_1, σ_2 to the widths of the Gaussian functions.

Following the QED formalism of [123] the following Expression for the differential internal bremsstrahlung decay rate in the e^+e^- center of mass frame is adopted, which is suitable for finite γ energies:

$$d\Gamma_{J/\psi\to e^+e^-\gamma} = d\Gamma_{J/\psi\to e^+e^-}\beta^3\frac{2\alpha}{\pi}\frac{dE_\gamma}{E_\gamma}\frac{M_{e^+e^-}}{M_{J/\psi}}\frac{1-\cos^2\theta_{e\gamma}}{\left(1-\beta^2\cos^2\theta_{e\gamma}\right)^2}\,d\Omega_\gamma \qquad (7.8)$$

where

$$d\Gamma_{J/\psi\to e^+e^-} = \frac{3}{3+\lambda}\left(1+\lambda\cos^2\theta_e\right)\Gamma_{J/\psi\to e^+e^-}\frac{d\Omega_e}{4\pi} \qquad (7.9)$$

where E_γ represents the γ energy, β is the lepton velocity, $\theta_{e\gamma}$ the angle between the lepton and the γ directions, Ω_γ the angle of γ, θ_e and Ω_e are the lepton angles, all in the e^+e^- center of mass frame. The parameter λ will be equal to zero for complete conservation of s-channel helicity. The rate for $J/\psi \to e^+e^-\gamma$ varies as $1/E_\gamma$ and has a sharp maximum at extremely small value of θ_γ.

Figure 7.10 a) shows the energy spectrum of the γ in the lab frame as generated by PHOTOS in the decay of the J/ψ. Figure 7.10 b) shows the $\sin(\theta_{e\gamma})$ in the lab frame for photons with $E_\gamma > 100$ MeV in the same frame [3].

[3]The peak at large values of $\sin(\theta_{e\gamma})$ is due to the incorrect assignment of the lepton to the radiated photon. A photon radiated by a lepton at a large angle has been associated to the other lepton. This feature of the Plot does not affect the physics analysis.

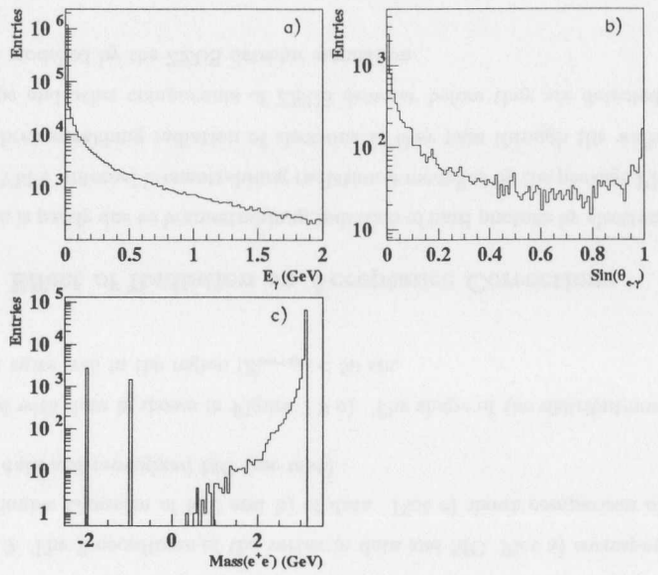

Figure 7.10: Internal bremsstrahlung radiation of electrons of the decay of the J/ψ calculated by PHOTOS. Plot a) shows the energy spectrum of photons in the lab frame. Plot b) shows the sinus of the angle between the radiated photon and the electron for $E_\gamma > 100$ MeV in the lab frame. Plot c) displays the spectrum of true $M_{e^+e^-}$ after internal bremsstrahlung radiation. The negative values correspond to events cut out by elasticity requirements (see text).

The effect of bremsstrahlung radiation in the measurement of $M_{e^+e^-}$ with CTD tracks is illustrated in Figure 7.11. The spectrum of $M_{e^+e^-}$ reconstructed with 2 tracks is distorted by bremsstrahlung radiation by creating a long tail at toward low values of $M_{e^+e^-}$. As a result, bremsstrahlung radiation creates a migration from higher W to lower W. The solid line in Figure 7.11 corresponds to the DIPSI MC. The radiation tail in the $M_{e^+e^-}$ is due to bremsstrahlung radiation of the electrons in the ZEUS detector only. The inclusion of internal bremsstrahlung in the ZEUSVM MC (dashed line)

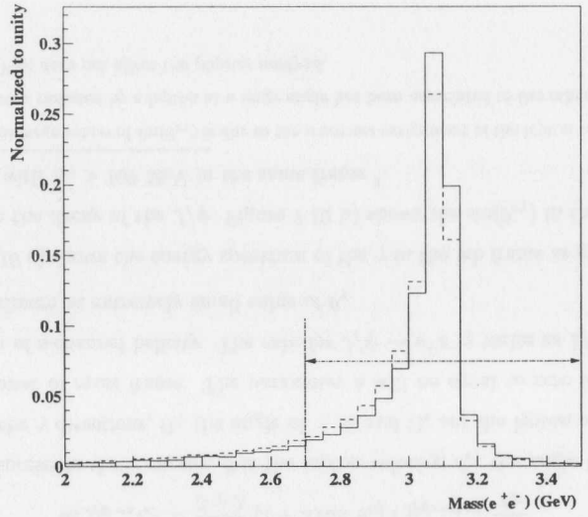

Figure 7.11: $M_{e^+e^-}$ reconstructed with 2 CTD tracks. The solid line corresponds to the DIPSI MC and the dashed line to the ZEUSVM MC. The inclusion of internal bremsstrahlung radiation in the ZEUSVM MC distorts further the $M_{e^+e^-}$ spectrum by depleting the region of the peak and enhancing the radiation tail. The horizontal dashed-doted line indicates the size of the signal mass window (see Section 9.1).

distorts further the $M_{e^+e^-}$ spectrum by depleting the region of the peak and enhancing the radiation tail.

The effect on the acceptance due to the addition of internal bremsstrahlung is illustrated in Figure 7.10 c). This Plot shows the true $M_{e^+e^-}$ after internal bremsstrahlung radiation of the electrons of the decay of the J/ψ events with two tracks in the kinematic range $60 < W < 130$ GeV. The elasticity requirement applied off-line will cut on energy depositions above a certain threshold not associated to the electromagnetic objects in the event. This cut corresponds roughly to $\sin(\theta_{e\gamma}) \sim 0.2$. About one third of events with hard radiation with $E_\gamma > 100$ MeV in the lab frame will be affected by the elasticity requirement, therefore, reducing the acceptance. The events that are

cut out due to this elasticity cut are given $M_{e^+e^-} = -2$ in Figure 7.10 c) and amount to some 2.5% of the events. Also, at the trigger level it is required that every single energy deposition in the BCAL above 700 MeV has a track pointing to it. This cut will affect hard bremsstrahlung radiation too. The events that are cut out due to this elasticity cut are given $M_{e^+e^-} = -1$ in Figure 7.10 c) and amount to some 1.5% of the events. After these elasticity requirements are applied, still a fraction of the events with hard radiation such that $M_{e^+e^-}$ is less than the lower bound of the mass window will be cut off, as illustrated Figure 7.10 c), accounting approximately for 2.5% of the events in this kinematic region.

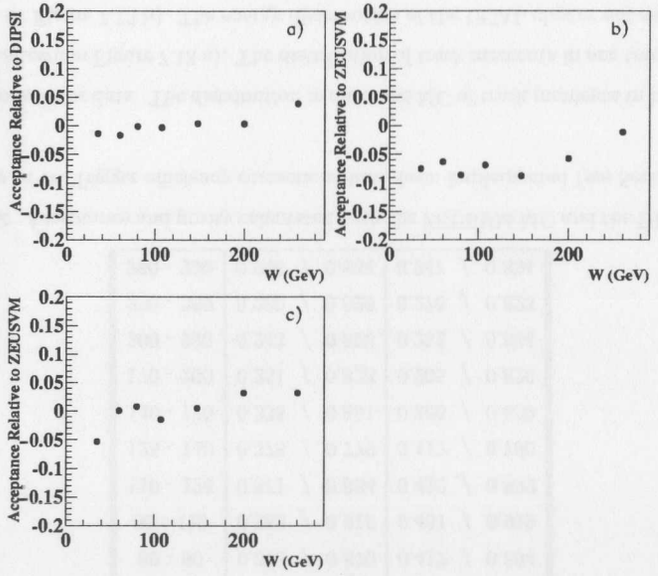

Figure 7.12: Plot a) corresponds to the acceptance calculated with the ZEUSVM MC without radiation corrections relative to the DIPSI MC . Plot b) shows the effect of switching in PHOTOS in the ZEUSVM MC and Plot c) the effect of switching in HERACLES.

In order to establish the effect of radiation and the compatibility of the DIPSI MC and the ZEUSVM MC, several samples of MC events were generated and passed through the ZEUS detector and trigger simulation. The acceptance correction calculated with the ZEUSVM MC relative to that of the DIPSI MC [4] is shown in Figure 7.12 a). The acceptance corrections calculated with both MC programs agree within 3%. The effect of the inclusion of final state radiation is illustrated in Figure 7.12 b). The relative change in the acceptance correction with the ZEUSVM MC after the inclusion of PHOTOS is maximum in the middle W range where the J/ψ is reconstructed mainly with two track events and is produced with small longitudinal boost. At high W, when zero track configurations start to switch in and the longitudinal boost is considerable, the emitted photon will be merged into the cluster deposited by the electron that emitted it. Figure 7.12 c) shows the effect of the inclusion of HERACLES into the ZEUSVM MC. This effect is sizeable at very low W and very high W.

Table 7.2 shows the acceptance in various W ranges calculated with the DIPSI MC and the ZEUSVM MC. The acceptance is largest in the middle W range. The acceptance is fairly flat at high W. The acceptance calculated by the ZEUSVM MC is systematically lower than that calculated with the DIPSI MC in the middle W range, as discussed above. The purities are in most of the bins better than 80%. Due to internal bremsstrahlung the ZEUSVM MC displays somewhat worse purities than the DIPSI MC. This effect disappears at very high W and very low W, where the migration is dominated by resolution effects.

Tables 7.3-7.4 show the acceptances in various W and t bins with the DIPSI MC and the ZEUSVM MC, respectively. Purities fall as $|t|$ grows. Purities are higher in the middle W range and fall below 20% at high W and high $|t|$.

The kinematics of the decaying electrons in MC may be compared to data. The data and MC set have passed the off-line cuts (see Section 6.4) and are reconstructed in the mass window (see Section 9.1). The W and t distributions are reweighted in MC to

[4] $(A_{ZEUSVM} - A_{DIPSI})/A_{DIPSI}$.

	ZEUSVM	DIPSI
W (GeV)	$\mathcal{A}$ / $\mathcal{P}$	$\mathcal{A}$ / $\mathcal{P}$
20 - 35	0.087 / 0.898	0.093 / 0.893
35 - 50	0.270 / 0.924	0.287 / 0.937
50 - 60	0.386 / 0.932	0.430 / 0.947
60 - 70	0.383 / 0.929	0.418 / 0.940
70 - 80	0.372 / 0.905	0.408 / 0.912
80 - 90	0.373 / 0.870	0.412 / 0.894
90 - 110	0.382 / 0.916	0.431 / 0.919
110 - 125	0.371 / 0.834	0.422 / 0.832
125 - 140	0.378 / 0.779	0.412 / 0.780
140 - 170	0.335 / 0.861	0.366 / 0.859
170 - 200	0.251 / 0.823	0.265 / 0.826
200 - 230	0.243 / 0.823	0.252 / 0.834
230 - 260	0.280 / 0.826	0.276 / 0.823
260 - 290	0.248 / 0.834	0.247 / 0.834

Table 7.2: Acceptance and purity calculated with the ZEUSVM MC and the DIPSI MC in ranges of W. Trigger efficiency corrections have been implemented (see Section 5.3).

accommodate the data. The distribution in data and MC of track momenta in two track events is shown in Figure 7.13 a). The distribution of track momenta in one track events is shown in Figure 7.13 b). The energy distribution of the UCAL cluster not associated to the track in in one track events is shown in Figure 7.13 c). The energy distribution of the UCAL clusters in zero track events is displayed in Figure 7.13 d). The data and MC sets have passed off-line cuts (see Section 6.4) and are reconstructed in the mass window (see Section 9.1). The contribution from non-resonant QED background has been subtracted. There is an important contribution from remaining background, specially at very low W and very high W. This contribution has not been removed. Control plots of the W for data and for the ZEUSVM MC for the three topologies, are shown in Figure 7.14 a) to c) and for the three topologies combined, Figure 7.14 d).

W(GeV)	$0< -t <0.2$	$0.2< -t <0.5$	$0.5< -t <0.85$	$0.85< -t <1.25$
20 - 50	0.178 / 0.838	0.189 / 0.618	0.239 / 0.418	0.325 / 0.296
50 - 70	0.406 / 0.910	0.416 / 0.778	0.495 / 0.626	0.574 / 0.529
70 - 90	0.394 / 0.889	0.411 / 0.767	0.434 / 0.647	0.618 / 0.499
90 - 125	0.407 / 0.868	0.438 / 0.707	0.479 / 0.581	0.565 / 0.455
125 - 170	0.364 / 0.793	0.410 / 0.572	0.518 / 0.403	0.748 / 0.207
170 - 230	0.212 / 0.781	0.285 / 0.443	0.442 / 0.201	0.813 / 0.138
230 - 290	0.230 / 0.816	0.275 / 0.476	0.415 / 0.243	0.669 / 0.101

Table 7.3: Acceptance and purity calculated with the DIPSI MC in bins of W and $-t$. Trigger efficiency corrections have been implemented (see Section 5.3).

W(GeV)	$0< -t <0.2$	$0.2< -t <0.5$	$0.5< -t <0.85$	$0.85< -t <1.25$
20 - 50	0.163 / 0.824	0.176 / 0.598	0.223 / 0.413	0.259 / 0.307
50 - 70	0.366 / 0.893	0.391 / 0.751	0.422 / 0.622	0.513 / 0.558
70 - 90	0.352 / 0.870	0.375 / 0.728	0.428 / 0.627	0.532 / 0.461
90 - 125	0.362 / 0.863	0.378 / 0.700	0.426 / 0.581	0.534 / 0.460
125 - 170	0.335 / 0.804	0.376 / 0.549	0.482 / 0.377	0.754 / 0.242
170 - 230	0.203 / 0.778	0.267 / 0.426	0.432 / 0.236	0.850 / 0.129
230 - 290	0.234 / 0.801	0.275 / 0.480	0.414 / 0.263	0.714 / 0.132

Table 7.4: Acceptance and purity calculated with the ZEUSVM MC in bins of W and $-t$. Trigger efficiency corrections have been implemented (see Section 5.3).

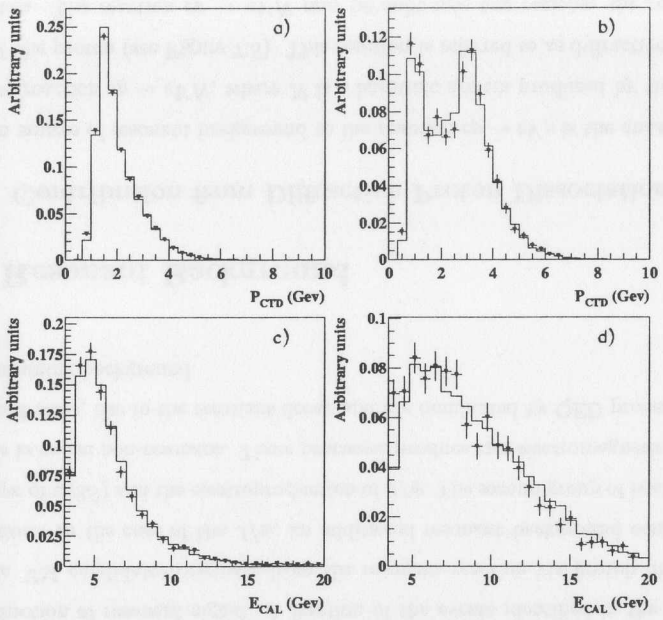

Figure 7.13: Control plots for measured quantities with the three topologies. Plot a) shows the momentum distribution of tracks in two track events. Plot b) displays the momentum distribution of the track in one track events and c) the energy of the object reconstructed with the UCAL. Plot d) shows the energy distribution of objects in zero track events. The data and MC set have passed the off-line cuts (see Section 6.4) and are reconstructed in the mass window (see Section 9.1). The contribution from non-resonant QED background has been subtracted. The contribution from remaining background has not been removed. This affects specially the very low W and very high W regions.

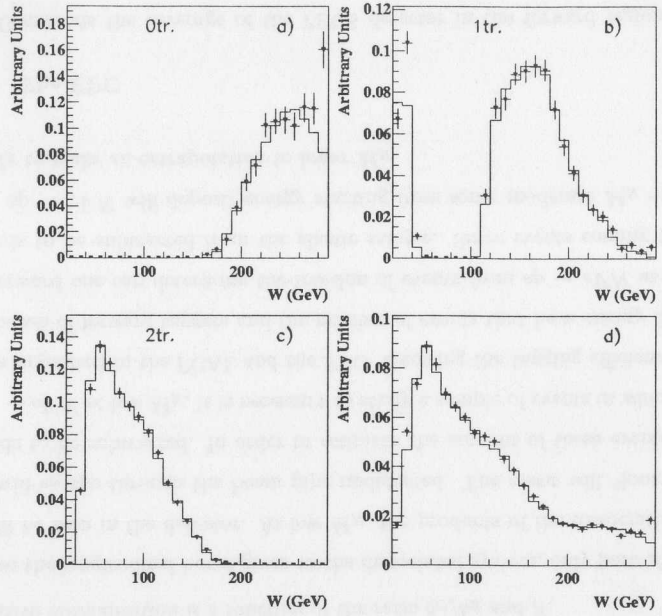

Figure 7.14: W distributions of data and ZEUSVM for the three topologies. Plots a) to c) and for the three topologies combined, Plot d). The data and MC set have passed off-line cuts (see Section 6.4) and are reconstructed in the mass window (see Section 9.1). The contribution from non-resonant QED background has been subtracted. The remaining background has not been subtracted.

Chapter 8

Background Studies

The sources of background relevant to the analysis of production of heavy VM's may be divided into two groups. The first group corresponds to processes that compete with the production of resonant signal. A fraction of the events identified in the analysis as elastic VM candidates originate from the resonant reaction via proton diffractive dissociation. In the case of the J/ψ, an additional resonant background comes from the decays of $\psi(2S)$ and the electroproduction of J/ψ. The second group of background processes is called non-resonant. These processes produce two electromagnetic objects in the final state, like in the resonant decay and are dominated by QED processes and other remaining background.

8.1 Resonant Background

8.1.1 Contribution from Diffractive Proton Dissociation

The main source of resonant background to the reaction $ep \to eVp$ is the quasi-elastic diffractive reaction $ep \to eVN$, where N is a hadronic system produced by the dissociation of the proton (see Figure 7.5). This reaction is referred to as diffractive proton dissociation. The reaction $ep \to eVN$ may be split into two regions: the resonant-like region, with $M_N < 2\,\text{GeV}$, and the decay of the proton into a continuum with

$M_N > 2\,\text{GeV}$:

$$\frac{d^2\sigma}{dM_N^2 dt} = \left(\frac{d\sigma}{dM_N^2}\right)_R e^{b_R t} + \left(\frac{d\sigma}{dM_N^2}\right)_C e^{b_C t} \tag{8.1}$$

and

$$\left(\frac{d\sigma}{dM_N^2}\right)_C \propto \frac{1}{M_N^\beta} \tag{8.2}$$

where the subscripts R and C refer to the resonant-like and the continuum region, correspondingly. The t dependence of the cross-sections is parameterized with a single exponential. This is a good approximation at $|t| \lesssim 1\,\text{GeV}^2$. β, b_R and b_C are parameters that need to be determined from data and fed into the MC generator.

The relative normalization of the resonant-like and continuum regions has to obey the Finite Mass Sum Rule (FMSR) (see Appendix E). According to Expression (E.7), this relative normalization is a function of the ratio b_C/b_R and β.

Due to the longitudinal boost given to the dissociated system, only part of the final state will be seen in the detector. At low M_N, the products of the dissociation of the proton will escape through the beam pipe undetected. The event will "look" elastic, and needs to be subtracted. In order to estimate the amount of these events coming from $ep \to eVN$ at low M_N, it is necessary to study a sample of events in which energy has been deposited in the FCAL and the FPC. Knowing the tagging efficiency of this configuration of forward taggers and the number of events that have energy deposited in the forward one can determine the fraction of events from $ep \to eVN$ at low M_N that needs to be subtracted from the elastic sample. Since events coming from the reaction $ep \to eVN$ will deposit energy starting from some moderate M_N one needs effectively to make an extrapolation to lower M_N.

8.1.1.1 The FPC

The FPC extends the coverage of the ZEUS detector in the forward region by one unit of rapidity. Therefore, one can study the reaction $ep \to eJ/\psi N$ at lower M_N as opposed to previous analyses and decrease the systematic error due to the uncertainty introduced by the extrapolation.

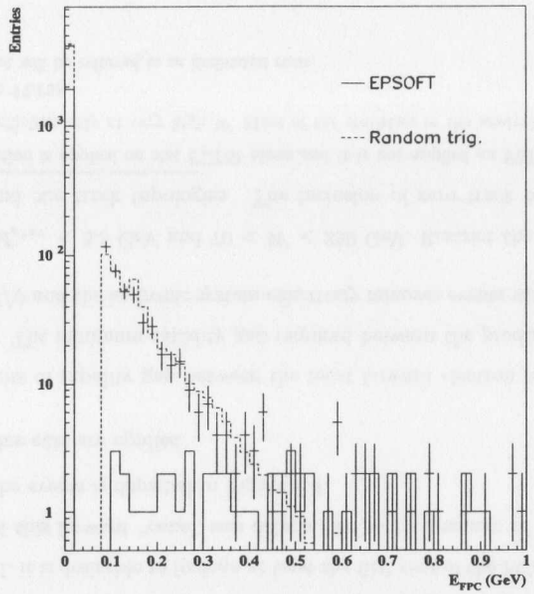

Figure 8.1: The energy distribution of the FPC for $E_{FPC} < 1$ GeV in a sample of data taken with the trigger selection of the analysis. The dashed line corresponds to data taken with random triggers. The solid line corresponds to the EPSOFT MC.

In order to calculate the tagging efficiency of the FPC, it is necessary to define the FPC tag. A tag in the FPC is defined as an energy deposition greater than a threshold, E_{tag}, $E_{FPC} > E_{tag}$. The value of E_{tag} cannot be zero since in real life the energy response of the FPC at low energies is dominated by noise. This effect is not fully simulated in MC. Figure 8.1 shows the energy spectrum of the FPC with $E_{FPC} < 1$ GeV observed in a data sample collected with the trigger selection of the analysis. The solid line corresponds to the energy response one would expect from the dissociation of the proton, as predicted by the EPSOFT MC. In order to make sure that the FPC energy spectrum at $E_{FPC} < 1$ GeV is due to noise one should look into data taken with random triggers. The same distribution is plotted as a

dashed line in Figure 8.1. The dashed histogram was normalized to the number of events in the sample of regular data. The energy response of the FPC is saturated by noise at $E_{FPC} < 0.5$ GeV. In order to stay away from the noise it was decided to set $E_{tag} = 1$ GeV.

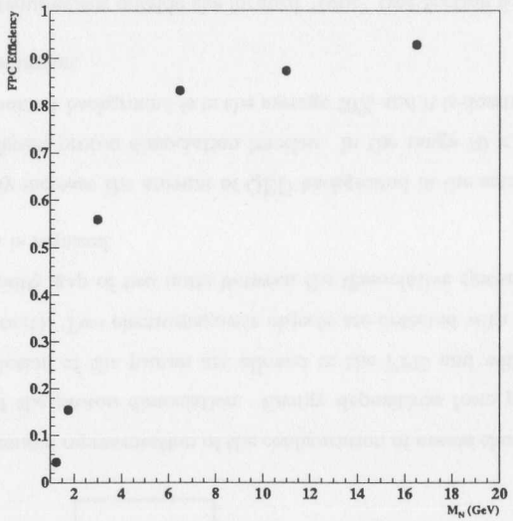

Figure 8.2: The tagging efficiency of the FPC as a function of the mass of the dissociated proton, M_N, calculated with the EPSOFT MC.

The tagging efficiency of the FPC is defined as follows:

$$\epsilon_{FPC} = \frac{Number\ of\ events\ with\ E_{FPC} > 1\ \text{GeV}}{Total\ Number\ of\ ep \rightarrow eVN\ events} \tag{8.3}$$

The tagging efficiency of the FPC is shown as a function of M_N in Figure 8.2 as calculated with the EPSOFT MC. The FPC detects particles coming from the dissociation of the proton at masses $M_N > 2.5$ GeV and reaches 90% efficiency for $M_N \approx 10$ GeV.

8.1.1.2 Dedicated Runs

The nominal trigger configuration requires a restriction at the FLT on the amount of energy deposited in the first ring of the FCAL [1]. In order estimate the contamination of proton dissociation, it was proposed to take data with a modified trigger selection [2]. This trigger selection allows large energy depositions in the FCAL. Due to high trigger rates a pre-scale factor of two was applied. The total amount of data taken with this modified trigger configuration corresponds to 3.4 pb^{-1}.

The main competing process to the reaction $ep \rightarrow eJ/\psi N$ via the breaking up of the proton is the inelastic production of J/ψ in the reaction $ep \rightarrow eJ/\psi X$. This is a non-diffractive process. In order to suppress this process we need to require a minimum rapidity gap between the most forward electron and the hadronic system. The dimensions of a forward "cone" are defined, where hadronic depositions are allowed. The bigger the dimensions of the forward "cone" the more backward the products of the decay of the J/ψ should be and the smaller will be the statistics available. In order to reduce the systematic uncertainty introduced by the energy leakage between the FPC and the FCAL it is desirable to include at least the first ring of the FCAL. The optimal dimensions of this forward "cone" was determined to be a square of 40x40 cm^2. The topology of the events is depicted in Figure 8.3.

Some off-line cuts are applied:

- Two units of rapidity gap between the most forward electron and the hadronic system. The minimum rapidity gap required between the products of the decay of the J/ψ and the hadronic system effectively removes events with $W < 70$ GeV.
- $2.7 < M_{e^+e^-} < 3.5$ GeV and $70 < W < 250$ GeV. Restrict the analysis to two track and one track topologies. The inclusion of zero track topologies would significantly increase the amount of QED background in the sample, which may have a different proton dissociation fraction. In the range $70 < W < 250$ GeV the non-resonant background is in the average 20% and it is dominated by Bethe-Heitler production.
- Elasticity requirement outside the forward "cone" (see Section 6.4).

A total number of 1584 events pass the selection cuts, out of which 188 have a tag in the FPC. The distribution of $M_{e^+e^-}$ of the data taken with the dedicated runs is shown

[1] This restriction is applied on slot FLT58 alone and it is not applied on FLT62. However, slot FLT62 is fully efficient only at very high W. Most of the statistics in the analysis comes from data triggered by slot FLT58.

[2] This data set will be referred to as dedicated runs.

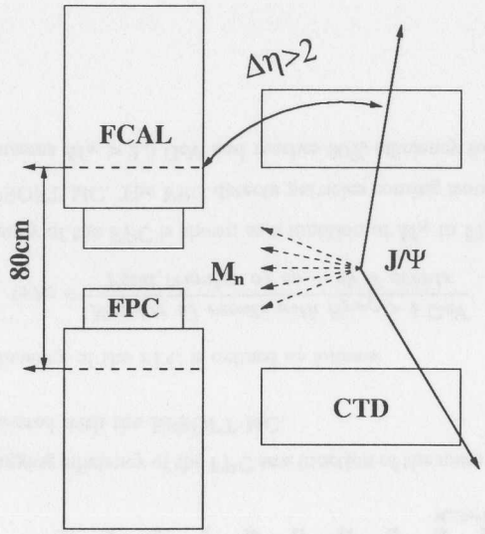

Figure 8.3: Schematic representation of the configuration of events chosen to study the normalization of the proton dissociation. Energy depositions from particles coming from the dissociation of the proton are allowed in the FPC and within a square of 40x40 cm^2 (see text). Two electromagnetic objects are detected with $M_{e^+e^-} \approx M_{J/\psi}$. A minimum rapidity gap of two units between the dissociative system and the most forward electron is required.

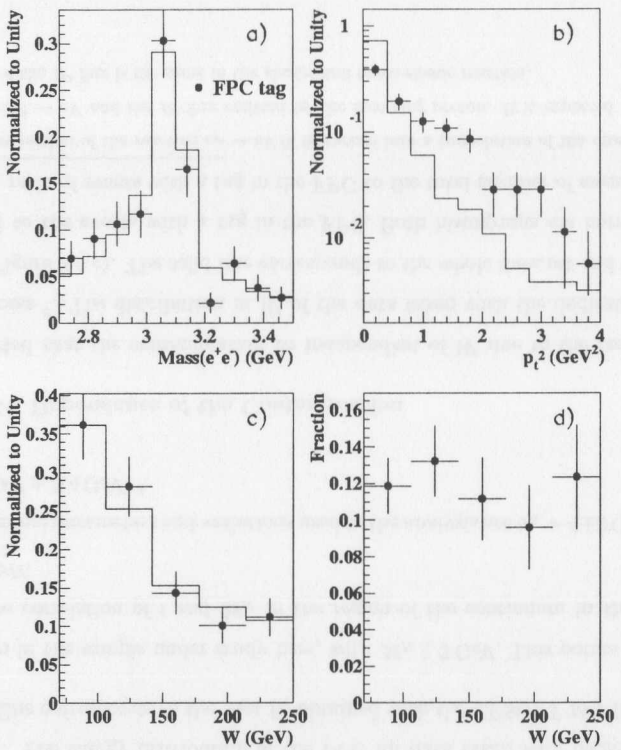

Figure 8.4: Data taken with the dedicated runs. The solid line corresponds to all the events and the points correspond to events with tag in the FPC. Plot a) corresponds to the mass spectrum, b) to the P_t^2 distribution, c) to the W distribution. Plot d) shows the ratio of the number of events with tag in the FPC to the total number of events in bins of W. In Plots b) and c) histograms have been normalized to unity.

in Figure 8.4 a). The P_t^2 of the J/ψ in events with a tag in the FPC is compared to the entire data sample in Figure 8.4 b). As expected, the P_t^2 dependence of the sample with a tag in the FPC is shallower [124, 125].

8.1.1.3 Sensitivity to β and b_C

The energy distribution in the FPC is sensitive to the parameter β in Expression (8.2). The steeper this distribution is the steeper will fall the energy distribution of the FPC. The parameter β is extracted by reweighting MC to give the best fit of the energy distribution in the FPC in data. The following procedure is followed

1. Reweight events in MC according to $M_N^{\beta_{nom}}/M_N^{\beta}$, where β_{nom} is the nominal value of β with which the MC sample was generated.
2. Calculate the binned likelihood that the distribution of the energy in the FPC in MC agrees with data.
3. Repeat 1 and 2 for different values of β till the likelihood is maximized.

This procedure has been performed with different MC generators (see Section 7.3). The best fit is obtained with the EPSOFT MC, shown in Figure 8.5. The value of β obtained with the EPSOFT MC is $\beta = 2.1 \pm 0.3(stat)^{+0.2}_{-0.2}(syst)$, where the systematic error corresponds to changing the energy scale of the FPC by $\pm 10\%$.

The reaction $ep \to eJ/\psi N$ has been studied through the muonic decay $J/\psi \to \mu^+\mu^-$ with enlarged statistics [126]. A global fit of the properties of the final state N in both channels has been performed, yielding $\beta = 2.5^{+0.3}_{-0.4}$ [127], where statistical and systematic errors have been added in quadrature. This value of β is chosen as nominal in this analysis. This value of β is compatible within errors at similar values of t with results obtained by other experiments [128, 129].

Figure 8.6 displays the P_t^2 distribution in data (solid points) taken in dedicated runs compared with the EPSOFT MC (solid line) for different values of b_C. The data prefer $b_C \approx 0.7\,\mathrm{GeV}^{-2}$. This is consistent with previous measurements performed in the ZEUS Collaboration [124, 125]. A fit to this data yields $b_C = 0.70 \pm 0.2\,\mathrm{GeV}^{-2}$. The error is obtained by adding systematic and statistical errors in quadrature. It should be noted that this measurement corresponds to $M_N \gtrsim 7\,\mathrm{GeV}$, with a median significantly

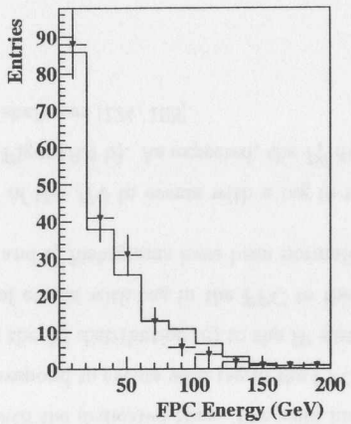

Figure 8.5: The energy distribution of the FPC for data taken with dedicated runs. The solid line corresponds to the best fit obtained with the EPSOFT MC (see text).

larger than in the sample under study here, with $M_N \gtrsim 3\,\mathrm{GeV}$. This points to a weak dependence correlation of t and M_N in the region of the continuum in the reaction $ep \to eJ/\psi N$.

The nominal parameters and variations used in the analysis are $b_R = 4 \pm 2\,\mathrm{GeV}^{-2}$ [130] and $b_C = 0.7 \pm 0.4\,\mathrm{GeV}^{-2}$.

8.1.1.4 W Dependence of the Contamination

It is expected that the contamination be independent of W due to the factorization of the process [3]. The distribution in W of the data taken with the dedicated runs is shown in Figure 8.4 c). The solid line corresponds to the whole data set and the points correspond to the events with a tag in the FPC. Both histograms are normalized to unity. The ratio of events with a tag in the FPC to the total number of events, f_{vis}, as

[3]The cross-section of the reaction $ep \to eVN$ factorizes into a convolution of the cross-section of the process $e\mathbb{P} \to eV$ and the $\mathbb{P}$ flux emitted by the incoming proton. It is expected that the W dependence of the $\mathbb{P}$ flux is the same in the elastic and quasi-elastic reaction.

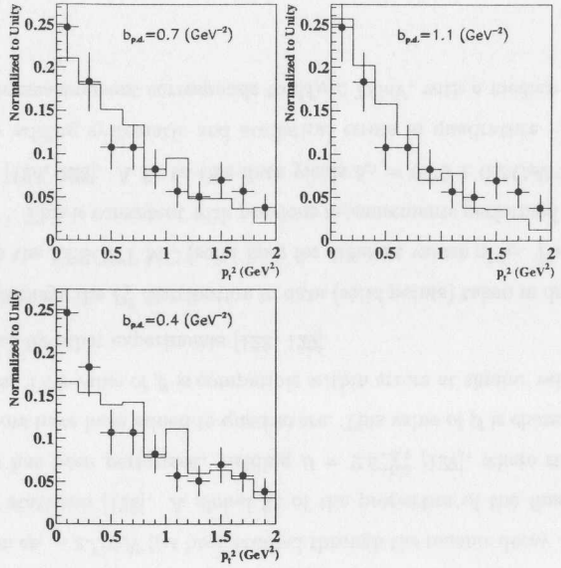

Figure 8.6: The P_t^2 distribution in data (solid points) taken in dedicated runs compared with the EPSOFT MC (solid line) for different values of b_C. The data prefers $b_C \approx 0.7\,\mathrm{GeV}^{-2}$.

a function of W is shown in Figure 8.4 d). The correlation between the contamination of proton dissociation in the elastic sample with W is observed to be weak. A straight line fit, $f_{vis} = P_0$, is performed to the histogram in Figure 8.4 d). The fit yields $P_0 = 0.118 \pm 0.0091$. A fit to a linear form $f_{vis} = P_0 + P_1 W$ yields $P_1 = -0.00009 \pm 0.00018$, consistent with a flat dependence. Within the statistics available in the present analysis it is possible to reduce the uncertainty in the deviation from a straight line to an error band of $\pm 10\%$.

It is important to check on the impact of the definition of the elasticity requirement (see Section 6.4). The fraction of proton dissociation in the elastic sample is sensitive to the definition of the threshold of the energy deposited in UCAL cells not associated to the hadronic system and the electrons of the decay of the J/ψ. The fraction of events

with tag in the FPC to the total amount of events has been calculated after increasing the values of the thresholds on the energy deposits in EMC, HAC0 and HAC1 sections. The values of the number of events observed and number of events with tag in the FPC after changing the energy threshold on UCAL EMC, HAC0 and HAC1 cells are given in Table 8.1. The value of f_{vis} remains stable with the definition of elasticity.

In the nominal analysis two units of rapidity between the hadronic system and the most forward electron were required. In order to check on the stability of this cut, this requirement was tightened to 3 units. The fraction of events with tag in the FPC increased by 10%.

	N	N_{FPC}	f_{vis}
$E_{EMC} < 200$ MeV	1584	188	0.119
$E_{EMC} < 300$ MeV	1701	204	0.120
$E_{EMC} < 400$ MeV	1743	215	0.123
$E_{EMC} < 500$ MeV	1780	223	0.125
$E_{EMC} < 1000$ MeV	1835	241	0.131
$E_{HAC0} < 350$ MeV	1637	198	0.121
$E_{HAC1} < 400$ MeV	1621	198	0.122

Table 8.1: Number of events observed, N, number of events with tag in the FPC, N_{FPC}, and $f_{vis} = N_{FPC}/N$ obtained with different values of the threshold on the energy deposition in UCAL EMC, HAC0 and HAC1 cells not associated to the hadronic system and the electrons of the decay of the J/ψ.

The fraction of events coming from proton dissociation remaining after a veto in the FPC, f, is calculated with the following Expression:

$$f = f_{vis}\left(\frac{1}{\epsilon_{FPC}} - 1\right) \tag{8.4}$$

where ϵ_{FPC} is calculated with the EPSOFT MC with the nominal parameters given in Section 8.1.1.3. Table 8.2 shows the values of ϵ_{FPC} and f for the nominal configuration of parameters (first row) and for variations of these parameters. To summarize, $f = (10.0^{+4.3}_{-4.0})\%$.

β	b_R (GeV^{-2})	b_C (GeV^{-2})	ϵ_{FPC}	f (%)
2.5	4	0.7	0.545	9.9
2.5	6	0.7	0.575	8.8
2.5	2	0.7	0.473	13.3
2.5	4	1.1	0.503	11.8
2.5	4	0.3	0.597	8.0
2.1	4	0.7	0.645	6.6
2.8	4	0.7	0.499	11.9

Table 8.2: Values of ϵ_{FPC} and f for the nominal configuration of parameters (first row) and for variations of these parameters (see Section 8.1.1.3) calculated with the EPSOFT MC.

8.1.1.5 P_t^2 Dependence of the Contamination

The P_t^2 dependence of the tagging efficiency of the FPC may be calculated with MC. The tagging efficiency increases with P_t^2. The values of expected proton dissociative events in bins of W and P_t^2, $N^{p.d.}_{W,P_t^2}$, are given in Table 8.3. The fraction of events coming from proton dissociation rises strongly with P_t^2 due to the different t dependence of the elastic and proton dissociative cross-sections. The fraction of proton dissociative events in the range $0 < P_t^2 < 0.2$ GeV^2 accounts to some $5 - 6\%$ and grows up to $25 - 45\%$ in the range $0.85 < P_t^2 < 1.25$ GeV^2.

8.1.2 The $\psi(2S)$ Contamination in J/ψ Signal

The $\psi(2S)$ is an orbital excitation of the J/ψ with a mass $M_{\psi(2S)} = 3.686$ MeV. This particle decays more than 50% of the times into the J/ψ plus a number of charged and uncharged hadrons. About 30% of the time the $\psi(2S)$ will decay into J/ψ + charged hadrons. The off-line selection cuts requires a maximum number of 2 vertex tracks

in the CTD and also all depositions in the UCAL be electromagnetic. Effectively, only three body decays in which the charged hadron escaped through the beam pipe missing the acceptance of the UCAL or a charged track of a very low momentum (less than 200 MeV) would survive the off-line cuts. Decays with more multiplicity would be even more suppressed. As a result, this channel will contribute marginally to the observed J/ψ signal. A relevant resonant background comes from the decay $\psi(2S) \rightarrow J/\psi\pi^0\pi^0$. The branching ratio of this decay is $\mathcal{B}(\psi(2S) \rightarrow J/\psi\pi^0\pi^0) = (18.2 \pm 2.3)\%$. Neutral particles do not leave a track in the CTD so the veto efficiency on these kinds of configurations is smaller. Events in which the γ fall within 25 cm of the electromagnetic objects of the decay of the J/ψ or low energy γ will pass the off-line cuts. The acceptance of this process and its contribution are estimated using MC. Other decays into neutral particles like $\psi(2S) \rightarrow J/\psi\pi^0$ and $\psi(2S) \rightarrow J/\psi\eta$ yield a smaller contribution since the total branching ratio is less than 3%.

Another relevant contribution comes from the leptonic decay $\psi(2S) \rightarrow e^+e^-$ with a branching ratio $\mathcal{B}(\psi(2S) \rightarrow e^+e^-) = (0.88 \pm 0.13)\%$. The contamination from this process depends strongly on the size of the search window and the resolution of $M_{e^+e^-}$. The acceptance of this process and its contribution are estimated using MC.

The normalization of the contamination of decays from the $\psi(2S)$ is determined by the ratio of the production cross-section $r = \sigma(ep \rightarrow e\psi(2S)p)/\sigma(ep \rightarrow eJ/\psi p)$. This ratio has been measured at HERA to be about $r \approx 0.15$ (see Chapter 10).

The fraction of the contamination of decays of the $\psi(2S)$ in a given bin is calculated as follows:

$$\mathcal{F}_{\psi(2S)\rightarrow J/\psi\pi^0\pi^0} = r\frac{\mathcal{A}_{\psi(2S)\rightarrow J/\psi\pi^0\pi^0}}{\mathcal{A}_{J/\psi\rightarrow e^+e^-}}\mathcal{B}(\psi(2S) \rightarrow J/\psi\pi^0\pi^0) \tag{8.5}$$

and

$$\mathcal{F}_{\psi(2S)\rightarrow e^+e^-} = r\frac{\mathcal{A}_{\psi(2S)\rightarrow e^+e^-}}{\mathcal{A}_{J/\psi\rightarrow e^+e^-}}\frac{\mathcal{B}(\psi(2S) \rightarrow e^+e^-)}{\mathcal{B}(J/\psi \rightarrow e^+e^-)} \tag{8.6}$$

Here $\mathcal{A}_{\psi(2S)\rightarrow J/\psi\pi^0\pi^0}, \mathcal{A}_{\psi(2S)\rightarrow e^+e^-}, \mathcal{A}_{J/\psi\rightarrow e^+e^-}$ are the corresponding acceptances calculated with the DIPSI MC (see Section 7.2.2). In the calculation of the acceptance of the process $ep \rightarrow e\psi(2S)p$ a number of assumptions need to be done:

1. The decay $\psi(2S) \rightarrow J/\psi\pi^0\pi^0$ is independent of the subsequent $J/\psi \rightarrow e^+e^-$. The decay width $\Gamma_{\psi\rightarrow J/\psi\pi^0\pi^0} = (41 \pm 5.6$ KeV) is almost an order of magnitude larger than $\Gamma_{J/\psi\rightarrow e^+e^-} = (5.16 \pm 0.3)$ KeV. The J/ψ will decay much later than the $\psi(2S)$ and, therefore, the two decays may be considered as independent.

2. The W dependence of $\sigma(ep \rightarrow e\psi(2S)p)$ is the similar to $\sigma(ep \rightarrow eJ/\psi p)$. It has been shown that the energy dependence of the production of VM's at HERA scales with the variable $M_V^2 + Q^2$ [131, 132, 133, 134] and $M_{\psi(2S)} \approx M_{J/\psi}$ (see Section 12.4).

3. The t dependence of $\sigma(ep \rightarrow e\psi(2S)p)$ was assumed to be the same as of $\sigma(ep \rightarrow eJ/\psi p)$. This feature of the elastic production of $\psi(2S)$ has been determined experimentally [135].

4. The contamination of proton dissociative production of $\psi(2S)$ is the same as that of the J/ψ.

It is known that the DIPSI MC does not fully describe the $M_{e^+e^-}$ spectrum due to the absence in it of the radiative corrections (see Section 7.2.2). However, in this Section we calculate the ratio of acceptances. This effect should cancel out in the ratio (see Equations (8.5) and (8.6)).

The acceptance and the fraction of events for the two decay modes in bins of W are shown in Table 8.4. The total amount of contamination depends on W and ranges between $2-3\%$. The decay $\psi(2S) \rightarrow J/\psi\pi^0\pi^0$ has largest acceptance in the middle W range since in this case the $\psi(2S)$ is produced at rest and, therefore, the products of its decay have the least energy. The acceptance drops as the longitudinal boost increases toward lower and higher values of W. Regarding the process $\psi(2S) \rightarrow e^+e^-$ the acceptance behaves in the reverse way. In the central bins in W, where the resolution of the reconstructed $M_{e^+e^-}$ is best ($\approx 30-40$ MeV), the upper bound of the mass window is $3.5 < M_{\psi(2S)}$. In this region, the contamination from this process in negligible. At low and high W the mass resolution degrades and the upper bound of the mass window

is increased to 3.7 GeV, so the acceptance is maximum in this kinematic region.

A similar discussion is applicable to the study of the contamination in bins of W and P_t^2. The acceptance and the fraction of events for the two processes in bins of W and P_t^2 are shown in Table 8.5.

Finally, the number of events subtracted coming from the contamination of the decay of $\psi(2S)$ is determined in each bin in the analysis:

$$N^i_{\psi(2S)} = N^i_{J/\psi}(\mathcal{F}^i_{\psi(2S)\to J/\psi\pi_0\pi_0} + \mathcal{F}^i_{\psi(2S)\to e^+e^-}) \tag{8.7}$$

where $N^i_{\psi(2S)}$ is the number of events from the contamination of the decay of $\psi(2S)$ in a given bin, $N^i_{J/\psi}$ is the total amount of resonant J/ψ events observed in the mass window [4] in a given bin and $\mathcal{F}^i_{\psi(2S)\to J/\psi\pi_0\pi_0}$, $\mathcal{F}^i_{\psi(2S)\to e^+e^-}$ are the corresponding fractions as listed in Tables 8.4-8.5.

The contribution to the total amount of background subtracted from the observed number of J/ψ events is given in Table 8.6 as a function of W, calculated with Expression (8.7). The contribution of the contamination from decays of $\psi(2S)$ accounts for $5-15\%$ of the total background depending on W.

8.1.3 Contribution from Electroproduction of J/ψ

Some marginal contamination in the analysis the J/ψ is expected to come from the process $ep \to eJ/\psi p$, $Q^2 > 1\,\text{GeV}$. Events with three electromagnetic objects are thrown out. In low Q^2 events, the scattered electron can hit the hadronic sections of the RCAL. This type of events will be thrown out by the elasticity requirement. The maximum accessible Q^2, Q^2_{max}, such that $Q^2 < Q^2_{max}$ is determined by the geometry of the RCAL and the Z component of the vertex. The distance from the nominal Interaction Point to the rear end of the RCAL is $d = 250\,\text{cm}$. The dimensions of the beam hole of the RCAL are approximately 2b×2b, where b = 5 cm. In the

[4] $N^i_{J/\psi}$ is equal to the total of observed J/ψ candidates minus background contributions except for the contamination from $\psi(2S)$ decays.

approximation $Q^2 \ll 4E_e^2W^2$ and neglecting the shift of the vertex in the transverse plane to the beam axis:

$$Q^2_{max} \approx E_e^2\left(1-\frac{W^2}{s}\right)\left(\frac{b}{d+Z_{vertex}}\right)^2 \tag{8.8}$$

The value Q^2_{max} grows as the Z_{vertex} moves to negative values towards the RCAL. The largest value of $Q^2_{max} \approx 0.5\ \text{GeV}^2$ is reached when $W = 20$ GeV and $Z_{vertex} = -50$ cm. Therefore, due to the geometry of the RCAL it is not expected to have a significant contamination coming from the electroproduction of J/ψ.

However, the finding efficiency of electrons falling in the edges of the acceptance of the RCAL, or in the HAC sections of the RCAL is not expected to be exactly 100%. Some marginal contribution from events in which the scattered electron falls in these areas is possible.

A sample of events from $ep \to eJ/\psi p$ with $1 < Q^2 < 1000\,\text{GeV}^2$ was generated with the ZEUSVM MC. The number of events from this process expected to contribute to the J/ψ signal in the photoproduction analysis is shown in Table 8.6 in bins of W.

8.2 Non-Resonant Background

8.2.1 QED Background

Two are the QED processes that contribute to the non-resonant background: the Bethe-Heitler process, mediated by photon-photon fusion, dominates the background at $50 < W < 230$ GeV and QED Compton with initial state radiation (ISR) that dominates the background at $W > 250$ GeV. The Bethe-Heitler process produces two tracks of opposite sign and the reconstructed $M_{e^+e^-}$ falls exponentially. The cross-section of this process falls with W faster than the production of J/ψ. Therefore, the ratio of signal to background improves as W grows till the QED Compton process switches in. The production rate of a $e\gamma$ pair via QED Compton with an invariant mass greater than $M_{e\gamma} > 2$ GeV is an order of magnitude larger than the rate of production

of resonant J/ψ. To suppress undesirable migration effects of the QED Compton peak into the search window, it was decided to limit the search for J/ψ to $W = 290$ GeV. In this energy range the effect of migration is small and the background is dominated by QED Compton with ISR, which has a smaller cross-section.

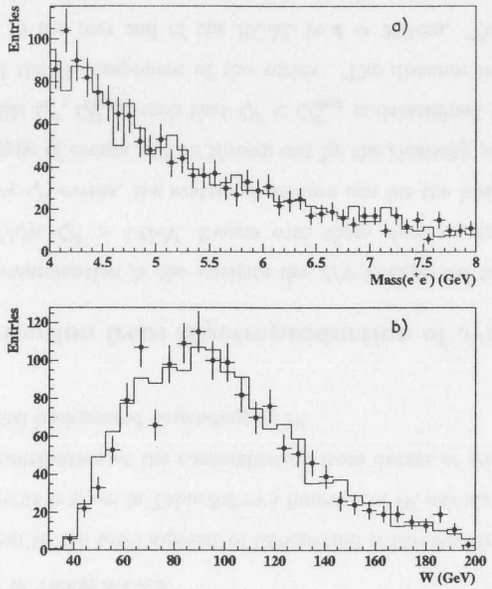

Figure 8.7: The LPAIR MC is normalized to data in the region $4 < M_{e^+e^-} < 8$ GeV in the range $50 < W < 200$ GeV with two track events only. The mass distribution is shown in a). The W distribution for events with $4 < M_{e^+e^-} < 8$ GeV is shown in b).

The Bethe-Heitler process is simulated by the LPAIR MC and QED Compton with ISR by the COMPTON MC. Both MC generate the elastic process and they are not used to generate proton dissociative events. In order to determine the normalization of the QED process following method is used [5]. The normalization factor is obtained

[5]It is assumed that the W and $M_{e^+e^-}$ distributions of events coming from proton dissociation is similar to those of the elastic process.

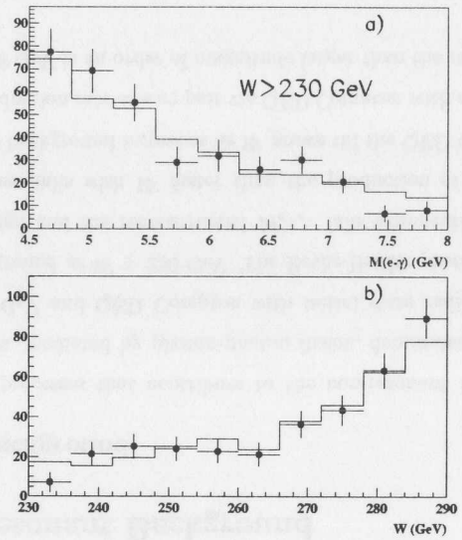

Figure 8.8: The COMPTON MC is normalized to data in the region $4.5 < M_{e^+e^-} < 8$ GeV in the range $W > 230$ GeV. The mass distribution is shown in Plot a). The W distribution for events with $4.5 < M_{e^+e^-} < 8$ GeV is shown in Plot b).

by normalizing MC to data in a region of $M_{e^+e^-}$ (or $M_{e\gamma}$) where we do not expect any resonances. Figure 8.7 a) shows the $M_{e^+e^-}$ distribution of events with two tracks in the range $4 < M_{e^+e^-} < 8$ GeV and $50 < W < 200$ GeV. The LPAIR MC is normalized to the number of events in data in this region. This normalization factor is used in Figure 8.7 b) to compare the W distributions of the LPAIR MC and data. The error on the normalization is dominated by systematic errors (shifting the mass window by ± 0.25 GeV) and amounts to a 5% relative error. The distribution from the LPAIR MC is then extrapolated to lower $M_{e^+e^-}$. The fraction of events from the Bethe-Heitler process in the mass window of the J/ψ goes from 25% at $W = 30$ GeV down to 6% at $W = 275$ GeV.

We proceed similarly with the COMPTON MC. Events with $W > 230$ GeV and

$4.5 < M_{e\gamma} < 8$ GeV [6] are used to normalize the MC. After subtracting the contribution from the Bethe-Heitler process the COMPTON MC is normalized to the number of events in data in this region. The $M_{e\gamma}$ distribution is shown in Figure 8.8 a). The W distribution is shown in Figure 8.8 b). The error on the normalization of the COMPTON MC is dominated by statistics resulting into a 5% relative error. The COMPTON MC is extrapolated to lower $M_{e\gamma}$. The fraction of events from QED Compton process in the mass window search of the J/ψ goes from 3% at $W = 200$ GeV up to 60% at $W = 275$ GeV.

8.2.2 Remaining Background

The remaining background is considerable at $W < 50$ GeV in two track configurations. The remaining background is expected to be dominated by $\pi^+\pi^-$ coming from the break up of the proton. It is observed that the remaining background decreases as W grows. The fraction of pionic background is expected to be small in one track configurations since we require the presence of at least one electromagnetic cluster of a minimum energy (see Section 6.4).

No MC is used to simulate the remaining background. The remaining background is subtracted by means of fits to the form of a single exponential (see Section 9.1). The functional form for the remaining background may be determined with data itself. A sample of events with two quality tracks of equal charge is selected. The determination of the charge of the track is well known for quality tracks for the transverse momentum typical in this analysis. It is not expected to have a contribution from decays of the J/ψ in which the charge of one the tracks has been poorly measured. The W distribution of such a sample is shown in Figure 8.9 a). The $M_{e^+e^-}$ distribution of this type of events is shown for events with $W < 50$ GeV in Figure 8.9 b) and with $W > 50$ GeV in Figure 8.9 c). Fits to the $M_{e^+e^-}$ distributions are performed in both ranges in W to

[6] The lower bound is set to avoid contamination from J/ψ.

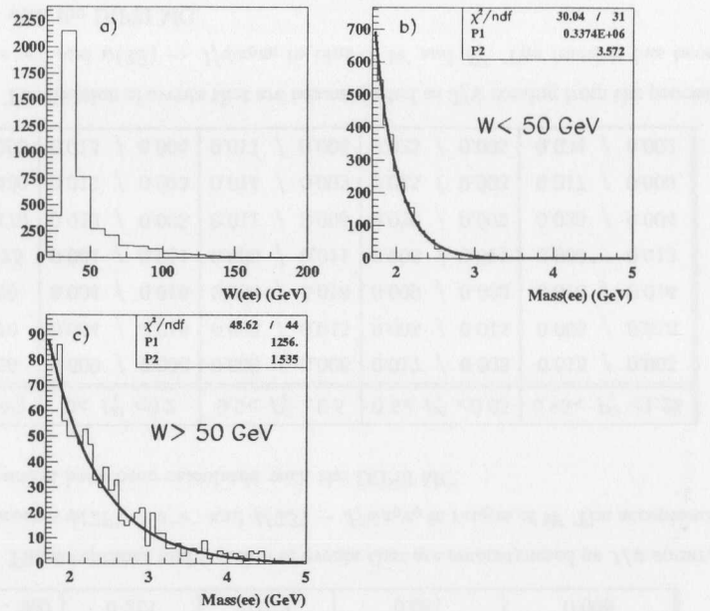

Figure 8.9: The shape of the $M_{e^+e^-}$ spectrum of the remaining background is investigated with a sample of events with tracks of equal charge. In Plot a) the W distribution of these events is shown. In Plot b) (events with $W < 50$) and Plot c) (events with $W > 50$) the reconstructed $M_{e^+e^-}$ spectra are fitted to an exponential function. The results of the fits are given in the boxes on the upper right corner.

an exponential function. The fits yield $\chi^2/n.d.f. \approx 1$ [7].

[7] $n.d.f.$ stands for number of degrees of freedom.

W (GeV)	-t (GeV^2)	N_{signal}	$N^{p.d.}_{W,P_t^2}$	$N^{p.d.\ +}_{W,P_t^2}$	$N^{p.d.\ -}_{W,P_t^2}$
20 - 50	0.00 - 0.20	1154	79.4	120.8	23.2
	0.20 - 0.50	842	66.8	99.3	30.2
	0.50 - 0.85	405	52.6	75.4	40.3
	0.85 - 1.25	154	40.2	52.3	32.7
50 - 70	0.00 - 0.20	1649	93.5	141.9	27.4
	0.20 - 0.50	876	78.6	116.7	35.7
	0.50 - 0.85	389	61.9	88.6	47.7
	0.85 - 1.25	160	47.3	61.3	38.8
70 - 90	0.00 - 0.20	1271	73.3	111.2	21.5
	0.20 - 0.50	651	61.6	91.4	28.1
	0.50 - 0.85	242	48.5	69.4	37.5
	0.85 - 1.25	146	37.1	48.0	30.5
90 - 125	0.00 - 0.20	1882	105.9	160.6	31.3
	0.20 - 0.50	903	89.1	131.9	40.7
	0.50 - 0.85	336	70.2	100.2	54.5
	0.85 - 1.25	147	53.6	69.2	44.4
125 - 170	0.00 - 0.20	1692	97.8	148.2	28.9
	0.20 - 0.50	877	82.2	121.7	37.7
	0.50 - 0.85	428	64.8	92.4	50.4
	0.85 - 1.25	154	49.5	63.8	41.1
170 - 230	0.00 - 0.20	927	63.5	96.2	18.8
	0.20 - 0.50	592	53.4	79.1	24.4
	0.50 - 0.85	300	42.1	60.0	32.7
	0.85 - 1.25	110	32.1	41.5	26.6
230 - 290	0.00 - 0.20	777	45.6	69.2	13.4
	0.20 - 0.50	407	38.3	56.9	17.4
	0.50 - 0.85	171	30.2	43.2	23.2
	0.85 - 1.25	116	23.0	29.9	18.9

Table 8.3: The number of J/ψ signal events, N_{signal}, compared to expected number of dissociative events, $N^{p.d.}_{W,P_t^2}$. $N^{p.d.\ +}_{W,P_t^2}$ and $N^{p.d.\ -}_{W,P_t^2}$ are the upper and lower total deviations.

W (GeV)	$\mathcal{A}_{\psi(2S)\to e^+e^-}$	$\mathcal{F}_{\psi(2S)\to e^+e^-}$	$\mathcal{A}_{\psi(2S)\to J/\psi\pi_0\pi_0}$	$\mathcal{F}_{\psi(2S)\to J/\psi\pi_0\pi_0}$
20 - 35	0.073	0.017	0.013	0.004
35 - 50	0.212	0.016	0.120	0.011
50 - 60	0.086	0.004	0.223	0.014
60 - 70	0.104	0.006	0.295	0.019
70 - 80	0.114	0.006	0.261	0.018
80 - 90	0.112	0.006	0.315	0.021
90 - 110	0.095	0.005	0.193	0.012
110 - 125	0.088	0.005	0.157	0.010
125 - 140	0.109	0.006	0.076	0.005
140 - 170	0.311	0.019	0.064	0.005
170 - 200	0.203	0.017	0.027	0.003
200 - 230	0.203	0.018	0.027	0.003
230 - 260	0.173	0.014	0.028	0.003
260 - 290	0.213	0.019	0.051	0.006

Table 8.4: The acceptance and fraction of events that are reconstructed as J/ψ coming from the process $\psi(2S) \to e^+e^-$ and $\psi(2S) \to J/\psi\pi_0\pi_0$ in ranges of W. The acceptance and the fraction have been calculated with the DIPSI MC.

W(GeV)	$0< P_t^2 <0.2$	$0.2< P_t^2 <0.5$	$0.5< P_t^2 <0.85$	$0.85< P_t^2 <1.25$
20 - 50	0.009 / 0.008	0.009 / 0.006	0.017 / 0.005	0.015 / 0.005
50 - 70	0.004 / 0.016	0.005 / 0.015	0.005 / 0.015	0.006 / 0.010
70 - 90	0.004 / 0.019	0.006 / 0.018	0.009 / 0.023	0.010 / 0.016
90 - 125	0.004 / 0.011	0.005 / 0.011	0.006 / 0.011	0.008 / 0.013
125 - 170	0.013 / 0.005	0.011 / 0.005	0.020 / 0.005	0.025 / 0.004
170 - 230	0.012 / 0.003	0.014 / 0.003	0.025 / 0.003	0.017 / 0.000
230 - 290	0.013 / 0.004	0.011 / 0.004	0.025 / 0.005	0.034 / 0.002

Table 8.5: The fraction of events that are reconstructed as J/ψ coming from the process $\psi(2S) \to e^+e^-$ and $\psi(2S) \to J/\psi\pi_0\pi_0$ in bins of W and P_t^2. The fraction has been calculated with the DIPSI MC.

W (GeV)	N_{BH}	N_{Comp}	N_r	$N_{\psi(2S)}$	N_{DIS}
20 - 35	163.0	0.0	53.5	15.7	0.0
35 - 50	430.9	0.0	450.0	49.3	1.1
50 - 60	281.6	0.0	90.6	29.7	0.8
60 - 70	258.7	0.0	148.9	35.1	1.5
70 - 80	243.2	0.0	83.2	29.7	0.3
80 - 90	189.0	0.0	116.3	30.3	0.3
90 - 110	327.5	0.0	117.9	35.5	0.8
110 - 125	179.3	0.0	56.2	20.6	0.1
125 - 140	176.7	0.6	43.5	13.8	0.3
140 - 170	298.7	24.1	70.2	45.8	0.4
170 - 200	149.7	56.8	5.1	23.3	0.6
200 - 230	119.5	135.4	6.2	19.0	0.1
230 - 260	93.7	297.6	51.1	12.9	0.0
260 - 290	42.1	576.6	166.1	17.6	0.0

Table 8.6: The different contributions to the background in bins of W in the analysis of the J/ψ. N_{BH} corresponds to the expected number of events from Bethe-Heitler process, N_{Comp} from the QED Compton process, N_r from the remaining background, $N_{\psi(2S)}$ from the contamination of decays of $\psi(2S)$ and N_{DIS} from the contribution the electroproduction of J/ψ.

Chapter 9

Elastic Photoproduction of J/ψ

The extension of the W range of the measurement of the elastic production of J/ψ is a central motivation behind this thesis work. The results of this work have been reported in [136, 137].

9.1 Extraction of the Resonant Signal

The procedure for the extraction of the signal in bins of W consists of several steps:

1. Subtract the number of events in the range $2 < M_{e^+e^-} < 5$ GeV for the Bethe-Heitler and QED Compton backgrounds.

2. Remove the remaining background via fits in the range $2 < M_{e^+e^-} < 5$ GeV. Two types of fits are performed:

   - Nominal fit:

   $$F^{e^+e^-} = A_{J/\psi} MC + A_r e^{-b_r M_{e^+e^-}} \tag{9.1}$$

   where MC is the $M_{e^+e^-}$ distribution, as predicted by MC, and $A_{J/\psi}, A_r, b_r$ are free parameters. The remaining background is treated with a single exponential (second term).

- A parameterization of the shape of the $M_{e^+e^-}$ spectrum is used:

$$F^{e^+e^-} = A_{J/\psi}((1 - A_{tail})G + A_{tail}B) + A_r e^{-b_r M_{e^+e^-}} \quad (9.2)$$

where $A_{J/\psi}$ corresponds to the normalization of the resonance signal, A_{tail} stands for the fraction of events that radiate, G is a Gaussian distribution for the mass, $M_{e^+e^-}$, with mean M and width σ_M, B is a function that parameterizes the bremsstrahlung tail:

$$B(M_{e^+e^-}, M, \sigma_M) = A \int_0^{M-\Delta} \frac{1}{M-x} G(M_{e^+e^-}, x, \sigma_M) dx \quad (9.3)$$

where A=$\ln \frac{M}{\Delta}$ is a normalization factor, and Δ is a cutoff parameter to be extracted from MC and is fixed to $\Delta = 0.05\,\text{GeV}$ [138]. In summary, the parameters $A_{J/\psi}, A_{tail}, M, \sigma_M, A_r, b_r$ are set to be free in the fits.

3. After obtaining A_r, b_r from the fits the number of resonant signal events are extracted in the mass window:

$$N^W_{signal} = N^W_{obs} - N^W_{QED} - N^W_r - N^W_{\psi(2S)} \quad (9.4)$$

where N^W_{obs} is the total number of candidates in the mass window, N^W_{QED} is the number of events predicted by the LPAIR MC and the COMPTON MC, N^W_r is the number of events from remaining background as calculated by the fits, $N^W_{\psi(2S)}$ is the number of events expected from the contamination of $\psi(2S)$ and N^W_{signal} is the number of resonant signal that will be fed into the calculation of the cross-section.

The same procedure is followed to extract the resonant signal in bins of the helicity angles.

When the resonant signal is extracted in W and P_t^2 bins the non-resonant background is subtracted by fits only; no MC is used to subtract the QED background. The procedure of extraction of signal starts with step 2. The number of signal events in a bin of W and P_t^2, $N^{W,P_t^2}_{signal}$, is defined as:

$$N^{W,P_t^2}_{signal} = N^{W,P_t^2}_{obs} - N^{W,P_t^2}_r - N^{W,P_t^2}_{\psi(2S)} \quad (9.5)$$

The error on the estimation of the normalization of the remaining background, δN_r, is extracted from the fits and is typically $\delta N_r \approx 0.1 N_r$. The statistical error on the estimation of the resonant signal is defined as:

$$\delta N_{signal} = \sqrt{N_{obs}} \oplus \delta N_r \quad (9.6)$$

The $M_{e^+e^-}$ distributions used for the extraction of the J/ψ resonant signal are presented in Section 9.1.1.

The error on the estimation of the non-resonant QED background is taken into account in the systematic error (see Section 8.2.1). Details on the systematic checks of the fitting procedure may be found in Section F.1. The stability check of the extraction of the signal with the definition of the elasticity requirement is presented in Section F.2.

9.1.1 $M_{e^+e^-}$ Spectra

The contribution of non-resonant QED background in ranges of W is shown in Figures 9.1 and 9.2. The nominal fits performed in step 2 of the procedure are shown in Figures 9.3 and 9.4. The values of the obtained parameters and the χ^2 of the fits are given in the top right corners of the plots. The comparison of data after subtraction of non-resonant background with the ZEUSVM MC is given in Figures 9.5 and 9.6.

A seen in Figures 7.14 a), 8.8 b) and in the last Plot of Figure 9.4, at $W > 260\,\text{GeV}$ and $2 < M_{e^+e^-} < 3\,\text{GeV}$ the non-resonant background is not saturated by the extrapolation of COMPTON MC. The QED Compton cross-section at $W > 290\,\text{GeV}$ is more than one order of magnitude greater than the cross-section of the J/ψ. A small error in the simulation of migration effects by MC may result into sizeable effects. The stability of the cross-section at high W in checked in Section F.3.

The $M_{e^+e^-}$ distributions in bins of W and P_t^2 are shown in Figures 9.7 and 9.8. The fits performed of the $M_{e^+e^-}$ spectra are shown. The values of the obtained parameters and the χ^2 of the fits are given in the top right corners of the Plots. The comparison of data after subtraction of non-resonant background with the ZEUSVM MC is given

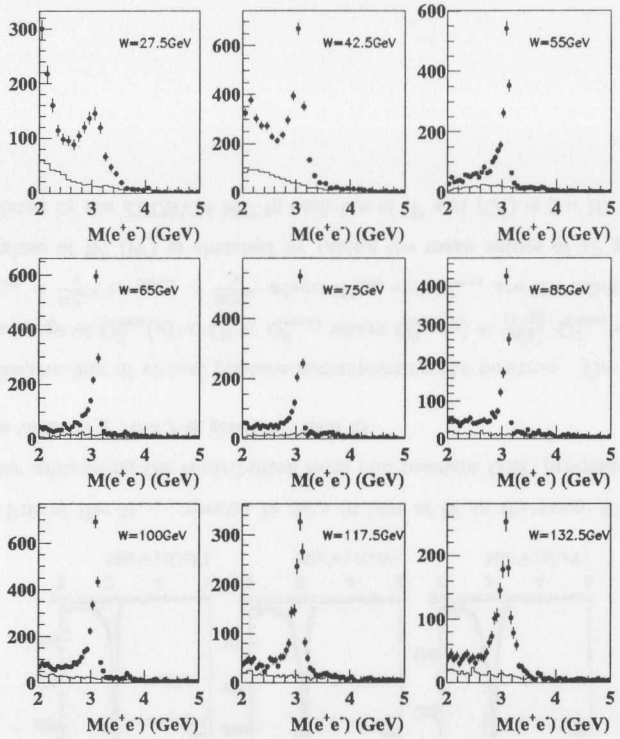

Figure 9.1: The $M_{e^+e^-}$ spectra in data in bins of W in the range $20 < W < 140$ GeV. The solid line corresponds to the contribution from QED processes (Bethe Heitler and QED Compton).

in Figures 9.9 and 9.10.

The $M_{e^+e^-}$ distributions after non-resonant background subtraction in bins of $\cos(\theta_h)$ and ϕ_h are shown in Figures 9.11 and 9.12, respectively.

Overall, the MC describes satisfactorily the $M_{e^+e^-}$ distributions observed in data.

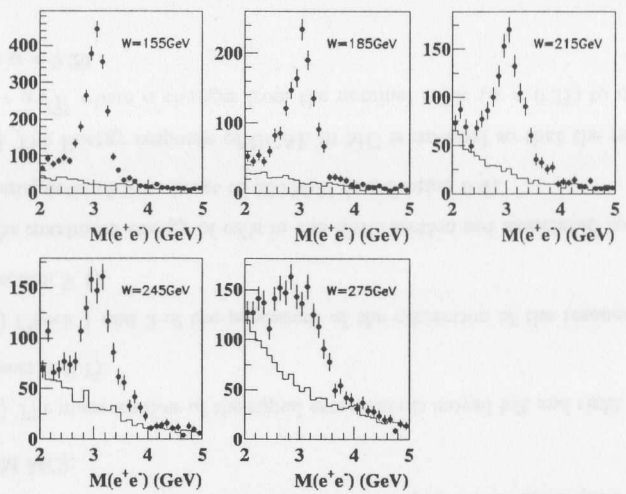

Figure 9.2: Same as Figure 9.1 for range $140 < W < 290$ GeV.

9.2 Procedure of Obtaining Cross-Sections

The ep cross-section for exclusive J/ψ meson photoproduction is determined using the Expression:

$$\sigma_{ep\to eJ/\psi p} = \frac{N_{signal}(1-f)}{\mathcal{A}\mathcal{B}\mathcal{L}} \tag{9.7}$$

where N_{signal} is the number of signal events in each range of W, f accounts for the fraction of events in the sample coming from proton dissociative events (see Section 8.1.1), $\mathcal{A}$ is acceptance, $\mathcal{B} = (5.93 \pm 0.1)\%$ is the branching ratio of $J/\psi \to e^+e^-$ [139] and $\mathcal{L}$ is the luminosity. The photoproduction cross-sections were determined by dividing the electroproduction cross-sections by the photon flux, calculated according to [140]:

$$\sigma_{\gamma p\to J/\psi p}(\langle W\rangle, \langle Q^2\rangle) = \frac{\int \Phi(y,Q^2)\sigma_{\gamma p\to J/\psi p}dydQ^2}{\int \Phi(y,Q^2)dydQ^2} = \frac{\sigma_{ep\to J/\psi p}}{\Phi_T} \tag{9.8}$$

with

$$\Phi(y,Q^2) = \frac{\alpha}{2\pi Q^2}\left[\frac{1+(1-y)^2}{y} - \frac{2(1-y)}{y}\left(\frac{Q^2_{min}}{Q^2} - \frac{Q^2}{M^2_{J/\psi}}\right)\right]\left(1+\frac{Q^2}{M^2_{J/\psi}}\right)^{-2} \tag{9.9}$$

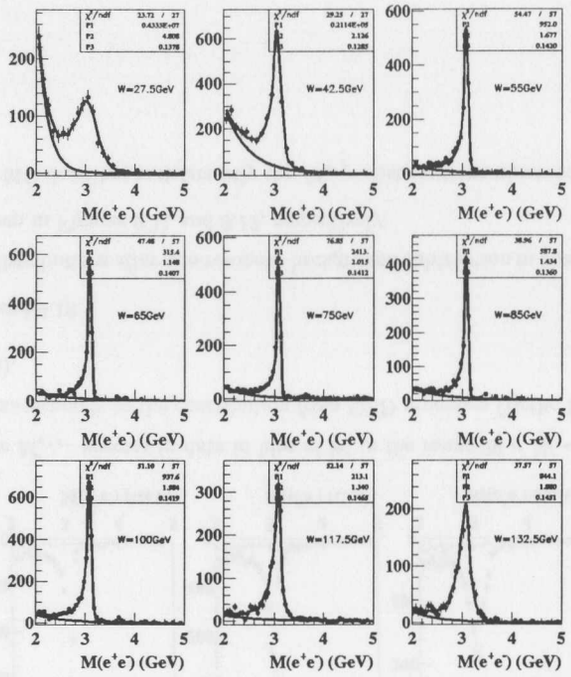

Figure 9.3: Fits of the $M_{e^+e^-}$ spectra in data in bins of W in the range $20 < W < 140$ GeV after subtracting the contribution from non-resonant QED processes. In the top right the value of $\chi^2/n.d.f$ is given for each fit.

Φ_T is the effective flux of virtual photons accompanying the positron. The integrals run over the range of $Q^2_{min}(y) < Q^2 < Q^2_{max}$, where $Q^2_{min}(y) = \frac{m_e^2 y^2}{(1-y)}$, $Q^2_{max} = 1\,\mathrm{GeV}^2$ and from $y_{min} = \frac{W^2_{min}}{s}$ to $y_{max} = \frac{W^2_{max}}{s}$ where W_{min} and W_{max} are the minimum and maximum values of W. $\langle W \rangle$ is obtained by taking the mean values of all generated events calculated by the ZEUSVM MC in each bin of W and $\langle Q^2 \rangle \approx 5 \times 10^{-5}\,\mathrm{GeV}^2$.

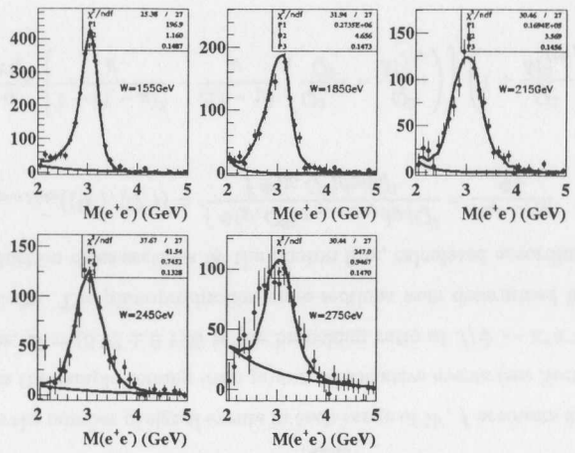

Figure 9.4: The same as in Figure 9.3 for the range $140 < W < 290$ GeV.

9.3 Systematic Uncertainties

A full systematic error analysis is performed on all the calculated cross-sections and parameters. Details of some of the relevant systematic and stability checks are reported in Sections F.1, F.2, F.3 and F.4. Below is the list of systematic checks (MC refers to the ZEUSVM MC):

{1}{2} The mass window of the signal extraction is moved left and right two bins (see Section F.1).

{3}{4} Check 1 and 2 of the procedure of the extraction of the resonant signal (see Section F.1).

{5} The maximum energy of cells in the EMC section not associated to the two electromagnetic objects is set to 300 MeV (see Section 6.4).

{6}{7} The Energy response of UCAL in MC is smeared so that the resolution $\sigma(E) = \alpha\sqrt{E}$ where α changes from the nominal value ($\alpha = 0.27$) to $\alpha = 0.25$ and to $\alpha = 0.29$.

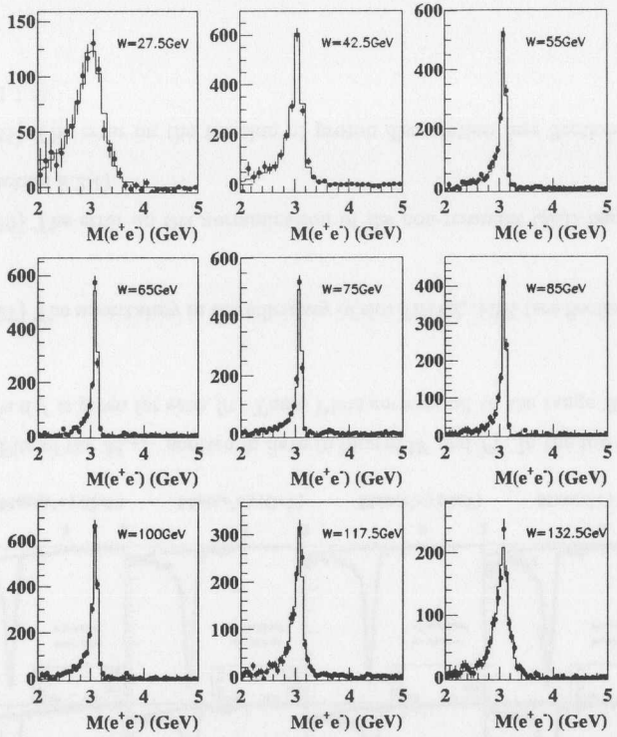

Figure 9.5: Signal in data after non-resonant background subtractions (QED processes plus remaining background) in bins of W in the range of $20 < W < 140$ GeV compared to ZEUSVM MC (solid line).

{8}{9} The position of the SRTD in MC is shifted in x by ± 3 mm (see Section C.2).

{10}{11} The position of the SRTD in MC is shifted in y by ± 3 mm (see Section C.2).

{12}{13} The cut on the energy of the electromagnetic object not associated to the track in one track events, $E_{nomatch}$, is changed in MC by $\mp 3\%$ (see Section A.1).

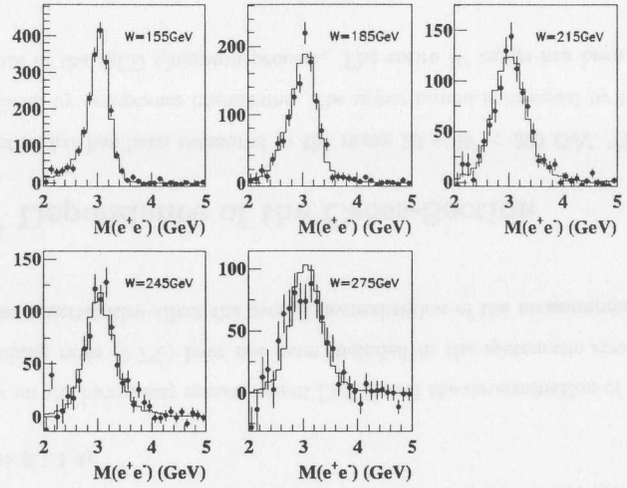

Figure 9.6: The same as in Figure 9.5 for the range $140 < W < 290$ GeV.

{14}{15} The cut on the energy of the electromagnetic clusters in zero track events is changed in MC by $\mp 3\%$ (see Section A.1).

{16}{17} The parameter α in the angular distribution $(1 + \alpha \cos^2 \theta_h)$ is changed by ∓ 0.05 and MC is reweighted (see Section 7.3.2).

{18}{19} The MC is reweighted according to $NWW_{true}^{\mp 0.05}$, where NW is the nominal weight and W_{true} is the true W (see Section 7.3.2).

{20}{21} The nominal t-slope in MC is changed by ∓ 0.2 GeV^{-2} (see Section 7.3.2).

{22}{23} The uncertainty in the tracking efficiency of slot FLT58, $\mp 1.5\%$ (see Section 5.4.1).

{24}{25} The uncertainty in the efficiency of the energy cut in slot FLT58 (see Section 5.4.1).

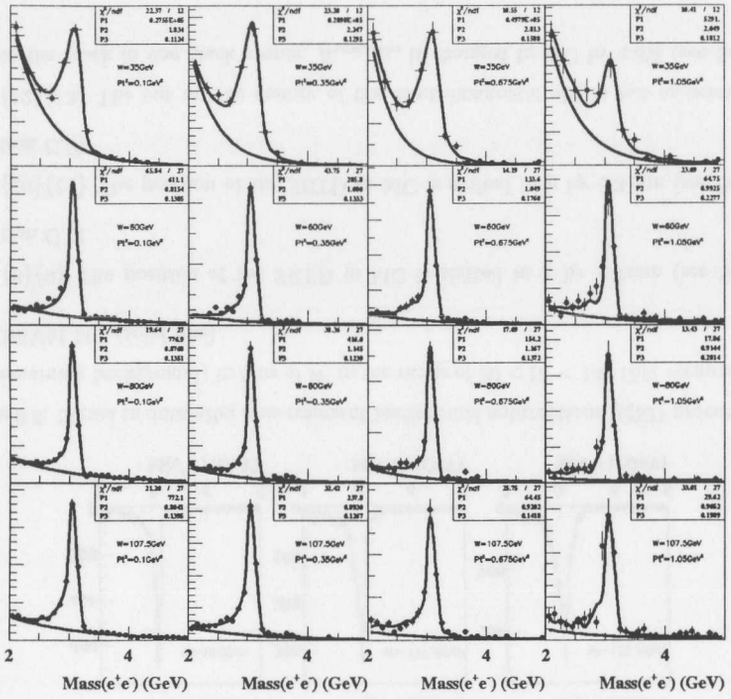

Figure 9.7: Fits of the $M_{e^+e^-}$ spectra in data in bins of W and P_t^2. In the top right the value of $\chi^2/n.d.f$ is given for each fit. These Plots correspond to the range $20 < W < 125$ GeV.

{26}{27} The uncertainty in the efficiency of slot FLT62, ±3% (see Section 5.4.2).

{28}{29} The error on the normalization of the non-resonant QED background (see Section 8.2.1).

{30}{31} The error on the fraction of proton dissociation (see Sections 8.1.1.4 and 8.1.1.5).

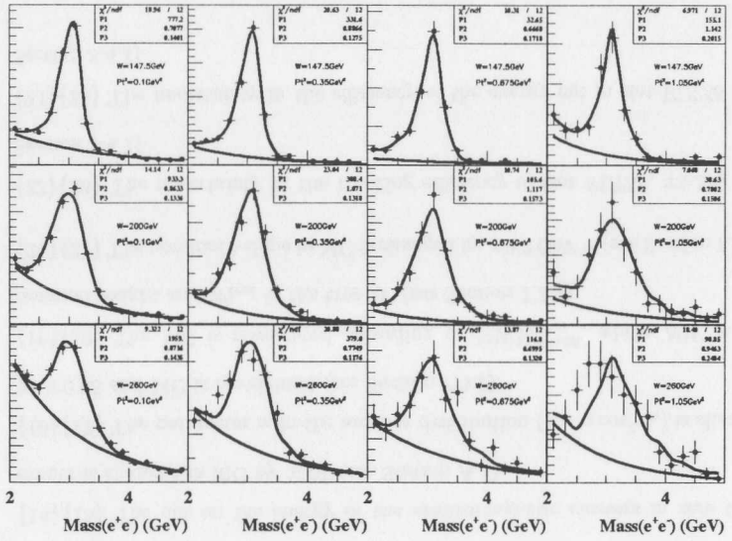

Figure 9.8: Same as in Figure 9.7 in the range $125 < W < 290$ GeV.

{32}{33} The error on the W dependence of the fraction of dissociation (see Section 8.1.1.4).

The error on the luminosity measurement (2.2%) and the determination of the electronic branching ratio (1.7%) have not been included in the systematic error uncertainty. These uncertainties affect the overall normalization of the measurement.

9.4 W Dependence of the Cross-Section

The resonant signal has been measured in the range $20 < W < 290$ GeV. The lower bound is defined by acceptance limitations. The upper bound is imposed by the overwhelming rate of the QED Compton process. The entire W range has been divided

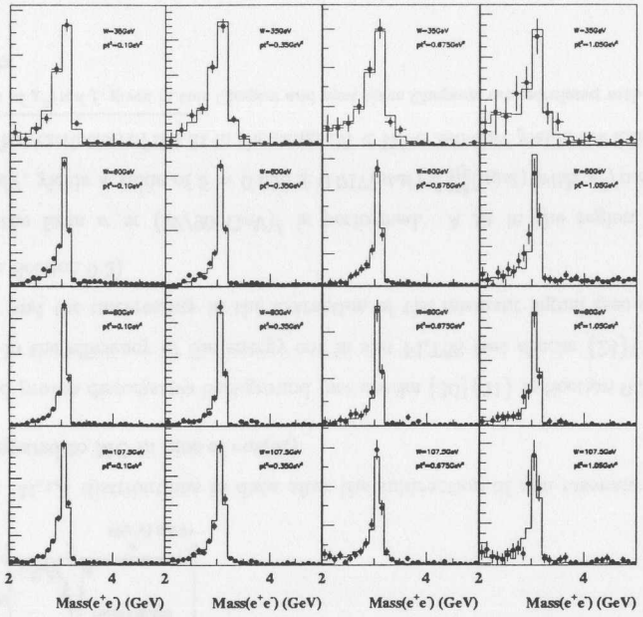

Figure 9.9: The $M_{e^+e^-}$ distributions in data in bins of W and P_t^2 after background subtraction in the range $20 < W < 125$ GeV. The solid lines correspond to the prediction of the ZEUSVM MC.

into 14 bins with a width depending on the resolution of the reconstruction of W. In each bin in W a mass window is been defined:

- In bins 3-9, $2.7 < M_{e^+e^-} < 3.5$ GeV. The lower bound is determined by the efficiency of the energy cut in slot FLT58 (see Section 5.4.1). The resolution of the CTD momentum in MC is some 15% worse than in data. To avoid this effect in the calculation of the acceptance the upper edge of the mass window is set to 3.5 GeV. The width of the bins in $M_{e^+e^-}$ is 50 MeV.

- In the rest of the bins $2.5 < M_{e^+e^-} < 3.7$ GeV, due to resolution. The width of the bins in $M_{e^+e^-}$ is 100 MeV.

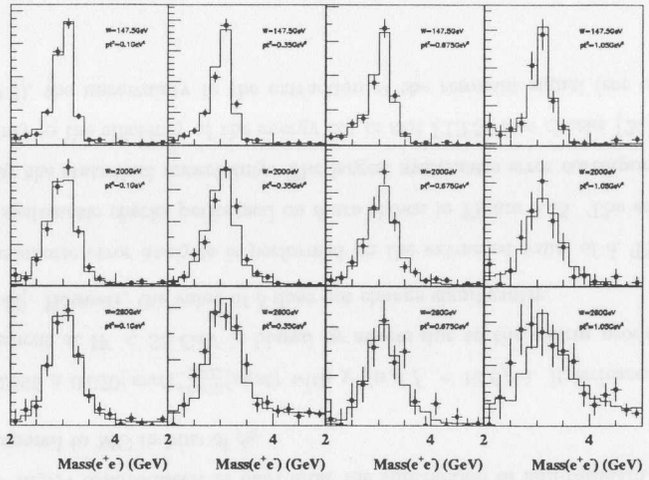

Figure 9.10: The same as in Figure 9.9 for the range $125 < W < 290$ GeV.

The corresponding values of signal events, acceptance and photon flux are given in Table 9.1.

In Figure 9.13 the results of this analysis are compared with ZEUS results obtained using the muonic decay channel with data taken during the 1996 and 1997 running periods [141, 126]. The results are also compared with measurements reported by the H1 Collaboration [142] and the experiment E401 [143]. The difference in the normalization between the results reported here and other measurements in Figure 9.13 is under discussion within the ZEUS Collaboration. Possible reasons for the discrepancy in the normalization may be due to the different treatment of the subtraction of the proton dissociative background and the definition of the electronic branching ratio. Nevertheless, the difference in the normalization of the cross-section does not affect the physics conclusions drawn in this work (see Chapter 12).

The results of the systematic error analysis on each value of $\sigma(\gamma p \rightarrow J/\psi\, p)$ are given in Figure 9.14. The dominant systematic errors are the uncertainty in the fraction

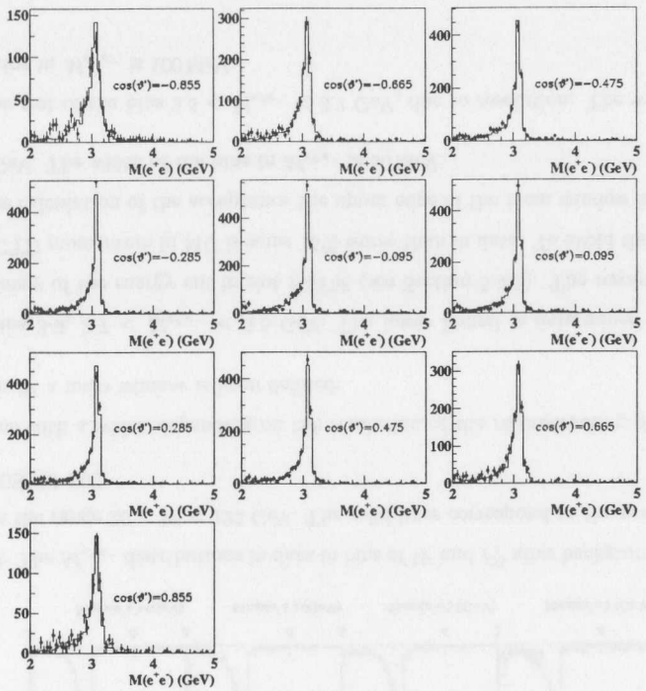

Figure 9.11: $M_{e^+e^-}$ distributions in data after the subtraction of non-resonant backgrounds compared to MC in bins of $\cos(\theta_h)$.

of subtracted proton dissociative background (see checks {30}{31} in Section 9.3), the uncertainty in the efficiency of the energy cut in slot FLT58 (see checks {24}{25} in Section 9.3) and the uncertainty in the extraction of the resonant signal (see checks $\{1\} - \{4\}$ in Section 9.3).

A fit of the form $\sigma \propto (W/90\ \text{GeV})^{\delta}$ is performed. A fit in the region $20 < W < 290$ GeV, yields a value of $\delta = 0.698 \pm 0.017(stat)^{+0.016}_{-0.019}(syst)$ with $\chi^2/n.d.f. = 13.6/12$ [1]. The restriction of the fit in the range $35 < W < 290$ GeV yields the following

[1]The values of $\chi^2/n.d.f.$ given in this Chapter and next three Chapters are calculated with statistical errors only.

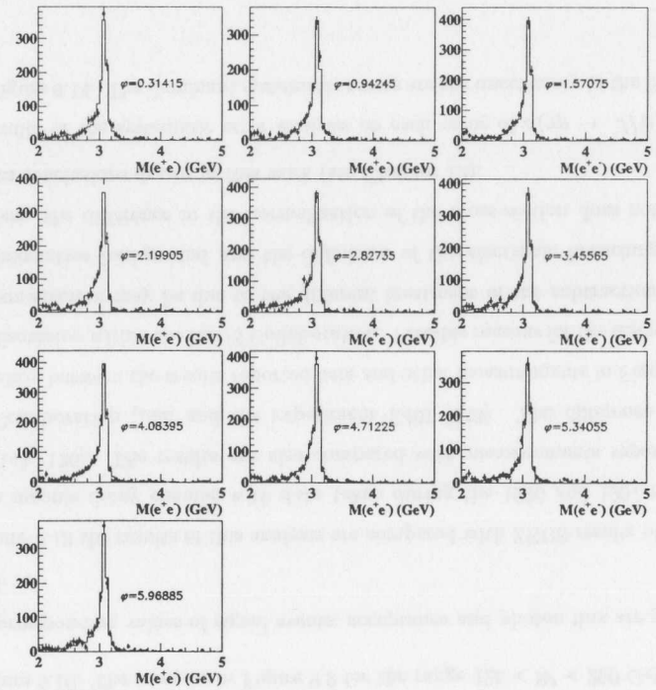

Figure 9.12: $M_{e^+e^-}$ distributions in data after the subtraction of non-resonant backgrounds compared to MC in bins of ϕ_h.

value $\delta = 0.695 \pm 0.020(stat)^{+0.025}_{-0.025}(syst)$ with $\chi^2/n.d.f. = 13.6/11$. It is feared that the measurement at $W < 35$ GeV is biased by effects due to the charm production threshold [144]. However, the value of δ does not change significantly.

A full systematic error analysis is performed on the extracted value of δ. The results of the systematic checks performed on δ are shown in Figure 9.15. The error is dominated by the statistical uncertainty. The largest systematic error corresponds to the uncertainty in the efficiency of the energy cut in slot FLT58 (see checks {24}{25} in Section 9.3), the uncertainty in the extraction of the resonant signal (see checks

W (GeV)	N_{obs}	N_{back}	$\mathcal{A}$	Φ	$\sigma(\gamma p \to J/\psi p)$ (nb)
20 - 35	982	232.3	0.087	0.06408	$36.7 \pm 1.6^{+2.4}_{-2.6}$
35 - 50	2681	931.3	0.270	0.03730	$47.7 \pm 2.0^{+3.2}_{-2.9}$
50 - 60	1978	402.8	0.386	0.01791	$62.4 \pm 1.9^{+3.9}_{-3.6}$
60 - 70	1821	444.2	0.383	0.01447	$68.2 \pm 2.4^{+4.5}_{-4.2}$
70 - 80	1577	356.3	0.371	0.01200	$75.2 \pm 2.6^{+5.0}_{-4.9}$
80 - 90	1420	335.9	0.373	0.01013	$78.6 \pm 3.0^{+5.4}_{-4.8}$
90 - 110	2499	481.8	0.382	0.01620	$89.4 \pm 2.4^{+5.4}_{-5.1}$
110 - 125	1604	256.1	0.371	0.00954	$104.4 \pm 3.3^{+6.1}_{-5.7}$
125 - 140	1470	234.9	0.378	0.00790	$113.4 \pm 3.7^{+6.7}_{-6.2}$
140 - 170	2303	439.2	0.334	0.01218	$125.4 \pm 3.4^{+8.5}_{-7.2}$
170 - 200	1362	235.5	0.250	0.00877	$140.8 \pm 4.9^{+9.0}_{-8.3}$
200 - 230	1161	280.2	0.243	0.00643	$154.6 \pm 6.3^{+9.7}_{-9.3}$
230 - 260	1208	455.4	0.280	0.00482	$153.0 \pm 7.6^{+16.4}_{-10.4}$
260 - 290	1490	802.4	0.248	0.00369	$206.7 \pm 13.6^{+16.2}_{-27.7}$

Table 9.1: The total cross-section of J/ψ in photoproduction for several ranges of W. N_{obs} is the total number of candidates, N_{back} is the number of non-resonant background plus the contamination of $\psi(2S)$ and electroproduction of J/ψ in the W range. $\mathcal{A}$ is the acceptance and Φ_T is the effective photon flux. The values of $\sigma(\gamma p \to J/\psi p)$ are given in nb with statistical and systematic errors.

$\{1\} - \{4\}$ in Section 9.3) and the uncertainty in the W dependence of the fraction of the proton dissociation background (see checks $\{32\}\{33\}$ in Section 9.3).

9.5 t Dependence of the Cross-Section

The t distribution is measured for $-t < 1.25$ GeV^2. The bound is imposed by the overwhelming resonant proton dissociative background and poor resolution and purity at large $|t|$. The analysis of the t dependence of the cross-section requires large statistics, since the rate of production of J/ψ falls exponentially with $|t|$. The bins in W defined

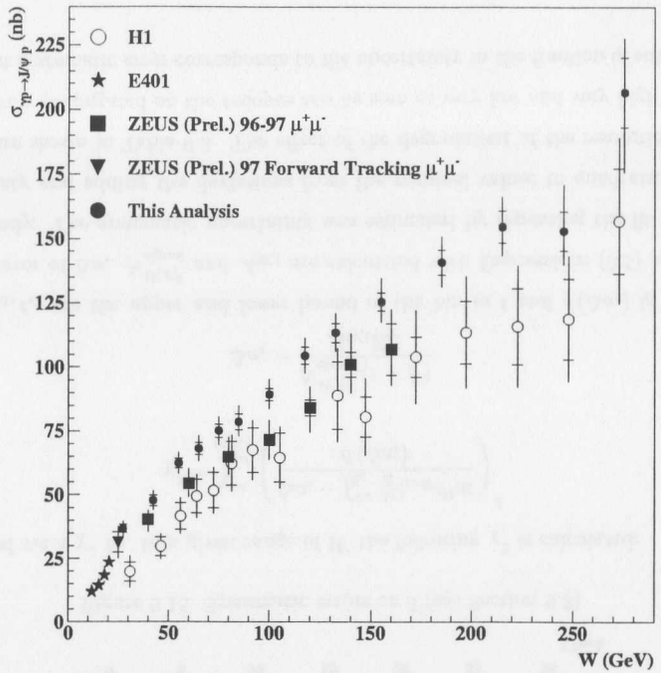

Figure 9.13: Comparison of $\sigma(\gamma p \to J/\psi p)$ obtained in this analysis with other measurements (see text).

in Section 9.4 have been merged in groups of two in order to increase statistics and provide for a stable result. The resulting 7 bins in W have been subdivided in four bins of t. The definition of t bins is the same for all 7 W bins. In each bin in W and t a mass window has been defined:

- First two bins in t and bins 2-4 in W, $2.7 < M_{e^+e^-} < 3.5$ GeV. The width of the bin in $M_{e^+e^-}$ is 100 MeV. In the last two bins in t in the same W range, $2.4 < M_{e^+e^-} < 3.6$ GeV, due to degradation of resolution. The width of the bin in $M_{e^+e^-}$ is 200 MeV.

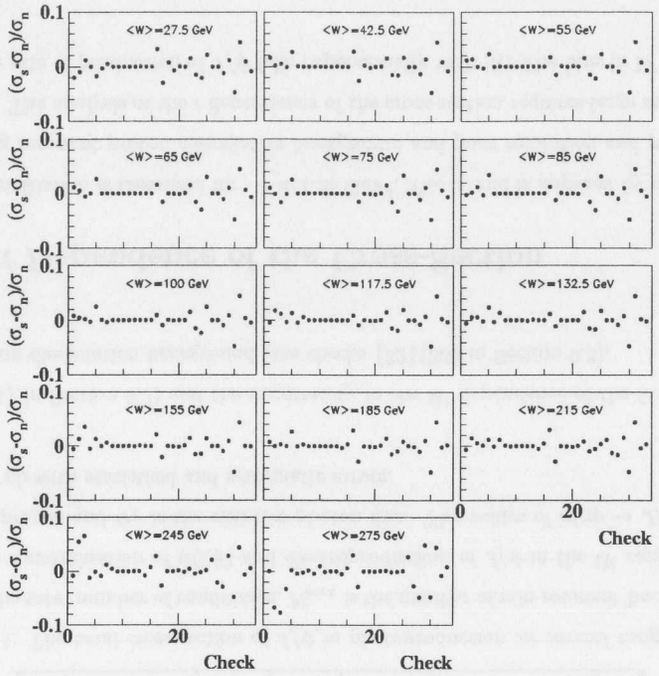

Figure 9.14: Systematic errors on $\sigma(\gamma p \to J/\psi p)$ (see Section 9.3).

- In the rest of the W range in the first two bins in t, $2.4 < M_{e^+e^-} < 3.5$ GeV and in the last two bins in t, $2.2 < M_{e^+e^-} < 4.4$ GeV due to the degradation of the resolution. The width of the bin in $M_{e^+e^-}$ is 200 MeV.

The results of $\mathrm{d}\sigma/\mathrm{dt}$ in bins of W and t are given in Table 9.2 [2].

The differential cross-section is parameterized as $\frac{d\sigma}{dt} = \frac{d\sigma}{dt}|_{t=0} e^{bt}$ for fixed W. The parameter b and the extrapolation of the differential distribution to $t = 0$, $\frac{d\sigma}{dt}|_{t=0}$, is

[2]The value of N_{signal} here has not been corrected yet for contamination from $\psi(2S)$ decays. This is taken into account in the calculation of the differential cross-section.

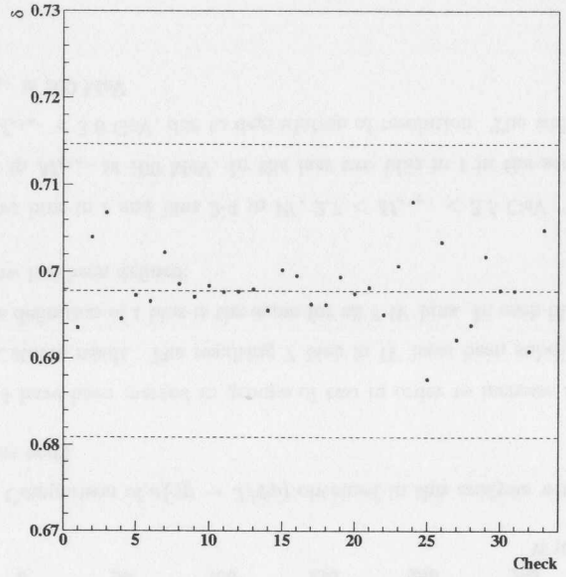

Figure 9.15: Systematic errors on δ (see Section 9.3).

extracted via a χ^2 fit. In a given range of W the following χ^2 is calculated:

$$\chi^2 = \sum_{i=1,4} \left(\frac{\Delta\sigma_i - \int_{t_{i1}}^{t_{i2}} \frac{d\sigma}{dt}|_{t=0} e^{bt} dt}{\delta(\Delta\sigma_i)} \right)^2 \tag{9.10}$$

and

$$\Delta\sigma_i = \frac{N_{signal}^{W,P_t^2}(1-F)}{\mathcal{A}_{W,t}\mathcal{B}\mathcal{L}} \tag{9.11}$$

where t_{i1}, t_{i2} are the upper and lower bound of the bin in t and $\delta(\Delta\sigma_i)$ is the statistical error of $\Delta\sigma_i$. N_{signal}^{W,P_t^2} and $\mathcal{A}_{W,t}$ are calculated with Expressions (9.5) and (7.5) respectively. The systematic uncertainty was estimated by repeating the fit for each uncertainty and adding the deviations from the nominal values in quadrature. The results are shown in Table 9.3. The effect of the degradation of the resolution in P_t^2 on the error propagated on the t-slopes can be seen at very low and very high W. The dominant systematic error corresponds to the uncertainty in the fraction of subtracted

proton dissociative background (see checks $\{30\} - \{33\}$ in Section 9.3).

Alternatively, a different method for the extraction of the t-slope is used:

1. Reweight MC to a given value of b according to a weight $e^{(b-b_{nom})t}$, where b_{nom} is the nominal parameter in the generation.

2. Calculate the likelihood probability N_{signal} in data and MC in the four bins in t in a given W range.

3. Repeat 1 and 2 till the likelihood is maximized.

This method does not require the calculation of the cross-section since MC is compared directly to the uncorrected P_t^2 distributions. In each range in W a parameter b is extracted. The results are shown in Table 9.4. The main systematic error remains the uncertainty on the determination of the proton dissociative background.

In Regge theory, we expect the $\gamma p \to Vp$ cross-section to be of the following form (see Equation (2.7)):

$$\frac{d\sigma}{dt} = Ae^{b_0 t}\left(\frac{W^2}{W_0^2}\right)^{2(\alpha(t)-1)} \tag{9.12}$$

where $\alpha(t)$ is the Regge trajectory and W_0 is chosen to be 90 GeV. It has been determined that the t dependence of the trajectory may be parameterized as:

$$\alpha(t) = \alpha_0 + \alpha' t \tag{9.13}$$

From Equation (9.12) it follows:

$$b = b_0 + 2\alpha' \ln \frac{W^2}{W_0^2} \tag{9.14}$$

The parameter α' may be extracted from the W dependence of the t-slopes that have been determined from the differential cross-sections. A χ^2 fit is performed on the t-slopes to the form given in Equation (9.14). Two parameters are set free, b_0 and α'. The result of the fit is $b_0 = 4.24 \pm 0.07(stat)^{+0.19}_{-0.11}(syst)$ and $\alpha' = 0.127 \pm$

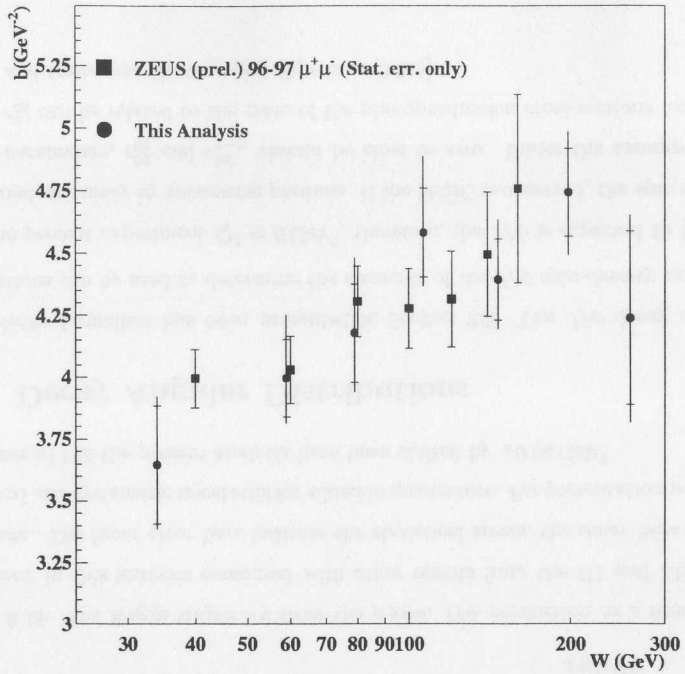

Figure 9.16: t-slopes are compared with ZEUS96-97 (Preliminary) $\mu^+\mu^-$ results.

$0.032(stat)^{+0.010}_{-0.023}(syst)$, with $\chi^2/n.d.f. = 5.3/5$. The systematic uncertainty was estimated by repeating the fit for each uncertainty and adding the deviations from the nominal value in quadrature. The dominant systematic error corresponds to the uncertainty in the fraction of subtracted proton dissociative background (see checks $\{30\} - \{33\}$ in Section 9.3).

The Regge trajectory may be determined by measuring the variation of the energy dependence of the elastic cross-section at fixed t, as shown in Equation (9.12) [145]. This method offers the advantage of being independent of the details of the subtraction of the proton dissociative background, since the latter may be considered to a good approximation constant with W. In Figure 9.17, the $d\sigma/dt$ data used in this determina-

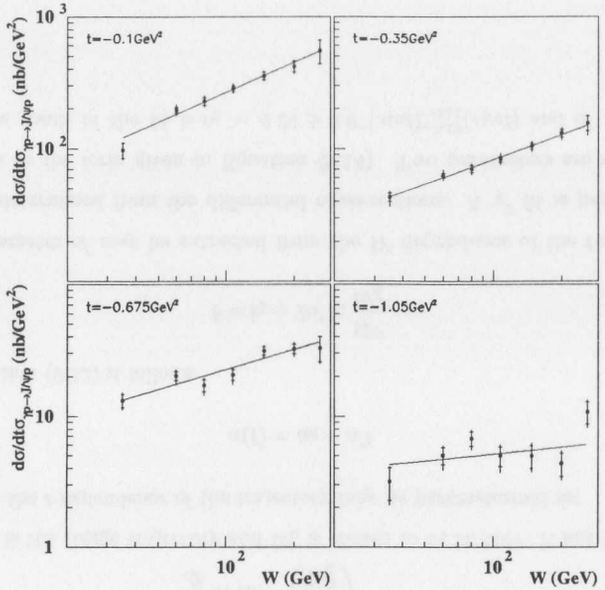

Figure 9.17: The differential cross-section $\frac{d\sigma}{dt}$ as a function of W at fixed t. The lines correspond to the results of fits of the form $d\sigma/dt \propto W^{2[2\alpha(t)-2]}$.

tion of $\alpha(t)$ are presented in t bins; the solid line in each t bin is the result of a fit of the form $d\sigma/dt \propto W^{2[2\alpha(t)-2]}$. The resulting values of $\alpha(t)$ are given in Table 9.5 and are illustrated in Figure 9.18 as a function of t. These values were fitted to the linear form given in Equation (9.13). The results of the fit are $\alpha(0) = 1.202 \pm 0.013(stat)^{+0.003}_{-0.012}(syst)$ and $\alpha' = 0.131 \pm 0.028(stat)^{+0.008}_{-0.019}(syst)\,\mathrm{GeV}^{-2}$ with $\chi^2/n.d.f. = 1.0/2$. The systematic uncertainty was estimated by repeating the fit for each uncertainty and adding the deviations from the nominal value in quadrature.

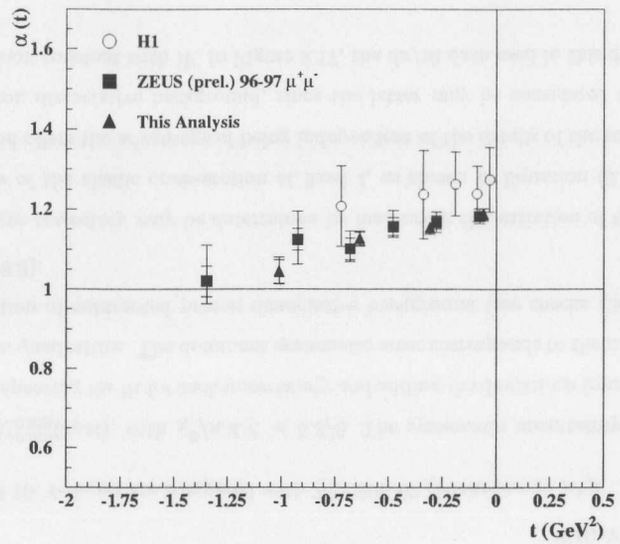

Figure 9.18: The Regge trajectory from the elastic J/ψ production as a function of t obtained in this analysis compared with other results from the H1 and ZEUS experiments. The inner error bars indicate the statistical errors, the outer bars are the statistical and systematic uncertainties added in quadrature. For presentation purposes the values of t of the present analysis have been shifted by $+0.04\,\mathrm{GeV}^2$.

9.6 Decay Angular Distributions

The helicity formalism has been presented in Section 2.5. The J/ψ decay angular distributions can be used to determine the elements of the J/ψ spin-density matrix.

In the present experiment $Q^2 \approx 0\,\mathrm{GeV}^2$, therefore, the J/ψ is expected to be produced predominantly by transverse photons. If the SCHC is observed, the spin density matrix parameters, r^{04}_{00} and r^{04}_{1-1}, should be close to zero. Under the assumption of SCHC, r^{04}_{00} can be related to the ratio of the photoproduction cross-sections for longitudinal and transverse photons (see Equation (2.21)).

The parameters r_{00}^{04} and r_{1-1}^{04} are extracted by means of one dimensional fits of the distributions of the helicity angles. The resonant signal is searched in bins of $\cos(\theta_h)$ and ϕ_h following the prescription explained in Section 9.1. Only events with two track topologies are used for the extraction of these parameters. The inclusion of other configurations would not increase significantly the sensitivity of our data to these parameters. No subtraction of the proton dissociative contribution is performed. It is assumed that the elastic and dissociative processes have the same angular dependence.

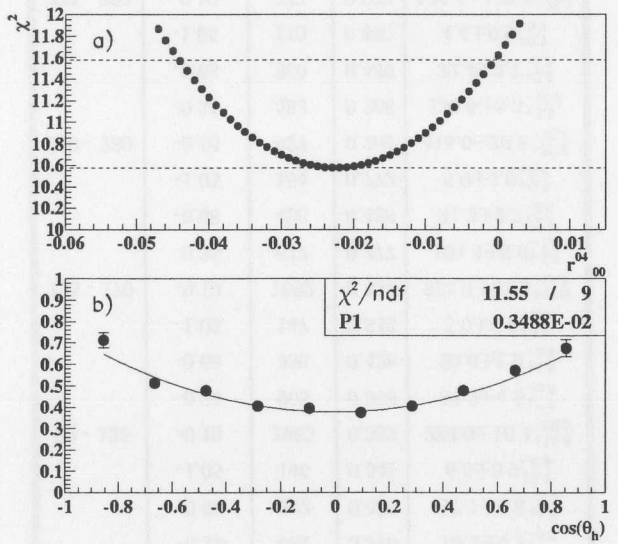

Figure 9.19: Plot a) shows the χ^2 of the distribution of N_{signal} in bins of $\cos(\theta_h)$ in data and MC after reweighting MC according to Equation (2.19) for different values of r_{00}^{04}. Plot b) shows the distribution of $\cos(\theta_h)$ in data corrected for acceptance fitted to the functional form given in Equation (2.19).

The parameters r_{00}^{04} and r_{1-1}^{04} are obtained using two methods:

1. Reweight MC according to Equation (2.19) and Equation (2.20) till the distribution of N_{signal} in bins of $\cos(\theta_h)$ and ϕ_h in data and MC agree best. The χ^2 of the distributions as a function of the parameters r_{00}^{04} and r_{1-1}^{04} are shown in Figure 9.19 a) and Figure 9.20 a), respectively.

2. χ^2 fits of the form of Equation (2.19) and Equation (2.20) are performed on data after correcting for acceptance. The fits are shown in Figure 9.19 b) and Figure 9.20 b).

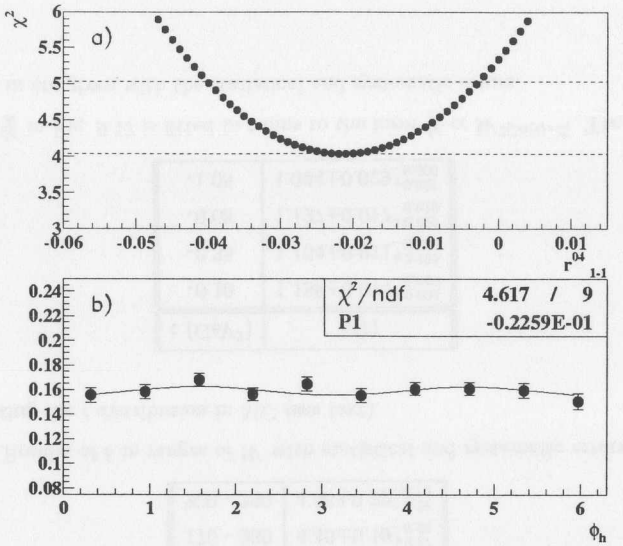

Figure 9.20: Plot a) shows the χ^2 of the distribution of N_{signal} in bins of ϕ_h in data and MC after reweighting MC according to Equation (2.20) for different values of r_{1-1}^{04}. Plot b) shows the distribution of ϕ_h in data corrected for acceptance fitted to the functional form given in Equation (2.20).

A full systematic error analysis is performed for the two methods. The first method yields $r_{00}^{04} = -0.022 \pm 0.025(stat) \pm 0.005(syst)$ and $r_{1-1}^{04} = -0.022 \pm 0.02(stat) \pm 0.005(syst)$. The second method yields $r_{00}^{04} = 0.003 \pm 0.025(stat) \pm 0.005(syst)$ and $r_{1-1}^{04} = -0.023 \pm 0.02(stat) \pm 0.005(syst)$. These results are consistent with SCHC.

W (GeV)	t (GeV^2)	N_{signal}	$\mathcal{A}$	$\frac{d\sigma}{dt}$ (nb/GeV^2)
20 - 50	-0.10	1154	0.163	$97.2\pm12.5^{+7.6}_{-8.1}$
	-0.35	842	0.177	$43.2\pm3.3^{+3.3}_{-5.6}$
	-0.68	405	0.225	$13.1\pm1.5^{+1.2}_{-1.4}$
	-1.05	154	0.265	$3.2\pm0.9^{+0.4}_{-0.6}$
50 - 70	-0.10	1649	0.366	$195.8\pm10.4^{+16.3}_{-13.8}$
	-0.35	876	0.392	$62.5\pm3.0^{+5.7}_{-4.6}$
	-0.68	389	0.425	$20.3\pm1.6^{+1.7}_{-2.4}$
	-1.05	160	0.520	$5.0\pm0.8^{+0.6}_{-0.9}$
70 - 90	-0.10	1271	0.352	$228.1\pm15.4^{+17.1}_{-15.5}$
	-0.35	651	0.376	$70.2\pm4.2^{+5.6}_{-5.7}$
	-0.68	242	0.430	$17.1\pm1.8^{+1.7}_{-2.2}$
	-1.05	146	0.541	$6.8\pm0.9^{+0.7}_{-0.9}$
90 - 125	-0.10	1882	0.362	$284.9\pm16.4^{+19.8}_{-20.2}$
	-0.35	903	0.378	$83.2\pm4.5^{+7.7}_{-6.6}$
	-0.68	336	0.428	$20.6\pm1.9^{+1.8}_{-2.8}$
	-1.05	147	0.543	$5.0\pm0.9^{+0.7}_{-0.9}$
125 - 170	-0.10	1692	0.334	$353.3\pm23.9^{+23.8}_{-19.8}$
	-0.35	877	0.377	$104.4\pm6.0^{+8.0}_{-7.8}$
	-0.68	428	0.488	$31.3\pm2.3^{+2.3}_{-3.0}$
	-1.05	154	0.772	$5.0\pm1.0^{+0.7}_{-0.8}$
170 - 230	-0.10	927	0.202	$418.0\pm39.8^{+30.8}_{-36.7}$
	-0.35	592	0.268	$130.9\pm8.3^{+9.9}_{-13.0}$
	-0.68	300	0.439	$32.4\pm2.7^{+2.6}_{-3.2}$
	-1.05	110	0.880	$4.4\pm0.9^{+0.7}_{-0.7}$
230 - 290	-0.10	777	0.233	$546.5\pm108.9^{+39.1}_{-38.9}$
	-0.35	407	0.276	$155.6\pm19.8^{+12.4}_{-23.2}$
	-0.68	171	0.421	$32.9\pm7.2^{+3.0}_{-3.7}$
	-1.05	116	0.738	$10.8\pm2.0^{+1.3}_{-1.6}$

Table 9.2: Results of $\frac{d\sigma}{dt}$ (nb/GeV^2) in ranges of W. Statistical and systematic errors are shown. N_{signal} is the total number of signal events, $\mathcal{A}$ is the acceptance.

W (GeV)	$\frac{d\sigma}{dt}\|_{t=0}$ (nb/GeV^2)	b (GeV^{-2})
20 - 50	$143.7\pm15.3^{+12.1}_{-15.6}$	$3.65\pm0.24^{+0.14}_{-0.11}$
50 - 70	$259.8\pm15.4^{+25.1}_{-18.1}$	$4.00\pm0.16^{+0.20}_{-0.09}$
70 - 90	$302.2\pm23.4^{+27.7}_{-24.6}$	$4.18\pm0.20^{+0.23}_{-0.13}$
90 - 125	$407.7\pm26.5^{+35.4}_{-31.3}$	$4.58\pm0.18^{+0.25}_{-0.11}$
125 - 170	$492.4\pm33.6^{+39.7}_{-34.5}$	$4.39\pm0.16^{+0.18}_{-0.11}$
170 - 230	$648.1\pm51.9^{+55.2}_{-77.2}$	$4.74\pm0.18^{+0.17}_{-0.18}$
230 - 290	$657.9\pm118.8^{+71.9}_{-102.1}$	$4.24\pm0.35^{+0.22}_{-0.24}$

Table 9.3: Results of $\frac{d\sigma}{dt}|_{t=0}$ and b in ranges of W with statistical and systematic errors (see text).

W (GeV)	b (GeV^{-2})
20 - 50	$3.43\pm0.11^{+0.19}_{-0.11}$
50 - 70	$3.99\pm0.10^{+0.20}_{-0.08}$
70 - 90	$4.22\pm0.12^{+0.21}_{-0.09}$
90 - 125	$4.63\pm0.12^{+0.27}_{-0.12}$
125 - 170	$4.46\pm0.12^{+0.24}_{-0.12}$
170 - 230	$4.46\pm0.19^{+0.27}_{-0.23}$
230 - 290	$4.58\pm0.22^{+0.28}_{-0.12}$

Table 9.4: Results of b in ranges of W with statistical and systematic errors obtained by reweighting the t distribution in MC (see text).

t (GeV^2)	$\alpha(t)$
-0.10	$1.188\pm0.014^{+0.004}_{-0.009}$
-0.35	$1.154\pm0.011^{+0.005}_{-0.012}$
-0.68	$1.127\pm0.017^{+0.011}_{-0.010}$
-1.05	$1.044\pm0.029^{+0.021}_{-0.009}$

Table 9.5: $\frac{d\sigma}{dt}$ in Fig. 9.17 is fitted in t bins to the form $\frac{d\sigma}{dt} \propto W^{2[2\alpha(t)-2]}$. The resulting values of α in are given with the statistical and systematic errors.

Chapter 10

Elastic Photoproduction of $\psi(2S)$

The resonance $\psi(2S)$ is classified as an orbital excitation of the charmed quark-antiquark bound state. The average distance between the quark-antiquark in this bound state is significantly larger than in the case of the J/ψ. This feature makes the study of the production cross-section of the $\psi(2S)$ interesting. In particular, the presence of a node in the wave function of the $\psi(2S)$ leads to a suppression in the photoproduction limit of the production rate of the $\psi(2S)$ with respect to the ground state, the J/ψ [146].

The measurement of the ratio $\sigma(\psi(2S))/\sigma(J/\psi)$ has the advantage that theoretical and experimental uncertainties in the normalization of the charmonium production cancel out. Results of the ratio $\sigma(\psi(2S))/\sigma(J/\psi)$ have been reported by the H1 [147] and ZEUS [148] Collaborations with earlier data.

The trigger and off-line selection are the same as those used for the analysis of the production of the J/ψ (see Chapter 9).

The results of this work were reported in [149].

10.1 Search Strategy

This analysis has two main experimental limitations. The first is related to the relatively low ratio of signal to expected background (QED and remaining background).

This ratio decreases with W. Also, the amount of background increases with the inclusion of one track and zero track topologies (see Section 11.1). The second is related to the fact that the $\psi(2S)$ sits relatively close to the J/ψ. The resolution of the reconstructed $M_{e^+e^-}$ is W dependent an degrades rapidly at low and high W with the inclusion of one track and zero track topologies. As the resolution of the reconstructed $M_{e^+e^-}$ gets worse an undesired contamination from the J/ψ into the mass window of the search of the $\psi(2S)$ increases.

These considerations lead to the restriction of the W range of the search of the $\psi(2S)$ resonance to $50 < W < 125$ GeV, which leaves the analysis to the study of two track topologies. In this range, the resolution of the reconstructed $M_{e^+e^-}$ ranges between 30 and 70 MeV, so the contamination from the decay of the J/ψ in the search mass window of the $\psi(2S)$ is expected to be small [1]. The mass window of the $\psi(2S)$ has been set to $3.5 < M_{e^+e^-} < 3.9$ GeV.

Acceptance corrections have been calculated with the DIPSI MC for both resonances. The effect of radiative corrections should cancel out in a first approximation. Two methods of the extraction of the signal have been attempted:

1. This method is used to extract the signal in the analysis of the J/ψ (see Section 9.1). The QED background and the contamination from the J/ψ decays are subtracted from data in bins of W (see Figure 10.1). Then a fit is performed of the form given in Expression (9.1). The remaining background is subtracted to extract the signal. The obtained spectra of $M_{e^+e^-}$ in different bins of W after background subtraction are shown in Figure 10.2. The solid histogram corresponds to the shape predicted by the DIPSI MC. This method yields a total number of 164.5 events. More details of the extraction are given in Table 10.1. Table 10.1 also gives the number of observed J/ψ signal events [2] in the same W

[1] $M_{\psi(2S)} = 3686$ MeV as opposed to $M_{J/\psi} = 3097$ MeV. On the other hand, the rate of production of J/ψ through the electronic decay is expected to be more than 50 times larger than the $\psi(2S)$.

[2] In this Chapter, the contamination from the decay of the $\psi(2S)$ has not been subtracted from the numbers of J/ψ signal events.

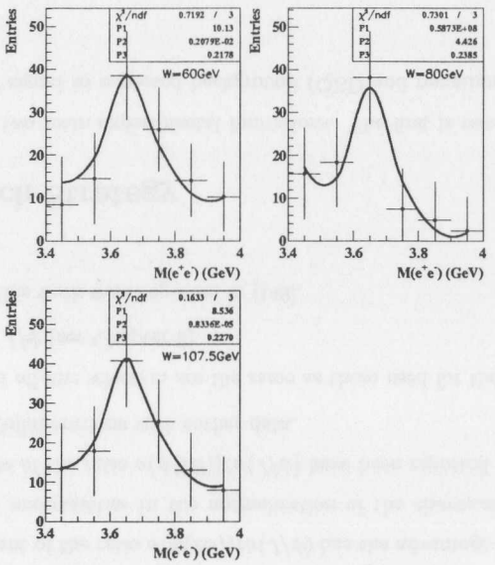

Figure 10.1: Spectra of $M_{e^+e^-}$ in different bins of W in data after subtraction of the QED background and contamination from J/ψ. The solid line corresponds to a fit according to method 1. The parameters and the χ^2 of the fits are given in the box on the upper right corner.

ranges, as obtained in Section 9.1.

2. After subtracting the expected contribution from QED background the resultant $M_{e^+e^-}$ spectrum is fitted in the range $2 < M_{e^+e^-} < 5$ GeV in one bin of W to the following functional form:

$$F^{e^+e^-} = A_{J/\psi} MC_{J/\psi} + A_{\psi(2S)} MC_{\psi(2S)} + A_{r1} e^{-b_{r1} M_{e^+e^-}} + A_{r2} e^{-b_{r2} M_{e^+e^-}} \quad (10.1)$$

where $MC_{J/\psi}$ and $MC_{\psi(2S)}$ are the $M_{e^+e^-}$ distributions, as predicted by the J/ψ and $\psi(2S)$ MC's, respectively, and $A_{J/\psi}, A_{\psi(2S)}, A_r, A_{r2}, b_{r1}$ and b_{r2} are free parameters. The result of the fit is shown in Figure 10.3. The $\chi^2/n.d.f = 22.1/25$ and the fit yields

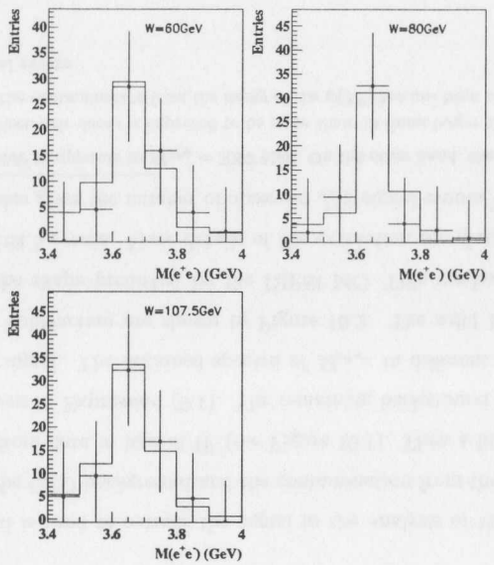

Figure 10.2: Spectra of $M_{e^+e^-}$ in different bins of W after background subtraction. The solid histogram correspond to the expected shape predicted by the DIPSI MC.

a total number of 158.8 $\psi(2S)$ signal events. The slopes of the remaining background are $b_{r1} = 1.67\,\mathrm{GeV}^{-2}$ and $b_{r2} = 1.99\,\mathrm{GeV}^{-2}$. The number of J/ψ signal events is 8655.3. A fit with of the remaining background with a one exponential for the remaining background in Expression (10.1) yields a total number of 158 and 8649.7 of $\psi(2S)$ and J/ψ signal events, respectively, with $\chi^2/n.d.f = 21.9/24$ and $b_r = 1.75\,\mathrm{GeV}^{-2}$, gives a good fit of the data too.

The fraction of proton dissociative background has been assumed to be the same as in the case of the J/ψ (see Section 8.1.1). SCHC has been assumed.

W (GeV)	N_{QED}	$N^c_{J/\psi}$	N_r	$N_{\psi(2S)}$	$N_{J/\psi}$
50 - 70	142.3	3.6	40.2	52.9	3019.2
70 - 90	162.0	1.3	20.5	48.3	2366.4
90 - 125	183.1	2.4	34.1	63.3	3422.2
50 - 125	487.4	7.3	94.8	164.5	8807.8

Table 10.1: Results of the extraction of the $\psi(2S)$ signal with method 1. N_{QED}, $N^c_{J/\psi}$ and N_r correspond to the number of events from QED processes, from the contamination of J/ψ and remaining background, respectively. $N_{\psi(2S)}$ and $N_{J/\psi}$ are the number of signal $\psi(2S)$ and J/ψ events extracted.

10.2 Results

The results are presented in terms of cross-section ratio, $\sigma(\psi(2S))/\sigma(J/\psi)$. This quantity is defined as:

$$\sigma(\psi(2S))/\sigma(J/\psi) = \frac{N_{\psi(2S)}}{N'_{J/\psi}} \frac{\mathcal{A}_{J/\psi}}{\mathcal{A}_{\psi(2S)}} \frac{\mathcal{B}_{J/\psi}}{\mathcal{B}_{\psi(2S)}} \tag{10.2}$$

where $N_{\psi(2S)}$ is the number of signal events of the $\psi(2S)$. $N'_{J/\psi} = N_{J/\psi}(1 - \mathcal{F}_{\psi(2S)})$, where $N_{J/\psi}$ is the number of J/ψ signal events and $\mathcal{F}_{\psi(2S)}$ is the fraction of J/ψ from the decay of the $\psi(2S)$ (see Section 8.1.2). $\mathcal{A}_{\psi(2S)}, \mathcal{A}_{J/\psi}, \mathcal{B}_{\psi(2S)}$ and $\mathcal{B}_{\psi(2S)}$ are the acceptance and electronic branching ratios of the $\psi(2S)$ and J/ψ, respectively. The branching ratios are $\mathcal{B}_{\psi(2S)} = (7.9 \pm 0.5) \cdot 10^{-3}$ and $\mathcal{B}_{J/\psi} = (5.93 \pm 0.1) \cdot 10^{-2}$ [150].

A full systematic error analysis has been performed following the guidelines of the J/ψ analysis. The largest systematic error corresponds to the change in the normalization of the QED background and shifting the mass window left and right by 100 MeV. It should be noted that the uncertainty in $\mathcal{B}_{\psi(2S)}$ has not been included in the systematic error. Table 10.2 shows the result of the ratio $\sigma(\psi(2S))/\sigma(J/\psi)$ obtained in this analysis. This result is compared with measurements by the H1 [147] and ZEUS [148] Collaborations with earlier data in Figure 10.4. Also shown is a compilation of measurements from fixed target experiments: three photoproduction experiments (deuterium target at SLAC [151], lithium target, NA14 [152] and deuterium target, E401 [143]) and muon production experiments (on iron target, EMC [153] and on tin and carbon, NMC [154]). Overall, the data accumulated at fixed target and HERA experiments show that the cross-section ratio, $\sigma(\psi(2S))/\sigma(J/\psi)$, is independent on W in a broad range of energies.

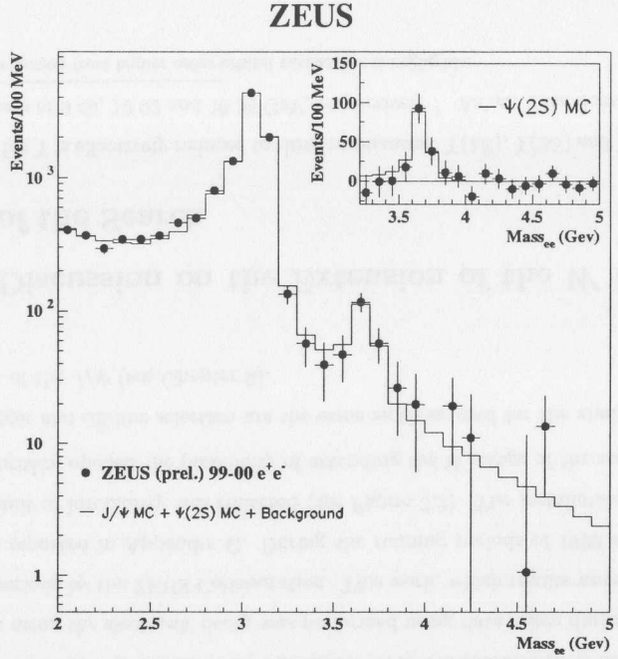

Figure 10.3: Spectrum of $M_{e^+e^-}$ after QED background subtraction with data taken during the 1999 and 2000 running periods. The solid histogram is the result of a global fit (see text). The small inset shows data after background subtraction in the region of the $\psi(2S)$. The solid histogram in the small window corresponds to the DIPSI MC.

$\langle W \rangle$ (GeV)	$N_{\psi(2S)}$	$N_{J/\psi}$	$\mathcal{A}_{\psi(2S)}$	$\mathcal{A}_{J/\psi}$	$\sigma(\psi(2S))/\sigma(J/\psi)$
88	158	8649.7	0.391	0.422	$0.15 \pm 0.03^{+0.04}_{-0.04}$

Table 10.2: Result of the ratio $\sigma(\psi(2S))/\sigma(J/\psi)$ obtained with data taken during the 1999 and 2000 running periods using the electronic channel. Errors are statistical and systematic. $N_{\psi(2S)}$, $N_{J/\psi}$, $\mathcal{A}_{\psi(2S)}$ and $\mathcal{A}_{J/\psi}$ correspond to the number of signal events and acceptance of $\psi(2S)$ and J/ψ, respectively.

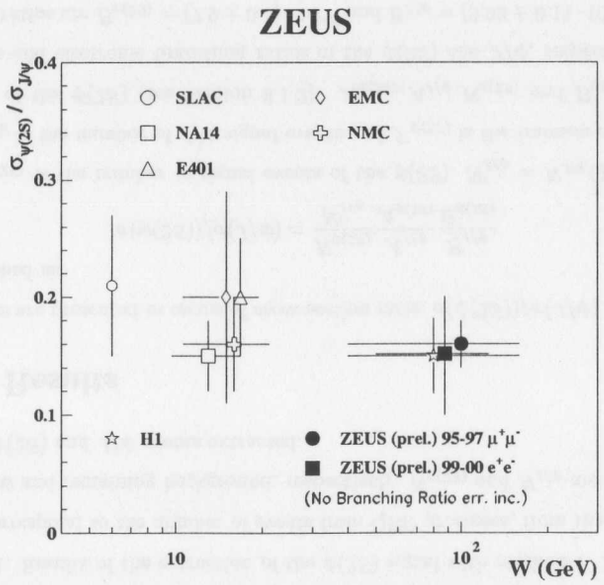

Figure 10.4: Cross-section ratio, $\sigma(\psi(2S))/\sigma(J/\psi)$, produced in this analysis compared with previous H1, ZEUS and fixed target experiments results (see text). ZEUS values do not include the uncertainty of the branching ratio, $\mathcal{B}_{\psi(2S)}$, in the systematic error.

Chapter 11

Search for Elastic Photoproduction of Υ Resonances

Excitement was generated by the report of an anomalously high cross-section production of Υ resonances by the H1 [142] and ZEUS [155] Collaborations. A search for Υ production using the electronic decay was performed using data taken during the 1996 and 1997 periods by the ZEUS Collaboration. This work, which results were presented in [156], is reported in Appendix G. During the running periods of 1999 and 2000 a larger amount of luminosity was collected (see Figure 3.2). The installation of a new trigger algorithm opened the possibility of extending the W range of the search.

The trigger and off-line selection are the same as those used for the analysis of the production of the J/ψ (see Chapter 9).

11.1 Discussion on the Extension of the W Range of the Search

The search for Υ is effectively reduced to three resonances: $\Upsilon(1S)$, $\Upsilon(2S)$ and $\Upsilon(3S)$ sitting at masses of 9.46, 10.02 and 10.36 GeV, respectively [1]. As our data does not allow

[1]The contribution from higher order orbital excitations is negligible.

the relative fractions of these resonances to be determined, we assume that the cross-sections times branching ratios as measured by CDF [157], $\sigma\mathcal{B}(\Upsilon(2S))/\sigma\mathcal{B}(\Upsilon(1S)) = 0.281 \pm 0.030(stat) \pm 0.038(syst)$ and $\sigma\mathcal{B}(\Upsilon(3S))/\sigma\mathcal{B}(\Upsilon(1S)) = 0.155 \pm 0.024(stat) \pm 0.021(syst)$. The $\Upsilon(1S)$ accounts for about 70% of the signal. The expected $M_{e^+e^-}$ spectrum of the $\Upsilon(1S), \Upsilon(2S)$ and $\Upsilon(3S)$ using two track topologies is illustrated in Figure 11.1. The expected $M_{e^+e^-}$ spectrum peaks at $M_{e^+e^-} \approx 9.5\,\text{GeV}$ with tails on the lower side due to bremsstrahlung radiation of electrons of the decay and on the higher side due $\Upsilon(2S)$ and $\Upsilon(3S)$ resonances.

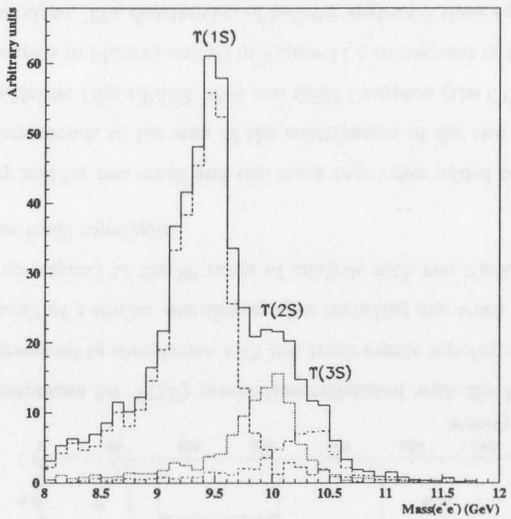

Figure 11.1: The expected $M_{e^+e^-}$ spectrum of the $\Upsilon(1S), \Upsilon(2S)$ and $\Upsilon(3S)$ resonances using two track topologies. The ratio of the cross-sections times branching ratios of the three resonances are assumed to be the same as measured by CDF (see text).

The typical resolution of the reconstructed mass ranges between 200 and 400 MeV for two track and one track topologies, respectively. This is illustrated in Figure 11.2. Since the average momentum of the decaying products of the Υ are a factor of three

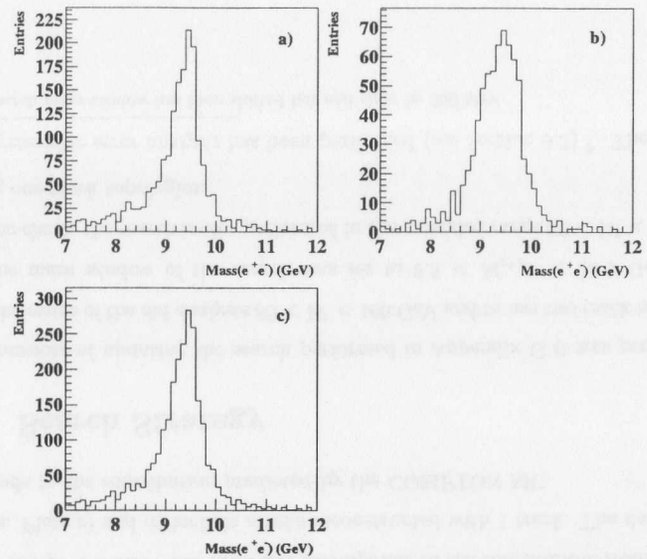

Figure 11.2: Plot a) shows the reconstructed $M_{e^+e^-}$ with two track topologies for $\Upsilon(1S)$. Plot b) shows $M_{e^+e^-}$ with one track topologies. Plot c) shows the effective $M_{e^+e^-}$ spectrum obtained using both topologies. The DIPSI MC is used.

greater than in the case of the J/ψ the resolution of the reconstructed mass with the CTD tracks only is of the same order as for one track topologies [2].

As in the case of the J/ψ, the inclusion of one track topologies allows from the one hand to extend the W range of the observation of VM production and, on the other, to flatten the acceptance with W (for more details see Chapters 5 and 7). The result of the acceptance calculation for two track topologies only compared to the result obtained by including one track topologies is shown in Figure 11.3 for $\Upsilon(1S)$. The horizontal lines illustrate the W ranges which the previous analysis was restricted to (see Appendix G) and the range of the extension due to the inclusion of one track topologies.

Plots in Figure 11.4 show the reconstructed $M_{e^+e^-}$ and W distributions for two

[2]The contribution from zero track events in the production of Υ resonances is negligible.

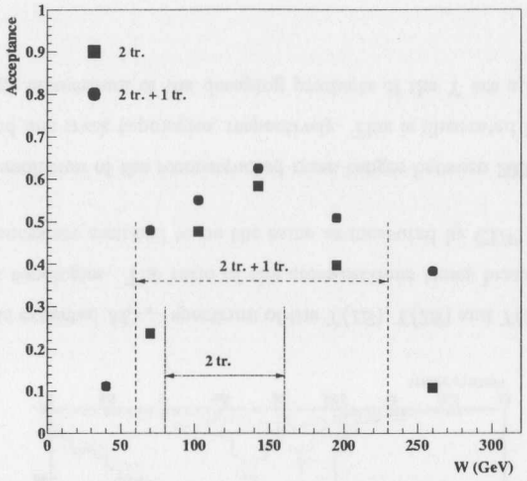

Figure 11.3: Acceptance for $\Upsilon(1S)$ production calculated with the DIPSI MC. The solid squares correspond to acceptance with two track events topologies only and solid circles are the result of a similar calculation after including one track topologies. The horizontal lines correspond to the W range of analysis with two track topologies only and including one track topologies.

track events only and for two track and one track topologies added together in data. The solid line corresponds to the sum of the contribution of the two dominant QED processes, Bethe-Heitler (the LPAIR MC) and QED Compton (the COMPTON MC). The dashed histogram in Plots c) and d) in Figure 11.4 correspond to the contribution of QED Compton alone. The distribution of helicity angles for these samples are given in Figure 11.5. The inclusion of one track events leads to a significant increase of the QED background processes. Figure 11.6 shows the distributions of reconstructed $M_{e^+e^-}$ and W in the region $8.5 < M_{e^+e^-} < 11$ GeV. The contribution from QED processes increases by a factor of 2.5 after including one track configurations (compare Plots a) and c) of Figure 11.6). This leads to a significant reduction of the ratio of signal to background (see Tables 11.1 and 11.2).

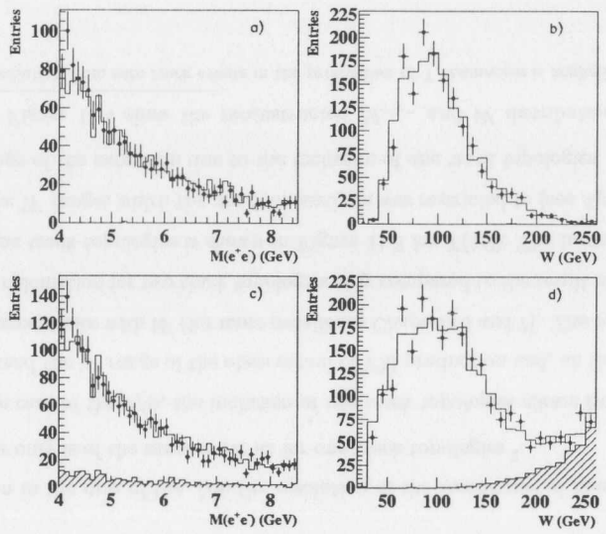

Figure 11.4: Plot a) shows the reconstructed $M_{e^+e^-}$ distribution for two track events in data. Plot b) shows the W distribution for the same sample of di-lepton events with $4 < M_{e^+e^-} < 8$ GeV. The solid line corresponds to the contribution from all QED processes. Plots c) and d) include events reconstructed with 1 track. The dashed MC corresponds to the contribution predicted by the COMPTON MC.

11.2 Search Strategy

For the purpose of updating the search performed in Appendix G it was preferred to stick to the range of the old analysis $80 < W < 160$ GeV and to use two track topologies only. The mass window of the search was set to $8.5 < M_{e^+e^-} < 10.9$ GeV. As a systematic check, the search is also performed in the extended range $60 < W < 230$ GeV including one track topologies.

Full systematic error analysis has been performed (see Section 9.3) [3]. The fraction

[3]The search mass window has been shifted left and right by 300 MeV.

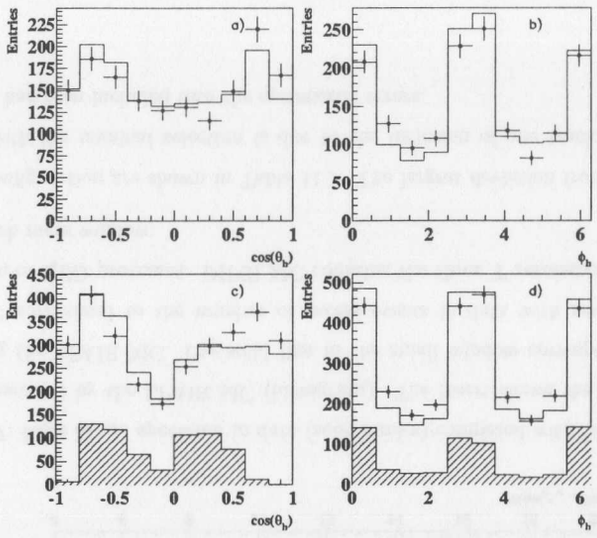

Figure 11.5: Plots a) and b) show the distributions of helicity angles for di-lepton events with $4 < M_{e^+e^-} < 8$ GeV in data. The solid line corresponds to the contribution from all QED processes. Plots c) and d) include events reconstructed with 1 track. The dashed MC corresponds to the contribution predicted by the COMPTON MC.

of contamination from resonant production of Υ resonances via proton dissociation was been assumed to the same as for the J/ψ. SCHC has been assumed.

The reconstructed invariant mass spectrum obtained is shown in Figure 11.7. The solid line in the main Plot corresponds to the expectation from QED processes and the solid circles to data. The small insert shows a blow up of the mass region of the Υ resonances in data after background subtraction. The data display an excess of events in the search mass window. A total number of 107 events are observed and 88.7 events are expected from QED background processes. Following the prescription of

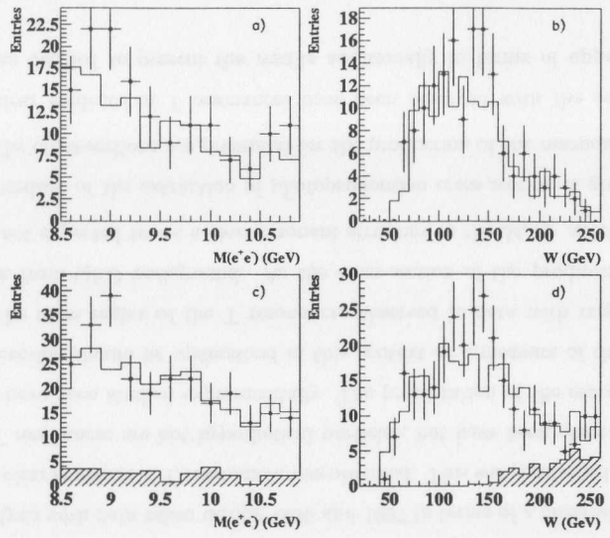

Figure 11.6: Plot a) shows the reconstructed $M_{e^+e^-}$ for two track events in the region of the Υ resonances in data. Plot b) shows the W distribution for the same sample of di-lepton events with $8.5 < M_{e^+e^-} < 11$ GeV. The solid line corresponds to the contribution from all QED process. Plots c) and d) include events reconstructed with 1 track. The dashed MC corresponds to the contribution predicted by the COMPTON MC.

Expression (G.3), $N_\Upsilon = 18.3 \pm 10.3$, the number of unresolved [4] signal events.

The solid line in the insert in Figure 11.7 corresponds to the expected shape of the reconstructed invariant mass of the three Υ resonances, as predicted by the DIPSI MC. The DIPSI MC has been normalized so as to yield a number of unresolved signal events in the search mass window equal to N_Υ observed in data.

A number of checks have been performed to test the stability of the result obtained in the nominal analysis. The results of these checks compared to the result of the

[4] Unresolved refers to the three Υ resonances.

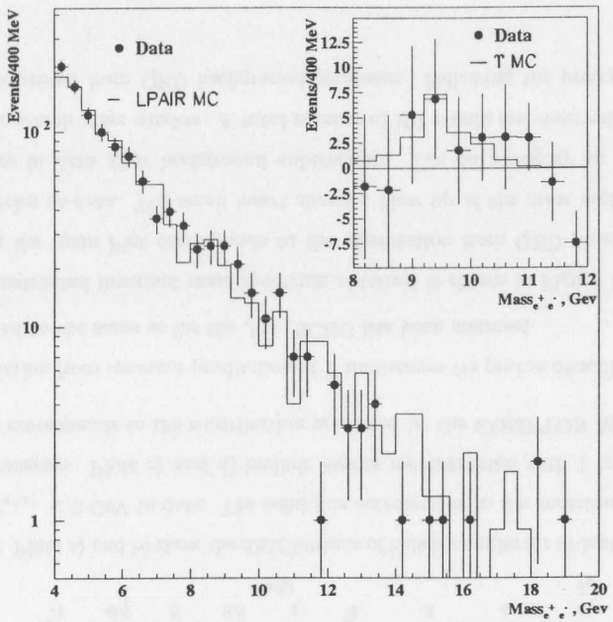

Figure 11.7: High $M_{e^+e^-}$ spectrum in data (solid circles) compared with Bethe-Heitler process generated by the LPAIR MC (histogram). The insert shows the signal after subtracting the LPAIR MC. The solid line in the small window corresponds to the DIPSI MC normalized to the number of excess events in data with respect to the expectation of QED processes. DIPSI MC contains the three ϒ resonances expected in the search mass window.

nominal configuration are shown in Table 11.1. The largest deviation from the result obtained with the nominal selection is due to the inclusion of one track topologies. This effect has been included into the systematic errors.

Selection	W (GeV)	Mass Window (GeV)	N_{obs}	N_{QED}	N_{Υ}
2Tr.	80 - 160	8.5 - 10.9	107	88.7	18.3±10.3
2Tr.	80 - 160	8.2 - 10.6	122	103.2	18.8±11.1
2Tr.	80 - 160	8.8 - 11.2	95	72	23±9.8
2Tr.	80 - 160	8.5 - 10	88	76.3	11.8±9.4
2Tr.	80 - 160	9 - 10	55	42.8	12.2±7.4
2Tr.	80 - 230	8.5 - 10.9	137	115.7	21.3±11.7
2Tr. + 1Tr.	60 - 230	8.5 - 10.9	260	248.5	11.5±16.1

Table 11.1: Results of various checks for the search of ϒ production with data taken during the 1999 and 2000 running period with different off-line selections. N_{obs} is the number of observed events in the selection, N_{QED} is the number of expected QED background and N_{Υ} is the number of unresolved signal events with an error calculated according to Expression (G.3).

11.3 Results

The results of the search of ϒ resonances using the electronic channel was presented in the analysis with data taken during 1996 and 1997 in terms of a cross-section, even though no clear evidence of ϒ resonances was observed. This was motivated by the fact that the ϒ resonances are not hypothetical particles, but have been observed and its properties have been studied experimentally. The presentation of the search in terms of a cross-section should be understood in this context as a measure of the excess of events in the mass region of the ϒ resonances observed in data with respect to the expectation from QED background. As the cross-section of the production of ϒ is small it is not expected to see a clear resonant structure in the $M_{e^+e^-}$ spectra.

The procedure of the extraction of photoproduction cross-section is given in Section 9.2. The cross-sections are presented for the production of the resonance $\Upsilon(1S)$.

As no clear evidence of ϒ resonances have been observed with the accumulated data, it was decided to present the results additionally in terms of upper limit on

$\langle W \rangle$	N_Υ	$\mathcal{A}_{\Upsilon(1S)}$	Φ_T	$F_{\Upsilon(1S)}$	$\sigma_{\gamma p \to \Upsilon(1S)p}$	$\sigma^{Limit}_{\gamma p \to \Upsilon(1S)p}$
120	18.3±10.3	0.52	0.05256	0.7	309±175	626
120	18.8±11.1	0.54	0.05256	0.7	306±179	632
120	23 ±9.8	0.48	0.05256	0.7	418±177	746
120	22.7±10	0.49	0.05256	0.8	240±191	597
120	12.2±7.4	0.41	0.05256	0.8	298±181	640
150	21.3±11.7	0.47	0.07153	0.7	293±161	582
140	11.5±16.1	0.54	0.09805	0.7	100±140	363

Table 11.2: Results of checks on Υ production with data taken during 1999 and 2000 running periods according to off-line selections given in Table 11.1. $\langle W \rangle$ (in GeV) and Φ_T are the average W and photon flux of the selection, respectively. N_Υ is the number of unresolved signal events with an error calculated according to Expression (G.3). $\mathcal{A}_{\Upsilon(1S)}$ and $F_{\Upsilon(1S)}$ are the acceptance and relative fraction of $\Upsilon(1S)$ in the selection, respectively. The results are expressed in terms of the cross-section of $\Upsilon(1S)$ production, $\sigma_{\gamma p \to \Upsilon(1S)p}$, and an upper limit to it according to a 95% CL, $\sigma^{Limit}_{\gamma p \to \Upsilon(1S)p}$, both expressed in pb. The error given to $\sigma_{\gamma p \to \Upsilon(1S)p}$ is statistical only.

the photoproduction cross-section. The calculation of the upper limit has been done following the prescription in [139].

The result of the checks performed in the present analysis compared with previous measurements are shown in Table 11.2 in terms of the $\Upsilon(1S)$ photoproduction cross-section and the upper limit to it according to the 95% confidence level (CL). The result of this analysis with full systematic errors is shown in the third row of Table 11.3. This result is consistent with previous analyses.

The results obtained in the present analysis are combined with those shown in Appendix G. For simplicity, both analysis have been treated as independent measurements and the combination was been performed by means of an error weighted average. The error associated to each measurement is the sum in quadrature of the statistical and systematic uncertainties. The systematic error has been set to be symmetric and equal

Selection	N_Υ	$\mathcal{A}_{\Upsilon(1S)}$	$\mathcal{L}(\text{pb}^1)$	$\sigma_{ep \to \Upsilon(1S)p}$	$\sigma^{Limit}_{\gamma p \to \Upsilon(1S)p}$
95-97 ($\mu^+\mu^-$)	17.1±7.5	0.43	43.2	$375 \pm 170^{+75}_{-64}$	697
96-97 (e^+e^-)	11.1±8.3	0.50	37	$255 \pm 191^{+41}_{-125}$	611
99-00 (e^+e^-)	18.3±10.3	0.52	55.3	$309 \pm 175^{+204}_{-271}$	626
96-00 (e^+e^-)	29.4±13.2	0.51	92.3	273±170	517
($\mu^+\mu^-$)-(e^+e^-)	46.5±15	-	125.5	320±125	-

Table 11.3: Results on the search of elastic photoproduction of $\Upsilon(1S)$ resonances with different data sets. N_Υ is the number of unresolved signal events with an error calculated according to Expression (G.3). $\mathcal{A}_{\Upsilon(1S)}$ is the acceptance of $\Upsilon(1S)$ in the selection. $\mathcal{L}$ is luminosity corresponding to each data set. The results are expressed in terms of $\sigma_{ep \to \Upsilon(1S)p}$, the cross-section of $\Upsilon(1S)$ production and an upper limit to it according to the 95% CL, $\sigma^{Limit}_{\gamma p \to \Upsilon(1S)p}$ both expressed in pb. The error given to the combined 96-00 and ($\mu^+\mu^-$)-(e^+e^-)results of $\sigma_{\gamma p \to \Upsilon(1S)p}$ corresponds to the statistical and systematic errors added up in quadrature.

to the average of the positive and negative systematic fluctuations. The results of the combination of 96-97 and 99-00 data analyses using the electronic channel are shown in Table 11.3.

The result of the 96-00 (e^+e^-) selection is consistent with the one obtained the 95-97 ($\mu^+\mu^-$) selection. The cross-sections obtained with the 96-00 (e^+e^-) selection has been combined with the result of the 95-97 ($\mu^+\mu^-$) selection. The combination of the results from both selections increase the significance of the excess of events seen in data in the mass region of the Υ resonances with respect to the QED background. The significance of the excess has grown from 2σ effect to a 3σ effect.

The results of this analysis are compared with the measurement published by the H1 Collaboration [142] in Figure 11.8. The value of the upper limit is obtained at $W = 120$ GeV. The dashed line corresponds to a functional form $\propto W^\delta$, with $\delta = 0.7$ so that to give the calculated limit at $W = 120$ GeV. The value of $\delta = 0.7$ is taken

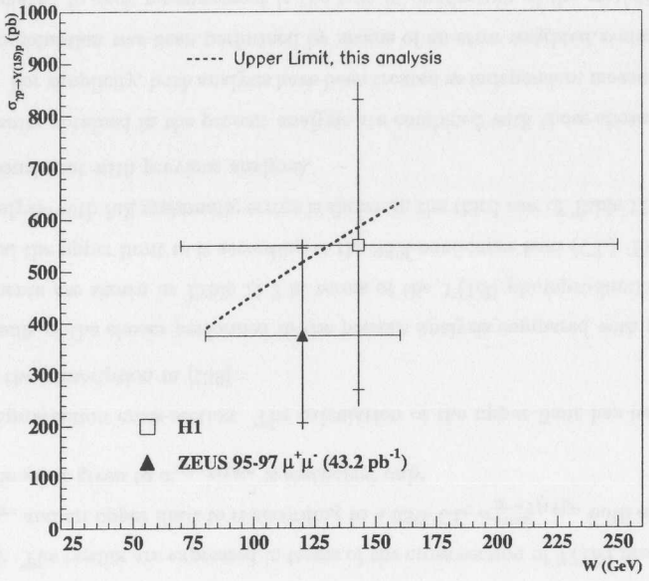

Figure 11.8: The values of upper limit obtained with the selection 96-00 (e^+e^-) is compared with the cross-sections published by the H1 and ZEUS Collaborations. The value of the upper limit is obtained at $W = 120$ GeV. The dashed line corresponds to the functional form $\propto W^{0.7}$ so that to give the calculated limit at $W = 120$ GeV.

from the one obtained in the case of J/ψ [5].

[5] Results of the parameter δ in the electroproduction regime have been reported ([122, 158] and [100, 159]). It has been observed that the steepness of the rise of the cross-section does not increase with the scale $Q^2 + M^2_{J/\psi}$ (see also Chapter 12).

Chapter 12

Discussion

12.1 Elastic Photoproduction of J/ψ

12.1.1 Sensitivity to the Saturation of the Cross-Section with W

One of the major motivations behind this work is to measure the W dependence of the cross-section in an extended W range. The measurement of an elastic exclusive state gives additional sensitivity in the study of the behavior of the cross-section at high energy. In particular, the measurement of an exclusive state for a given value of Q^2 has the advantage that the cross-section is evaluated at a fixed value of the scale of the interaction. It is possible to disentangle the non-trivial scale dependence of the cross-section in the region of transition from hard to soft QCD interactions from the energy dependence of the cross-section.

The energy dependence of $\sigma(\gamma p \to J/\psi p)$ is sensitive to the square of the gluon density in the proton probed at an effective scale $\mu^2 = \xi M^2_{J/\psi}$ and $x = \frac{\xi M_{J/\psi}}{W^2}$ (see Section 2.6.2). The saturation of the cross-section at high energy may be interpreted as a saturation of the gluon density in the proton at small x.

In Section 9.4 it has been shown that the measured cross-section may be param-

eterized with a simple power form, $\sigma(\gamma p \to J/\psi p) \propto W^{\delta}$. The extraction of a W independent δ may be interpreted as an indication that we are not sensitive to saturation effects at small x.

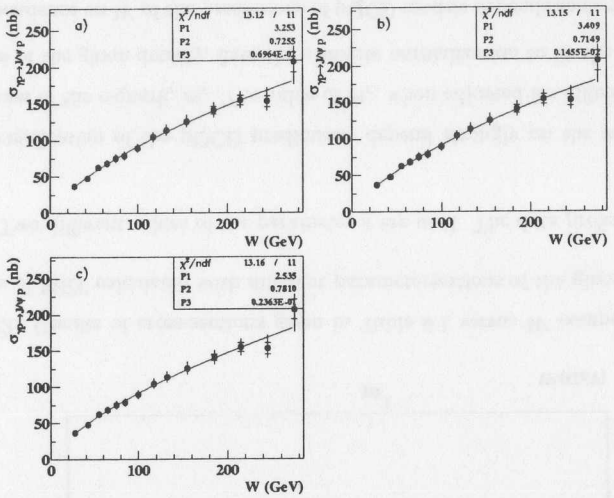

Figure 12.1: Fits to $\sigma(\gamma p \to J/\psi p)$ with different parameterizations of the W dependence of δ (see text).

In this Section the W dependence of the power δ is explored by means of fits to various parameterizations of the cross-section. Fits of the cross-sections have been performed to the following parameterizations of δ as a function of W ($\sigma(W) = AW^{\delta(W)}$):

a) $\delta = \delta_0 \frac{1+B}{1+B(W/90)}$

b) $\delta = \delta_0 \frac{1+B}{1+B(W/90)^2}$

c) $\delta = \delta_0 \frac{1}{1+B \ln W/90}$

In each fit three parameters are free. The parameter δ_0 corresponds to the value of δ at $W = 90$ GeV and B is a parameter implemented to account for the W dependence of δ. The values of the parameters δ_0 and B of the fits of the cross-sections to the three functional forms are given in Table 12.1. The parameters B obtained from the three fits are consistent with zero within errors. We do not observe a change in the dynamics of the process in the extended W range of the measurement. The J/ψ photoproduction data may be consistent with no saturation.

Fit	δ_0	B	$\chi^2/n.d.f.$
a	$0.73 \pm 0.04^{+0.05}_{-0.04}$	$0.007 \pm 0.01^{+0.014}_{-0.012}$	13.1/11
b	$0.71 \pm 0.03^{+0.03}_{-0.02}$	$0.001 \pm 0.002^{+0.003}_{-0.002}$	13.2/11
c	$0.78 \pm 0.15^{+0.19}_{-0.11}$	$0.02 \pm 0.04^{+0.05}_{-0.03}$	13.2/11

Table 12.1: Values of the parameters δ_0 and B obtained from the fits of the cross-sections to three different functional forms.

12.1.2 Comparison with Models

In Section 2.6 a description of representative models developed for the description of the elastic production of VM's has been presented. The calculations made in the framework of these models provide a connection between the behavior of the total DIS cross-sections with the production of VM's. It is a milestone for the understanding of the physics involved at HERA to describe simultaneously both the total DIS and other subprocesses, in particular the elastic production of VM's.

Figure 12.2 shows the comparison of the photoproduction cross-section $\sigma(\gamma p \to J/\psi p)$ with the prediction by MRT [57] with various parameterizations of the gluon density: GRV [160], CTEQ5M [161] and MRST99 [162]. Figure 12.3 shows the comparison with the predictions of FMS [58]. Two parameterizations of the gluon density are used, CTEQ4L [163] and MRSTLO [58]. FMS uses a parameter κ to set the scale at which the gluon density is probed, $Q^2 = \kappa/\langle r \rangle$, where r is the transverse size of the

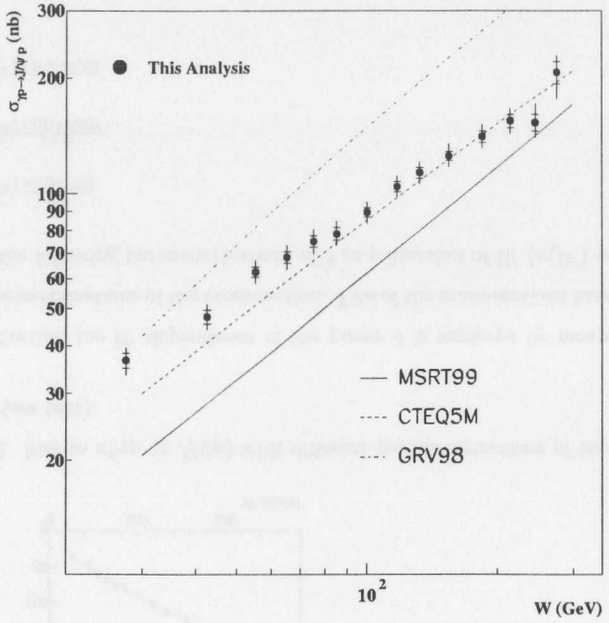

Figure 12.2: Results of cross-sections given in Table 9.1 versus W compared to the predictions of MRT calculated with different parameterizations of the gluon density.

$q\bar{q}$ pair [1]. Two different values of the parameter κ are used. The data prefer a value of $\kappa = 4$.

The normalization of the pQCD predictions depend strongly on the value of the effective mass of the c-quark, m_c. The value of m_c, when adjusted for different parameterizations of the gluon density, fixes the absolute normalization to fit the data.

The dependence on W of the predictions of pQCD models depends somewhat on the choice of the parameterizations of the gluon density. Even so, these models are able to

[1] In the work [58] the parameter κ is referred to as λ. The original notation has not been used in this Chapter in order to avoid confusion with λ_{eff} and λ_V used in Section 12.4.

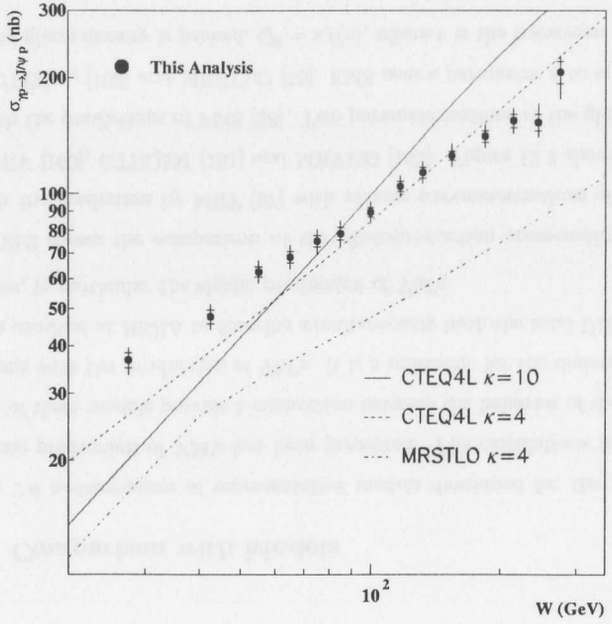

Figure 12.3: The same as in Figure 12.2 with the predictions of FMS (see text).

describe reasonably well the W dependence of the cross-section. Given the freedom to adjust m_c, the normalization of the predictions remains the largest uncertainty in the calculations.

The models mentioned above predict $\sigma_{q\bar{q}-p}$ based on pQCD calculation by inputting the gluon density of the proton. GBW performed a fit of the existing DIS (F_2) data with a simple parameterization for $\sigma_{q\bar{q}-p}$ [23]. Based on the parameterization of $\sigma_{q\bar{q}-p}$, $\sigma(\gamma p \to J/\psi p)$ is calculated [164] (see Equation (2.24)).

The GBW calculation performed in [164] has been updated. The value of the t-slope used there has been changed according to Expression (9.14) with the value of b_0 and α' obtained in Section 9.5. Figure 12.4 shows the comparison of the modified

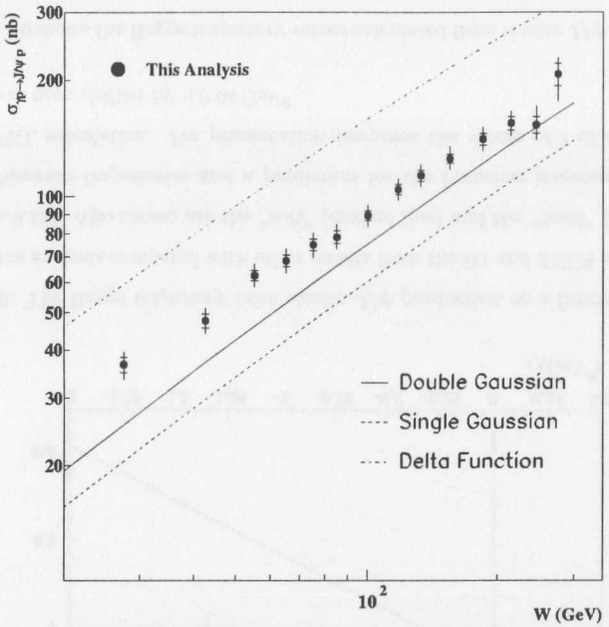

Figure 12.4: The same as Figure 12.2 with predictions from GBW. The lines correspond to different parameterizations of the wave function of the J/ψ (see text).

calculation with data for different forms of the assumption of J/ψ the wave function. Each corresponds to a different assumption about the internal motion of the quarks in the J/ψ. The dashed-dotted line in Figure 12.4 corresponds to a delta type of wave function (the transverse momentum and longitudinal momentum of the quarks do not fluctuate), the dashed line to a single Gaussian (transverse motion of quarks is allowed according to a Gaussian distribution) and the solid line to a double Gaussian (both longitudinal and transverse momentum fluctuate according to Gaussian distributions).

The shape of the W dependence is well described by the calculations. The absolute normalization of the calculation depends strongly on which wave function is chosen.

The more realistic double Gaussian wave function is preferred by the data. However, the choice of the wave function has little impact on the prediction the dependence on W. This observation is important for the discussion in Section 12.4.

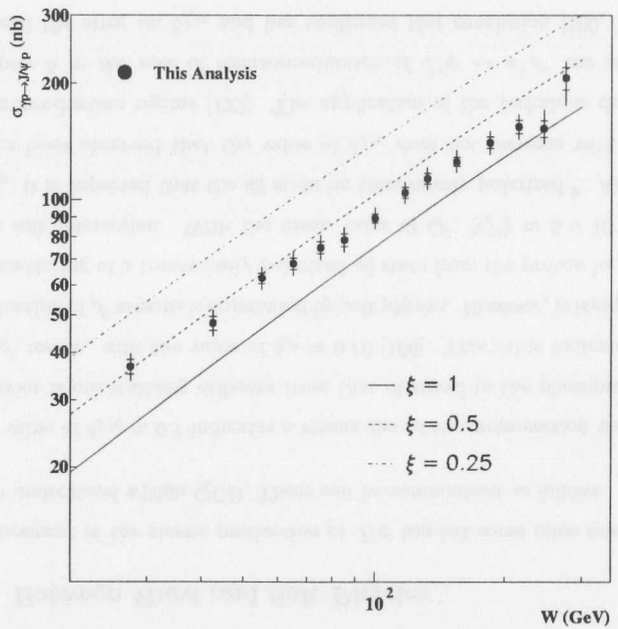

Figure 12.5: The same as Figure 12.4 for different definitions of ξ (see text).

In the calculation performed in [164] the assumption was made that the scale of the interaction is $M^2_{J/\psi}$. This assumption has been modified here to $\xi M^2_{J/\psi}$ where ξ is a parameter. The results of the calculations are shown in Figure 12.5 for three different values of ξ. The normalization of the calculation depends on ξ: the prediction grows as ξ gets smaller. This is understandable since the total DIS cross-section grows as $x = \frac{\xi M^2_{J/\psi}}{W^2} \to 0$ (see Equation (2.24)). Note also that the choice of ξ does not have a strong impact on the dependence of the prediction on W. This is because the steepness

of the rise of the total DIS cross-section changes relatively slowly with $Q^2 = \xi M_{J/\psi}^2$ [26].

12.1.3 The Regge Trajectory

One of the motivations behind this work is to determine whether the measured high energy cross-sections can be expressed in terms of a universal Pomeron trajectory.

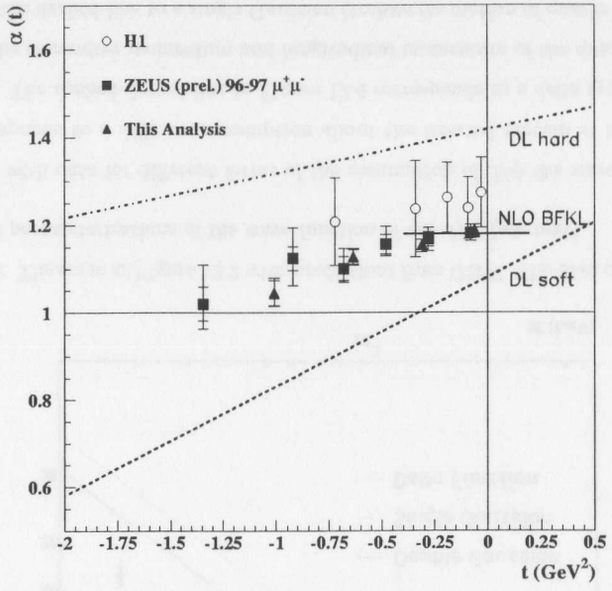

Figure 12.6: The Regge trajectory from elastic J/ψ production as a function of t obtained in this analysis compared with other results from the H1 and ZEUS experiments (see Figure 9.18). Also shown are the "soft" (dashed line) and the "hard" (dot-dashed line) DL Pomeron trajectories and a prediction for the Pomeron intercept based on a NLO BFKL calculation. For presentation purposes the values of t of the present analysis have been shifted by $+0.04\,\mathrm{GeV}^2$.

Figure 12.6 shows the Regge trajectory values calculated from elastic J/ψ production as a function of t from the H1 and ZEUS experiments compared with the trajectories expected from "soft" and "hard" Pomerons. The data lie in between them. It may be concluded that the Regge trajectory from elastic J/ψ is a combination of the "soft" and "hard" Pomeron trajectories.

Also plotted in Figure 12.6 as a horizontal line near $t = 0$ is the Pomeron intercept based on a QCD NLO BFKL calculation [165]. The intercept of the BFKL Pomeron lies close to that determined from the data in this experiment. However, this theory cannot accommodate the observed t-dependence described in Section 9.5.

In Section 12.4.3 the parameters of the Regge trajectory from elastic J/ψ production will be compared with those obtained from other VM's at different values of Q^2.

12.1.4 Between Hard and Soft Physics

The measurement of the elastic production of J/ψ has left some open questions that need to be understood within QCD. These can be summarized as follows:

1. The value of $\delta_{J/\psi} \approx 0.7$ indicates a strong rise of the cross-section with W. This behavior is qualitatively different from that observed in the photoproduction of the ρ^0 meson, with the value of $\delta_{\rho^0} \approx 0.16$ [166]. This value indicates that the production of ρ^0 mesons is dominated by soft physics. However, it is expected that the scattering of a transversely polarized $q\bar{q}$ state from the proton be dominated by a soft interaction. With the mean value of Q^2, $\langle Q^2 \rangle \approx 5 \times 10^{-5}\,\mathrm{GeV}^2 \ll M_{J/\psi}^2$, it is expected that the $q\bar{q}$ state be transversely polarized [2]. Additionally, it has been observed that the value of $\delta_{J/\psi}$ does not increase with Q^2 in the electroproduction regime [122]. The application of the technique developed in Chapter 5 in the case of electroproduction of $J/\psi \to e^+e^-$ has significantly reduced the error on $\delta_{J/\psi}$ and has confirmed this conclusion [100, 159]. This indicates that the W dependence of the longitudinal and transversely polarized

[2] The ratio of longitudinal to transversely polarized production of VM's is proportional to Q^2/M_V^2 for $Q^2 \lesssim 1\,\mathrm{GeV}^2$.

$q\bar{q}$ off the proton are similar for the same final state. This is consistent with the observation made that $R = \sigma_L/\sigma_T$ in the electroproduction of ρ^0 meson is constant with W [42].

2. Strong shrinkage is indicative of soft physics. Within pQCD it is expected that shrinkage be zero or very small. However, it has been observed that the value of $\alpha' = 0.127 \pm 0.032(stat)^{+0.010}_{-0.023}(syst)\,\mathrm{GeV}^{-2}$ deviates from zero by some three standard deviations. It is not clear whether pQCD can accommodate this large value. This suggests that the interaction leading to the photoproduction of J/ψ has a sizeable components of soft physics.

12.2 Elastic Photoproduction of $\psi(2S)$

Figure 10.4 shows the cross-section ratio $\sigma(\psi(2S))/\sigma(J/\psi)$ obtained in Chapter 10 compared with previous H1, ZEUS and fixed target experiments results. Accumulated data indicate a clear suppression of the $\psi(2S)$ production relative to the J/ψ. Within the parton model the production of VM's is factorized: the photon fluctuates into a $q\bar{q}$ pair that scatters on the proton and subsequently forms the VM bound state. The amplitude of the process is given in Equation (2.23). The absolute normalization of the cross-section depends strongly on the VM wave function.

The wave function of the $\psi(2S)$ displays a "node-type" shape with an additional feature that the radius at which the wave function suffers this node is similar to the average distance between the quark-antiquark in the photoproduction limit. Hence, the node effect is expected to be strongest in the case of the charmonium as opposed to other VM's. Calculations within the parton model have predicted that the production cross-section ratio $\sigma(\psi(2S))/\sigma(J/\psi) = 0.17$ [146], consistent with the experimental results (see Figure 10.4). This is a victory for the parton model. VDM, in contrast, fails in predicting the rate of the $\psi(2S)$ production as the couplings of the J/ψ and $\psi(2S)$ to the photon are predicted to be similar [167].

12.3 Elastic Photoproduction of Υ Resonances

Results on the elastic production of Υ resonances with decay through the electronic channel have been reported in Section 11.3. No clear resonant structure has been observed in the $M_{e^+e^-}$ spectrum. However, data show an excess of events over the expected QED background within the search mass window. A combination of these results with a previous result by the ZEUS Collaboration [155] increases the significance of the excess of data events over the expected QED background from two to three standard deviations. It is necessary to accumulate more data in order to produce a reliable measurement of the cross-section of the elastic photoproduction of Υ resonances.

The original pQCD calculations by FKS [59] were based on a model used for the production of J/ψ and undershoot the data of Υ production by a factor of five. These calculations have been updated by FMS [60] and agree well now with the data. Off-diagonal contributions ("skewedness") and a larger value of the real part of the amplitude have pushed up the predictions. pQCD calculations from MRT [61] agree well with data too. A more refined treatment of non-relativistic effects, of the real part of the amplitude and of "skewedness" have lead to the enhancement of the predicted cross-section. A calculation based on the parton-hadron duality applied to $b\bar{b}$ also gives a good agreement with data [61]. Further data taking is required in order to refine pQCD calculations.

pQCD calculations predict that $\delta_{\Upsilon(1S)}$ be significantly larger than $\delta_{J/\psi}$. In order to confirm this a manifold increase in luminosity is required.

12.4 Overview of Elastic VM Production at HERA

The steepness of the rise of the VM production with W is basically driven by the gluon density in the proton, which is probed at an effective scale, $\mu^2 = \xi(Q^2 + M_V^2)$ (where ξ is an unpredicted factor) at low x $\left(x = \frac{Q^2+M_V^2}{W^2}\right)$. Assuming a flavor independent production mechanism the relative production rates should scale approximately with

the square of the quark charges, i.e. the relative production rates should scale as $\rho^0 : \omega : \phi : J/\psi : \Upsilon(1S) = 9 : 1 : 2 : 8 : 2$, referred here as SU(5) ratios (see Table 2.1). It is interesting to determine how the interaction changes the SU(5) ratios.

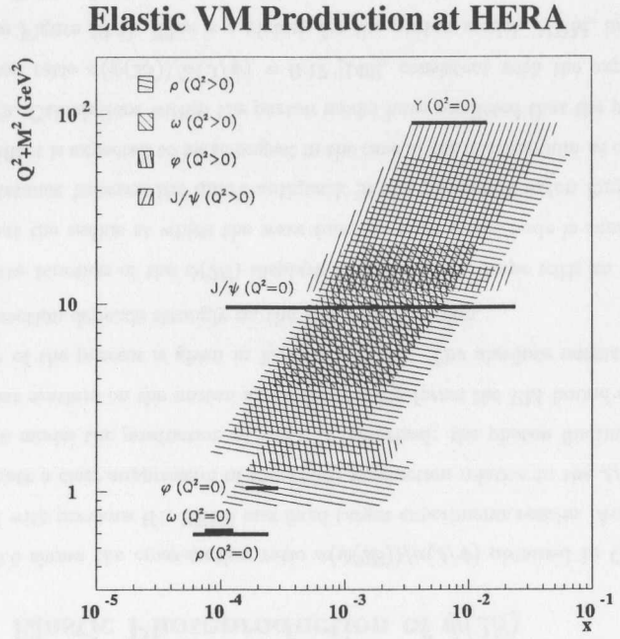

Figure 12.7: Illustration of the coverage in the $(Q^2 + M_V^2)$-x plane of the measurement of the elastic VM production at HERA made so far.

The H1 and ZEUS Collaborations have measured the cross-sections of the elastic production of vector mesons $ep \to eVp$, where $V = \rho^0, \omega, \phi, J/\psi, \psi(2S)$ over a wide range of W, from photoproduction ($Q^2 \simeq 0$) to $Q^2 = 100\,\mathrm{GeV}^2$ [3]. The kinematic

[3]The available data used in this discussion is: photoproduction of ρ^0 [166], photoproduction of ω [168], photoproduction of ϕ [169], photoproduction of J/ψ [142, 136, 137], photoproduction of $\psi(2S)$ [135], photoproduction of Υ [142, 155], electroproduction of ρ^0 [170, 171, 172], electroproduction of ω [173], electroproduction of ϕ [131, 174] and electroproduction of J/ψ [175, 176]. For

range of DIS and VM production overlap at HERA giving us the chance to examine more deeply fundamental issues of the physics of hadronic interactions. Figure 12.7 illustrates the coverage in the $(Q^2 + M_V^2)$-x plane of the measurement of the diffractive VM production at HERA made so far.

12.4.1 The Scale in Elastic VM Production

Recent results on the elastic VM production at HERA have shown that the W dependence of the total cross-section, $\sigma(\gamma^* p \to Vp)$, and the t dependence of the differential cross-section, $d\sigma(\gamma^* p \to Vp)/dt$, is dependent on Q^2 and M_V^2, suggesting that the observables of the interaction are functions of these two variables [134, 177] (see other relevant publications [132, 131, 133]).

It has been shown that the relative production ratios reach approximately the SU(5) ratios at $Q^2 \gg M_V^2$. However, Figure 12.8 [4] shows the total cross-section ratios $\sigma_\omega, \sigma_\phi, \sigma_{J/\psi}$ to σ_ρ being approximately constant with $Q^2 + M_V^2$. This indicates that the dynamics of the scattering of the $q\bar{q}$ state on the proton do not alter the VM production ratios. The ratio $\sigma_{J/\psi}/\sigma_\rho$ in Figure 12.8 is systematically higher than the predicted SU(5) ratio [134, 178, 177]. This effect seems to be independent from $Q^2 + M_V^2$. A possible reason for it may lie in the differences in the wave functions of light and heavy VM's.

Figure 12.9 shows the values of δ obtained from different VM's for different values of Q^2. The upper Plot shows δ as a function of Q^2. The lower Plot shows δ as a function of $Q^2 + M_V^2$. In the upper Plot the measured values of δ in the photoproduction of heavy VM's stand together with those of the light VM's. If one orders the values of δ as a function of $Q^2 + M_V^2$ one sees that the δ in the photoproduction of heavy VM's

simplicity, labels "H1" and "ZEUS" refer to both final and preliminary results. With regards to the photoproduction of J/ψ the data used in this review correspond to results from this analysis reported earlier in [136, 137] unless the label "This analysis" is specified. In the latter case updated data reported in this thesis is used.

[4]This Plot has the label of "ZEUS Preliminary".

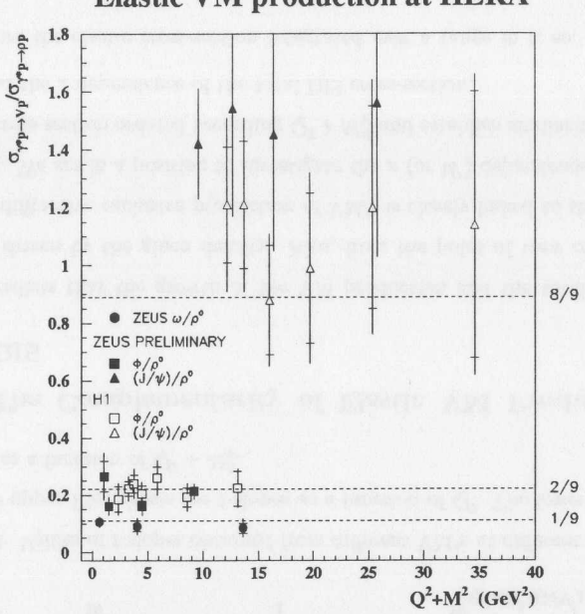

Figure 12.8: The total cross-section ratios $\sigma_\omega, \sigma_\phi, \sigma_{J/\psi}$ to σ_{ρ^0} as a function of $Q^2 + M_V^2$ at fixed W compared to the SU(5) ratios.

are comparable to the δ measured in the electroproduction of light VM's.

Figure 12.10 shows the values of the t-slopes obtained from different VM's at different scales. The upper Plot shows the t-slopes as a function of Q^2. The lower Plot shows the t-slopes as a function of $Q^2 + M_V^2$. The slope parameter, b, is proportional to the squared transverse size of the interaction, $b \propto R^2_{q\bar{q}-p}$ (see Section 2.1). At small values of $Q^2 + M_V^2$ the transverse size of the $q\bar{q}$ is large. As $Q^2 + M_V^2$ increases, the transverse size of the $q\bar{q}$ decreases. At very large $Q^2 + M_V^2$ the t-slope is a measure of the transverse size of the proton. This indicates that the value of $Q^2 + M_V^2$ is setting the scale of the interaction, i.e. governs the transverse size of the colliding objects in the reaction. It is relevant to mention that the transverse size in the interaction depends weakly

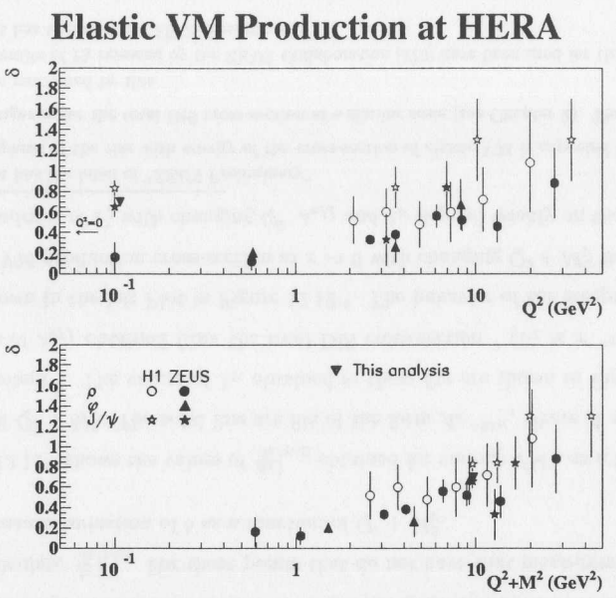

Figure 12.9: Values of δ obtained from different VM's at different Q^2. The upper Plot shows δ as a function of Q^2. The lower Plot shows δ as a function of $Q^2 + M_V^2$.

on the polarization of the VM. This is seen by comparing the t-slopes obtained from the photoproduction of the J/ψ (transverse polarization) and electroproduction of ρ^0 meson (mainly longitudinal polarization) at similar values of $Q^2 + M_V^2$.

This qualitative discussion illustrates that the wave function of the VM may affect the absolute normalization of the cross-sections of heavy VM's relative to light VM's but affects little the shape of their W and t behaviors. The data suggest that δ and b (W and t behaviors) of the elastic VM production are universal functions of the variable $Q^2 + M_V^2$, irrespective of the type of VM. The combination $Q^2 + M_V^2$ seems to be a good choice of scale of the interaction in elastic VM production. This is an important step needed to compare the elastic VM and total DIS cross-sections.

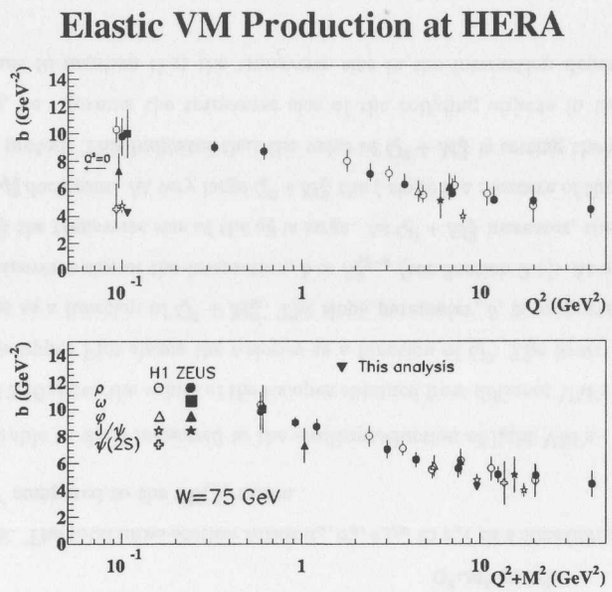

Figure 12.10: Values of t-slopes obtained from different VM's at different Q^2 at $W = 75\,\text{GeV}$. The upper Plot shows the t-slopes as a function of Q^2. The lower Plot shows the t-slopes as a function of $Q^2 + M_V^2$.

12.4.2 The Complementarity of Elastic VM Production to DIS

LO QCD predicts that the growth of the VM production and the total DIS cross-sections are driven by the gluon density. Also, from the point of view of the dipole picture, the diffractive exclusive production of VM's is closely linked to the total DIS cross-section. We are in a position to investigate the x (or W) dependence of the VM production cross-section ordered according $Q^2 + M_V^2$ and establish similarities between the latter and the x dependence of the total DIS cross-section.

We measure the elastic cross-section integrated over a range in t, so, assuming a

single exponential, the following relation holds:

$$\left.\frac{d\sigma}{dt}\right|_{t=0} \approx \sigma b \tag{12.1}$$

where b is extracted by each experiment for each VM from the differential cross-sections. We may present $\left.\frac{d\sigma}{dt}\right|_{t=0}$ in bins of $Q^2 + M_V^2$. The $\left.\frac{d\sigma}{dt}\right|_{t=0}$ in bins of $Q^2 + M_V^2$ plot utilizes the following steps:

1. Scale the cross-sections to that of the ρ^0 meson according to the SU(5) ratios.
2. Make appropriate bins in $Q^2 + M_V^2$. The center of the bin is calculated as the error weighted average of the points in the bin.
3. The cross-section of each point is shifted to the error weighted average in each bin. For simplicity, this is done according to the parameterization of the $Q^2 + M_V^2$ dependence of the VM cross-sections.
4. For those points that come with their measurement of b we use the latter value to calculate $\left.\frac{d\sigma}{dt}\right|_{t=0}$. For those points that do not have that measurement we use the parameterization of b as a function of $Q^2 + M_V^2$.

Figure 12.11 [5] shows the values of $\left.\frac{d\sigma}{dt}\right|_{t=0}$ obtained for various VM's as a function of x in bins of $Q^2 + M_V^2$. The solid line are fits of the form $Ax^{-2\lambda_V}$, where A and λ_V are free parameters [6]. The values of λ_V obtained in these fits are shown in Figure 12.12. The values of λ_{eff} obtained from the total DIS cross-section [7] ($F_2 \propto x^{-\lambda_{eff}}$ at fixed Q^2) are shown in the left Plot in Figure 12.12 [8]. The behavior of the steepness of the rise of the VM production cross-section as $x \to 0$ with changing $Q^2 + M_V^2$ is similar to the x dependence of F_2 with changing Q^2. λ_{eff} and λ_V depend weakly on the scale (Q^2

[5] This Plot has the label of "ZEUS Preliminary".

[6] The steepness of the rise with energy of the cross-section of elastic VM is expected to be about twice as stronger as for the total DIS cross-section at a similar scale (see Chapter 2). The factor 2 in front of λ_V is motivated by this.

[7] Recent results of F_2 released by the ZEUS Collaboration [179] have been used for this fits [180].

[8] This Plot has the label of "ZEUS Preliminary".

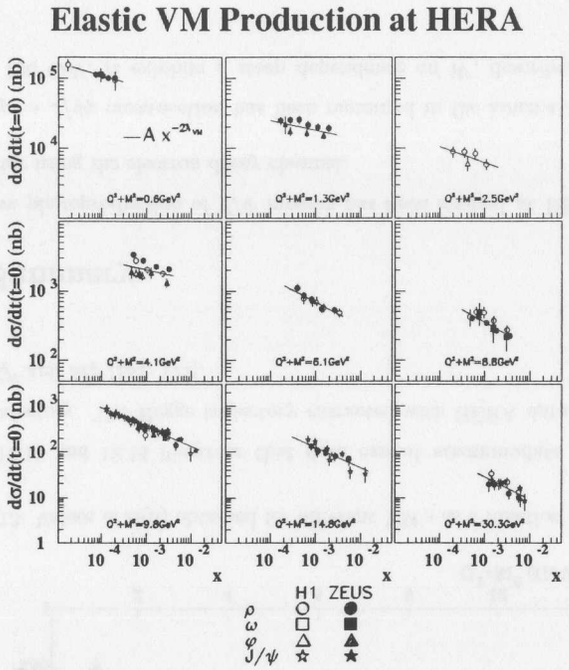

Figure 12.11: Elastic $\frac{d\sigma}{dt}|_{t=0}$ for various VM's as a function of x in bins of $Q^2 + M_V^2$ (see text). The solid lines are fits of the form $Ax^{-2\lambda_V}$.

and $Q^2 + M_V^2$, respectively). This correlation becomes stronger at larger scales. The similarities between λ_V and λ_{eff} are evident.

This qualitative discussion serves as an indication that the dynamics that drive the increase with energy of the total DIS and VM cross-sections are very similar. From the point of view of the dipole model, both cross-sections may be easily related to each other (see Equations (1.14) and (2.24)): $\sigma_{q\bar{q}}$ is the underlying cross-section to both processes. A theoretical description of $\sigma_{q\bar{q}}$ should be able to describe simultaneously both the total DIS and VM cross-sections. The addition of VM data to the analysis of $\sigma_{q\bar{q}}$ enhances the sensitivity of HERA data to issues like the interface between "hard"

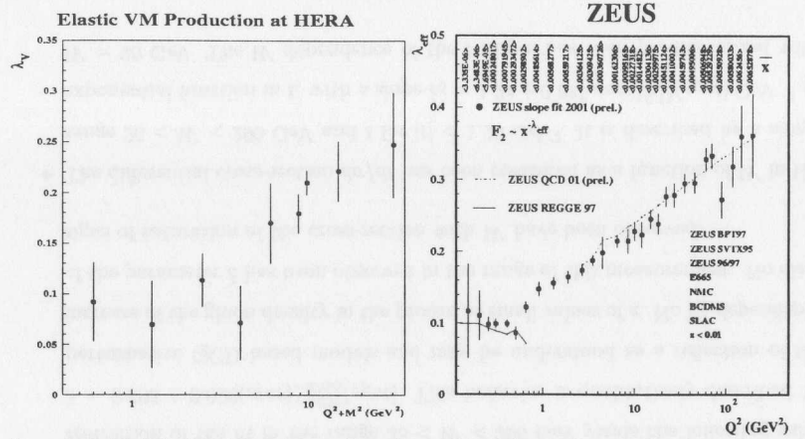

Figure 12.12: The left Plot shows the values of λ_V obtained from the fit of the elastic VM cross-sections, $\frac{d\sigma}{dt}|_{t=0}$, in bins of $Q^2 + M_V^2$ to the form $Ax^{-2\lambda_V}$. The right Plot shows the values of λ_{eff} obtained by fitting the proton structure function, F_2, at fixed Q^2 to $Ax^{-\lambda_{eff}}$.

and "soft" physics and saturation effects.

12.4.3 Is There an Universal Pomeron Trajectory?

Figures 12.13 and 12.14 show the parameters of Regge trajectories extracted from the production of different VM's at HERA [9] as a function of $Q^2 + M_V^2$. Figure 12.13 shows a clear correlation between $\alpha(0)$ and $Q^2 + M_V^2$. This is understandable since the steepness of the rise of cross-sections increases with $Q^2 + M_V^2$. Figure 12.14 displays a weak correlation between α' and $Q^2 + M_V^2$. There seems to be an indication that the value of α' (or "shrinkage") decreases with $Q^2 + M_V^2$. The value of α' for the photoproduction of ρ^0 meson lies above the one obtained for the photoproduction of J/ψ and for the electroproduction of ρ^0 meson. More precise determination of the Regge trajectory in the electroproduction regime will shed light on the dependence of

[9] No data from fixed target experiments were used for the extraction of the Regge trajectories.

the α' with the scale of the interaction.

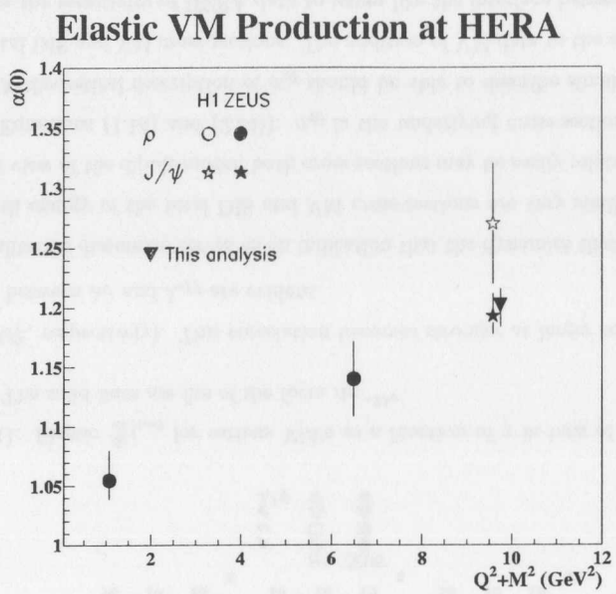

Figure 12.13: Values of $\alpha(0)$ obtained for different VM's as a function of $Q^2 + M_V^2$.

Figures 12.13 and 12.14 illustrate that data cannot accommodate one universal Pomeron trajectory. The Regge trajectory extracted with HERA data only seem to depend on Q^2 and M_V^2 [181, 177].

12.5 Summary

The exclusive photoproduction of J/ψ mesons has been studied at HERA with the ZEUS detector using the electron decay channel.

- The $\gamma p \to J/\psi p$ cross-section has been measured in the kinematic range $20 < W < 290$ GeV. It exhibits a steep dependence on W, described by a single

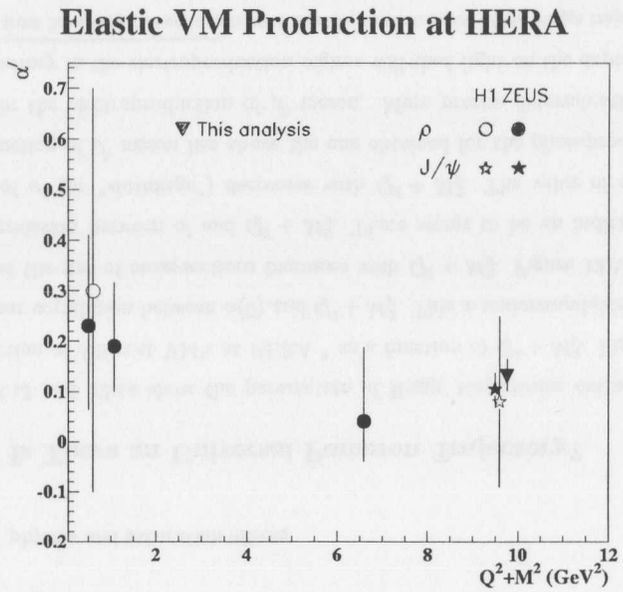

Figure 12.14: Values of α' obtained for different VM's as a function of $Q^2 + M_V^2$.

power-like behavior of the type W^δ with $\delta = 0.698 \pm 0.017(stat)^{+0.016}_{-0.019}(syst)$. The restriction of the fit in the range $35 < W < 290$ GeV yields the following value $\delta = 0.695 \pm 0.020(stat)^{+0.025}_{-0.025}(syst)$. This behavior is qualitatively described by perturbative QCD based models and may be understood as a reflection of the increase of the gluon density in the proton at small values of x. No W dependence of the parameter δ has been observed in the range of this measurement. No clear signs of saturation of the cross-section with W have been observed.

- The differential cross-section $d\sigma/dt$ has been measured as a function of W in the range $20 < W < 290$ GeV and t for $|t| < 1.25$ GeV^2. It is described by a single exponential function in t, with a slope $b_0 = 4.24 \pm 0.07(stat)^{+0.19}_{-0.11}(syst)$ GeV^{-2} at $W = 90$ GeV. The W dependence of the t-slopes has been parameterized with

Expression (9.14) with $\alpha' = 0.127 \pm 0.032(stat)^{+0.010}_{-0.023}(syst)\,\mathrm{GeV}^{-2}$.

- The Regge trajectory has been determined from the W and t dependence of $d\sigma/dt$ in the range $20 < W < 290$ GeV and $|t| < 1.25$ GeV^2. The fit yields $\alpha(0) = 1.202 \pm 0.013(stat)^{+0.003}_{-0.012}(syst)$ and $\alpha' = 0.131 \pm 0.028(stat)^{+0.008}_{-0.019}(syst)\,\mathrm{GeV}^{-2}$. The data show that α' is small but different from zero. The measured intercept is neither compatible with the "soft" Pomeron mechanism alone nor with the "hard" Pomeron mechanism alone.

- The J/ψ spin density matrix elements r^{04}_{00} and r^{04}_{1-1} have been measured using the decay angular distributions defined in the helicity frame. Their values are consistent with the s-channel helicity conservation hypothesis.

- These pieces of experimental information suggest the presence of both "hard" and "soft" physics in the dynamics underlying the photoproduction of the J/ψ in this kinematical region.

The exclusive photoproduction of $\psi(2S)$ mesons has been studied at HERA with the ZEUS detector using the electron decay channel.

- The ratio $\sigma(\psi(2S))/\sigma(J/\psi)$ has been measured in the range $50 < W < 125\,\mathrm{GeV}$, yielding $0.15 \pm 0.03^{+0.04}_{-0.04}$. This value is consistent with previous measurements and confirms the suppression of the production of $\psi(2S)$ with respect to the production of J/ψ, as predicted within the parton model.

The exclusive photoproduction of Υ resonances has been studied at HERA with the ZEUS detector using the electron decay channel.

- No clear evidence of Υ resonances has been found through the electronic channel with data taken during the 1996 through 2000 running periods. The combined upper limit to the photoproduction cross-section of $\Upsilon(1S)$ at a 95% CL is $\sigma^{Limit}_{\gamma p \to \Upsilon(1S) p} = 517\,\mathrm{pb}$.

An overview of the accumulated elastic VM production at HERA indicates:

- The W and t behaviors of the cross-sections seem to depend little on the details of the wave function and polarization of the VM. The quantity $Q^2 + M_V^2$ is a good choice of the scale of the interaction. After correcting the VM cross-sections by the SU(5) ratios the absolute normalization of the cross-sections of heavy VM's is larger than that of light VM's.

- Data indicate that the dynamics that drive the increase of the total DIS and VM cross-sections are similar. This suggests the need for a phenomenological framework that describes simultaneously both total DIS and VM cross-sections.

- All data cannot accommodate one universal Pomeron trajectory. The parameters of the Regge trajectories extracted with HERA data seem to depend on Q^2 and M_V^2.

Appendix A

UCAL Energy Response to EM Showers at Low Energies

The ZEUS Collaboration has developed extensive efforts to understand the energy scale and energy resolution of the UCAL "in situ" using various techniques for energy depositions, E, $E > 10\,\text{GeV}$. Studies of the UCAL energy response to electromagnetic showers at low energies ($E < 10\,\text{GeV}$) are described here. This study is central to the extension of the W range of the measurement of the diffractive production of heavy VM's, $V \to e^+e^-$ (see Chapter 5).

A.1 Energy Scale

A.1.1 Method

There are different methods for the calibration of detectors "in situ" with data. For each method a functional relation, a function of the energy scale, S, energy response of the UCAL, E, and other experimental variables, ζ, is defined:

$$\xi = F(E, \zeta) \tag{A.1}$$

Each event i in the data sample selected for calibration defines a variable ξ_i according to Equation (A.1), where E_i, ζ_i are the energy and other variables in the event, respectively. For the whole data sample a distribution of ξ is obtained. The value of S is defined as the scale factor such that the distribution of $F(E/S, \zeta)$ is centered at zero. If the peak of the distribution of ξ is centered at zero then S=1 and data do not need to be corrected. The same procedure is performed on the MC simulation. This method provides for an absolute determination of the energy scale of the response of the UCAL in data independent of the MC simulation. Also, it provides an absolute determination of the energy scale of the MC simulation. For purposes of the physics analysis it is useful to determine the difference of the scale in data and MC, $S_{MC} - S_{Data}$.

A.1.2 Energy Scale of RCAL

Two methods are used to determine the energy scale of electromagnetic showers in the RCAL: the comparison of energy and CTD momentum of tracks and the P_t balance of the electromagnetic objects in high $M_{e^+e^-}$ elastic QED processes.

The data and the ZEUSVM MC events used in the first method pass the following off-line cuts:

- Event triggered by slot FLT58 (see Section 5.4.1).
- At least one isolated electromagnetic cluster in the RCAL with a track matched to it (see Section 6.4).
- The electromagnetic clusters should fall into the fiducial region of the RCAL defined in Figure A.1.
- The tracks should have crossed at least 7 superlayers of the CTD.
- Elasticity requirement is imposed on the event (see Section 6.4).

Figure A.2 shows the distribution of the energy of electromagnetic clusters and momentum of matched tracks in data and MC. The data contain both resonant J/ψ

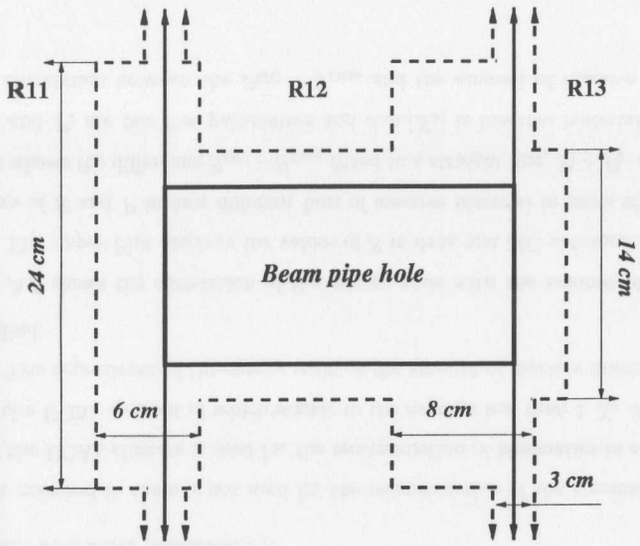

Figure A.1: The dimensions of the fiducial cuts applied on the position of electromagnetic clusters in the RCAL. Clusters in the region between the beam pipe hole and the dashed lines are excluded.

and QED processes. The energy distributions peak at $E = 2$ GeV, but enough statistics is left in the interesting range of $3 < E < 5$ GeV, not explored before.

The following function is chosen to extract the scale factor for data and MC:

$$F(E,P) = \frac{E}{P} - 1 \tag{A.2}$$

The CTD momentum of the track, P, goes into the denominator of the first term of Equation (A.2) as the resolution of $1/P$ is Gaussian. As a result, the ratio E/P has also a Gaussian distribution.

Distributions are made in bins of CTD momentum, which is the variable that is best determined in the dynamic range of the present analysis. The peaks of the distributions in bins of P are fitted to Gaussian functions. Each fit produces a mean value, which is

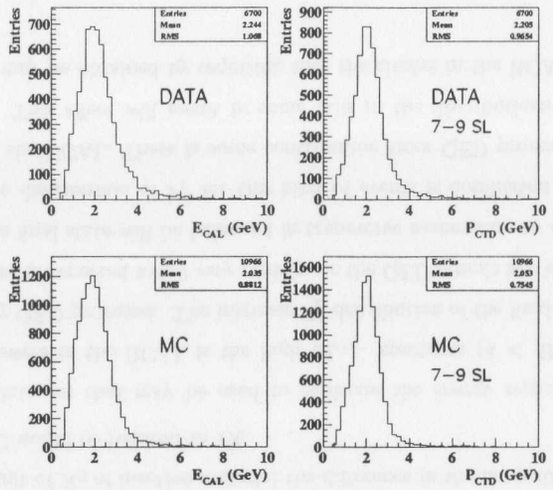

Figure A.2: Distribution of energy of electromagnetic clusters and momentum tracks in data and the ZEUSVM MC. The data contain both resonant J/ψ and QED processes.

the scale, S.

The results of S are shown in Figure A.3. The upper Plot displays the values of S in data and MC obtained in four different bins of P. The lower Plot shows the difference $S_{MC} - S_{Data}$. The difference of S in data and MC as a function of momenta may be fitted to a straight line with a free parameter P_1. The result of the fit shows that the scale in MC is larger than in data by some 3.5%.

The UCAL clusters in the events selected in this study are located in an region of the UCAL in front of which there stands a relatively large amount of inactive material. Figure A.4 shows the distribution of inactive material in units of radiation length, X_0, that a track needs to cross before reaching the UCAL in the selected sample. Tracks need to cross in the average 2 units of X_0 ranging from 1 to 3 X_0. The energy loss due to inactive material is corrected for using MC simulation [182]. This is done the same way in data and in MC. In the analysis of the J/ψ the energy of clusters with a

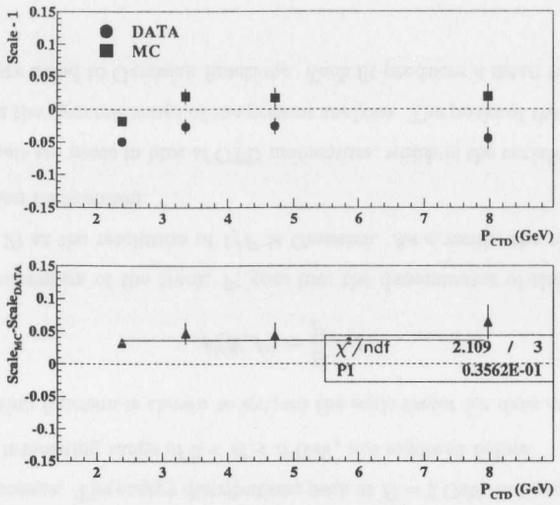

Figure A.3: The upper Plot displays the values of S in data and MC obtained using the comparison of UCAL energy, E, and CTD momentum, P, in four different bins of P. The lower Plot shows the difference $S_{MC} - S_{Data}$ as a function of P fitted to a straight line with a free parameter P_1.

long track matched to them is not used for the reconstruction of the kinematics. The energy of the UCAL clusters is used for the reconstruction of kinematics in a different region of the UCAL in front of which stands in the average less than 1 X_0 of inactive material. The dependence of the energy scale on the amount of inactive material needs to be studied.

Figure A.5 shows the correlation of the energy scale with the amount of inactive material. The upper Plot displays the values of S in data and MC obtained using the comparison of E and P in four different bins of inactive material in units of X_0. The lower Plot shows the difference $S_{MC} - S_{Data}$ fitted to a straight line, $P_1 + P_2 \cdot d.m.[X_0]$, where P_1 and P_2 are two free parameters and $d.m.[X_0]$ is inactive material in units of X_0. A correlation between the $S_{MC} - S_{Data}$ and the amount of inactive material

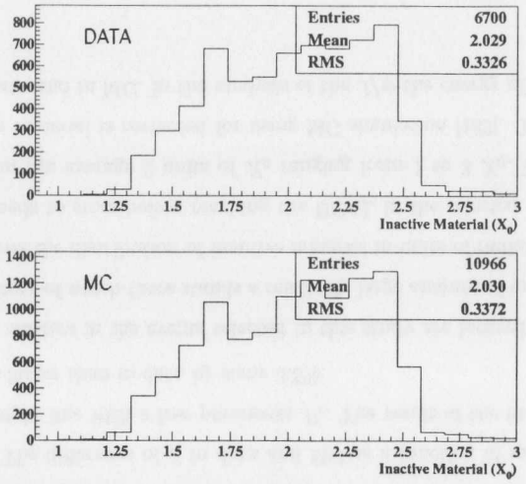

Figure A.4: Distribution of inactive material in units of radiation length, X_0, that a track needs to cross before reaching the UCAL (see text). The upper Plot corresponds to data and the lower Plot to MC.

is observed, which may explain a significant part of the different of the scale in the present selection of events. If the straight line in Figure A.5 is extrapolated to the region of 1 unit of X_0 of inactive material the difference in the normalization between data and MC would be reduced to 1%.

Another data set that may be used to calibrate the energy response to electromagnetic showers in the RCAL is the high $M_{e^+e^-}$ spectrum ($4 < M_{e^+e^-} < 8\,\text{GeV}$) dominated by QED processes. The intrinsic P_t^2 distribution of the final state in elastic QED processes is expected to fall very rapidly. In the QED sample two electromagnetic objects in the final state will be balanced in transverse momentum to a good approximation. The distribution of P_t^2 for this kind of events is dominated by the energy resolution of the UCAL. There is some contribution from QED processes via proton dissociation. This effect will result in some tails in the distributions in data. The energy scale may be obtained by requiring that the cluster in the RCAL be balanced

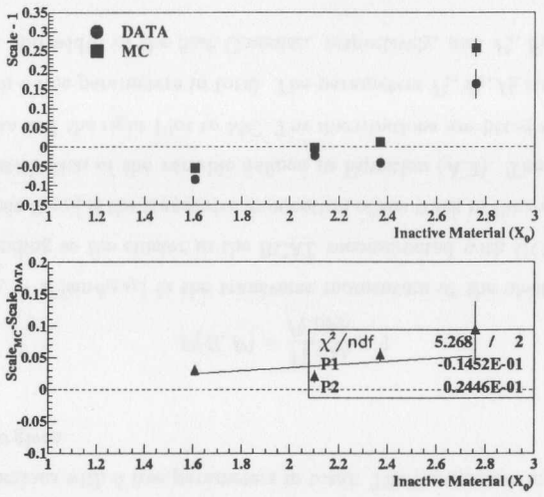

Figure A.5: The upper Plot displays the values of S in data and MC obtained using the comparison of UCAL energy, E, and CTD momentum, P, in four different bins of inactive material in units of radiation length, X_0. The lower Plot shows the difference $S_{MC} - S_{Data}$ fitted to a straight line with two free parameters, $P_1 + P_2 \cdot d.m[X_0]$, where $d.m[X_0]$ is inactive material in units of X_0.

in transverse momentum with a long track. The intrinsic P_t^2 distribution of the final state may bias the absolute determination of the energy scale. However, this effect will cancel out of one looks into $S_{MC} - S_{Data}$ provided that MC describes the kinematics of the QED final state.

The following class of events is used to calibrate the RCAL using the "P_t balance" method:

- The event triggered by slot FLT58 (see Section 5.4.1).
- The presence in the event of one long tracks (7 or 9 superlayers) and an electromagnetic cluster in the RCAL.

- Require $4 < M_{e^+e^-} < 8$ GeV.
- Elasticity requirement. This will get rid of a significant fraction of proton dissociative events in data (see Section 6.4).

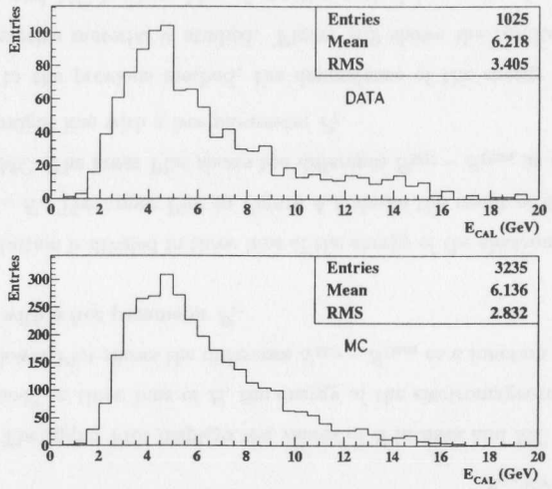

Figure A.6: The energy distribution of the electromagnetic clusters in the RCAL in the set of events selected for the "P_t balance" method in data and MC. MC corresponds to elastic Bethe Heitler process (the LPAIR MC). The data are dominated by Bethe Heitler process with some contribution from QED Compton and proton dissociative processes.

Figure A.6 shows the energy distribution of the electromagnetic cluster in the RCAL in the set of events selected for the "P_t balance" method in data and MC. MC corresponds to elastic Bethe Heitler process (the LPAIR MC). The energy distributions both in data and MC peak at $E = 4.5$ GeV and enriched the calorimeter studies at low energy in the range $5 < E < 10$ GeV.

The following function is defined to study the energy scale with the "P_t balance"

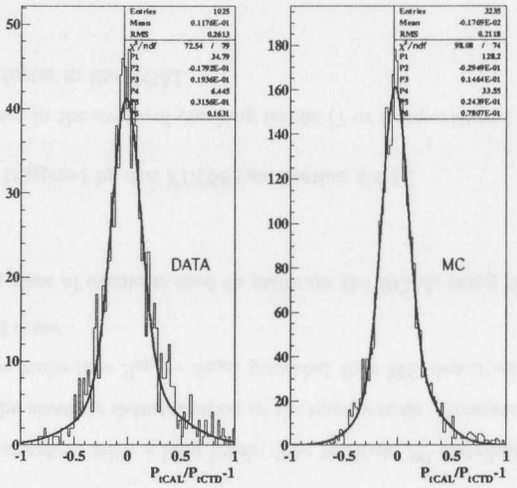

Figure A.7: The distribution of $\frac{P_{t\ CAL}}{P_{t\ CTD}} - 1$, where $P_{t\ CAL} = E|\sin\theta_{CAL}|$ is the transverse momentum of the electromagnetic object corresponding to the cluster in the RCAL reconstructed with UCAL energy, and $P_{t\ CTD} = P|\sin\theta_{CTD}|$ is the transverse momentum of the track in the events selected for the "P_t balance" method. The left Plot corresponds to data and the right Plot to MC. The distributions are fitted to two Gaussian functions with 6 free parameters in total. The parameters and the $\chi^2/n.d.f.$ of the fits are given.

method:

$$F(E,P) = \frac{P_{t\ CAL}}{P_{t\ CTD}} - 1 \tag{A.3}$$

where $P_{t\ CAL} = E|\sin\theta_{CAL}|$ is the transverse momentum of the electromagnetic object corresponding to the cluster in the RCAL reconstructed with UCAL energy, and $P_{t\ CTD} = P|\sin\theta_{CTD}|$ is the transverse momentum of the track in the event. Figure A.7 shows the distribution of the variable defined in Equation (A.3). The left Plot corresponds to data and the right Plot to MC. The distributions are fitted to two Gaussian functions with 6 free parameters in total. The parameters P_1, P_2, P_3 correspond to the height, mean and width of the first Gaussian, respectively, and P_4, P_5, P_6 correspond

to the height, mean and width of the second Gaussian, respectively. The value of S is defined as the mean value of the first Gaussian.

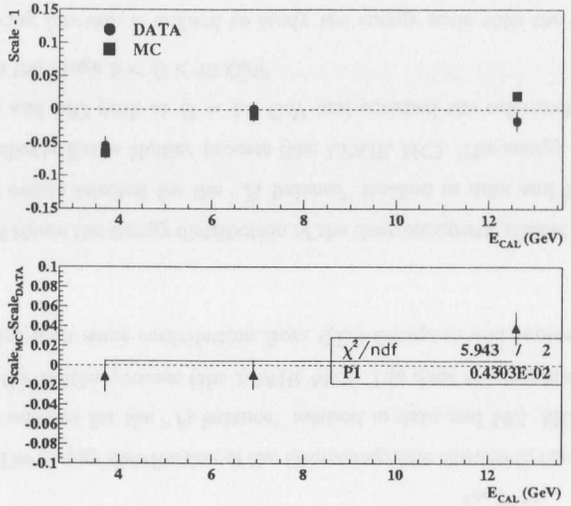

Figure A.8: The upper Plot displays the values of S in data and MC obtained using the "P_t method" in three bins of E, the energy of the electromagnetic cluster in the RCAL. The lower Plot shows the difference $S_{MC} - S_{Data}$ as a function of E fitted to a straight line with a free parameter P_1.

The distribution is divided in three bins of the energy of the electromagnetic cluster in the RCAL, E. The upper Plot in Figure A.8 shows the result of the energy scale in data and MC. The lower Plot shows the difference $S_{MC} - S_{Data}$ as a function of E fitted to a straight line with a free parameter P_1.

Similarly to the previous method, the dependence of the energy scale with the amount of inactive material is studied. Figure A.9 shows the results of the energy scale in data and MC in three bins of inactive material in units of radiation length X_0. The lower Plot shows the difference $S_{MC} - S_{Data}$ fitted to a straight line with two free parameters, $P_1 + P_2 \cdot d.m.[X_0]$. Here the energy scale is also correlated with the

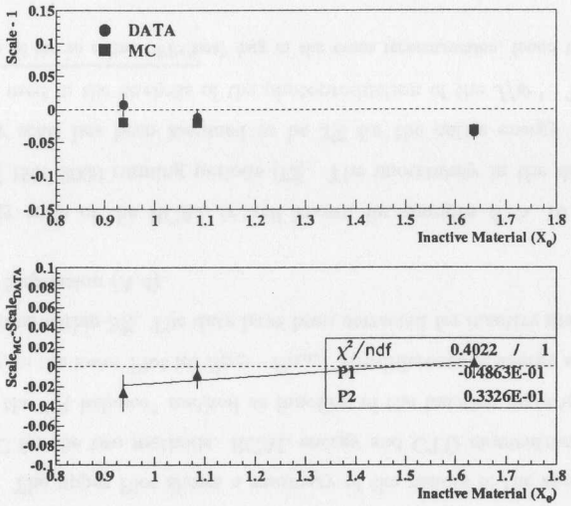

Figure A.9: The upper Plot displays the values of S in data and MC obtained using the "P_t balance" method in three bins of inactive material in units of radiation length, X_0. The lower Plot shows the difference $S_{MC} - S_{Data}$ fitted to a straight line with two free parameters, $P_1 + P_2 \cdot d.m.[X_0]$, where $d.m[X_0]$ is inactive material in units of X_0.

amount of inactive material crossed by the electromagnetic object. The correlation is similar to that obtained using the method of the comparison of the UCAL energy and the CTD momentum displayed in Figure A.5.

At this point it was decided to parameterize the correlation of the difference of the energy scale in data and MC as a function of the inactive material in units of X_0 for the entire energy range covered by both methods:

$$S_{MC} - S_{Data} = 0.015 - 0.025 \cdot d.m.[X_0] \tag{A.4}$$

The error on the parameter P_2 of the correlation is ± 0.01. For practical purposes, in the analysis of the photoproduction of J/ψ, $d.m. \approx 1\ X_0$, which leads to a correction of the order of 1% in the average. The correlation of the difference of the energy scale in data

and MC most probably has little to do with a possible non-linear response of UCAL. The improper simulation of the pre-showering of electrons as they pass through the inactive material in front of the UCAL is a probable candidate to explain this effect. The energy loss by pre-showering of an electron for different thickness of absorber material in front of the UCAL prototype was studied in [183] in data and [184] in MC. It has been shown that the energy loss of an electron due to the absorber depends strongly on the energy of the electron for energies $E < 5$ GeV.

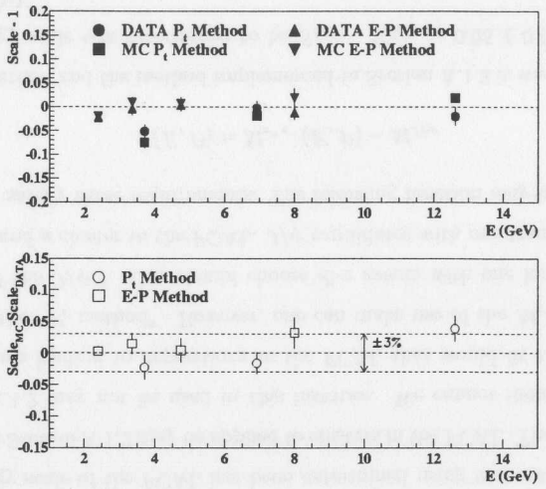

Figure A.10: The upper Plot shows a summary of the results of S for data and MC as a function of the energy for the two methods: the RCAL energy and CTD momentum comparison method and the "P_t balance" method. Similarly, in the lower Plot for $S_{MC} - S_{Data}$. The difference of energy scales in data and MC in the range $3 < E < 10$ GeV remains within 3%. The data have been corrected for inactive material effects according to Expression (A.4).

Figure A.10 displays summary Plots of the energy scale studies at low energy. The upper Plot shows the results of the energy scales for data and MC for the two methods as a function of the energy. Similarly, in the lower Plot for $S_{MC} - S_{Data}$. The data have

been corrected for inactive material effects according to Expression (A.4). Figure A.11 displays a summary of results of the energy scale as a function of the inactive material. The upper Plot shows a summary of the results of the energy scales of data and MC for the two methods as a function of the inactive material in units of X_0. Similarly, in the lower Plot for $S_{MC} - S_{Data}$.

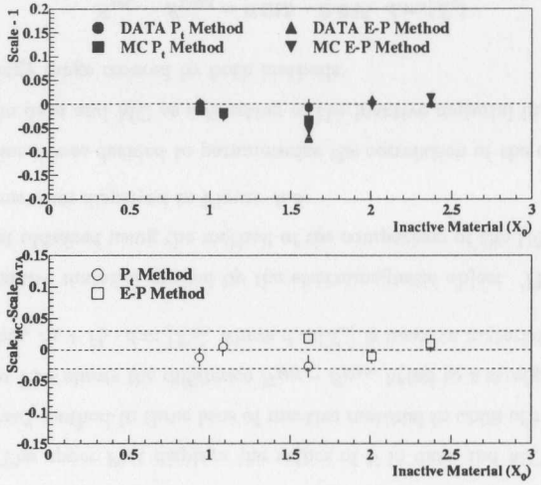

Figure A.11: The upper Plot shows a summary of the results of the energy scales of data and MC for the two methods: RCAL energy and CTD momentum comparison method and the "P_t balance" method as function of the inactive material in units of X_0. Similarly, in the lower Plot for $S_{MC} - S_{Data}$. The difference of energy scales in data and MC remains within 3%. The data have been corrected for inactive material effects according to Expression (A.4).

The energy scale of the RCAL is well known for energies $E > 10$ GeV in the conditions of 1999-2000 running periods [73]. The uncertainty in the determination of the energy scale has been assumed to be 3% for the entire energy range $3.5 < E < 20$ GeV used in the analysis of the photoproduction of the J/ψ [1]. The error on

[1] As a result of the so called "FPChot" bug in the event reconstruction, found in the summer of 2001, the values of S in data and MC will decrease by an offset between 0.0025 and 0.005. The difference will remain unchanged.

the energy scale has been propagated to the systematic error of the cross-section (see Section 9.3).

A.1.3 Energy Scale of FCAL

The response to electromagnetic showers in the FCAL is the worst known of all the sections of the UCAL. The energy scale "in situ" of the FCAL at energies $E > 10$ GeV is practically unknown. This is due to the fact that not enough data have been taken to collect a sizeable set of events with electrons scattered at large angles (very high Q^2 events). The production of J/ψ offers almost an unique opportunity to quantify $S_{MC} - S_{Data}$ for the electromagnetic section of the FCAL.

The energy scale of the FCAL has been determined using two methods. The first method used Section A.1.2 may be applied to clusters in the FCAL. The second method in Section A.1.2 may not be used in this instance. We cannot identify a dominant physics process leading to depositions in the FCAL that would fit the requirements imposed by the "P_t method". However, one can make use of the $M_{e^+e^-}$ spectrum in the region of the J/ψ [2]. One should choose di-e events with one long enough track in the CTD and a cluster in the FCAL. J/ψ candidates with one track topology with $W < 35$ GeV satisfy these requirements. The following function may be used:

$$F(E,P) = M_{e^+e^-}(E,P) - M_{J/\psi} \tag{A.5}$$

Using this method and the method implemented in Section A.1.2 it was found that the relative energy scale was determined to be $S_{MC} - S_{Data} = 0.05 \pm 0.03$, in the range $3 < E < 10$ GeV.

The $M_{e^+e^-}$ spectrum of J/ψ candidates at $W < 35$ GeV after background subtraction is shown in Figure 9.5. The energy of electromagnetic clusters in the FCAL has been corrected in data by +5%.

[2] This method may be also used for the calibration of the RCAL.

A.2 Energy Resolution of RCAL

Two selections are used to compare the resolution of the energy response in data and MC: the sample used in Section A.1 to calibrate the energy response of the RCAL using the method of the comparison of CTD momentum and UCAL energy and the elastic QED Compton selection. Elastic QED events are allowed in the trigger selection developed in Chapter 5).

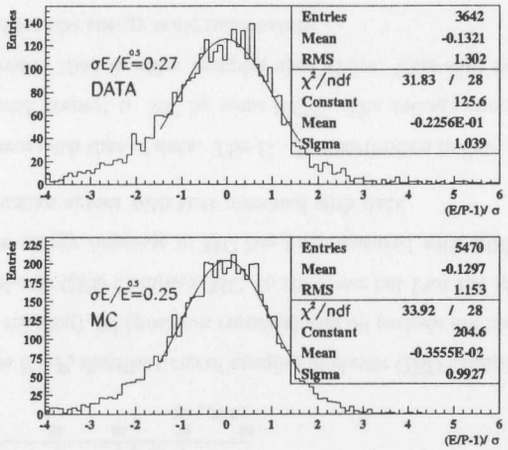

Figure A.12: The distribution of $(E/P-1)$ over the resolution of that variable for the set of events used in the method of the comparison of CTD momentum and UCAL energy. The distributions in data and MC have been fitted to a Gaussian function. The resolution of the energy response of the RCAL has been parameterized with $\sigma_E = \alpha\sqrt{E}$ so that the sigma the Gaussian is approximately equal to unity.

Figure A.12 shows the distribution of $(E/P-1)$ over the resolution of that variable for the set of events used in the method of the comparison of CTD momentum and UCAL energy. The distributions in data and MC have been fitted to a Gaussian function. The resolution of CTD momentum was taken from the parameterization obtained in Appendix B (see Expression (B.5)). The contribution of the resolution of

CTD momentum to the variable $(E/P-1)$ is small compared to the contribution of the UCAL energy resolution. The resolution of the energy response of the RCAL has been parameterized with $\sigma_E = \alpha\sqrt{E}$ so that the sigma the Gaussian is approximately equal to unity in both data and MC. The resolution of the energy response simulated by MC is somewhat better than that seen in data. The values obtained are $\alpha_{Data} = 0.27$ and $\alpha_{MC} = 0.25$. According to this the energy response in the MC should be smeared with $0.1\sqrt{E}$.

In events from elastic QED Compton process a photon and an electron end up in the RCAL that carry the energy of the incoming electron. The $E - P_z$ in the event, calculated with the UCAL information of the two electromagnetic clusters should be close to $2E_e = 55$ GeV, where E_e is the energy of the incoming electron. After applying all corrections listed in Section 6.2.2, including the correction parameterized in Expression (A.4), the $E - P_z$ in data and MC may be compared.

The off-line cuts to select elastic QED Compton are:

- Two electromagnetic clusters in the RCAL with $W > 290$ GeV.
- Elasticity requirement (see Section 6.4).

Several samples of elastic QED Compton events taken during the various periods of the 1999 and 2000 running were selected and compared to the COMPTON MC. The distributions in data and MC have been fitted to Gaussian functions. The parameters of the fits show the stability of the energy scale and the resolution of the RCAL over the running periods of 1999 and 2000. It was observed that the energy resolution in MC was too good compared to data.

Figure A.13 displays the $E - P_z$ distributions of samples of elastic QED Compton taken during various periods of the 1999 and 2000 running merged in one and compared with elastic QED Compton MC. In the lower left Plot the MC is overlaid on top of the data. This Plot shows that data and MC do not display undesirable long resolution tails. The energy response in MC has been smeared with $0.06\sqrt{E}$ so that the width of

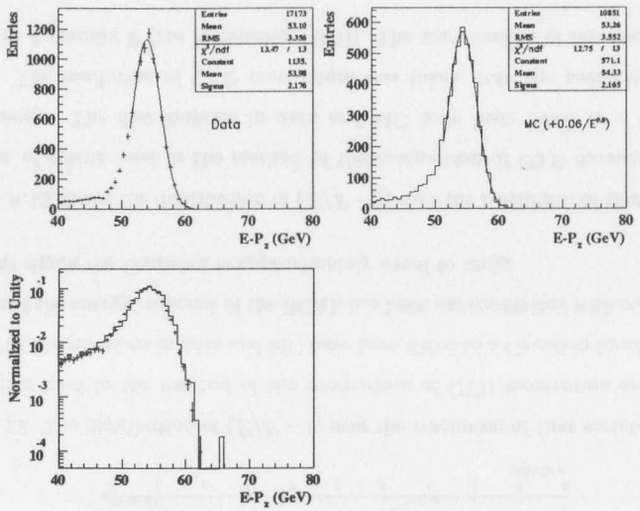

Figure A.13: The $E-P_z$ distributions of samples of elastic QED Compton taken during the 99 (electron running), 99 (positron running) and 00 periods are merged in one and compared with elastic QED Compton MC. In the lower left Plot the MC is overlaid on top of data. The energy response in MC has been smeared with $0.06\sqrt{E}$ so that the width of the Gaussian agrees with that obtained with data.

the Gaussian agrees with that of data. The $E-P_z$ distribution in data is in this sample slightly shifted with respect to MC by some 0.65%. The average energy of clusters in this sample is greater than in other samples used above. This shift is well within the 3% error claimed for the energy scale uncertainty.

The difference in resolution in data and MC may be dependent on the amount of inactive material. This effect is not studied here. Instead, a conservative variation of the amount of smearing applied on MC is made as a systematic check. The nominal smearing applied on MC is $0.06\sqrt{E}$. As a systematic check, the smearing in MC was set to zero and to $0.15\sqrt{E}$ (see Section 9.3).

Appendix B

CTD Studies

This Appendix contains studies of the CTD momentum scale and resolution [138]. The determination of the cross-section of the photoproduction of J/ψ became a precision measurement. The understanding of the basic features of the response of the CTD had become relevant to the measurement. The parameters of the response of the CTD as extracted here may be used for other physics analyses performed with the ZEUS detector. Also, the CTD momentum is used for calibration of other components of the ZEUS detector. For this purpose, it is relevant to know the momentum scale of the CTD to a high level of accuracy.

B.1 CTD Momentum Scale

A combined analysis of the CTD momentum scale is done in data and MC by reconstructing the invariant mass of two tracks in the vicinity of the J/ψ resonance for two decay modes: $J/\psi \to e^+e^-$ and $J/\psi \to \mu^+\mu^-$.

Electrons are likely to radiate while passing through the beam pipe and the CTD, which results in the distortion of the di-e mass spectrum. For $V \to e^+e^-$ there appears a long tail at lower masses, the radiation tail, produced by electrons with momentum, which has been decreased due to radiation losses. The shape of the long radiation tail

in the $M_{e^+e^-}$ spectrum may be studied independently in data and MC. This way, the simulation of bremsstrahlung losses in MC may be checked.

A large sample of di-e pairs is obtained from the elastic photoproduction selection (see Section 5.3) taken during the 1996 and 1997 running periods. Some off-line selection cuts are applied in order to reject π and μ contamination. All clusters matched to tracks are required to have at least 90% of its energy in the EMC section. It is required that the most energetic UCAL cell not associated to the two tracks in the event be less than 150 MeV (200, 300) for EMC (HAC0, HAC1). Some 10000 di-e candidates with an invariant mass ranging between 2.7< $M_{e^+e^-}$ <3.3 GeV with 30< W <160 GeV survive these cuts.

Also, a large sample of di-μ pair candidates is obtained from the elastic photoproduction selection taken during the 1996 and 1997 running periods. Over 9500 di-μ candidates are available in a mass range 2.3< $M_{\mu^+\mu^-}$ <4 GeV in the same W range as in the electron sample.

The DIPSI generator was used to simulate the elastic photoproduction of J/ψ [185] [1].

Some additional basic requirements are applied to the two samples:

- The event should have only tracks originating from the vertex.
- The Z coordinate of the vertex should fulfill the requirement $|Z_{vertex}| < 40$ cm.

Given that a substantial fraction of electrons radiate, the shape of the $M_{e^+e^-}$ spectrum in the vicinity of a resonance peak cannot be described by a Gaussian. The resolution of the resonance peak in the $M_{e^+e^-}$ spectrum, being determined by the resolution of the momentum measurement with the CTD can be clearly distinguished from the radiation tail, as seen in Figure B.1. The $M_{e^+e^-}$ spectrum is evaluated as the sum of two shapes: a Gaussian term plus a bremsstrahlung tail which consists in the convolution of a Gaussian function with a bremsstrahlung spectrum.

[1] When this analysis was performed the ZEUSVM MC was not yet interfaced with the PHOTOS package (see Section 7.2.1).

In the case of MC, when only the signal from the decay of the VM is present, the $M_{e^+e^-}$ spectrum splits into two components:

$$F^{e^+e^-}(M_{e^+e^-},\sigma_M) = A_{J/\psi}((1-A_{tail})G(M_{e^+e^-},M,\sigma_M)+A_{tail}B(M_{e^+e^-},M,\sigma_M)) \quad \text{(B.1)}$$

where G is a Gaussian distribution of $M_{e^+e^-}$, with mean M and width σ_M, B is the bremsstrahlung tail given in Expression (9.3). A_{tail} is the fraction of events that radiate. In the case of data, an additional term should be added to take account of the Bethe-Heitler, process. The shape of the non-resonant background, $BH(M_{e^+e^-})$, is taken from the LPAIR MC and is kept fixed. In the case of data, the Expression (B.1) should be completed with an additional term $P(M_{e^+e^-}) = A_{BH}BH(M_{e^+e^-})$, where A_{BH} is a free parameter.

Bremsstrahlung radiation in the case of muons is small, so that the $M_{\mu^+\mu^-}$ spectrum may be described with a Gaussian function:

$$F^{\mu^+\mu^-}(M_{\mu^+\mu^-},\sigma_M) = A_{J/\psi}G(M_{\mu^+\mu^-},M,\sigma_M) \quad \text{(B.2)}$$

In the case of the data, the Expression (B.2) should be completed with an additional term $P(M_{\mu^+\mu^-}) = A_{BH}BH(M_{\mu^+\mu^-})$.

In order to determine the scale of the momentum measurement using the resulting spectrum of the invariant mass of two tracks a momentum "shift", P_{shift}, is applied to data and MC samples in order to make the Gaussian term in Expressions (B.1) and (B.2) peak at the mass of the resonance, i.e M=$M_{J/\psi}$. The method used to determine the CTD momentum scale comprises two basic steps:

1. A χ^2 fit is performed on the $M_{e^+e^-}$ and $M_{\mu^+\mu^-}$ spectra in MC. The χ^2 is defined as:

$$\chi^2 = \sum_{i=1}^{N_{bin}} \frac{(N_i^{MC} - F(m_i,\sigma_M))^2}{N_i^{MC}} \quad \text{(B.3)}$$

where i runs over N_{bin}, the number of bins in mass, N_i^{MC} is the number of events in a given mass bin i and m_i is the central value of the mass bin i. Here, in the case of the electrons $A_{J/\psi}, A_{tail}, \sigma_M$ from Expression (B.1), Δ from Expression (9.3)

and P_{shift} are set as free parameters. In the case of muons, $A_{J/\psi}, \sigma_M$ from (B.2) and P_{shift} are set as free parameters.

2. The same fit is performed on the data sample. In this case, the Bethe-Heitler term is added to Expressions (B.1) and (B.2). The parameter A_{BH} is set free additionally to those parameters fitted in the case of the MC.

The final value of the momentum scale is obtained by performing steps 1 and 2 for a sample of events that contain only full length tracks, which have best resolution, for both the muon and electron selections. The fits performed over the mass spectra reconstructed with long tracks in data and MC in both electron and muon selections are shown in Figure B.1 and B.2, respectively. The same procedure may be done for events that contain shorter tracks. However, resolution degrades very fast as tracks get shorter.

The results of the momentum shift obtained in these fits are shown in Table B.1. Results are shown for both the electron and muon samples. In the case of electrons the CTD momentum has to be scaled up by 4.5 and 1.5 per mill in data and MC, respectively. In the muon case, the CTD momentum has to be scaled up by 4.0 and 1.0 per mill in data and MC, respectively. The relative CTD momentum shift between data and MC is 3 per mill for both electron and muon samples. The statistical error on the values of P_{shift} are very small, no larger than 0.2 of the per mill. The systematic error coming for the selection of bins and bin widths in the χ^2 fits have been estimated to be 0.5 per mill. The values of P_{shift} obtained for data are consistent with the indication that CTD momentum scale in data are somewhat below unity and should be corrected.

The χ^2 fits performed on events that contain shorter tracks are shown in Figure B.3 for data and in Figure B.4 for MC. There different samples are chosen: events with 9 super layer tracks + 7 super layer tracks, 9SL+5SL and 9SL+3SL. Due to lack of statistics in data other classes of events were not considered. In Table B.1 the result of χ^2 fits performed for these configurations are shown for muons and electrons.

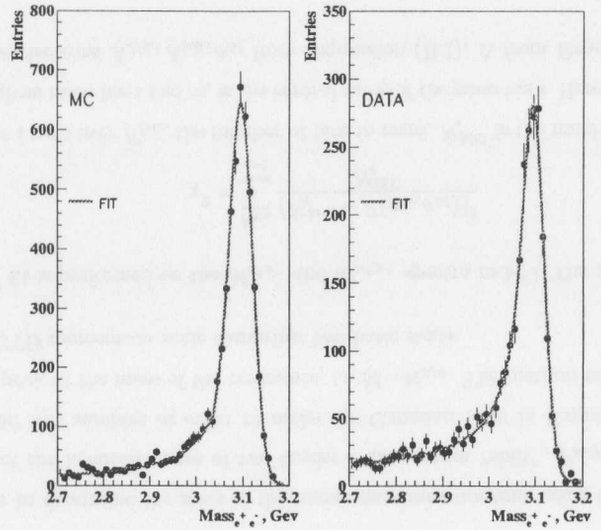

Figure B.1: $M_{e^+e^-}$ spectra in the region of the J/ψ for data and the DIPSI MC with full length tracks only. The solid line is the result of the fits according to the Expression (B.1) (see text).

	$(P_{shift} - 1) \times 10^{-3}$					
	e^+e^-			$\mu^+\mu^-$		
	DATA	MC	$P^{Data}_{shift} - P^{MC}_{shift}$	DATA	MC	$P^{Data}_{shift} - P^{MC}_{shift}$
9SL-9SL	4.5	1.5	3.0	4.0	1.0	3.0
9SL-7SL	5.5	1.9	3.4	4.2	1.7	2.5
9SL-5SL	7.5	1.8	5.7	5.7	2.5	3.2
9SL-3SL	5.4	1.8	3.6	3.8	1.9	1.9

Table B.1: Results of P_{shift} of the χ^2 fit performed on data and MC for events for different track configurations for muons and electrons.

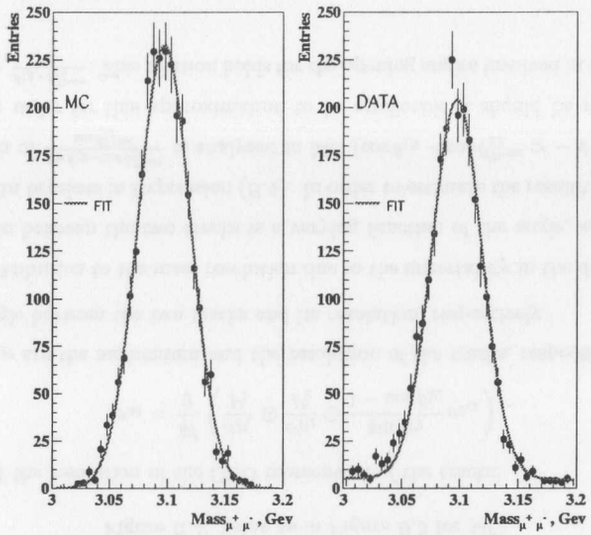

Figure B.2: Same as in Figure B.1 for $\mu^+\mu^-$.

In the case of the electrons, as seen in the left Plot of Figure B.1, the radiation tail in the region of $M_{e^+e^-} \approx 3\,\text{GeV}$ are somewhat different in data and MC. The results obtained for the parameters responsible for the bremsstrahlung radiation in Expression (9.3), A_{tail} and Δ for the case of the electrons for data and MC are shown in Table B.2. It is seen that the estimated value of A_{tail} in data in substantially greater than that obtained for MC in the case of long tracks [2]. This difference gets smaller for shorter tracks. The bremsstrahlung radiation shifts somewhat the peak of the reconstructed $M_{e^+e^-}$ spectrum towards lower masses. This effect may be estimated by comparing the results of P_{shift} for electrons and muons. In average the values obtained for P_{shift} in data for the electron case are somewhat larger than those obtained for muons. This effect is stronger for track configurations that contain shorter tracks, for which the contribution of bremsstrahlung radiation is greater. However, in terms

[2]The inclusion of internal bremsstrahlung, thanks to the implementation of PHOTOS in the ZEUSVM MC (see Section 7.2.1) solved this discrepancy, as seen in the $M_{e^+e^-}$ spectra in Section 9.1.1.

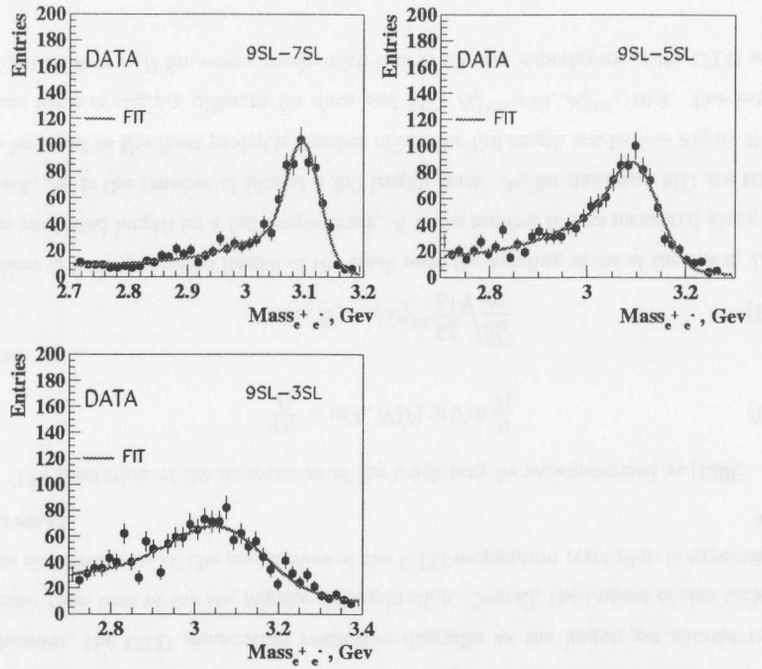

Figure B.3: Same as in Figure B.1 for data, for track configurations that contain short tracks.

of the reconstructed mass $M_{e^+e^-}$ the additional shift towards lower masses is small, accounting for a small fraction of 1%.

B.2 CTD Momentum Resolution

In the previous Section the $M_{e^+e^-}$ and $M_{\mu^+\mu^-}$ spectra in data and MC were fitted to Expressions (B.1) and (B.2), and the mass resolution, σ_M, was extracted (see Table B.3). The obtained values of the mass resolution for that sample may be interpreted

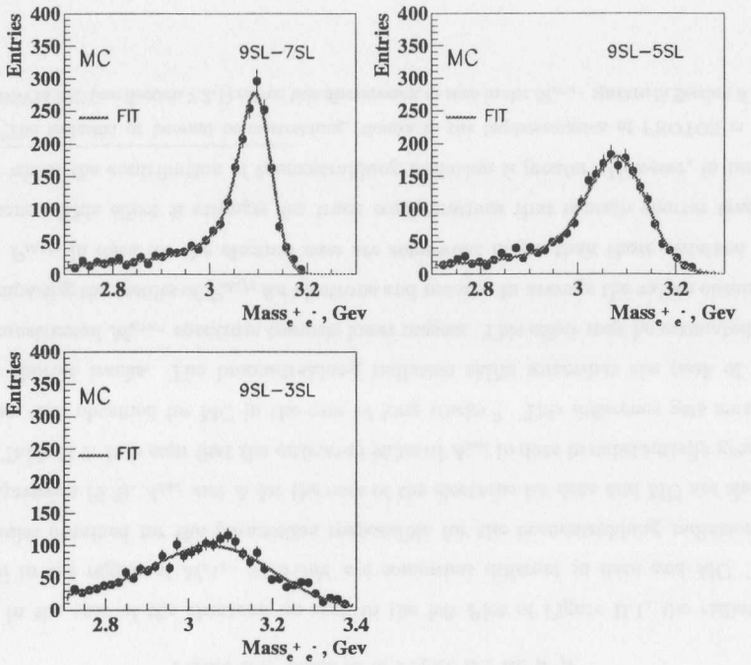

Figure B.4: Same as in Figure B.3 for MC.

in terms of the resolution of the CTD momentum of the tracks:

$$\sigma_M = \frac{M}{2}\left(\frac{\sigma_{P_1}}{P_1} \oplus \frac{\sigma_{P_2}}{P_2} \oplus \frac{\sin\theta_{12}}{1-\cos\theta_{12}}\sigma_{\theta_{12}}\right) \tag{B.4}$$

where P, σ_P are the momentum and the resolution of the tracks, respectively, θ_{12},$\sigma_{\theta_{12}}$ are the angle between the two tracks and its resolution, respectively.

The contribution to the mass resolution due to the uncertainty in the determination of the angle between the two tracks is a varying function of the angle, as seen in the third term in brackets in Expression (B.4). In order to estimate the resolution of θ_{12} the distribution of $\frac{\cos\theta_{12}-\cos\theta_{12}^{True}}{\sin\theta_{12}^{True}}$ is analyzed in MC ($\cos\theta_{12} - \cos\theta_{12}^{True} \simeq -\sin\theta_{12}^{True}(\theta_{12} - \theta_{12}^{True})$). In order for this approximation to be applicable it should be required that $\sin\theta_{12}^{True} \gg \frac{\theta_{12}-\theta_{12}^{True}}{2}$. This relation holds for the opening angles involved in this analysis.

	A_{tail}		Δ	
	DATA	MC	DATA	MC
9SL-9SL	0.61	0.45	2.3E-2	3.0E-2
9SL-7SL	0.57	0.53	8.5E-2	2.9E-2
9SL-5SL	0.65	0.72	6.4E-2	7.3E-3
9SL-3SL	0.75	0.72	3.8E-2	1.5E-2

Table B.2: Results of the parameters responsible for bremsstrahlung radiation, A_{tail} and Δ with the χ^2 fit performed on MC for different tracks configurations for electrons.

The obtained distribution is fitted with a Gaussian function, yielding $\sigma_{\theta_{12}} = 5.2 \cdot 10^{-3}$ rad. This value is fixed in Expression (B.4). The contribution from this term is small for track configurations with large angles. This is the case for events in which both tracks have crossed the 9 CTD superlayers. This term is expected to give a larger contribution for events that contain short tracks since the angle between the two tracks is smaller. However, the CTD momentum resolution degrades as the length get shorter much faster than that of the the angular determination. Overall, the impact of this term on the determination of the parameters of the CTD momentum resolution is expected to be small.

The resolution of the momentum of the track may be parameterized as [139]:

$$\frac{\sigma_{P_t}}{P_t} = \alpha(L,N)P_t \oplus \beta \oplus \frac{\eta}{P_t} \tag{B.5}$$

and

$$\alpha(L,N) = (\alpha\prime)^{2.5}\frac{L_0^2}{L^2}\sqrt{\frac{N_0}{N}} \tag{B.6}$$

where L is the projected length of the track onto the bending plane of the track, L_0 is the projected length for a full length track, N is the number of hits measured along the track, N_0 is the number of hits of a full length track. N_0 for data and MC are taken to be equal to the most probable number of hits for full length tracks (see Figure B.5). This value is slightly different for data and MC: N_0^{Data}=73, N_0^{MC}=70.5. The values of parameters α, β for vertex tracks with hits in all nine superlayers of the CTD were

previously quoted as α=0.005 and β=0.016, where P_t is in GeV. The third term is due to multiple Coulomb scattering before the particle reaches the CTD [186].

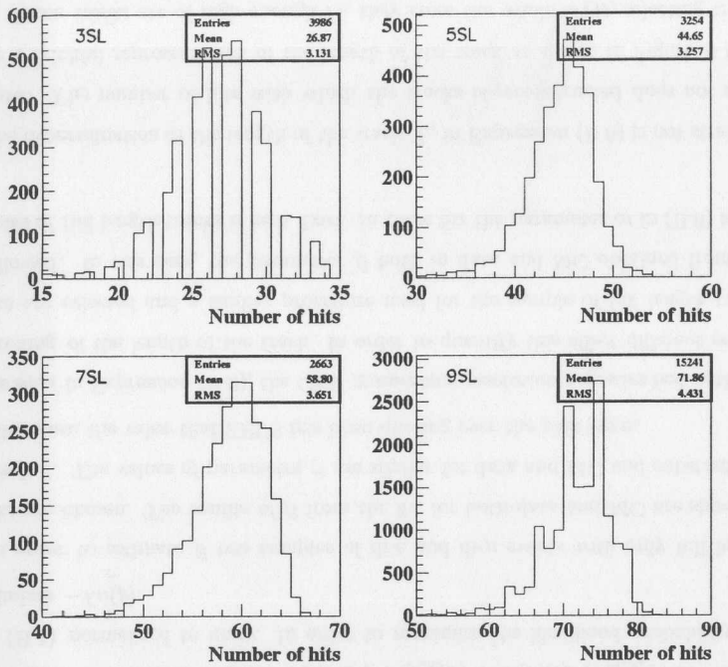

Figure B.5: Distributions of the number of CTD hits per track for different track lengths in data: tracks that have crossed 3,5,7 CTD superlayers and full length tracks.

The first term of the Expression (B.5), which follows from the error on the track radius of curvature, grows with P_t. In order to determine the parameter α one needs to have a large lever arm in P_t, therefore, one needs to study momentum resolution for very high P_t tracks. Studies for high P_t tracks have been performed in which CTD momentum was compared with UCAL clusters for high P_t tracks ($P_t > 10\,\text{GeV}$) depositing energy on the BCAL. From these studies is was concluded that α_{MC}=0.0063 and α_{Data}=0.0054 [187]. For full length tracks, in the region of P_t of consideration here,

we are specially sensitive to the second term of the Expression (B.5), i.e. the parameter β.

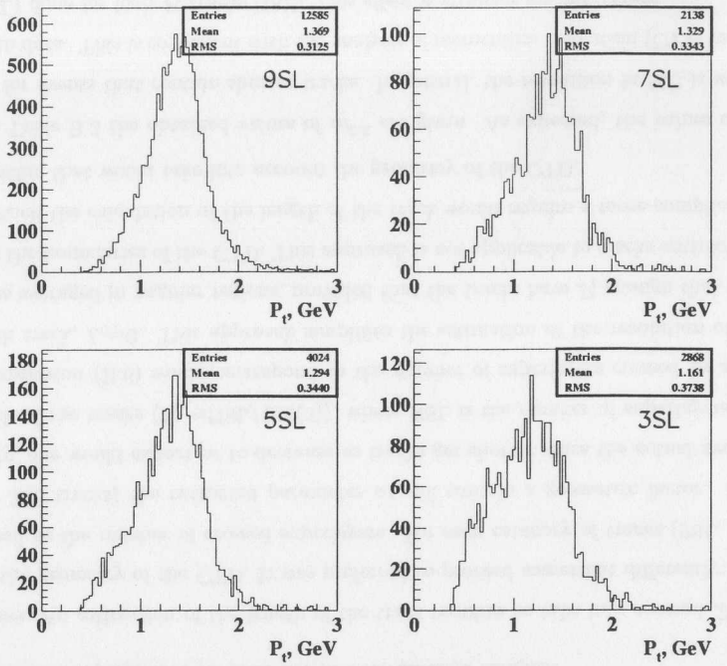

Figure B.6: P_t distribution of CTD tracks of different length in di-e events in the $M_{e^+e^-}$ region of J/ψ in data.

The P_t distribution of CTD tracks for the electron sample is shown in Figure B.6. Similar distributions are observed in the di-μ sample. The average P_t of the tracks of the analyzed sample is around 1.3 GeV with a minimum P_t of about 0.5 GeV. The contribution of multiple scattering in Expression (B.5) is significant for low momentum tracks with P_t <300 MeV. The value of parameter η is taken from studies with low momentum tracks [186] and it is fixed at η =0.0014.

The method for the extraction of the parameters in Expressions (B.5)-(B.6) com-

prises one more additional step with respect to the procedure explained in the previous Section. By accomplishing fits on the shape of the $M_{e^+e^-}$ spectrum of a given sample of di-e, a set of parameters is obtained that will be fixed here, namely, the parameter of the momentum shift P_{shift}, the parameters responsible for bremsstrahlung radiation, A_{tail} and Δ in Expression (9.3) and, in the case of data, the normalization of the Bethe-Heitler background. Similarly for the muon sample. Based on that set of parameters obtained in the previous Section for a given sample of di-e and di-μ an unbinned likelihood fit is performed. The mass resolution σ_M of a given di-e is parameterized according to Expressions (B.4)-(B.5)-(B.6). A likelihood probability is defined:

$$p = \prod_{n=1}^{N} f(M_{e^+e^-}, \sigma_{M_{e^+e^-}}) \tag{B.7}$$

where N is the number of points, $f(M_{e^+e^-}, \sigma_{M_{e^+e^-}})$ is $F(M_{e^+e^-}, \sigma_{M_{e^+e^-}})$ in Expression (B.1) normalized to unity. In order to maximize the likelihood probability one minimizes $-Ln(p)$.

In order to estimate β two samples of di-e and di-μ events with only full length tracks are chosen. The results of β from the fit, for both data and MC are shown in Table B.3. The values of parameter β are similar for data and MC and substantially smaller than the value that ZEUS has been quoting over the past years.

As seen in Expression (B.6), the CTD momentum resolution degrades fast with the shortening of the length of the track. In order to quantify this effect different sets of tracks are selected and a similar procedure used for the sample of full length tracks is followed. In this case, the parameter β both in data and MC obtained from the samples of full length tracks is kept fixed. In these fits the parameter $\alpha\prime$ in (B.6) is left free.

The determination of the length of the track, L, in Expression (B.6) is not straightforward. The number of hits with which the tracks is reconstructed does not seem to be a faithful representation of the length of the track as shown in Figure B.5 for data. Since tracks are of high enough P_t, they cross the whole CTD, selecting tracks based on the number of crossed superlayers is like selecting tracks according to angular

		e^+e^-		$\mu^+\mu^-$	
		DATA	MC	DATA	MC
σ_M (MeV)	9SL-9SL	22.0	24.6	21.7	22.7
	9SL-7SL	29.5	31.5	30.8	30.6
	9SL-5SL	50.1	56.6	51.7	57.5
	9SL-3SL	99.4	135.5	95.4	123.7
β	9SL-9SL	6.4E-3	6.0E-3	6.3E-3	5.2E-3
$\alpha\prime^{2.5}$	9SL-7SL	5.8E-3	6.3E-3	5.7E-3	6.2E-3
	9SL-5SL	5.2E-3	6.3E-3	5.3E-3	6.5E-3
	9SL-3SL	3.8E-3	4.6E-3	3.2E-3	4.2E-3

Table B.3: Results of σ_M from the χ^2 fit and for the parameters β and $\alpha\prime$ from the likelihood fits performed on data and MC for different samples.

regions. An estimation of the length of the track requires to take into account Z_{vertex} and the geometry of the CTD. It was preferred to proceed somewhat differently: L is defined as the number of crossed superlayers. For each category of tracks (9SL, 7SL, 5SL, 3SL tracks) the extracted parameter $\alpha\prime$ will contain a geometric factor. Intuitively, one would expect $\alpha\prime$ to decrease as tracks get shorter since the actual average length of the tracks $\langle L \rangle \approx$NSL/$\langle \sin(\theta) \rangle$, where NSL is the number of superlayers. L_0 in Expression (B.6) would correspond to the number of superlayers crossed by a full length track, L_0=9. This approach simplifies the estimation of the resolution of the tracks averaged in angular regions, provided that the tracks have P_t enough that they cross the boundaries of the CTD. This approach is not applicable to tracks with low P_t for which the calculation of the length of the track would require a more complicated algorithm that would take into account the geometry of the CTD.

In Table B.3 the obtained values of $\alpha\prime^{2.5}$ are given. As expected, the values of $\alpha\prime$ drop for events that contain shorter tracks. In general, the resolution in MC is worse that in data. This is consistent with the analysis of momentum resolution (CTD versus UCAL) done for high P_t tracks [187]. This effect is stronger for 3SL tracks.

Appendix C

Alignment Studies

The alignment of the main sections of the UCAL and the SRTD had become a central issue for the ZEUS Collaboration during 1999. It was necessary to determine the alignment "in situ" of the various sections of the UCAL and assign a certain precision to it.

The extension of range of W of the measurement of heavy VM's required the implementation of UCAL and SRTD information. A good alignment of the SRTD was important to reduce systematic errors, specially at very high W.

C.1 UCAL

The alignment of the BCAL is not crucial for the analysis of the production of heavy VM's. The alignment of the BCAL was performed in [188] and is not reported in this work. The kinematics of the decay products of the heavy VM's that fall into the acceptance of the BCAL are reconstructed with the information from the CTD. The UCAL is used when the products of the decay of the VM fall out of the acceptance region of the CTD in which tracks of a good quality are reconstructed. The regions of the FCAL and RCAL that do not overlap with this fiducial region of the CTD correspond approximately to the first three inner rings.

C.1.1 Method

It is a convention adopted in the ZEUS Collaboration that the various components of its detector be aligned with respect to the CTD. The CTD is considered to be a rigid object aligned with respect to the absolute reference system set by HERA. For the alignment of the RCAL and FCAL we compare the extrapolation of CTD tracks on the face of these sections of the UCAL with the position of the corresponding clusters. A sample of events with isolated CTD tracks associated to a cluster in the RCAL or FCAL is selected. For the extraction of the position of each component a function is defined which is sensitive to the parameters of the alignment, (x_0, y_0, z_0). For each track-cluster a variable is defined:

$$\zeta = F(\mathbf{r}_{CAL}, \mathbf{r}_{CTD}) \tag{C.1}$$

where $\mathbf{r}_{CAL}$ is the three vector of the position of the cluster reconstructed by the UCAL and $\mathbf{r}_{CTD}$ is the three vector of the position of the extrapolated track on the face of the UCAL. The parameters x_0, y_0, z_0 (r_0) are such that the distribution of $F(\mathbf{r}_{CAL} - \mathbf{r}_0, \mathbf{r}_{CTD})$ is centered at zero.

The parameters of the alignment are obtained independently for data and MC. In MC the position of the various components of the UCAL are aligned with respect to the absolute system of coordinates. Hence, in MC $x_0, y_0, z_0 = 0$. This is a test of the correctness and sensitivity of the method.

Events in data are selected with the trigger algorithm developed for the study of heavy VM production (see Section 5.3). A UCAL cluster is matched to CTD track if the distance between its extrapolation to the face of the UCAL and the position of the cluster is less than 15 cm. The generator DIPSI (see Section 7.2) is used to generate elastic J/ψ events. The following criteria at the off-line level are followed for the selection of events with at least one track-cluster matching:

- The track should have crossed at least 5 CTD superlayers and have a momentum larger than 1 GeV. This is necessary to improve the determination of the position

of the extrapolated track on the face of the UCAL.

- Elasticity requirement (see Section 6.4). This requirement secures that the track-cluster are isolated.

A sample of events collected during the 96-97 running periods was selected. This analysis was repeated with data taken during the 99-00 running period as well [1].

The reconstruction of the position of the cluster with the help of the CTD track involves the extrapolation of the track to the face of the UCAL. It is conceivable that the residual magnetic field outside the volume of the CTD is not well described in MC. This may result into an unknown shift $\mathbf{r}_{CTD}$ with respect to $\mathbf{r}_{CAL}$. This effect will be different for positively and negatively charged particles and for particles of different momenta. The comparison of UCAL and CTD position reconstruction is made on a sample that has a similar number of positively and negatively charged particles. Nevertheless, as a check, the same procedure for the extraction of the alignment parameters of the RCAL and FCAL is made for positively and negatively charged particles independently. Also, as a systematic check, the cut of the minimum momentum of the CTD track is changed.

C.1.2 RCAL

In order to align the x and y position of the RCAL the following simple function is used:

$$F(x_{CAL}, x_{CTD}) = x_{CAL} - x_{CTD} \tag{C.2}$$

One should check the distributions of $x_{CAL} - x_{CTD}$ and $y_{CAL} - y_{CTD}$ in MC are centered at zero. These distributions in MC are shown in Figure C.1. The upper two Plots correspond to the comparison of UCAL and CTD coordinates for the left half of

[1] The description of the geometry of the ZEUS detector was changed based on independent analyses of the alignment of the various sections of the UCAL performed with data collected during the 96-97 running periods. Various analyses were performed with data collected 99-00 running period to check the correctness of the changes implemented in the description of the geometry of the ZEUS UCAL.

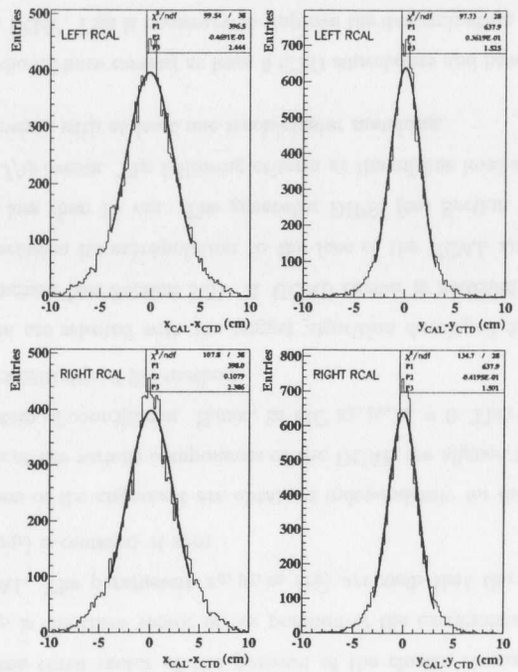

Figure C.1: The position of electromagnetic clusters reconstructed in the RCAL and the CTD are compared in MC. x_{CAL} and y_{CAL} correspond to the x and y position reconstructed in the RCAL, respectively. x_{CTD} and y_{CTD} correspond to the x and y position of the extrapolated CTD track to the face of the RCAL, respectively. The upper two Plots correspond to the left half of the RCAL. The lower two Plots correspond to the right half of the RCAL. The solid lines correspond to fits to a Gaussian function. The result of these fits are given in the boxes on the top right corner.

the RCAL. The lower two Plots correspond to the right half of the RCAL. The solid lines correspond to fits to a Gaussian function. The result of these fits are given in the boxes on the top right corner. The mean of the Gaussian functions are consistent

with correct alignment ($x_0, y_0 = 0$) within ± 1 mm. The widths of the distributions are dominated by the resolution of the position reconstruction with the UCAL. The width of the $x_{CAL} - x_{CTD}$ distribution is significantly wider than that of $y_{CAL} - y_{CTD}$ mainly because of the geometry of the electromagnetic cells in the RCAL [2].

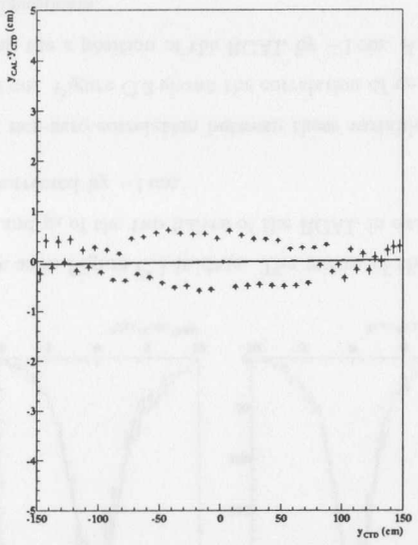

Figure C.2: Scatter plot of $y_{CAL} - y_{CTD}$ versus y_{CTD} in MC. The solid line corresponds to a linear fit.

The RCAL and FCAL do not reconstruct the z position of the clusters [3]. In order to check the alignment of the RCAL in z one should look into the correlation of $x_{CAL} - x_{CTD}$ and x_{CTD} or $y_{CAL} - y_{CTD}$ and y_{CTD}. A shift in the z direction of the RCAL will result into a non-zero correlation. In the approximation that the shift in z, $|z_0| \ll$

[2]The electromagnetic cells in the RCAL are 20 cm wide in x and 10 cm high in y.

[3]The depth of electromagnetic and hadronic showers is a known function of the ln(E). Based on this an estimate the z position of a shower may be made.

$|Z_{RCAL}|$, where Z_{RCAL}, is the z position of the RCAL one gets:

$$x_{CAL} - x_{CTD} \approx \frac{x_{CTD}}{Z_{RCAL}} z_0 \tag{C.3}$$

This Expression is valid for the y position, as well. As illustrated in Figure C.1 the distribution of $y_{CAL} - y_{CTD}$ is narrower than $x_{CAL} - x_{CTD}$ and, therefore, is more sensitive to shifts in the position of the UCAL. The correlation between $y_{CAL} - y_{CTD}$ and y_{CTD} in MC is shown in Figure C.3. According to Expression (C.3) the correlation between $y_{CAL} - y_{CTD}$ and y_{CTD} is close to a linear one. The value obtained with a linear fit gives a value of z_0 consistent with zero within ± 3 mm.

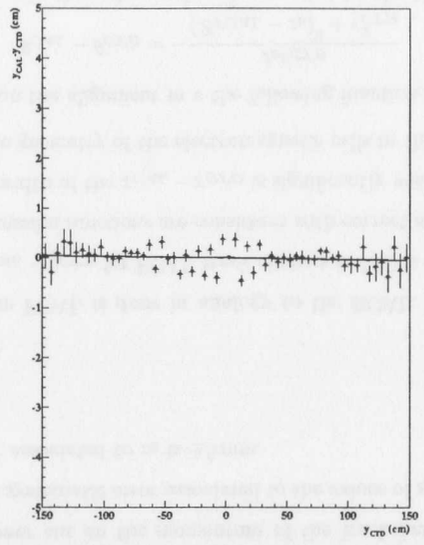

Figure C.3: Same as in Figure C.2 in data. The z position of the RCAL has been corrected by -1 cm.

Figures C.1 and C.2 illustrate that the method of the alignment gives an answer in MC that is consistent with $x_0, y_0, z_0 = 0$. Before checking the alignment in x and y of the two halves of the RCAL it is necessary to check on the correlation of $y_{CAL} - y_{CTD}$

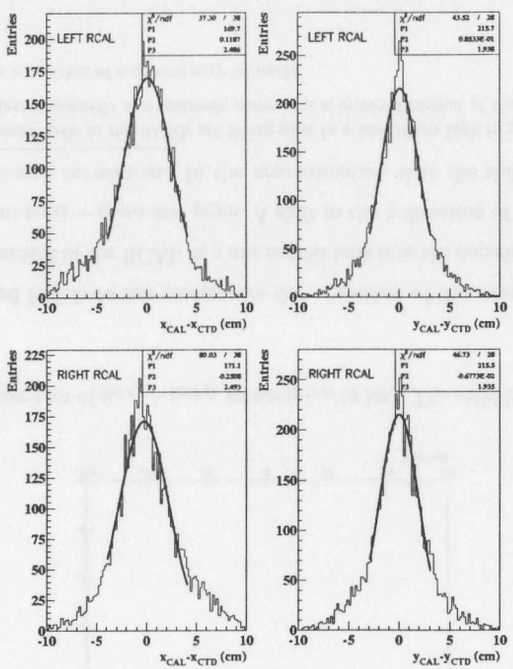

Figure C.4: The same as in Figure C.1 in data. The means of the Gaussian functions correspond to the x_0 and y_0 of the two halves of the RCAL in data. The z position of the RCAL has been corrected by -1 cm.

and y_{CTD} in data. A non-zero correlation between these variables was found in data consistent with $z_0 = 1$ cm. Figure C.3 shows the correlation of $y_{CAL} - y_{CTD}$ and y_{CTD} in data after correcting the z position of the RCAL by -1 cm. After the correction is done the correlation disappears.

The $x_{CAL} - x_{CTD}$ and $y_{CAL} - y_{CTD}$ distributions in data after correcting the z position of the RCAL are shown in Figure C.4. The values of x_0 and y_0 obtained from the Gaussian fits of the $x_{CAL} - x_{CTD}$ and $y_{CAL} - y_{CTD}$ distributions in data are

summarized in Table C.1.

	x_0 (mm)	y_0 (mm)	z_0 (mm)
Left	1.2	0.9	10.0
Right	2.5	0.7	10.0

Table C.1: The values of x_0, y_0 and z_0 for the RCAL, given in mm.

The same procedure has been performed with positively and negatively charged tracks. Also, the lower cut on the momentum of the track has been changed from 1 GeV to 3 GeV. The systematic error associated to the values of x_0 and y_0 in Table C.1 is ± 2 mm. The error associated to z_0 is ± 5 mm.

C.1.3 FCAL

The alignment of the FCAL is done in analogy to the RCAL. The distributions of $x_{CAL} - x_{CTD}$ and $y_{CAL} - y_{CTD}$ for FCAL track-clusters in MC is shown in Figure C.5. The means of the Gaussian functions are consistent with correct alignment ($x_0, y_0 = 0$) within ± 1 mm. The width of the $x_{CAL} - x_{CTD}$ is significantly wider than $y_{CAL} - y_{CTD}$ mainly because of the geometry of the electromagnetic cells in the FCAL [4].

In order to check on the alignment in z the following function is chosen:

$$\theta_{CAL} - \theta_{CTD} = -\frac{z_0 r_{CTD}}{(Z_{FCAL} - z_0)^2 + r_{CTD}^2} \tag{C.4}$$

where θ_{CAL} and θ_{CTD} are the polar angle reconstructed by the UCAL and the CTD, respectively. Z_{FCAL} is the z position of the FCAL. The distributions of $\theta_{CAL} - \theta_{CTD}$ in bins of $r_{CTD} = \sqrt{x_{CTD}^2 + y_{CTD}^2}$ are fitted to a Gaussian function. The mean values of the fits to Gaussian functions performed for different values of r_{CTD} in MC are shown in Figure C.6. The values of the means of the Gaussian functions are fitted to a function of the form given in Expression (C.4). The obtained parameter z_0 is consistent with zero within ± 3 mm.

[4] The electromagnetic cells in the FCAL are 20 cm in x and 5 cm in y. Electromagnetic cells in the FCAL are half the size in y than those in the RCAL.

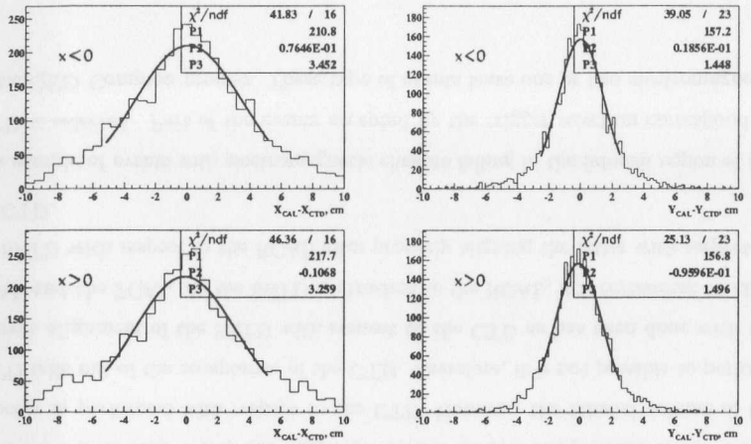

Figure C.5: Same as in Figure C.1 for the FCAL in MC. $x < 0$ corresponds to the left half of the FCAL and $x > 0$ to the right half.

Figures C.5 and C.6 illustrate that the method of the alignment gives an answer in MC that is consistent with $x_0, y_0, z_0 = 0$ in the FCAL too. Before checking the alignment in x and y of the two halves of the FCAL in data it is necessary to check on the correlation of $\theta_{CAL} - \theta_{CTD}$ and r_{CTD}. This correlation is illustrated in Figure C.7. The mean values of the Gaussian fits have been fitted to a function of the form given in Expression (C.4). The obtained parameter $z_0 = 1\,\text{cm}$ deviates significantly from zero and is consistent with the shift in z observed in the RCAL in the previous Section.

The $x_{CAL} - x_{CTD}$ and $y_{CAL} - y_{CTD}$ distributions in data after correcting the z position of the FCAL by $-1\,\text{cm}$ are shown in Figure C.8. The values of x_0 and y_0 obtained from the Gaussian fits of the $x_{CAL} - x_{CTD}$ and $y_{CAL} - y_{CTD}$ distributions in data are summarized in Table C.2. It is noteworthy that the obtained values of the y_0 for both halves are similar and $y_0 \approx 0.4\,\text{cm}$.

Various systematic checks have been performed. The same procedure has been performed with positively and negatively charged tracks. Also, the lower cut on the

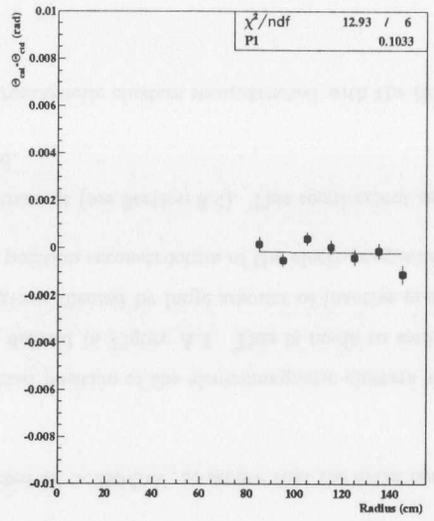

Figure C.6: The $\theta_{CAL} - \theta_{CTD}$ distributions in bins of r_{CTD} have been fitted to a Gaussian function in MC. The solid circles correspond to the mean value of the fitted Gaussian functions. The solid line corresponds to a fit to a function of the form given in Expression (C.4). The results of the fit are shown in the box on the top right corner.

momentum of the track has been changed from 1 GeV to 3 GeV. The systematic error associated to the values of x_0 and y_0 in Table C.2 is $\pm 2\,\text{mm}$. The systematic error associated to z_0 is $\pm 5\,\text{mm}$.

	x_0 (mm)	y_0 (mm)	z_0 (mm)
Left	2.3	5.4	10.0
Right	1.2	3.6	10.0

Table C.2: The values of x_0, y_0 and z_0 for the FCAL, given in mm.

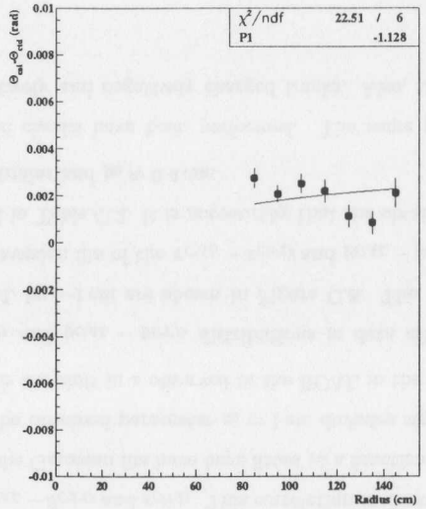

Figure C.7: The same as in Figure C.6 in data.

C.2 SRTD

C.2.1 Method

As stated in Section C.1.1, the alignment of the various components of the ZEUS detector is performed with respect to the CTD. However, the fiducial volume of the SRTD falls out of the acceptance of the CTD. Therefore, it is not possible to perform a direct alignment of the SRTD with respect to the CTD as has been done with the RCAL and the FCAL. As the SRTD is attached to the RCAL, it is convenient to align the SRTD with respect to the RCAL after properly aligning the latter with respect to the CTD.

A sample of events with electromagnetic clusters falling in the fiducial region of the SRTD is selected. Part of the events accepted by the trigger selection correspond to elastic QED Compton process. These type of events leave one or two electromagnetic

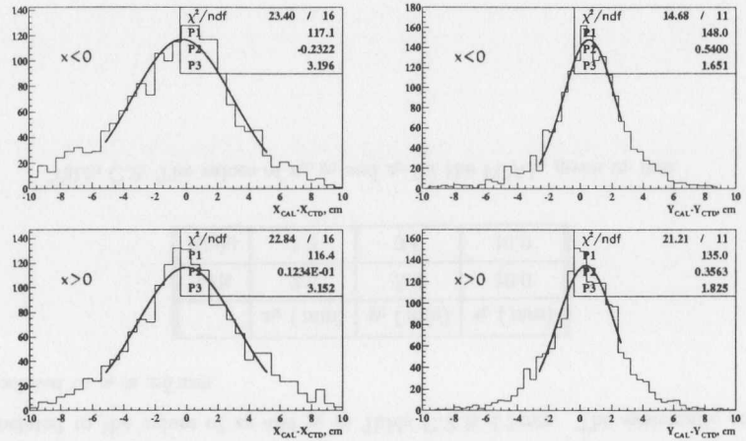

Figure C.8: Same as in Figure C.5 in data. The position in z of the FCAL has been corrected by -1 cm.

clusters in the fiducial region of the SRTD. The topology of these events are similar to events coming from the decay of J/ψ at very high W. The following off-line cuts were applied on the selected sample:

- The reconstructed $W > 290$ GeV, to secure that the event consists of electromagnetic clusters.
- The reconstructed position of the electromagnetic clusters should be within the fiducial region defined in Figure A.1. This is made to avoid transverse energy leakage and regions affected by large amount of inactive material. These effects may affect the position reconstruction of the electromagnetic clusters.
- Elasticity requirement (see Section 6.4). This requirement secures that the clusters are isolated.

The x and y of electromagnetic clusters reconstructed with the RCAL and the SRTD

are compared, in analogy to Expression (C.2):

$$F(x_{SRTD}, x_{CAL}) = x_{SRTD} - x_{CAL} \tag{C.5}$$

The alignment of the SRTD with the respect to the CTD comes out from Expressions (C.2)-(C.5):

$$< x_{SRTD} - x_{CTD} > \approx < x_{SRTD} - x_{CAL} > + < x_{CAL} - x_{CTD} > \tag{C.6}$$

The offsets x_0, y_0, z_0 have been calculated for the RCAL and applied to the position reconstruction of the RCAL. The z position of the SRTD with respect to the RCAL has been fixed to the number given by the mechanical design [5].

C.2.2 Results

The distributions of $x_{SRTD} - x_{CAL}$ and $y_{SRTD} - y_{CAL}$ in MC are shown in Figure C.9 for the two halves of the SRTD independently. The distributions are fitted to a Gaussian function. The mean values of the Gaussian function are consistent with zero within ± 2 mm.

The same distributions in data are shown in Figure C.10. The values of the offsets observed in the alignment of the SRTD are given in Table C.3. The left half of the SRTD seems to be too low by about 0.5 cm. This is an important effect that should be corrected in data for further physics analysis.

	x_0 (mm)	y_0 (mm)
Left	1.2	-5.5
Right	2.4	-0.2

Table C.3: The values of x_0 and y_0 obtained from the fits to a Gaussian function of the $x_{SRTD} - x_{CAL}$ and $y_{SRTD} - y_{CAL}$ distributions for the SRTD in data. The values of x_0 and y_0 are given in mm.

[5] The x and y positions reconstructed with the SRTD are extrapolated to the face of the UCAL.

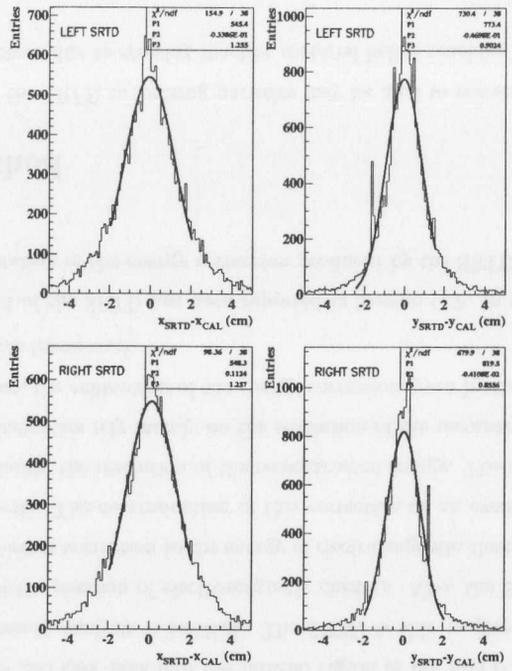

Figure C.9: The distribution of $x_{SRTD} - x_{CAL}$ and $y_{SRTD} - y_{CAL}$ in the two halves of the SRTD in MC. The solid lines correspond to fits to Gaussian functions. The results of the fits are given on the top right corner.

Various checks have been performed to estimate the systematic error associated to the values of the offsets of the SRTD position given in Table C.3. The analysis was redone for various cuts on the energy of the energy cluster, from 1 to 5 GeV. Also, the analysis has been restricted to various regions of the fiducial area of the SRTD. The variation of the offsets of the SRTD position remains within ± 2 mm.

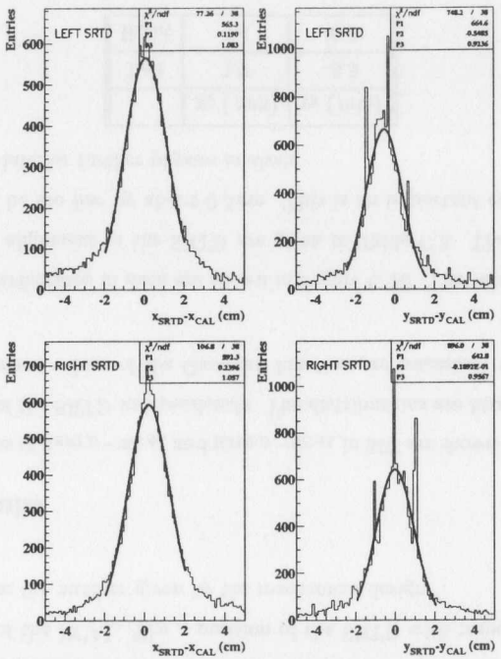

Figure C.10: The same as in Figure C.9 in data.

Appendix D

Calibration of the SRTD

This detector plays a crucial role in the extension of the W range of the measurement of the production of heavy VM's. Effectively, at least one electron of the decay of the J/ψ at $W > 200$ GeV falls into the fiducial region of the SRTD. The use of the SRTD in the present analysis is twofold. The SRTD is able to give a more precise determination of the position of electromagnetic clusters. Also, the SRTD is used to give an event-by-event correction to the energy of electromagnetic clusters due to losses in inactive material. The determination of this correction on an event-by-event basis increases significantly the resolution of the reconstructed energy. The resolution of the reconstructed kinematics rely mainly on the resolution of the reconstructed energy at high W. Therefore, the calibration of the energy correction given by the SRTD plays a central role in this thesis work.

The alignment of the SRTD has been reported in Section C.2. In the present Appendix the calibration of the energy correction produced by the SRTD is reported.

D.1 Method

The response of the SRTD to ionizing particles may be used to correct for the loss of energy of an electron due to crossing inactive material before reaching the UCAL. For

this purpose, the presampler method may be used [189]. The presampler method makes a simple assumption: the amount of energy loss by electromagnetically is proportional to the number of charged particles created in the course of the interaction with the inactive material. Due to the presence of inactive material in front of the UCAL particles will create "pre-showers". Charged particles created in the pre-shower will loose energy through ionization in the active material of the SRTD. The response of the SRTD is proportional to the number of charged particles that cross it. Therefore, the response of the SRTD is proportional to the energy loss by the particle in the inactive material. The output of the SRTD has been calibrated off-line in terms of number of mip's [1]. A simple linear relation is used:

$$E_{CAL} = E_{Corr} - \alpha_{SRTD} N^{mip}_{SRTD}/2 \tag{D.1}$$

where E_{CAL} is the energy measured in the UCAL, E_{Corr} is the energy corrected for inactive material losses, N^{mip}_{SRTD} is the number of mip's measured by the SRTD. α_{SRTD} is a free parameter that needs to be calculated separately for data and MC. The factor $\frac{1}{2}$, is applied to N^{mip}_{SRTD} because the SRTD is made of two planes and the response is "double".

Provided that the energy scale of the UCAL is constant with energy, the parameter α_{SRTD} may be extracted by looking into the correlation between the response of the UCAL and N^{mip}_{SRTD}. For this purpose, it is relevant to use a sample of events in data and MC coming from a process that provides electromagnetic objects [2]. This is done by selecting events coming from QED Compton process. This process has a large cross-section that will provide sizeable statistics for this analysis. This type of events have an electron and a photon in the final state. Most of these events contain two electromagnetic clusters within the fiducial region of the SRTD. It is proposed to look into the correlation of the total energy deposited in the two electromagnetic clusters, $E_{CAL} = E^1_{CAL} + E^2_{CAL}$ and the total number of mip's measured in the SRTD, $N^{mip}_{SRTD} =$

[1] mip stands for minimum ionizing particle.

[2] A photon converts into e^+e^- as it passes through material. The multiplicity of the pre-shower provided by a photon is assumed to be similar to that of an electron.

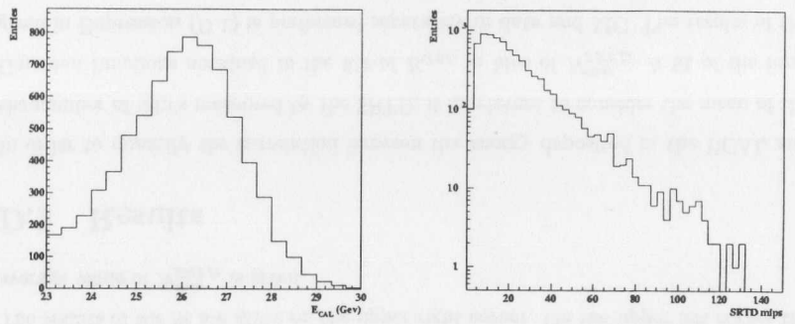

Figure D.1: The left Plot displays the total energy deposited in the two electromagnetic clusters, $E_{CAL} = E^1_{CAL} + E^2_{CAL}$, in the QED Compton selection in data. The right Plot corresponds to the total number of mip's measured in the SRTD, $N^{mip}_{SRTD} = N^{mip,1}_{SRTD} + N^{mip,2}_{SRTD}$.

$N^{mip,1}_{SRTD} + N^{mip,2}_{SRTD}$. QED Compton events with the invariant mass of the electron and photon in the final state, $M_{e\gamma} > 1.5$ GeV are allowed in the trigger selection described in Chapter 5. Some additional off-line cuts are applied:

- Two electromagnetic clusters within the fiducial region of the RCAL defined in Figure A.1.
- Two electromagnetic clusters within the fiducial region of the SRTD.
- Elasticity requirement (see Section 6.4).
- Reconstructed $W > 290$ GeV. This requirement is made to restrict the analysis to from QED Compton process.

The data sample used is a fraction of the data taken during the 1999 and 2000 running periods. The MC chosen corresponds to the COMPTON program (see Section 7.2.5).

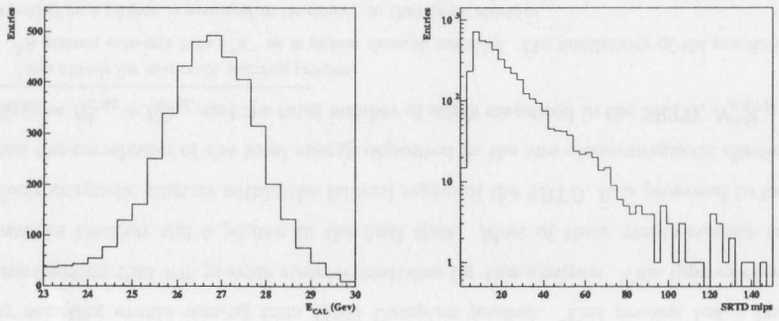

Figure D.2: Same as in Figure D.1 for the COMPTON MC.

The distribution of energy deposited in the two electromagnetic clusters and the total number of mip's measured in the SRTD in the QED Compton selection in data is shown in Figure D.1. The same distributions for MC are given in Figure D.2. It is observed that both in data and MC the distribution of E_{CAL} is not symmetric. In MC this is due to initial state radiation of the incoming electron in the *ep* scattering. The initial state radiation reduces the energy available to the final state electron and photon. Additionally, in data at lower energies there is a contamination from the decay of the J/ψ and other remaining background (see Section 8.2.2). This explains the enhancement of events at lower energies in data with respect to MC.

In order to quantify the correlation between the energy deposited in the UCAL and the number of mip's measured by the SRTD, E_{CAL} is studied in bins of N^{mip}_{SRTD}. A fit to a Gaussian function is performed on the distribution of E_{CAL} in the range $24.5 < M_{e^+e^-} < 29$ GeV. This procedure is performed independently in data and MC. The results of the parameters of the Gaussian fit of the E_{CAL} in bins of N^{mip}_{SRTD} are shown in Figure D.3 and Figure D.4 for data and MC, respectively.

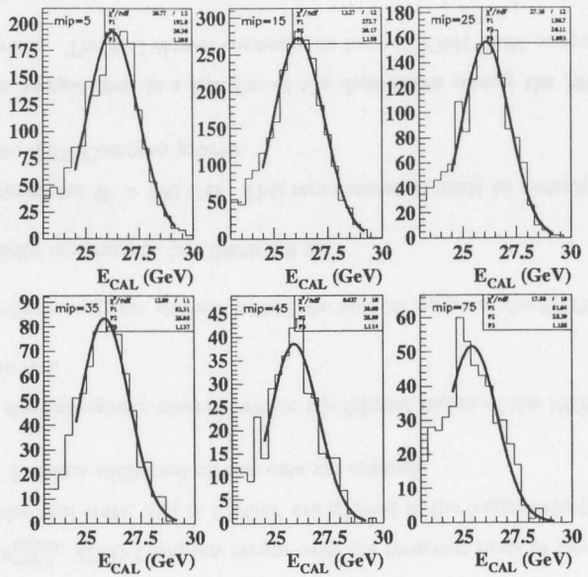

Figure D.3: The distributions of energy deposited in the two electromagnetic clusters, $E_{CAL} = E^1_{CAL} + E^2_{CAL}$, in different ranges of the total number of mip's measured in the SRTD, $N^{mip}_{SRTD} = N^{mip,1}_{SRTD} + N^{mip,2}_{SRTD}$, in the QED Compton selection in data. The distributions are fitted to a Gaussian function in the range $24.5 < M_{e^+e^-} < 29$ GeV. The results of the fit are given on the upper right corner. On the upper left corner the average value of N^{mip}_{SRTD} is given.

D.2 Results

In order to quantify the correlation between the energy deposited in the UCAL and the number of mip's measured by the SRTD, it is relevant to consider the mean of the Gaussian functions obtained in the fits of E_{CAL} in bins of N^{mip}_{SRTD}. A fit of the form given in Expression (D.1) is performed separately in data and MC. The results of the

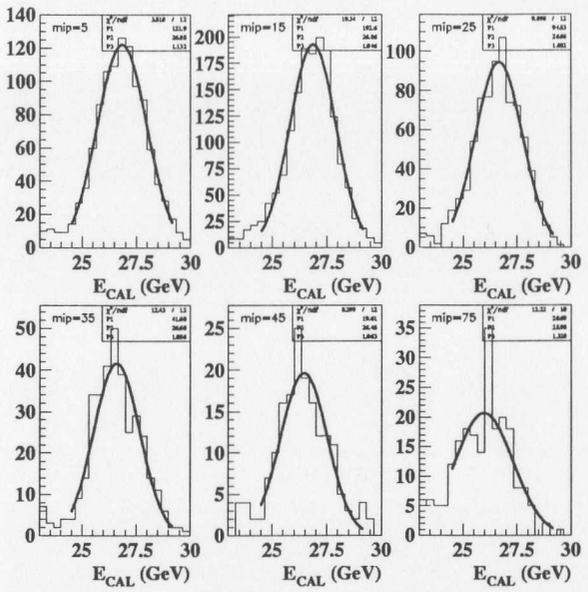

Figure D.4: Same as in Figure D.3 for the COMPTON MC.

fits are given in the left and right Plots of Figure D.5 for data and MC, respectively.

The parameters of the fits shown in Figure D.5 correspond to $\alpha_{SRTD}^{Data} = (0.025 \pm 0.002)$ GeV/mip for data and $\alpha_{SRTD}^{MC} = (0.022 \pm 0.002)$ GeV/mip for MC. These two values are used to correct off-line the energy of electromagnetic clusters in data and MC (see Section 6.2). These values are significantly smaller than $\alpha_{SRTD}^{Data} = (0.044 \pm 0.004)$ GeV/mip [105] and $\alpha_{SRTD}^{Data} = (0.055 \pm 0.0005)$ GeV/mip [190] obtained for the conditions of the 1994 and 1995 running periods, respectively. In these analyses the fiducial cuts on the RCAL were not so stringent as in the present work. Additionally, the Vertex Detector was not present during the 1999 and 2000 running conditions, decreasing further the amount of inactive material that electrons and photons need to cross before reaching the SRTD. The deviation from the linear ansatz assumed in

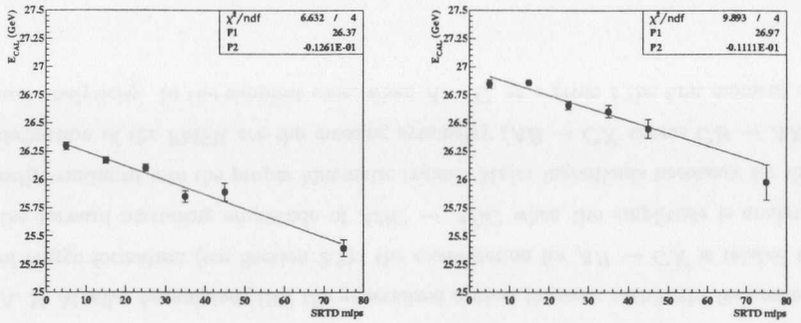

Figure D.5: The mean of the Gaussian functions obtained in the fits shown in Figure D.3 and Figure D.4 are plotted as a function of the average number of SRTD mip's and fitted to a linear function (see Expression (D.1)). The left Plot corresponds to data and the right Plot to MC. The results of the fits are given on the upper right corner.

Expression (D.1) was studied in [190]. The contribution from an additional term in Expression (D.1) proportional to $(N_{SRTD}^{mip} / 2)^2$ was found to be non-negligible. The average value of N_{SRTD}^{mip} is strongly correlated with the average amount of inactive material that the electron or photons need to cross before reaching the SRTD. As the average inactive material in this analysis is about a factor of two smaller than in those analyses, it is expected that the value of α_{SRTD}^{Data} obtained here be significantly smaller than those obtained in the conditions of the 1994 and 1995 running periods. The value of α_{SRTD}^{Data} obtained here is consistent with those obtained in [191] and [73] for the running conditions of 1996-1997 and 1998-1999, respectively.

The results of the fits given in Figure D.5 show that the extrapolation of E_{CAL} to $N_{SRTD}^{mip} = 0$ (parameter P_1 in the box on the upper right corner) is lower in data with respect to MC by about 2%. This is explained by the fact that a number of corrections has not been applied to the energy response of the UCAL. These corrections were applied in the final off-line analysis (see Section 6.2). This "shift" between the energy

response of data and MC does not change the conclusions drawn here.

Appendix E

Finite Mass Sum Rule

In the conditions of the ZEUS detector only the continuum part of the diffractive proton dissociative reaction $ep \to eVN$ is observed. A significant fraction of this spectrum escapes undetected through the beam pipe. These types of events "look" like elastic and need to be subtracted from the elastic sample. In this work, dedicated runs have been taken to measure the rate of events with masses $M_N \gtrsim 3\,\text{GeV}$ (see Section 8.1.1). In order calculate the fraction of events coming from the reaction $ep \to eVN$ with $M_N \lesssim 3\,\text{GeV}$ in the elastic sample, it is necessary to relate the resonant-like region and the continuum to each other. The Finite Mass Sum Rule (FMSR) provides this connection [192].

The FMSR is an extension of the Finite Energy Sum Rule (FESR) [28]. The FESR applies to the reaction $AB \to X$ whereas the FMSR relates to $AB \to CX$. A. H. Mueller formulated [193] the generalized optical theorem within the framework of Regge formalism (see Section 2.2): the cross-section for $AB \to CX$ is related to the forward scattering amplitude of $ABC \to ABC$ when the amplitude is analytically continued into the proper kinematic region. Major ingredients necessary for the derivation of the FMSR are the crossing symmetry ($AB \to CX$ versus $CB \to AX$) and analyticity. In the simplest case, when $A = C$, at a given t the first moment of

the FMSR may be written as [28]:

$$|t|\frac{d\sigma_{el}}{dt}+\int_0^{\nu_0}\nu\left(\frac{d^2\sigma}{dtd\nu}\right)_R d\nu=\int_0^{\nu_0}\nu\left(\frac{d^2\sigma}{dtd\nu}\right)_C d\nu \tag{E.1}$$

where $\nu = M_N^2 - m_p^2 - t$ is the variable of cross symmetry and m_p is the mass of the proton. The area below the extrapolation of $\nu\left(\frac{d^2\sigma}{dtd\nu}\right)_C$ from the high ν (continuum) to the low ν region equals to the area below the resonant-like cross-section $\nu\left(\frac{d\sigma^2}{dtd\nu}\right)_R$ plus the elastic cross-section multiplied by $|t|$. The FMSR is illustrated in Figure E.1. The validity of the FMSR in the low $|t|$ regime has been verified in $pp \to pN$ to a high degree of accuracy [194].

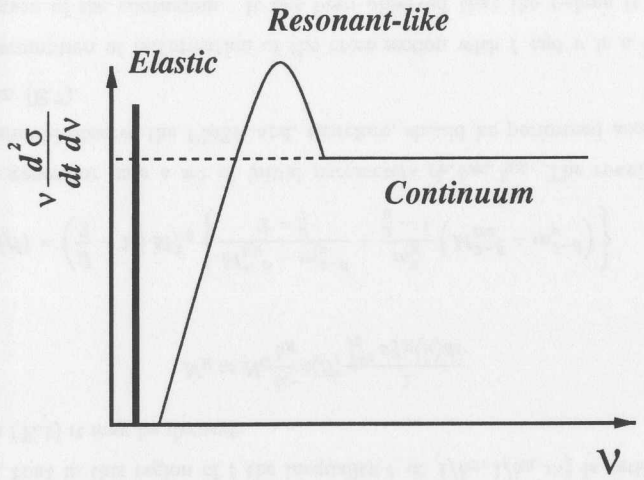

Figure E.1: First moment of the Finite Mass Sum Rule. The area below the extrapolation of $\nu\frac{d^2\sigma}{dtd\nu}$ from the high ν to the low ν region equals to the area below the resonant-like region plus the elastic cross-section.

The MC generator used should comply with Expression (E.1). This has been checked for the DIFFVM program (see Section 7.2.6). This check has been performed in a region of small enough values of $|t|$ such that the first term in the left hand side of

Equation (E.1) is much smaller than the other terms, but $|t| \ll t_{min}$ [1] to avoid the suppression of the production of large masses [195].

As pointed out in Section 8.1.1, the dissociation of the proton may be split into two regions in M_N (or ν), the resonant-like region and the continuum. In order to turn Formula (E.1) into a straightforward analytical expression used to relate the number of events generated in the resonant-like region and the continuum some assumptions must be done:

1. The cross-section factorizes with t and ν, i.e. $\frac{d^2\sigma}{dtd\nu} \propto f(t)f(\nu)$.
2. The cross-section of the production of M_N in the continuum has a power-like behavior $\propto 1/M_N^\beta$, where $\beta > 2$. The extrapolation of the high ν region into the low mass region is performed according to this functional form. The t dependence is parameterized with a single exponential, e^{bt}. Parameters β and b need to be determined from the experiment.
3. The transition between the resonant-like region and the continuum region is smooth and it happens at $\nu_0 \approx 3\,\mathrm{GeV}^2$, independent of the energy.

Following the considerations above, the generation of resonant-like states is performed according to:

$$\frac{d^2n_R}{dtd\nu} = A_R f_R(\nu) e^{b_R t} \tag{E.2}$$

and

$$A_R = N_R b_R \tag{E.3}$$

where $N_R = \int \frac{d^2n_R}{dtd\nu} dtd\nu$ is the total number of generated events in the resonant-like region ($\nu < \nu_0$), b_R is the average t-slope of the resonant-like region and $f_R(\nu)$ is a function that contains the resonant-like structure of the spectrum with the proper normalization:

$$\int_0^{\nu_0} f_R(\nu)d\nu = 1 \tag{E.4}$$

[1] The kinematically smallest possible in the reaction $ep \to eVN$, t_{min}, is $|t_{min}| \approx \frac{M_V^2 M_N^2}{W^2}$.

The continuum part of the spectrum is generated as follows:

$$\frac{d^2n_C}{dtd\nu} = A_C \frac{e^{b_C t}}{\left(\nu + m_p^2 + t\right)^{\frac{\beta}{2}}} \tag{E.5}$$

and

$$A_C = N_C b_C \left(\frac{\beta}{2} - 1\right) M_{N0}^{\beta-2} \tag{E.6}$$

where $N_C = \int \frac{d^2n_C}{dtd\nu} dtd\nu$ is the total number of generated events in the continuum region $(\nu > \nu_0)$, b_C is the t-slope of the continuum region and $M_{N0}^2 = \nu_0 + m_p^2 + t$. The left hand side of Equation (E.1) may be easily calculated by inserting Expression (E.5). Provided that in this region of t the inequality $t \ll 1/b_C, 1/b_R, m_p^2$ is verified, from Equation (E.1) it may be derived:

$$N_R \approx N_C \frac{b_C}{b_R} \kappa(\beta) \frac{1}{\int_0^{\nu_0} \nu f_R(\nu) d\nu} \tag{E.7}$$

where

$$\kappa(\beta) = \left(\frac{\beta}{2} - 1\right) M_{N0}^2 \left\{ \frac{M_{N0}^{4-\beta} - m_p^{4-\beta}}{2 - \frac{\beta}{2}} + \frac{m_p^2}{\frac{\beta}{2} - 1} \left(M_{N0}^{2-\beta} - m_p^{2-\beta}\right) \right\} \tag{E.8}$$

The MC generator uses a set of initial parameters β_0, b_{R0}, b_{C0}. The reweighting of the MC should observe the FMSR and, therefore, should be performed according to Expression (E.7).

The assumption of factorization of the cross-section with t and ν is a valid one in the region of the continuum. It has been observed that the t-slope is constant down to values $\nu \gtrsim 8\,\text{GeV}^2$ ([125, 126] and also See Section 8.1.1). This is not valid for $\nu \lesssim 8\,\text{GeV}^2$. Expression (E.7) is a coarse approximation that may be used provided that the variation applied on parameters β, b_R, b_C is large enough so that the correlation of t and ν in the low mass region may be neglected. An average t-slope of the resonant-like region, $b_R = 4 \pm 2\,\text{GeV}^{-2}$, in the reaction $ep \to eJ/\psi N$ [130] has been used.

Appendix F

Stability Checks of results of Elastic Photoproduction of J/ψ

F.1 Stability of the Procedure of Extraction of the Signal

As a systematic check, the mass window has been shifted left and right by two bins [1]. By shifting the mass window right and left systematic effects due to the inappropriate description of the $M_{e^+e^-}$ distribution in data by MC are taken into account.

An effect that needs to be studied is the dependence of the results of the extraction of the signal on the ranges of the fit. In the nominal procedure a fit is performed on the $M_{e^+e^-}$ distribution in the range $2 < M_{e^+e^-} < 5$ GeV. In order to check the stability of the result of the fits, the latter are performed in different ranges:

1. Change the lower bound of the fit to 2.7 GeV in the range $50 < W < 170$ GeV and 2.3 GeV in the rest of the W range.

2. Change the upper bound of the fit to 4.5 GeV. This checks the assumption made in the nominal fit according to which the remaining background is fit to a single

[1] For the definition of the bin size see Sections 9.4 and 9.5.

exponential functional form for the whole range $2 < M_{e^+e^-} < 5$ GeV.

W (GeV)	N_{signal}^{Nom}	N_{signal}^{Left}	N_{signal}^{Right}	N_{signal}^{Check1}	N_{signal}^{Check2}
20 - 35	765.4	802.3	660.3	774.4	765.4
35 - 50	1800.2	1908.8	1666.3	1809.1	1798.4
50 - 60	1605.8	1679.3	1541.7	1605.6	1600.3
60 - 70	1413.4	1466.6	1361.4	1405.7	1413.7
70 - 80	1250.7	1296.2	1199.9	1230.6	1249.4
80 - 90	1115.7	1140.4	1070.0	1129.5	1112.4
90 - 110	2053.6	2139.6	1955.6	2057.3	2047.8
110 - 125	1368.6	1399.3	1312.6	1385.1	1363.6
125 - 140	1249.2	1274.9	1181.3	1256.6	1247.4
140 - 170	1910.0	1961.6	1786.6	1977.9	1901.2
170 - 200	1150.4	1177.9	1047.7	1154.3	1150.4
200 - 230	900.0	884.9	836.3	905.2	901.2
230 - 260	765.5	743.3	753.2	815.4	756.1
260 - 290	706.2	685.1	621.3	652.0	683.0

Table F.1: Number of observed J/ψ events obtained following the nominal procedure, N_{signal}^{Nom}, compared with the results obtained by shifting left and right by two bins in $M_{e^+e^-}$ the mass window, N_{signal}^{Left} and N_{signal}^{Right}, respectively, and changing the range of the fits, N_{signal}^{Check1} and N_{signal}^{Check2}, respectively. The values of N_{signal} have not been corrected for contamination from $\psi(2S)$ decays.

The results of N_{signal} in bins of W are given in Table F.1. The same procedure has been performed in bins of W and P_t^2. The deviation from the nominal signal events is included in the systematic error (see Section 9.3).

F.2 Stability of Results of $\sigma(\gamma p \to J/\psi p)$ with the Definition of the Elasticity Requirement

In this Section we check the stability of the results of $\sigma(\gamma p \to J/\psi p)$ with the definition of E_{max} (see Section 6.4). Most of the cells not associated to the two electromagnetic object are concentrated in the electromagnetic section of the UCAL. The UCAL has a larger number of electromagnetic cells compared to hadronic cells. Additionally, one would expect that a significant fraction of inelastic events with low particle multiplicity may leave low energy depositions in the UCAL. Low energetic pions are likely to look like electromagnetic clusters as they cannot penetrate through the whole depth of electromagnetic section of the UCAL to make it to the hadronic section.

Figure F.1 shows the distributions of E_{max}. for different sections of the UCAL. The points correspond to data after the application of off-lines cuts except for the elasticity requirement (see Section 6.4) and the empty histogram to MC. The MC simulation reproduces only a fraction of the noise produced by the UCAL. For instance, fake energy depositions due to sparks are not implemented in the simulation. Therefore, it is not expected that the long tails seen in the logarithmic scale in Plots b) and c) of Figure F.1 be reproduced by MC. The distribution of E_{max} in the EMC, Plot a), shows a clear enhancement of the data with respect to the MC description of the noise at $E_{max} > 200\,\text{MeV}$.

Three effects are sensitive to the definition of elasticity: the contribution from production of J/ψ via the dissociation of the proton (see Section 8.1.1), hard final state QED radiation of the electrons of the decay of the J/ψ (see Section 7.3.4) and the contribution of J/ψ coming from the decay of the $\psi(2S)$ (see Section 8.1.2). The contribution from different processes is shown in Figure F.1. The dependence of the fraction of proton dissociative background on the definition of elasticity has been studied for different values of the cut on E_{max} (see Table 8.1). A mild dependence is seen with cuts up to $E_{max} < 400$ MeV. It is expected that the contribution from pro-

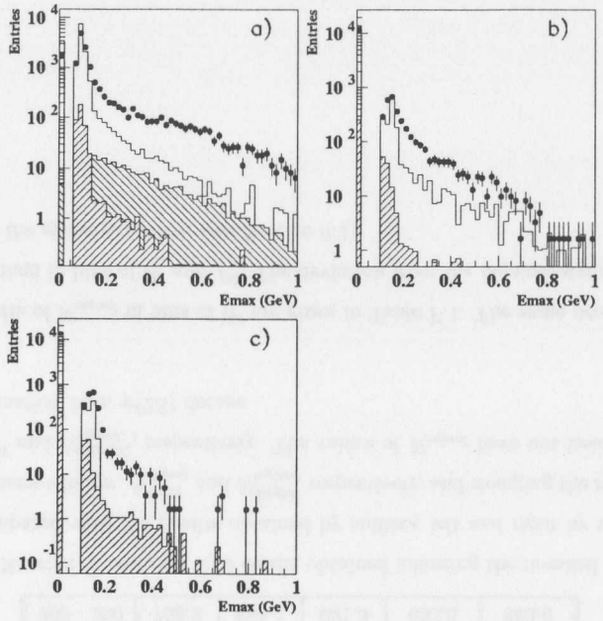

Figure F.1: Distributions of the energy of the most energetic cell in the UCAL not associated to any of the electromagnetic objects, E_{max}. Plots a), b), c) correspond to EMC, HAC0 and HAC1 cells, respectively. Solid points correspond to data and the solid line to the contribution of elastic J/ψ (the ZEUSVM MC), elastic $\psi(2S)$ (the DIPSI MC) and proton dissociative J/ψ (the EPSOFT MC). The shaded histograms correspond to the contribution from elastic $\psi(2S)$ and proton dissociative J/ψ. Off-line cuts have been applied except for the elasticity requirement (see Section 6.4).

ton dissociative J/ψ be larger and the contribution from $ep \to J/\psi X$ show up with $E_{max} < 1$ GeV.

The procedure of extraction of the signal, the calculation of acceptance corrections and cross-sections was repeated for several cuts on E_{max}. The values of the variation of the cross-section for different values of the cut on E_{max} are given in Table F.2 and

	$\Delta\sigma/\sigma$ for cut on E_{max}(MeV) in EMC			
W(GeV)	250	300	400	1000
20 - 35	-0.028	-0.040	-0.048	-0.061
35 - 50	-0.002	0.012	0.016	0.026
50 - 60	0.007	0.015	0.025	0.036
60 - 70	0.020	0.026	0.033	0.030
70 - 80	0.014	0.025	0.025	0.052
80 - 90	0.024	0.039	0.047	0.061
90 - 110	0.025	0.034	0.039	0.041
110 - 125	0.016	0.025	0.024	0.024
125 - 140	0.027	0.033	0.033	0.062
140 - 170	0.018	0.024	0.031	0.042
170 - 200	-0.001	0.045	0.011	0.042
200 - 230	0.036	0.031	0.048	0.059
230 - 260	0.007	0.008	0.009	0.047
260 - 290	0.005	0.004	0.015	0.075

Table F.2: Relative deviation of $\sigma(\gamma p \to J/\psi p)$ in ranges of W for different cuts on the energy of the most energetic cell in the electromagnetic section of the UCAL not associated to the two electromagnetic objects in the event (see text).

in Figure F.2. The value of the variation is positive in the average and increases with relaxing the cut on E_{max}, as expected. The variation remains within few percent and it is partially explained by the increase of the contribution from proton dissociative and inelastic production of J/ψ.

By relaxing the cut on E_{max} the amount of remaining non-resonant background changes significantly, increasing the statistical error on the determination of the cross-section. This is illustrated in Figure F.2 by the increase of the error bars as the cut on E_{max} is relaxed.

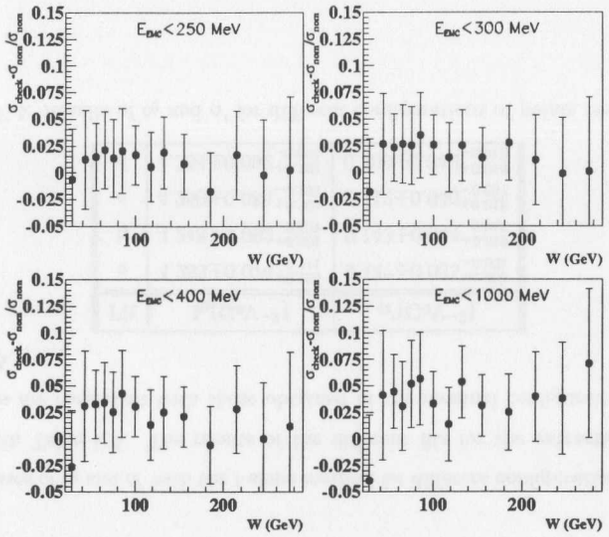

Figure F.2: Relative deviation of $\sigma(\gamma p \to J/\psi p)$ in ranges of W for different cuts on the energy of the most energetic cell in the electromagnetic section of the UCAL not associated to the two electromagnetic objects in the event (see text).

F.3 Stability of Results with the Performance of the SRTD

The number of bad SRTD strips increased during the 1999 and 2000 running periods. It is necessary to check the stability of the results and calculate the cross-sections for runs in which the SRTD had a small number of dead strips. A check has been performed in which runs in data have not been used with more than 5% of SRTD dead strips. This requirement throws out a considerable amount of luminosity leaving the analysis with $32.52\,\mathrm{pb}^{-1}$ of data. The value of the cross-sections in the last two bins in W changed from the values given in Table 9.1 to $145.5\pm9.7(stat)$ and $198.1\pm17.1(stat)$ nb, respectively. These results are in reasonable agreement with the nominal results given in Table 9.1.

F.4 Stability of the Regge Trajectory and t-slopes

The results should not depend significantly on the W and t ranges. It is known that the purities at high $|t|$ are low, specially at high W, due to the poor resolution of the UCAL at low energies. Also the first and the last bin in W display a large background contribution.

For this purpose, the parameters of the Regge trajectory have been extracted following the prescription given in Section 9.5 for the following configurations of points:

a. Take out the bins with $230 < W < 290$ GeV.

b. Take out the bins with $170 < W < 290$ GeV.

c. Take out the bins with $20 < W < 50$ GeV.

d. Take out bins with $-t > 0.85$ GeV^2.

The results of the values of $\alpha(0)$ and α' for these configurations of points are given in Table F.3. The results are consistent with those obtained in the nominal configuration given in Section 9.5.

Fit	$\alpha(0)$	$\alpha'(\mathrm{GeV}^{-2})$
a	$1.206\pm0.014^{+0.003}_{-0.011}$	$0.144\pm0.029^{+0.007}_{-0.017}$
b	$1.203\pm0.017^{+0.005}_{-0.005}$	$0.132\pm0.037^{+0.007}_{-0.011}$
c	$1.191\pm0.017^{+0.006}_{-0.020}$	$0.129\pm0.037^{+0.015}_{-0.029}$
d	$1.195\pm0.015^{+0.003}_{-0.010}$	$0.107\pm0.038^{+0.008}_{-0.015}$

Table F.3: Results of $\alpha(0)$ and α' for different configurations of points (see text).

To check the reliability of the extraction of the t-slopes it is relevant to extract these parameters in a restricted t range. The results of the fits in the range $0 < |t| < 0.85$ GeV

are given in Table F.4 and are consistent with the nominal results given in Table 9.3. The statistical errors of the t-slopes given in Table F.4 are larger than the nominal ones due to the reduction of the lever arm in the fitting in t. The systematic errors are somewhat smaller than the nominal ones. The systematic error is dominated by the uncertainty in the subtraction of the proton dissociative background. In absolute terms, the uncertainty on the differential cross-section grows with the increase of the contamination, the systematic error grows with $|t|$.

W (GeV)	b (GeV^{-2})
20 - 50	$3.58 \pm 0.30^{+0.13}_{-0.10}$
50 - 70	$4.13 \pm 0.20^{+0.19}_{-0.07}$
70 - 90	$4.67 \pm 0.24^{+0.20}_{-0.08}$
90 - 125	$4.76 \pm 0.21^{+0.22}_{-0.08}$
125 - 170	$4.29 \pm 0.21^{+0.19}_{-0.10}$
170 - 230	$4.54 \pm 0.24^{+0.18}_{-0.16}$
230 - 290	$5.02 \pm 0.56^{+0.20}_{-0.20}$

Table F.4: Results of b in ranges of W with statistical and systematic errors obtained with the nominal method excluding points with $|t| > 0.85$ GeV.

The values of b_0 and α' with the t-slope method for different configurations of points are given in Table F.5. The results of the different fits for the extraction of these parameters are consistent with those obtained in the nominal configuration given in Section 9.5.

Fit	b_0(GeV^{-2})	α'(GeV^{-2})
a	$4.253 \pm 0.074^{+0.190}_{-0.111}$	$0.147 \pm 0.035^{+0.008}_{-0.021}$
b	$4.248 \pm 0.082^{+0.201}_{-0.107}$	$0.143 \pm 0.044^{+0.010}_{-0.010}$
c	$4.260 \pm 0.084^{+0.204}_{-0.108}$	$0.112 \pm 0.040^{+0.015}_{-0.037}$
d	$4.354 \pm 0.092^{+0.183}_{-0.084}$	$0.109 \pm 0.042^{+0.010}_{-0.015}$

Table F.5: Results of b_0 and α' for different configurations of points (see text).

Appendix G

Search for Elastic Photoproduction of $\Upsilon \rightarrow e^+e^-$ with 96-97 Data

The data used in this Appendix were taken during the 1996 and 1997 running period and corresponds to an integrated luminosity of 37 pb^{-1}. This material is based on the work presented in [138]. The results of this work were reported in [156].

G.1 Bremsstrahlung Radiation

In this analysis it was attempted to reduce the effect of bremsstrahlung radiation of electrons of the decay of the Υ on the acceptance using the UCAL (mainly BCAL) information in place of CTD momentum of tracks that radiated a strong photon.

For those electrons that radiate strongly the CTD momentum measurement will be substantially smaller than the energy of the UCAL cluster. The CTD momentum, P, may be compared on an event-by-event basis to the energy of the deposited UCAL cluster, E. For a given track-cluster pair a simple function is calculated:

$$F(P,E) = \frac{\frac{1}{P} - \frac{1}{E}}{\sigma(\frac{1}{P}) \oplus \sigma(\frac{1}{E})} \qquad \text{(G.1)}$$

Figure G.1 shows the distribution of $F(P,E)$ for data and the LPAIR MC. The data sample corresponds to di-e with 4< $M_{e^+e^-}$ <20 GeV. The resolution from CTD mo-

mentum is taken from the parameterization obtained in Appendix B. The resolution of E in the BCAL was parameterized as $\sigma_E = 32\%\sqrt{E}$ [196]. In Figure G.1 a long radiative tail is seen at high values of $F(P,E)$. For those events the CTD momentum lies below the energy of the UCAL cluster, which contains the energy deposition of the radiated hard photon. For tracks for which $F(P,E) > \zeta$, where ζ is a parameter, one might consider to replace the measurement of the CTD momentum by the energy of the UCAL cluster and subsequently reconstruct $M_{e^+e^-}$.

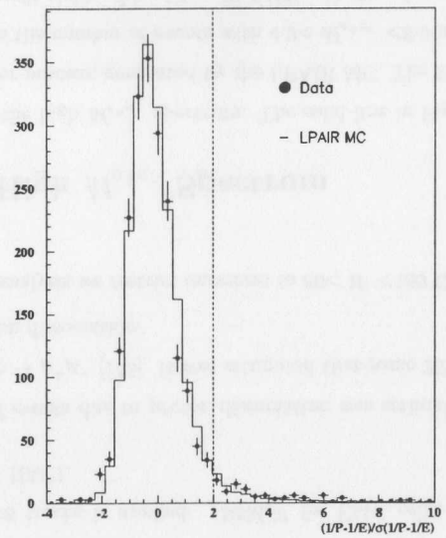

Figure G.1: P is compared with E of the matching cluster in data and MC, by plotting $F(P,E)$ (see text).

	CTD Only	ζ=5	ζ=3	ζ=2	ζ=1.5
A (%)	44.9	46.8	48.3	49.6	50.2

Table G.1: Acceptance for $\Upsilon(1S) \to e^+e^-$ calculated with the DIPSI MC for different values of ζ.

Figure G.2 shows the reconstructed $M_{e^+e^-}$ spectrum for Υ(1S) for different values of ζ with the DIPSI MC. As tracks with too high $F(P,E) > \zeta$ are replaced by the measured UCAL energy, the radiation tail in the $M_{e^+e^-}$ spectrum disappears.

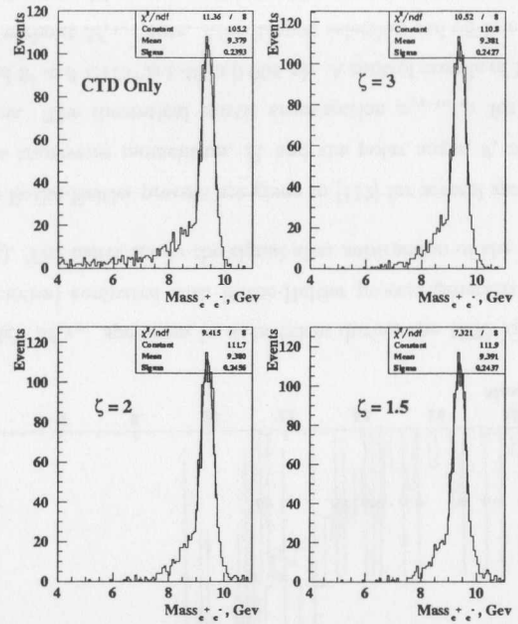

Figure G.2: $M_{e^+e^-}$ spectrum reconstructed with CTD tracks only (upper left Plot) and for different values of ζ (see text) for $\Upsilon(1S)$ with the DIPSI MC.

Table G.1 shows acceptance $\Upsilon(1S) \to e^+e^-$ calculated with the DIPSI MC for different values of ζ. The acceptance is calculated for 80< W <160 GeV and a $M_{e^+e^-}$ window of 8.5< $M_{e^+e^-}$ < 10.9 GeV. As seen in Figure G.2, events with electrons that have radiated strongly may be recovered to the mass window of the extraction of the signal. An optimal value of ζ is to be taken not to dismiss tracks for which $F(P,E)$ is high due to intrinsic resolution. The value of ζ=2 is chosen.

G.2 Trigger and off-line selection

The trigger selection HFL06 is used. The logic of this trigger selection in the conditions of the 1996 and 1997 running periods is given in Section 5.3.

The off-line selection is very similar to that presented in Section 6.4. Two are the differences:

- The UCAL energy of the cluster matched to a track with $F(P,E) > 2$ (see Expression (G.1)) is used in place of the CTD momentum.
- The elasticity requirement. The cuts on the most energetic cell not associated with the two tracks is applied: 150 MeV for EMC cells, 200 MeV for HAC0, 300 MeV for HAC1.

The fraction of events due to proton dissociation was estimated for elastic photoproduction of $J/\psi \to \mu^+\mu^-$ [155]. It was estimated that some 25% of events would be coming from proton dissociation.

In the present analysis we restrict ourselves to 80< W <160 GeV.

G.3 The High $M_{e^+e^-}$ Spectrum

Figure G.3 shows the high $M_{e^+e^-}$ spectrum. The solid line in Figure G.3 corresponds to the Bethe-Heitler process, generated by the LPAIR MC. The Bethe-Heitler MC has been normalized to the number of events with 4.2< $M_{e^+e^-}$ <8.5 in data by means of a χ^2 fit. The resulting fit yields $\chi^2/n.d.f. = 21.5/(21-1)$. The shape of the reconstructed $M_{e^+e^-}$ of the normalized MC sample nicely follows the data up to high $M_{e^+e^-}$ of 20 GeV, as seen in Figure G.3.

In order to estimate the fraction of proton dissociative Bethe-Heitler events in the sample the following procedure was accomplished. The LPAIR generator does not calculate cross-sections for an arbitrary set of kinematic cuts. The theoretical cross-

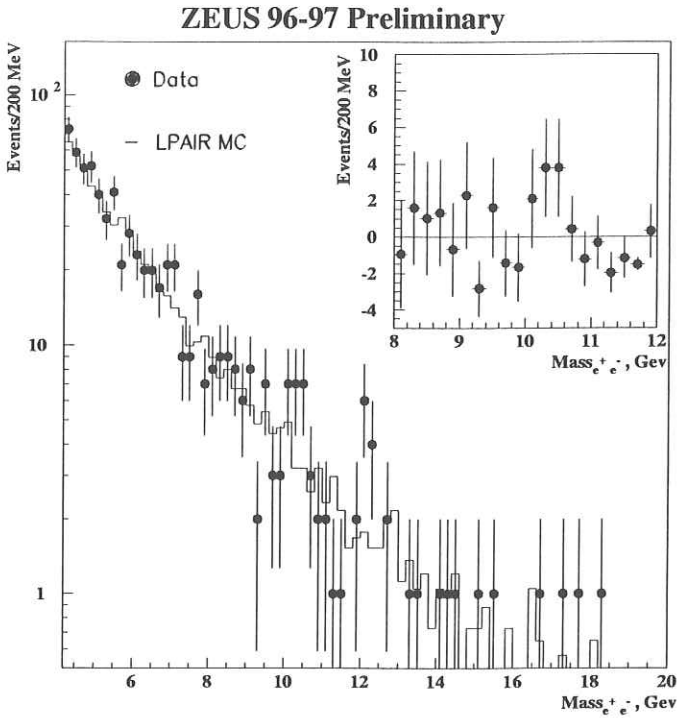

Figure G.3: High $M_{e^+e^-}$ spectrum in data taken during the 1996 and 1997 running periods (solid circles) compared with Bethe-Heitler process generated by the LPAIR MC (histogram). The insert shows the signal after subtraction of the LPAIR MC.

sections for the Bethe-Heitler process are given in [112] for several specific cuts in the energy, $E_{e'}$, the transverse momentum, P_t and the polar angle, θ, of the elastically produced leptons. The theoretical elastic cross-section $\sigma_{\gamma\gamma\to e^+e^-}$ for $E_{e'}$ >0.5 GeV, P_t >0.5 GeV and 5° < θ <175° is 1.450±0.004 nb. A control sample of 10000 events has been generated without $M_{e^+e^-}$ cuts. After trigger selection and off-line cuts 111 events are reconstructed in the $M_{e^+e^-}$ range of 4.2< $M_{e^+e^-}$ <8.5 GeV and 80< W <160 GeV. The total amount of data events in that $M_{e^+e^-}$ range is 656, where for the present

luminosity one would expect to have 595.5 elastic Bethe-Heitler pairs. The fraction of proton dissociative inelastic Bethe-Heitler is estimated to be 10%±10% (the error comes from the statistical error of the estimation of events with 4.2< $M_{e^+e^-}$ <8.5 GeV in the control sample).

The mass window for the search of the Υ signal is chosen to be 8.5< $M_{e^+e^-}$ < 10.9 GeV. The value of the lower bound is taken from the shape of the reconstructed $M_{e^+e^-}$ in MC for the lowest lying resonance $\Upsilon(1)$ (see Figure G.2). The upper bound of the mass window is chosen to cope with excited heavier states $\Upsilon(2S)$ and $\Upsilon(3S)$ [155].

The Υ signal is extracted by subtracting the number events resulting from the extrapolation of the normalized Bethe Heitler MC sample to the $M_{e^+e^-}$ region of the mass window from the number of data events observed in the mass window:

$$N_\Upsilon = N_{MW}^{Data} - N_{MW}^{BH} \tag{G.2}$$

The error on N_Υ is defined as:

$$\Delta N_\Upsilon = \sqrt{N_{MW}^{Data}} \tag{G.3}$$

In the mass window defined above 69 events are seen in data, 57.9 are expected from Bethe-Heitler process, resulting in N_Υ=11.1±8.3.

G.4 Systematic Checks

The following set of checks were done:

- The tracking efficiency of the FLT58, ±5% [155].
- Uncertainty on the proton dissociative background (+9,-2) [155].
- Shifting the mass window for the extraction of the Υ signal by ±300 MeV: (-48,-7)%.
- Using a different mass region for the normalization of the Bethe-Heitler background, 4< $M_{e^+e^-}$ <8.5 GeV and 4.4< $M_{e^+e^-}$ <8.5 GeV: (-2,+7.5)%.

- Varying the $\cos\theta_h$ distribution used in MC that required by s-channel helicity conservation ($1+\cos^2\theta_h$) to a flat distribution: -6%.
- Varying the dependence of $\sigma_{\gamma p\to\Upsilon p}$ on W ($\sigma_{\gamma p\to\Upsilon p} = AW^\delta$) in MC. The theoretical prediction δ is changed by ±1:(1.5,-1)%.
- Varying cuts on the amount the energy of the most energetic cell not associated to the two tracks by ±50 MeV: (5.5,-1)%,(3,0.7)%,(0,0)% (EMC ,HAC0 and HAC1, respectively).
- Varying the value of ζ to ζ=1.5,2.5 (see Section G.1): (-4,-4)%.
- Uncertainty in the electronic branching ratio $\mathcal{B}(\Upsilon(1S)\to e^+e^-)$ [139]: (7,-7)%.

All of these uncertainties are added in quadrature yielding an overall systematic error on $\sigma_{\gamma p\to\Upsilon p}$ of $(16,-49)$%. The statistical error on the measurement yields 75%, bigger than the systematic uncertainties.

G.5 The Cross-Section

The procedure of the extraction of the photoproduction cross-section is described in Section 9.2. The cross-sections times branching ratios of the first three Υ resonances are assumed to be the same as measured by CDF [157]. The result is presented in terms of the cross-section of the production of the $\Upsilon(1S)$ resonance:

$$\sigma_{\gamma p\to\Upsilon(1S)\,p} = 255 \pm 191(stat)^{+41}_{-125}(syst) \text{ pb at } W = 120 \text{ GeV}$$

The result obtained in this present analysis, being lower, is consistent within errors with the result published by the ZEUS Collaboration [155].

Bibliography

[1] J. I. Friedman, H. W. Kendall, Ann. Rev. Nucl. Sci. **22**, 203;
Gargamelle Collaboration, T. Eichten et al., Phys. Lett. **B44** (1973) 274.

[2] J. D. Bjorken, Phys. Rev. **163** (1967) 1767;
J. D. Bjorken, Phys. Rev. **179** (1969) 1547.

[3] R. P. Feynman, Phys. Rev. Lett. **23** (1969) 1415.

[4] J. D. Bjorken and E. A. Paschos, Phys. Rev. **185** (1969) 1975.

[5] F. Halzen and A. D. Martin, *Quarks and Leptons* (John Wiley Sons Inc., New York, 1984).

[6] J. C. Collins, D. E. Soper and G. Sterman, Nucl. Phys. **B261** (1961) 104.

[7] V. N. Gribov and L. N. Lipatov, Sov. J. Nucl. Phys. **15** (1972) 675;
Y. L. Dokshitzer, Sov. Phys. JETP **46** (1977) 641;
G. Altarelli and G. Parisi, Phys. Lett. **126** (1977) 298.

[8] K. Prytz, Phys. Lett. **332** (1994) 393.

[9] A. Zamolodchikov, B. Kopeliovich and L. Lapidus, JETP Lett. **33** (1981) 595.

[10] E. M. Levin, M. G. Ryskin, Sov. J. Nucl. Phys. **45** (1987) 150.

[11] A. H. Mueller, Nucl. Phys. **B335** (1990) 115.

[12] A. H. Mueller, Nucl. Phys. **B415** (1994) 373.

[13] N. Nikolaev, B. G. Zakharov, Z. Phys. **C49** (1991) 607.

[14] J. R. Forshaw and D. A. Ross, *QCD and the Pomeron* (Cambridge University Press, Cambrigde, 1986).

[15] E. M. Levin et al., Z. Phys. **C74** (1997) 671.

[16] V. N. Gribov, E. M. Levin and M. G. Ryskin, Nucl. Phys. **B188** (1981) 555;
V. N. Gribov, E. M. Levin and M. G. Ryskin, Phys. Rep. **100** (1983) 1.

[17] E. Gotsman et al., Phys. Lett. **B425** (1998) 369;
E. Gotsman et al., Nucl. Phys. **B539** (1999) 535.

[18] E. Gotsman, Has HERA Reached a New QCD Regime?, DESY 00-149 (2000).

[19] M. Froissart, Phys. Rev. **123** (1961) 1503.

[20] The ISR Staff, Phys. Lett. **B34** (1971) 425.

[21] U. Amaldi and K. R. Schubert, Nucl. Phys. **B166** (1980) 301.

[22] A. Capella, Nucl. Phys. **B593** (2001) 336;
A. Capella, Phys. Rev. **D63** (2001) 054010.

[23] K. Golec-Biernat and M. Wüsthoff, Phys. Rev. **D59** (1998) 014017.

[24] A. Caldwell, Recent Developments in QCD, Invited talk at the DESY Theory Workshop, October 1997.

[25] B. Mellado, Perturbative/Non-perturbative QCD Interface in *ep* Physics, Book of Proceedings of 98 QCD and High Energy Hadronic Interactions XXXIIIrd Rencontres de Moriond, Les Arcs, Savoie, France, March 21-28 1998, 483.

[26] ZEUS Collaboration, J. Breitweg et al., Eur. Phys. J. **C7** (1999) 609.

[27] ZEUS Collaboration, J. Breitweg et al., Z. Phys. **C75** (1997) 215.

[28] K. Goulianos, Phys. Rep. **101** (1983) 169.

[29] D. R. O. Morrison, CERN Preprint D.Ph. II/Phys 73-46 (1973).

[30] M. L. Good and W. D. Walker, Phys. Rev. **120** (1960) 1854.

[31] E. Predazzi, Diffraction: Past, Present and Future, Lectures given at Hadrons VI Florianopolis, Brazil, hep-ph/9809454.

[32] T. Regge, Nuovo Cimento **14** (1959) 951;
T. Regge, Nuovo Cimento **18** (1960) 947.

[33] P. D. B. Collins, *An Introduction to Regge Theory and High Energy Physics* (Cambridge University Press, 1977).

[34] I. I. Pomeranchuk, Sov. Phys. JETP **7** (1958) 499.

[35] A. Donnachie and P. V. Landshoff, Phys. Lett. **B296** (1992) 227.

[36] E. Levin, Lectures on Regge theory, DESY 97-213 (1997).

[37] A. Levy, Low x Physics at HERA, DESY 97-013 (1997).

[38] J. J. Sakurai, Ann. Phys. **11** (1960) 1;
M. Gell-Mann et al., Phys. Rev. Lett. **8** (1962) 261;
S. L. Glashow, Phys. Rev. Lett. **7** (1961) 469;
Y. Nambu and J. J. Sakurai, Phys. Rev. Lett. **8** (1962) 79.

[39] J. J. Aubert et al., Phys. Rev. **33** (1974) 1404;
J.-E. Augustin et al., Phys. Rev. Lett. **33** (1974) 1406.

[40] S. W. Herb, Phys. Rev. Lett. **39** (1977) 252.

[41] J. J. Sakurai, Phys. Rev. Lett. **22** (1969) 981.

[42] ZEUS Collaboration, J. Breitweg et al., Exclusive Electroproduction of ρ mesons, Paper submitted to the XXXX International Conference on High Energy Physics, July 2000, Osaka, Japan (Abstract 880).

[43] L. Stodolsky, Phys. Rev. Lett. **18** (1967) 135.

[44] E. D. Bloom et al., Phys. Rev. Lett. **23** (1969) 930.

[45] J. J. Sakurai, D. Schildknecht, Phys. Lett. **B40** (1972) 121;
R. Devenish, D. Schildknecht, Phys. Rev. **D14** (1975) 93.

[46] V. N. Gribov, Sov. Phys. JETP **14** (1970) 1308.

[47] D. Schildknecht, Acta Phys. Polon. **B28** (1997) 2291.

[48] K. Schilling, P. Seyboth and G. Wolf, Nucl. Phys. **B15** (1970) 397;
K. Schilling and G. Wolf, Nucl. Phys. **B61** (1973) 381.

[49] B. Humbert and A. C. D. Wright, Phys. Lett. **B65** (1976) 463;
B. Humbert and A.C.D. Wright, Phys. Rev. **D 15** (1977) 2503.

[50] A. Donnachie and P. V. Landshoff, Phys. Lett. **B437** (1998) 408.

[51] Y. Y. Balitsky and L. N. Lipatov, Sov. J. Nucl. Phys. **28** (1978) 822;
V. S. Fadin, E. A. Kuraev and L. N. Lipatov, Sov. Phys. JETP **44** (1976) 443;
V. S. Fadin, E. A. Kuraev and L. N. Lipatov, Sov. Phys. JETP **45** (1977) 199.

[52] V. S. Fadin, L. N. Lipatov, Phys. Lett. **B429** (1998) 127;
M. Ciafaloni, G. Camici, Phys. Lett. **B430** (1998) 349.

[53] H. Joos, Phys. Lett. **B24** (1966) 103;
K. Kajantie, J. S. Trefil, Phys. Lett. **B24** (1966) 106.

[54] N. Nikolaev, B. G. Zakharov, Z. Phys. **C53** (1991) 331.

[55] M. G. Ryskin, Z. Phys. **C57** (1993) 89.

[56] S. J. Brodsky et al., Phys. Rev. **D50** (1994) 3134.

[57] A. D. Martin, M. G. Ryskin and T. Teubner, Phys. Rev. **D62** (1997) 014022.

[58] L. Frankfurt, M. McDermott and M. Strikman, JHEP **0103** (2001) 045.

[59] L. Frankfurt, W. Koepf and M. Strikman, Phys. Rev. **D57** (1998) 512.

[60] L. Frankfurt, M. McDermott and M. Strikman, JHEP **9902** (1999) 002.

[61] A. D. Martin, M. G. Ryskin and T. Teubner, Phys. Lett. **B454** (1999) 339.

[62] HERA: A Proposal for a Large Electron Proton Colliding Beam Facility at DESY, *DESY-HERA-81/10*, Hamburg (1981).

[63] ZEUS Collaboration, M. Derrick et al., The ZEUS Detector, Status Report, 1993.

[64] B. Foster et al., Nucl. Instrum. Methods **A338** (1994) 254.

[65] ZEUS Collaboration, A Microvertex Detector for ZEUS, DESY-PRC 97-01 (1997).

[66] A. Andresen et al., Nucl. Instrum. Methods **A309** (1991) 101.

[67] M. Derrick et al., Nucl. Instrum. Methods **A309** (1991) 77.

[68] A. Bernstein et al., Nucl. Instrum. Methods **A336** (1993) 23.

[69] B. Surrow, Measurement of the Proton Structure Function F_2 at Low Q^2 and Very Low x with the ZEUS Beam Pipe Calorimeter at HERA, Ph.D. thesis, Univ. of Hamburg, 1998, DESY-THESIS-1998-004.

[70] T. Monteiro, Study of Exclusive Electroproduction of ρ Mesons at Low Q^2 Using the ZEUS Beam Pipe Calorimeter at HERA, Ph.D. thesis, Univ. of Hamburg, 1998.

[71] A. Bamberger et al., Nucl. Instrum. Methods **A450** (2000) 235.

[72] G. García López, Two Different Cases of Calorimetry in High Energy Physics: the ATLAS Liquid Argon Electromagnetic End Cap and the ZEUS Forward Plug Calorimeter, Ph.D. thesis, Univ. Autonoma de Madrid, 2000.

[73] F. Goebel, Measurement of the Diffractive Contribution to the DIS Cross Section Using the ZEUS Forward Plug Calorimater, Ph.D. thesis, Univ. of Hamburg, 2001.

[74] J. B. Birks, *The Theory and Practice of Scintillator Counting* (Pergamon Press, Oxford, 1964).

[75] M. Ernst, Indentifikation von Electronen im ZEUS-Kalorimeter und Hadron-Elektron-Separator, Diploma Thesis, Univ. of Hamburg, 1991.

[76] R. Wichmann, Properties of the Hadronic Final State in Diffractive Deep Inelastic Scattering Tagged with the Leading Proton Spectrometer of ZEUS, Ph.D. thesis, Univ. of California, Santa Cruz, 2000.

[77] S. Bhadra et al., Design and Test of a Forward Neutron Calorimeter for the ZEUS Experiment, DESY 97-006 (1997).

[78] ZEUS Collaboration, M. Derrick et al., Z. Phys. **C74** (1997) 207.

[79] ZEUS Collaboration, M. Derrick et al., Z. Phys. **C72** (1996) 399.

[80] J. Krüger, DESY F35-92-02 (1992).

[81] W. A. Shurcliff, J. Opt. Soc. Am. **41** (1951) 209;
R. C. Garwin, Rev. Sci. Instrum. **31** (1960) 1010;
F. Engler et al., Phys. Lett. **B29** (1969) 321;
G. Keil, Nucl. Instrum. Methods **89** (1970) 111.

[82] H. Fessler et al., Nucl. Instrum. Methods **A240** (1985) 284;
B. Loehr et al., Nucl. Instrum. Methods **A257** (1987) 145;
L. Labarga et al., Nucl. Instrum. Methods **A249** (1986) 228.

[83] E. Bernardi et al., Nucl. Instrum. Methods **A262** (1987) 229.

[84] A. Bamberger et al., Nucl. Instrum. Methods **A401** (1995) 63.

[85] H. Bethe, W. Heitler, Proc. Roy. Soc. **A 146** (1934) 83..

[86] J. Andruskow et al., DESY 92-066 (1992).

[87] K. Piotrzkowski, Experimental Aspects of the Luminosity Measurement in the ZEUS Experiment, Ph.D. thesis, University of Hamburg, 1993, DESY F35D–93–06.

[88] W. Smith et al., The ZEUS Trigger System, ZEUS Note 89-084 (1989).

[89] W. Smith et al., Global First Level Trigger Timing, ZEUS Note 90-011 (1990).

[90] C. Youngman et al., DESY 92-150A (1992).

[91] L. Hervas, The Readout for the ZEUS Calorimeter, Ph.D. thesis, Universidad Autónoma de Madrid, 1991, DESY F35D–91–01.

[92] J. W. Dawson et al., Conceptual Design of the Calorimeter First-Level Trigger Processor, ZEUS Note 89-086 (1989).

[93] G. P. Heath et al., Design of the CTD First Level Trigger Track Finding Processors, ZEUS Note 89-118 (1989).

[94] R. Halsall et al., The ZEUS Central Tracking Detector First Level Trigger Processor, ZEUS Note 89-120 (1989).

[95] R. Halsall et al., The Veto Wall Detector for ZEUS, ZEUS Note 89-098 (1989).

[96] S. de Jong, The ZEUS Second Level Calorimeter Trigger: Physics Simulation, Design and Implementation, Ph.D. thesis, Univ. van Amsterdam, 1990.

[97] H. Uijterwaal, The Global Second Level for ZEUS, Ph.D. thesis, Univ. van Amsterdam, 1990.

[98] H. van der Lugt, The Data-Acquisition and Second Level Trigger System for the ZEUS Calorimeter, Ph.D. thesis, NIKHEF, 1995.

[99] F. Benard, The 1995 TLT Filter Software, ZEUS Note 95-164 (1995).

[100] T. Abe, Measurement of Exclusive J/ψ Electroproduction in High-Energy ep Collisions at HERA, Ph.D. thesis, Univ. of Tokyo, 2001.

[101] L. A. T. Bauerdick et al., DESY-95-236 (1995).

[102] E. Tscheslog, ZEUS Reconstruction Program, Organization and Control, ZEUS Note 91-037 (1991).

[103] G. F. Hartner, VCTRAK (3.07/04): Off-line Output Information, ZEUS Note 97-064 (1997).

[104] G. M. Briskin, Diffractive Dissociation in *ep* Deep Inelastic Scattering, Ph.D. thesis, Tel Aviv University, 1998.

[105] J. Ng, W. Verkerke, An Overview of SRTD Analysis, ZEUS Note 95-037 (1995).

[106] R. Brun et al., GEANT3, CERN DD/EE/81-1 (1987).

[107] R. van Woundenberg, ZGANA Version 3.05/01, User Manual and Documentation, (1993).

[108] K. Muchorowski, Calculating Radiative Corrections to Exclusive ρ Electroproduction at the ZEUS Detector with HERACLES, ZEUS Note 97-014 (1997).

[109] M. Arneodo, L. Lamberti, and M. Ryskin, Comp. Phys. Commun. **100** (1996) 195.

[110] A. Kwiatkowski, H. Spiesberger and H.-J. Möhring, Comp. Phys. Comm. **69** (1992) 155.

[111] E. Barberio, B. van Eijk, Z. Was, Comp. Phys. Comm. **66** (1991) 115, CERN-TH-5857-90;
E. Barberio and Z. Was, Comp. Phys. Comm. **79** (1994) 291, CERN-TH-7033-93.

[112] B. H. Y. Hung, K. Long, ZLPAIR, A Monte Carlo Generator for Lepton Pair Production by 2-Photon Process for ZEUS, ZEUS Note 95-013 (1995).

[113] J. A. M. Vermaseren, Nucl. Phys. **B229** (1983) 347.

[114] A. Courau, P. Kessler, Phys. Rev. **D46** (1992) 117.

[115] M. Kasprzak, Inclusive Properties of Diffractive and Non-Diffractive Processes at HERA, Ph.D. thesis, Warsaw University, 1996, DESY F35D-96-16;
M. Kasprzak, EPSOFT - A Monte Carlo Generator in Soft Photon-Proton Collisions, ZEUS Note 95-069 (1995).

[116] L. Adamczyk, Vector Meson Photoproduction at Large Momentum Transfer at HERA, Ph.D. thesis, Univ. of Mining and Metallurgy, Krakow, 1999, DESY-THESIS 1999-045.

[117] M. Inuzuka, Measurement of the Diffractive Cross Section in low Q^2 *ep* Scattering at HERA, Ph.D. thesis, Univ. of Tokyo, 2000.

[118] A. Mastroberardino, DIFFVM - a Monte Carlo Generator for Diffractive Processes in *ep* Scattering, ZEUS Note 98-057 (1998).

[119] T. Sjötrand, Comp. Phys. Comm. **82** (1994) 74.

[120] T. Kleiss, W. J. Stirling and S. D. Ellis, Comp. Phys. Comm. **40** (1986) 359.

[121] S. Ming, Elastic Electroproduction of J/ψ at HERA, Ph.D. thesis, Univ. of Iowa, 1997.

[122] ZEUS Collaboration, J. Breitweg et al., Exclusive Electroproduction of Charmonium at HERA, Paper submitted to the XXXX International Conference on High Energy Physics, July 2000, Osaka, Japan (Abstract 879).

[123] J. M. Jauch and F. Rohrlich, *Theory of Photons and Electrons*, (2nd ed. Springer-Verlag, Berlin, 1976).

[124] ZEUS Collaboration, M. Derrick et al., Eur. Phys. J. **C14** (1999) 213.

[125] ZEUS Collaboration, J. Breitweg et al., Proton-Dissociative Diffractive Photoproduction of Vector Mesons at Large $|t|$, Paper submitted to the XXXX International Conference on High Energy Physics, July 2000, Osaka, Japan (Abstract 884).

[126] A. Bruni, private communication.

[127] H. Abramowicz, private communication.

[128] ISR Collaboration, M. Albrow et al., Nucl. Phys. **B108** (1975) 1.

[129] CDF Collaboration, F. Abe et al., Phys. Rev. **D50** (1994) 5535.

[130] M. St-Laurent, private communication.

[131] H1 Collaboration, C. Adloff et al., Phys. Lett. **B483** (2000) 360.

[132] B. Clerbaux, VM Production at HERA, hep-ph/9908519.

[133] B. Naroska, VM Production at HERA, Proceedings of XXXVth Rencontres de Moriond, Les Arcs, France, February 2000, 360.

[134] B. Mellado, Diffractive VM Production at HERA, Book of Proceedings of ICHEP200, July 27 - August 3 2000, Osaka, Japan, Vol. 1, 444, hep-ex/0011050.

[135] H1 Collaboration, C. Adloff et al., Diffractive $\psi(2S)$ Photoproduction at HERA, Paper submitted to the XXXX International Conference on High Energy Physics, July 2000, Osaka, Japan (Abstract 987).

[136] ZEUS Collaboration, J. Breitweg et al., Exclusive Photoproduction of J/ψ Mesons, Paper submitted to the XXXX International Conference on High Energy Physics, July 2000, Osaka, Japan (Abstract 878).

[137] ZEUS Collaboration, S. Chekanov et al., Exclusive Photoproduction of J/ψ mesons at HERA, Paper submitted to the International Europhysics Conference on High Energy Physics, July 12-18, 2001, Budapest, Hungary (Abstract 548).

[138] B. Mellado, Elastic Photoproduction of $\Upsilon \to e^+e^-$, ZEUS Note 99-055 (1999).

[139] Particle Data Group, D. E. Groom et al., The European Physical Journal **C15** (2000) 1.

[140] V. N. Gribov et al., Sov. Phys. JETP **14** (1962) 1308;
V. M. Budnev, I. F. Ginzburg, G. V. Meledin and V. G. Serbo, Phys. Rev. **C15** (1975) 181.

[141] A. Polini, Exclusive Photoproduction of $J/\psi \to \mu^+\mu^-$ in $e-p$ Interactions at HERA, Ph.D. thesis, Univ. of Bologna, 2000, DESY-THESIS-2000-048.

[142] H1 Collaboration, C. Adloff et al., Phys. Lett. **B483** (2000) 23.

[143] E401 Collaboration, M. Binkley et al., Phys. Rev. Lett. **50** (1983) 302.

[144] R. Fiore, L. L. Jenkovszky and F. Paccanoni, Eur. Phys. J. **C10** (1999) 461.

[145] A. Levy, Phys. Lett. **B424** (1998) 191.

[146] B. Z. Kopeliovich et al., Phys. Lett. **B309** (1993) 179.

[147] H1 Collaboration, C. Adloff et al., Phys. Lett. **B421** (1998) 385.

[148] A. Bruni, Elastic J/ψ, $\psi(2S)$ and Υ Photoproduction at HERA, Talk given at 8th International Workshop on Deep-Inelastic Scattering DIS2000, 25th - 30th April 2000, Liverpool, UK.

[149] ZEUS Collaboration, S. Chekanov et al., Exclusive Photoproduction of $\psi(2S)$ at HERA, Paper submitted to the International Europhysics Conference on High Energy Physics, July 12-18, 2001, Budapest, Hungary (Abstract 562).

[150] Particle Data Group, D. E. Groom et al., The Review of Particle Physics, Particle Listings 2001, http://pdg.lbl.gov/2001/mxxx.html, To be published.

[151] U. Camerini et al., Phys. Rev. Lett. **35** (1975) 483.

[152] NA14 Collaboration, R. Barate et al., Z. Phys. **C33** (1987) 505.

[153] EMC Collaboration, J. J. Aubert et al., Nucl. Phys. **B213** (1983) 1.

[154] NMC Collaboration, P. Amaudraz et al., Nucl. Phys. **B371** (1992) 553.

[155] ZEUS Collaboration, J. Breitweg et al., Phys. Lett. **B437** (1998) 432.

[156] P. Merkel, Elastic/Diffractive Onium Production in *ep* in Photoproduction and DIS, Talk given at the International Europhysics Conference on High Energy Physics, Parallel Session WG5, July 15-21, 1999, Tampere, Finland.

[157] CDF Collaboration, F. Abe et al., Phys. Rev. Lett. **75** (1995) 4358.

[158] ZEUS Collaboration, S. Chekanov et al., Exclusive Electroproduction of Charmonium at HERA, Paper submitted to the International Europhysics Conference on High Energy Physics, July 12-18, 2001, Budapest, Hungary (Abstract 559).

[159] R. Ciesielski, private communication.

[160] M. Glück, E. Reya, and A. Vogt, Eur. Phys. J. **C5** (1998) 461.

[161] H. L. Lai et al., MSU-HEP-903100.

[162] A. D. Martin et al., Eur. Phys. J. **C4** (1998) 463.

[163] H. L. Lai et al., Phys. Rev. **D55** (1997) 1280.

[164] A. Caldwell and M. Soares, Vector Meson Production in the Golec-Biernat Wusthoff Model, hep-ph/0101085.

[165] S. J. Brodsky et al., JETP Lett. **70** (1999) 155.

[166] H1 Collaboration, S. Aid et al., Nucl. Phys. **B463** (1996) 3;
ZEUS Collaboration, J. Breitweg et al., Eur. Phys. J. **C2** (1998) 247.

[167] T. H. Bauer et al., Rev. Mod. Phys. **50** (1978) 261.

[168] ZEUS Collaboration, M. Derrick et al., Z. Phys. **C73** (1996) 73.

[169] ZEUS Collaboration, M. Derrick et al., Phys. Lett. **B377** (1996) 259.

[170] H1 Collaboration, C. Adloff et al., Eur. Phys. J. **C13** (2000) 371.

[171] ZEUS Collaboration, J. Breitweg et al., Eur. Phys. J. **C6** (1999) 603.

[172] ZEUS Collaboration, S. Chekanov et al., Exclusive Electroproduction of ρ^0 Mesons at HERA, Paper submitted to the International Europhysics Conference on High Energy Physics, July 12-18, 2001, Budapest, Hungary (Abstract 594).

[173] ZEUS Collaboration, J. Breitweg et al, Phys. Lett. **B487** (2000) 273.

[174] ZEUS Collaboration, J. Breitweg et al., Exclusive Electroproduction of ϕ Mesons at HERA, Paper submitted to the XXIX International Conference on High Energy Physics, July 23-29 1998, Vancouver, Canada (Abstract 793).

[175] H1 Collaboration, C. Adloff et al., Eur. Phys. J. **C10** (1999) 373.

[176] ZEUS Collaboration, J. Breitweg et al., Exclusive Electroproduction of Charmonium at HERA, Paper submitted to the XXXX International Conference on High Energy Physics, July 2000, Osaka, Japan (Abstract 438).

[177] B. Mellado, Elastic Vector Meson Production at HERA, Proceedings of the International Europhysics Conference on High Energy Physics, July 12-18, 2001, Budapest, Hungary, PRHEP-hep2001/033, hep-ex/0111008.

[178] ZEUS Collaboration, J. Breitweg et al., A Compilation of Vector Meson Cross Sections at HERA: Test of SU(4) Relation Using the $Q^2 + M_V^2$ Variable, Paper submitted to the International Europhysics Conference on High Energy Physics, July 12-18, 2001, Budapest, Hungary (Addendum to abstracts 548, 559, 594).

[179] ZEUS Collaboration, S. Chekanov et al., Eur. Phys. J. **C21** (2001) 3.

[180] U. Fricke, Phenomenology of the Proton Structure Function F_2 at low Q^2, Talk given at the International Workshop on Deep Inelastic Scattering, 27 April - 1 May, 2001, Bologna, Italy.

[181] A. Kreisel, Exclusive Vector Meson Electroproduction at low t at HERA, Talk given at the International Workshop on Deep Inelastic Scattering 27 April - 1 May 2001, Bologna, Italy.

[182] A. Caldwell, et al., An Electron Energy Correction Method: A Preliminary Implementation and Its Effect on the F_2 Measurement, ZEUS Note 94-051 (1994); A. Caldwell, et al., An Attempt to Unfold the Dead Material Distribution in the ZEUS Detector, ZEUS Note 94-047 (1994).

[183] J. Krüger, Length of Calorimeters and Effect of Absorbers in Front of Calorimeter, DESY-90-163 (1990).

[184] N. Kawulski, Vergleich zwischen experimentellen Daten und Simulation im ZEUS Kalorimeter, Diploma Thesis, Univ. of Hamburg, 1991.

[185] L. Lamberti, A Monte Carlo Generator for Diffractive J/ψ Production, ZEUS Note 93-113 (1993);
M. Arneodo, L. Lamberti, DIPSI Generator (Update), ZEUS Note 96-021 (1996).

[186] R. Hall-Wilton, et al., The CTD Tracking Resolution, ZEUS Note 99-024 (1999).

[187] B. Straub, private communication.

[188] A. Caldwell, W. Liu, B. Mellado, B. Straub, BCAL Electron Studies Part II: Energy Scale Calibration, ZEUS Note 98-018 (1998).

[189] H. Grabosch et al., A Prototype Presampler for the Uranium-Scintillator Calorimeter in ZEUS, ZEUS Note 93-059 (1993).

[190] J. Cole, A Study of Positron Energy Correction in 1995 DIS Data Using the SRTD, ZEUS Note 98-022 (1998).

[191] N. Tunning, Measurement of the Proton Structure Function F_2 at HERA Using the 1996 and 1997 ZEUS Data, Ph.D. thesis, NIKHEF, Amsterdam, 2001.

[192] M. B. Einhorn, J. Ellis and J. Finkelstein, Phys. Rev. **D5** (1972) 2063;
A. I. Sanda, Phys. Rev. **D6** (1972) 280.

[193] A. H. Mueller, Phys. Rev. **D2** (1970) 2963.

[194] Y. Akimov et al., Analysis of Diffractive $pd \to Xd$ and $pp \to Xp$ Interactions and Test of the Finite Mass Sum Rule, FERMILAB-Pub-76/36-EXP (1976).

[195] E. Lohrmann, private communication.

[196] ZEUS Collaboration, J. Breitweg et al., Eur. Phys. J. **C16** (2000) 253.